

Designing Low-Dimensional Hybrid Lead Halide Perovskites for Excitonic Photophysics, Chiroptics and Water-Stability

A Thesis

*Submitted in Partial Fulfillment of the Requirements
for the Degree of*

Doctor of Philosophy

By

Tariq Ahmad Sheikh

(20173505)



**Department of Chemistry,
Indian Institute of Science Education and Research (IISER)
Pune, India - 411008**

December 2021

DECLARATION

I declare that this written submission represents my ideas in my own words and wherever others' ideas have been included, I have adequately cited and referenced the original sources. I also declare that I have adhered to all principles of academic honesty and integrity and have not misrepresented, fabricated or falsified any idea/data/fact/source in my submission. I understand that violation of the above will be cause for disciplinary action by the Institute and can also evoke penal action from the sources which have thus not been properly cited or from whom proper permission has not been taken when needed.

Date: 16-12-2021



Tariq Ahmad Sheikh

(ID: 20173505)

CERTIFICATE

I certify that the work incorporated in the thesis entitled “**Designing Low-Dimensional Hybrid Lead Halide Perovskites for Excitonic Photophysics, Chiroptics and Water-Stability**” submitted by **Mr. Tariq Ahmad Sheikh** was carried out by the candidate, under my supervision. The work presented here or any part of it has not been included in any other thesis submitted previously for the award of any degree or diploma from any other university or institution. For the completion of the thesis, a few results are taken from collaborators after their permissions and are clearly mentioned in the thesis.

Date: 16-12-2021

Angshuman Nag
Dr. Angshuman Nag
(Research Supervisor)

Acknowledgments

I would like to thank everyone who have contributed directly or indirectly during the course of my PhD. I cannot list everyone here, but honestly, I am grateful to each and everyone who has helped me throughout this journey.

First of all, I would like to thank my thesis supervisor, Dr. Angshuman Nag, from the core of my heart. The efforts he put in shaping me as an independent researcher are really commendable. He was always actively involved in my work and provided valuable support throughout my journey. I would always look up to him for his distinguished mentoring practices in my career. In addition to his professionalism, there was always a personal touch in his supervision. Dear Sir, I will always cherish the time spent with you and wish to stay connected scientifically and personally for the lifetime.

I would like to acknowledge my research advisory committee members, Dr. Arup Rath from NCL Pune and Prof. Partha Hazra from IISER Pune, for their valuable comments and suggestions during my RAC meetings.

I would like to heartily acknowledge our collaborators, Dr. Pankaj Mandal and Miss Shabnum Maqbool at IISER Pune, Prof. Shailaja Mahamuni and Dr. Aparna Shinde at Savitribai Phule Pune University (SPPU) and Prof. Arindam Chowdhury and Mr. Nithin Pathoor at IIT Bombay. I have personally visited their labs and carried out my experiments with their help. Visiting their labs and interacting with them gave me an opportunity to learn so many new things and various new experimental techniques.

I would like to thank the Department of Chemistry, IISER Pune, for giving me an opportunity to carry out my PhD and also for the wonderful research facilities, without which research would not have been this enjoyable. I would also like to acknowledge the office and departmental staff at IISER Pune for promptly helping me whenever required.

I would like to thank Dr. Pramod Pillai and Prof. Partha Hazra's groups at IISER Pune, Prof. Narayan Pradhan's group at the Indian Association for the Cultivation of Science (IACS), Kolkatta, and Prof. D D Sarma's group at Indian Institute of Science (IISc), Bangalore, for various experimental measurements. I would also like to acknowledge SAIF IIT Bombay for EPR and ICP-AES measurements.

I would like to thank all my teachers who have taught me from day one of my schooling. I have reached this stage because of my teachers only. I am highly thankful to the faculty members of

the Department of Chemistry, University of Kashmir, for motivating and guiding me in choosing my research direction. I also acknowledge the faculty members of the Department of Chemistry, IISER Pune, who have taught me during my coursework.

A big thanks to all my lab mates for providing a wonderful environment in the lab. Working with you guys was always fun. I appreciate each and every moment spent with you, not only in the lab but outside of the lab as well. The parties and the trips we had together were always fun and a lot more enjoyable. Every one of you have contributed directly or indirectly to my work. Some of you are co-authors in my papers. I appreciate the dedication and the hard work you put in to carry out the experiments and finish the projects in time. I would always be happily ready to work or collaborate with any one of you.

I would like to thank all my friends and my family members for supporting and helping me whenever needed. I have immense gratitude and appreciation for my friends at IISER Pune. Debashree, Manzoor, Jayashree, Neetu, Debashish, Aslam, Shabnum, Shumanto, Minhaj and Borish, you guys have become a big part of life during these years. The time spent while discussing research and having weekend cooking sessions is etched in my mind and brings me endless joy. Such a cordial environment brought the best out of me at professional and personal levels. On a lighter note, I became a better cook by feeding you all. Again thanks to my family for letting me stay away from home showing trust and confidence in me.

Last but not least, I would like to acknowledge the university grants commission (UGC), India, for providing me with the fellowship during my PhD, without which living here and carrying out my research would have been really difficult.

List of Abbreviations

0D: Zero dimensional

1D: One dimensional

2D: Two dimensional

3D: Three dimensional

4,4'-EDP: 4,4'-ethylenedipyridinium

4,4'-TMDP: 4,4'-trimethylenedipyridinium

BA: Butylammonium

CB: Conduction band

CBM: Conduction band maximum

CCT: Correlated color temperature

CD: Circular dichroism

CIE: International commission on illumination

CRI: Color-rendering index

c-AFM: Conductive atomic force microscopy

DA: Decylammonium

DDA: Dodecylammonium

DSC: Differential scanning calorimetry

EPR: Electron paramagnetic resonance

EQE: External quantum efficiency

FA: Formamidinium

FESEM: Field emission scanning electron microscopy

FRET: Förster resonance energy transfer

FWHM: Full width at half maximum

HA: Hexylammonium

HDA: Hexadecylammonium

List of Abbreviations

- HFB:** Hexafluorobenzene
- HOMO:** Highest occupied molecular orbital
- ICP-OES:** Inductively coupled plasma atomic emission spectroscopy
- IRF:** Instrument response function
- LED:** Light-emitting diode
- LUMO:** Lowest unoccupied molecular orbital
- MA:** Methylammonium
- MBA:** Methylbenzylammonium
- NIR:** Near-infrared
- NMR:** Nuclear magnetic resonance
- OA:** Octylammonium
- PCE:** Power conversion efficiency
- PEA:** Phenethylammonium
- PL:** Photoluminescence
- PLQY:** Photoluminescence quantum yield
- PMT:** Photomultiplier tube
- PXRD:** Powder X-ray diffraction
- SCXRD:** Single crystal X-ray diffraction
- SHG:** Second harmonic generation
- STE:** Self-trapped exciton
- TCSPC:** Time-correlated single-photon counting
- TDA:** Tetradecylammonium
- VB:** Valance band
- VBM:** Valance band maximum
- UV:** Ultraviolet

Three-dimensional (3D) lead halide perovskites have attracted a lot of attention in the last decade due to their astonishing semiconducting properties. Recently, lower-dimensional hybrid perovskites are being widely explored for various optical and optoelectronic applications. The main focus of this thesis is to explore various types of interactions in lower-dimensional hybrid perovskites to understand their excitonic properties and introduce some new functionalities. Two-dimensional (2D) layered hybrid perovskites are Van der Waals solids with a quantum well structure. These 2D layered hybrid perovskites show some unique properties like quantum confinement in bulk-sized crystals, very high exciton binding energies and large polaron formation. However, the band gap and the emission properties of the 2D layered hybrid perovskite single crystals are not understood properly. In this thesis, the band gap and the emission properties of 2D layered hybrid perovskite single crystals are explored by using optical absorption, variable temperature steady-state and time-resolved photoluminescence and spatially resolved fluorescence microscopy imaging. The 2D inorganic layers in layered hybrid perovskites are considered electronically isolated. However, the literature studies hint that this may not be completely true. So we explored the interactions between the 2D inorganic layers by using experimental methodologies like molecular intercalation and varying interlayer separation. By using the interactions between the inorganic layers and the organic cations, we introduced chirality in 2D layered hybrid lead iodide perovskites and studied the effect of the induced chirality on their excitonic properties. We also explored the interactions between the organic cations to address one of the major challenges of the lead halide perovskites, which is their water stability.

Chapter 1: Introduction

This chapter gives an introduction to the various semiconductors and the motivation of the work done in this thesis. After a brief introduction to semiconductors, lead halide perovskites are discussed with emphasis on the perovskite structure. The discussion on perovskite structure leads to 2D layered hybrid perovskites. Layered perovskites are natural quantum wells, so the quantum well structure is discussed with an emphasis on the quantum confinement effect. One- and zero-dimensional (1D and 0D) perovskites are also briefly discussed. Hybrid perovskites consist of an anionic inorganic framework and organic cations, and this hybrid structure gives rise to various types of interactions. The interactions present in the lower dimensional perovskites are briefly discussed. In the end, the scope of the thesis is provided by discussing some of the important optical properties, ways to introduce new functionalities and possible ways to address the water instability issue of the lower dimensional hybrid perovskites.

Chapter 2: Dual Excitonic Emissions in 2D Layered Hybrid Lead Halide Perovskites

2D layered hybrid lead halide perovskites show some surprising properties. This chapter discusses the unusual band gap and light emission properties in layered hybrid lead halide perovskite single crystals, like butylammonium lead iodide [(BA)₂PbI₄]. Room-temperature optical absorption along with steady-state and time-resolved photoluminescence (PL) reveal that the (BA)₂PbI₄ single crystals show dual excitonic emissions at room temperature. Temperature-dependent PL of (BA)₂PbI₄ single crystals shows a reversible transition in the PL peak energy, around ~250 K, while cooling down the sample from room temperature and around ~275 K while heating the sample to room temperature. The transition in the PL emission arises from the reversible structural phase transition, which is confirmed by the variable-temperature single crystal X-ray diffraction (SCXRD). A structure-band gap relationship is established in (BA)₂PbI₄ by using the temperature-dependent PL and SCXRD data. Finally, a series of 2D layered hybrid lead halide perovskite single crystals are synthesized by varying the A-site organic cations and the halide ions. The single crystals of all these layered hybrid lead halide perovskites show the dual excitonic emission, irrespective of the organic cations or the halide ions.

Chapter 3: Interlayer Interactions in 2D Layered Hybrid Perovskites

2D layered hybrid halide perovskite single crystals show dual excitonic emissions. The appearance of two excitonic emissions from the same single crystal is quite surprising. It seems as if there are two band gaps, which is not possible. In this chapter, we intend to find the origin of the two excitonic emissions observed in 2D layered hybrid halide perovskites. We used spatially resolved fluorescence microscopy imaging to find the spatial distribution of the two emissions in the (BA)₂PbI₄ single crystal. Both the emissions are present throughout the crystal; however, the lower energy emission is dominant at the edges of the crystal. The higher energy emission is assigned to the excitonic transition from the isolated 2D perovskite layers, and the lower energy emission originates from the interactions between the 2D inorganic layers, dominant at the layer edges of the crystal. These assignments are verified by experimental methodologies like molecular intercalation between the 2D perovskites layers and tuning the interlayer separation. This chapter suggests that the inorganic layers in layered hybrid perovskites are not completely isolated from each other, as considered previously. The adjacent inorganic layers interact with each other, and the probability of these interactions is higher at the layer edges of the crystal.

Chapter 4: Emission Splitting and Higher Exciton Binding Energies in Chiral Layered Hybrid R- and S- α -Methylbenzylammonium Lead Iodide Perovskites

Layered hybrid perovskites are composed of semiconducting inorganic layers that are separated from each other by insulating organic cations. This layered architecture gives rise to an interface between the inorganic layers and the organic cations. The organic-inorganic interfaces give us an opportunity to introduce some novel functionalities by combining good semiconducting properties of inorganic sub-lattices with the properties of organic molecules, like chirality. This chapter explores the effect of induced chirality on the excitonic properties of layered hybrid R- and S- α -methylbenzylammonium lead iodide [(R- and S- α -MBA)₂PbI₄]. We synthesized (Rac-, R- and S- α -MBA)₂PbI₄ (Rac = racemic) perovskites. The SCXRD shows the chiral structures for (R- and S- α -MBA)₂PbI₄, which is further confirmed by the circular dichroism. To see the effect of chirality on the excitonic properties, we studied the temperature-dependent PL in (Rac-, R- and S- α -MBA)₂PbI₄. The temperature-dependent PL shows that the induced chirality splits the PL emission in these chiral (R- and S- α -MBA)₂PbI₄ at lower temperatures. Moreover, a higher exciton binding energy is also observed in (R- and S- α -MBA)₂PbI₄ compared to the achiral (Rac- α -MBA)₂PbI₄.

Chapter 5: Stabilizing Lower Dimensional Lead Halide Perovskites by Intermolecular Cation- π Interactions

Lead halide perovskites dissociate in water/moisture quite easily. This makes lead halide perovskites and their devices quite unstable in ambient conditions. For the purpose of commercialization, lead halide perovskites need to be completely stabilized in water and moist conditions. In this chapter, we introduced a strategy to stabilize lower-dimensional hybrid lead halide perovskites in water by using long-range intermolecular cation- π interactions between the A-site aromatic organic cations. We chose 4,4'-trimethylenedipyridinium (4,4'-TMDP) and 4,4'-ethylenedipyridinium (4,4'-EDP) cations, capable of showing long-range intermolecular cation- π interactions, as the A-site cations. Using 4,4'-TMDP and 4,4'-EDP as the A-site cations, completely water-stable 1D (4,4'-TMDP)Pb₂Br₆ and (4,4'-EDP)Pb₂Br₆ perovskites are synthesized. The stability of these 1D perovskites in other polar and non-polar solvents is also verified. These completely water-stable 1D perovskites show a warm white light emission, suitable for both indoor and outdoor lighting. Finally, a backlit light-emitting diode (LED) is fabricated from the water stable (4,4'-TMDP)Pb₂Br₆, which shows a stable white emission.

Appendix 1: Mn Doping in Centimeter Sized 2D Layered Butylammonium Lead Bromide, (BA)₂PbBr₄, Single Crystals

Apart from the four working chapters, this thesis also includes an appendix chapter. The appendix discusses the doping of Mn²⁺ ions in (BA)₂PbBr₄ single crystals. A bright dopant emission is observed in these Mn-doped (BA)₂PbBr₄ single crystals. This is among the first reports of Mn-doping in layered perovskite single crystals.

Thesis Summary and Future Outlook

In this section, we have summarized the work presented in this thesis. The relevance of results presented in this thesis, with the existing literature, is provided. Finally, a future research outlook is provided based on the compositional flexibility of the hybrid perovskite structure.

Table of Contents

Chapter 1: Introduction

1.1 Semiconductors.....	2
1.2 Traditional Semiconductor Materials.....	3
1.3 Lead Halide Perovskite.....	4
1.4 Perovskite Structure.....	6
1.5 2D Layered Hybrid Perovskites.....	7
1.6 Quantum Confinement and Quantum Well Structure.....	9
1.7 1D and 0D Perovskites.....	12
1.8 Interactions in Lower-Dimensional Hybrid Perovskites.....	12
1.8.1 Interactions between the inorganic layers in layered hybrid perovskites.....	13
1.8.2 Interactions between the inorganic framework and organic cations.....	14
1.8.3 Interactions between the organic cations.....	14
1.9 Water Instability a Major Challenge.....	14
1.10 Scope of this Thesis.....	16
1.11 References.....	19

Chapter 2: Dual Excitonic Emissions in 2D Layered Hybrid Lead Halide Perovskites

Abstract.....	29
Graphical Abstract.....	29
2.1 Introduction.....	30
2.2 Experimental Section.....	30
2.2.1 Chemicals.....	30
2.2.2 Synthesis of C ₄ H ₉ NH ₃ I, C ₆ H ₁₃ NH ₃ I and C ₈ H ₁₅ NH ₃ I.....	31
2.2.3 Synthesis of 2D (C ₄ H ₉ NH ₃) ₂ PbI ₄ or (BA) ₂ PbI ₄ single crystals.....	31
2.2.4 Synthesis of 2D (C ₆ H ₁₃ NH ₃) ₂ PbI ₄ or (HA) ₂ PbI ₄ single crystals.....	31
2.2.5 Synthesis of 2D (C ₈ H ₁₅ NH ₃) ₂ PbI ₄ or (OA) ₂ PbI ₄ single crystals.....	31
2.2.6 Synthesis of C ₄ H ₉ NH ₃ Br and C ₈ H ₉ NH ₃ Br.....	31
2.2.7 Synthesis of 2D (C ₄ H ₉ NH ₃) ₂ PbBr ₄ or (BA) ₂ PbBr ₄ single crystals.....	32
2.2.8 Synthesis of 2D (C ₈ H ₉ NH ₃) ₂ PbBr ₄ or (PEA) ₂ PbBr ₄ single crystals.....	32
2.2.9 Characterization.....	32
2.3 Results and Discussion.....	33

Table of Contents

2.3.1 Synthesis and characterization of (BA) ₂ PbI ₄ single crystals.....	33
2.3.2 Optical properties of (BA) ₂ PbI ₄ single crystals.....	34
2.3.3 Temperature-dependent PL of (BA) ₂ PbI ₄ single crystals.....	37
2.3.4 Temperature-dependent single crystal XRD of (BA) ₂ PbI ₄	39
2.3.5 Extending the dual excitonic emission to other layered perovskites single crystals.....	43
2.4 Conclusion.....	44
2.5 References.....	44

Chapter 3: Interlayer Interactions in 2D Layered Hybrid Perovskites

Abstract.....	49
Graphical Abstract.....	49
3.1 Introduction.....	50
3.2 Experimental Section.....	51
3.2.1 Chemicals.....	51
3.2.2 Synthesis of butylammonium iodide (C ₄ H ₉ NH ₃ I)	51
3.2.3 Synthesis of butylammonium lead iodide [(BA) ₂ PbI ₄] single crystals.....	51
3.2.4 Synthesis of hexylammonium lead iodide [(HA) ₂ PbI ₄] single crystals.....	51
3.2.5 Synthesis of octylammonium lead iodide [(OA) ₂ PbI ₄], decylammonium lead iodide [(DA) ₂ PbI ₄], dodecylammonium lead iodide [(DDA) ₂ PbI ₄], tetradecylammonium lead iodide [(TDA) ₂ PbI ₄], and hexadecylammonium lead iodide [(HDA) ₂ PbI ₄] single crystals.....	52
3.2.6 Synthesis of phenethylammonium tin iodide [(PEA) ₂ SnI ₄] single crystals.....	52
3.2.7 Iodine intercalation in (BA) ₂ PbI ₄ single crystals.....	52
3.2.8 Hexane intercalation in (DA) ₂ PbI ₄ single crystals.....	52
3.2.9 Hexafluorobenzene (HFB) insertion in (PEA) ₂ SnI ₄ single crystals forming (PEA) ₂ SnI ₄ :HFB single crystals.....	53
3.2.10 Characterization.....	53
3.2.11 Fluorescence microscopy imaging and spatially resolved spectroscopy.....	53
3.3 Results and Discussion.....	54
3.3.1 Spatially resolved PL in (BA) ₂ PbI ₄ single crystal.....	54
3.3.2 Iodine intercalation in (BA) ₂ PbI ₄ single crystal.....	56
3.3.3 Hexane intercalation in (DA) ₂ PbI ₄ single crystal.....	58
3.3.4 HFB intercalation in (PEA) ₂ SnI ₄ single crystal.....	60
3.3.5 Tuning the interlayer separation.....	64

Table of Contents

3.4 Conclusion.....	66
3.5 References.....	67

Chapter 4: Emission Splitting and Higher Exciton Binding Energies in Chiral Layered Hybrid R- and S- α -Methylbenzylammonium Lead Iodide Perovskites

Abstract.....	72
Graphical Abstract.....	72
4.1 Introduction.....	73
4.2 Experimental Section.....	74
4.2.1 Chemicals.....	74
4.2.2 Synthesis of (Rac-, R- and S- α -MBA) ₂ PbI ₄ single crystals.....	74
4.2.3 Preparation of (Rac-, R- and S- α -MBA) ₂ PbI ₄ thin films.....	75
4.2.4 Characterization.....	75
4.3 Results and Discussion.....	76
4.3.1 Synthesis and crystal structure of (Rac-, R- and S- α -MBA) ₂ PbI ₄ single crystals....	76
4.3.2 Chiroptical properties of (Rac-, R- and S- α -MBA) ₂ PbI ₄	79
4.3.3 Temperature-dependent PL in (Rac-, R- and S- α -MBA) ₂ PbI ₄	82
4.4 Conclusion.....	86
4.5 References.....	86

Chapter 5: Stabilizing Lower Dimensional Lead Halide Perovskites by Intermolecular Cation- π Interactions

Abstract.....	91
Graphical Abstract.....	91
5.1 Introduction.....	92
5.2 Experimental Section.....	93
5.2.1 Chemicals.....	93
5.2.2 Synthesis of (4,4'-TMDP)Pb ₂ Br ₆ single crystals.....	93
5.2.3 Synthesis of (4,4'-EDP)Pb ₂ Br ₆ single crystals.....	94
5.2.4 Synthesis of (4,4'-TMDP)Br ₂	94
5.2.5 Characterization.....	94

Table of Contents

5.2.6 NMR spectroscopy.....	95
5.2.7 Water stability tests of (4,4'-TMDP)Pb ₂ Br ₆ and (4,4'-EDP)Pb ₂ Br ₆ single crystals..	95
5.2.8 White LED fabrication of (4,4'-TMDP)Pb ₂ Br ₆	95
5.2.9 CIE (International Commission on Illumination), correlated color temperature (CCT) and color-rendering index (CRI) calculation.....	95
5.3 Results and Discussion.....	96
5.3.1 Synthesis and structure showing cation- π stacking.....	96
5.3.2 Nuclear magnetic resonance (NMR) spectroscopy probing the cation- π interactions.....	98
5.3.3 Optical characterization of (4,4'-TMDP)Pb ₂ Br ₆	103
5.3.4 Water stability of (4,4'-TMDP)Pb ₂ Br ₆	105
5.3.5 Application in white-LED.....	106
5.3.6 Extending the cation- π interactions to other hybrid perovskite systems.....	107
5.4 Conclusion.....	110
5.5 References.....	111
Appendix 1: Mn Doping in Centimeter Sized 2D Layered Butylammonium Lead Bromide, (BA)₂PbBr₄, Single Crystals.....	116
Thesis Summary and Future Outlook.....	132
List of Publications.....	138

Chapter 1

Introduction

1.1 Semiconductors

Metals conduct electricity, while the insulators don't. Semiconductors conduct as well as resist the electrical current. In its pristine form, a semiconductor is an insulator but abruptly changes to a conductor upon perturbation. The perturbation can be in the form of light irradiation, electrical bias, or doping. Upon perturbation, the semiconductor becomes highly conducting and is termed to be in the "on" state. This dual and completely opposite conductivity behavior makes semiconductors an interesting class of materials. These semiconductors can act as electrical switches or gates, and hence constitute major components in almost all electronic applications. The switching from the "off" to "on" state in semiconductors arises due to their finite band gap and very high carrier mobility (Figure 1.1).

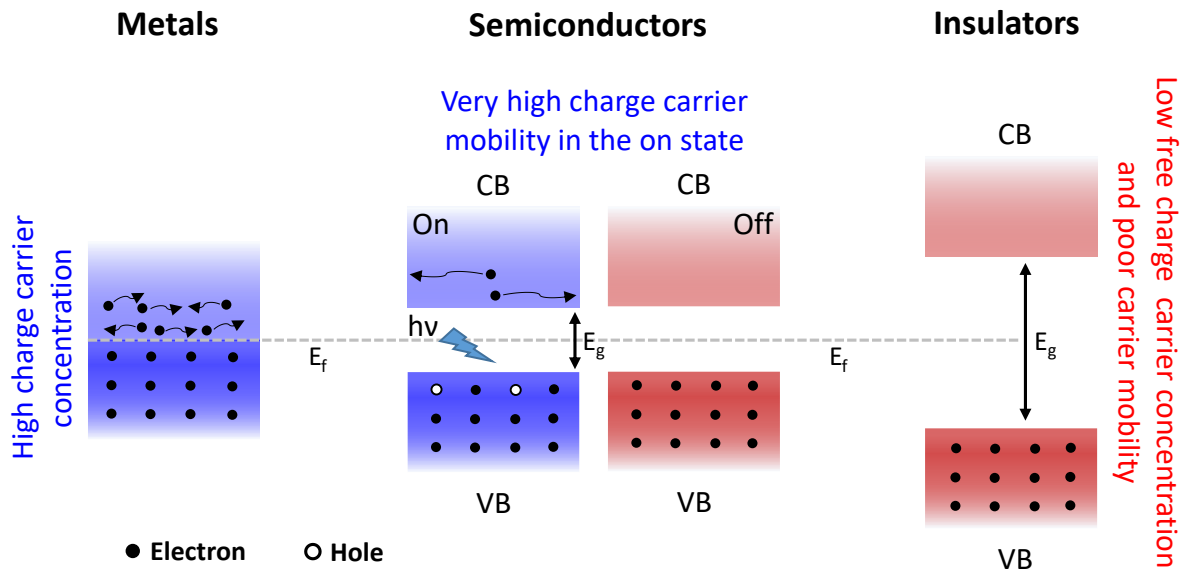


Figure 1.1: Schematic showing the band diagram of metals, semiconductors and insulators. VB = Valance band, CB = Conduction band, E_g = Band gap, E_f = Fermi level, the energy level where the probability of finding an electron is half. One way of turning on a semiconductor is by light irradiation, as shown in the schematic. Same can be done by doping or by applying an electric bias.

From the band theory of solids, we know that the valance band is completely filled with electrons and the conduction band is completely empty. In metals, we do not have valance and conduction bands separated by a band gap. Instead, the band is partially occupied, giving rise to a sea of free electrons, which conduct the electricity. Insulators have a large band gap, and their charge carrier mobility is also low. Hence insulators do not conduct electricity. Semiconductors have a moderate band gap, and in their pristine form, there are no free charge carriers; hence these do not conduct electricity. However, the band gap in semiconductors is

usually small, and a minor perturbation can easily create delocalized charge carriers. Due to their high charge carrier mobility, semiconductors conduct electricity easily in their “on” state. The electrical conductivity of semiconductors can be increased by multiple orders of magnitude upon a minor perturbation. Efficient modulation between on- and off-states make semiconductors a special class of materials for electronic and optoelectronic devices.

1.2 Traditional Semiconductor Materials

When we think of semiconductors, silicon is the first name that comes to our mind. Silicon shows a very high charge carrier mobility and large diffusion length.¹⁻² Also, silicon is highly abundant in the earth’s crust. This makes silicon the most explored and widely used semiconducting material. The commercial solar cells are mostly constituted of silicon. Apart from solar cells, silicon is widely used in electronic components like transistors, diodes, circuit boards and integrated circuits. However, silicon is an indirect band gap material, which makes it a poor light absorber and emitter. In silicon solar cells, for efficient light absorption, thick silicon absorber layers are required. This increases the cost as well as the size and weight of these solar cells. Also, the poor light emission limits the use of silicon in the lighting and display technology.

The above-mentioned problems of silicon prompted the researchers to look for direct band gap semiconductors. Over the course of time, a number of direct band gap semiconductors have been synthesized, the most common being the gallium arsenide (GaAs), gallium nitride (GaN), indium phosphide (InP), cadmium sulphide (CdS), cadmium selenide (CdSe), cadmium telluride (CdTe), indium gallium arsenide (InGaAs), copper indium gallium selenide (CIGS), etc. These direct band gap semiconductors have been used in various applications ranging from light harvesting to light emission. For example, GaAs shows the highest solar cell efficiency of 30.5%³ among the single-junction solar cells, almost touching the Shockley-Queisser limit of the highest possible efficiency of 33.16%.⁴

Some of these traditional direct band gap semiconductors show astonishing semiconducting properties. For example, GaAs, the most widely used direct band gap semiconductor, shows very high charge carrier mobilities and long diffusion lengths.¹ However, it has been found that good semiconducting properties largely depend on the quality of the crystals. Defect states, if present, quench the charge carriers, thus hugely affecting the semiconducting properties. To get rid of the defects and to improve the crystallinity, approaches like highly sophisticated epitaxial growth or high temperature (>1000 °C) synthesis have been followed. Though these

methods improve the crystal quality, at the same time increase the synthesis and processing cost hugely. This is one of the main reasons for the GaAs based solar cells not being able to replace the commercial silicon solar cells. It is to be noted that for the applications where the cost does not matter, the highly expensive traditional direct band gap semiconductors like GaAs are the materials of choice; for example, the use of GaAs based solar cells in space missions.

1.3 Lead Halide Perovskites

Recently, lead halide perovskites have emerged as a wonderful class of semiconducting materials.⁵⁻¹² These perovskites show amazing optoelectronic and photovoltaic properties like very high absorption coefficients, long charge carrier diffusion lengths and carrier lifetimes, small electron and hole effective masses, intense photoluminescence, narrow emission linewidths, high dielectric constants and strong ferroelectric polarization.¹³⁻¹⁷ Due to their astonishing semiconducting properties, lead halide perovskites have been explored for a wide range of applications like solar cells, light-emitting diodes (LEDs), photodetectors, sensors, lasers, photocatalysts, etc.¹⁸⁻²⁰

The history of lead halide perovskites dates back to the 1890s, and the perovskite structure of these halide compounds was first time reported by Moller in 1958.²¹⁻²² However, the actual boom of lead halide perovskites started in 2009 when Kojima et al. reported the first perovskite-based solar cell from methylammonium lead iodide, with an initial power conversion efficiency (PCE) of 3.8%.²³ In a time span of just two years, the reported PCE of the perovskite solar cells exceeded 10%, which was quite remarkable compared to the traditional solar cell materials.⁵ From 2012, the research on these perovskite solar cells took the speed, and in less than a decade, the perovskite solar cells started to compete with the traditional solar cells and surpassing many of them.³ The current PCE of these perovskite solar cells is 25.8%, which is quite comparable to that of the benchmark single-crystalline silicon solar cells, with a PCE of 26.1%, which took more than four decades to reach this number.^{3, 24-25} Apart from solar cells, halide perovskites have been studied for various other applications like LEDs, photodetectors, sensors, lasers, photocatalysts, etc.^{16-17, 19, 26}

One of the interesting features of lead halide perovskites is their band gap and emission color tunability over the entire visible range (Figure 1.2).²⁷ Lead iodide perovskites show the band gap in the red region, whereas the lead bromide perovskites absorb and emit in the green region. The band gap can be further shifted to the blue region by using chloride as the anion. The mixed halide compositions are also possible, which show the band gap and emission in-between that

of the pure single halide compositions. For example, CsPbI_3 shows the band gap and emission in the red region, and CsPbBr_3 shows the band gap and emission in the green region, whereas the $\text{CsPbBr}_x\text{I}_{3-x}$ has the band gap in the yellow region and also emit the yellow light. The band gap tunability in these halide perovskites gives us the advantage to make the LEDs that span the whole visible region.²⁸ Also, by using the mixture of chloride, bromide and iodide perovskites as the active layer, pure white LEDs have been fabricated.²⁹ The external quantum efficiency (EQE) of some of the perovskite-based LEDs has crossed 20%, which is quite similar to that of the commercial LEDs.³⁰

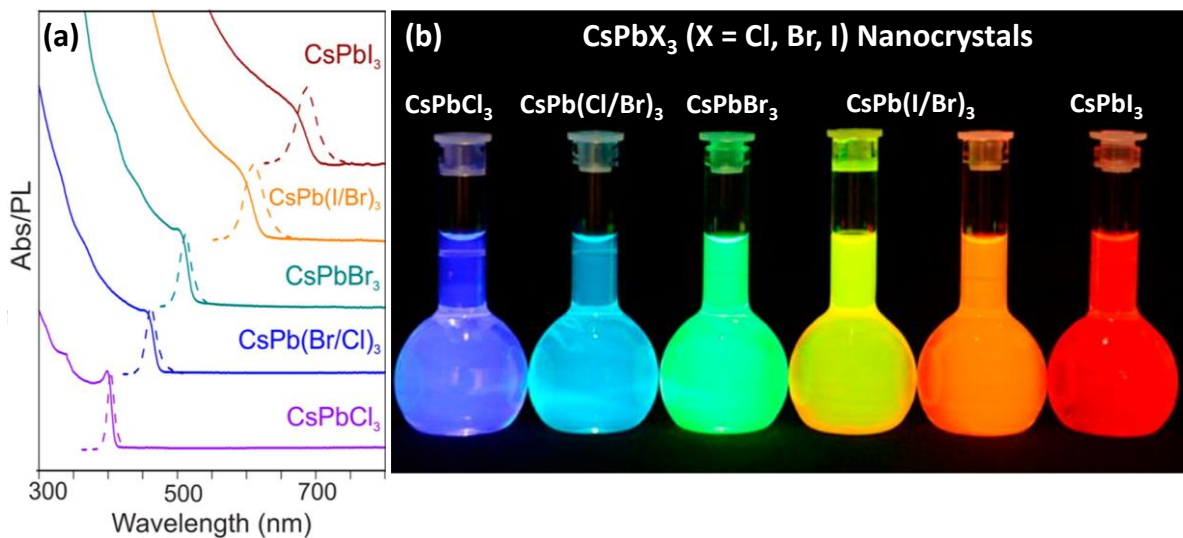


Figure 1.2: (a) Absorption (solid lines) and PL (dashed lines) spectra of colloidal CsPbX_3 nanocrystals, showing the bandgap tunability over the entire visible range. (b) Photograph of the vials containing the colloidal solutions of CsPbX_3 under UV light. A bright emission is observed, which changes systematically from blue to green to red upon changing the halide composition from pure chloride (CsPbCl_3) to bromide (CsPbBr_3) to pure iodide (CsPbI_3). The figures are reprinted from reference 27 with permission. Copyright © 2015, American Chemical Society.

Semiconducting properties largely depend on the quality of the crystals or films. Highly defect-free samples are required for good semiconducting properties. Surprisingly, lead halide perovskites show amazing semiconducting properties irrespective of the presence of defects, unlike the traditional semiconductors like GaAs or CdSe. This has been attributed to their defect tolerant band structure.^{8, 31} In these perovskites, both the valence band maximum and the conduction band minimum are antibonding in nature. The nonbonding defect states are either shallow or lie within the valence or conduction band and hence do not quench the charge carriers, thereby making them defect tolerant (Figure 1.3). This defect tolerant nature makes lead halide perovskites a unique class of materials. The complicated and expensive synthetic

methods or high temperatures are not required for making these lead halide perovskites, contrary to the traditional semiconductors. Very simple solution-processable methods are used for synthesizing these materials. This solution processibility makes their synthesis and device fabrication very easy and cost-effective.

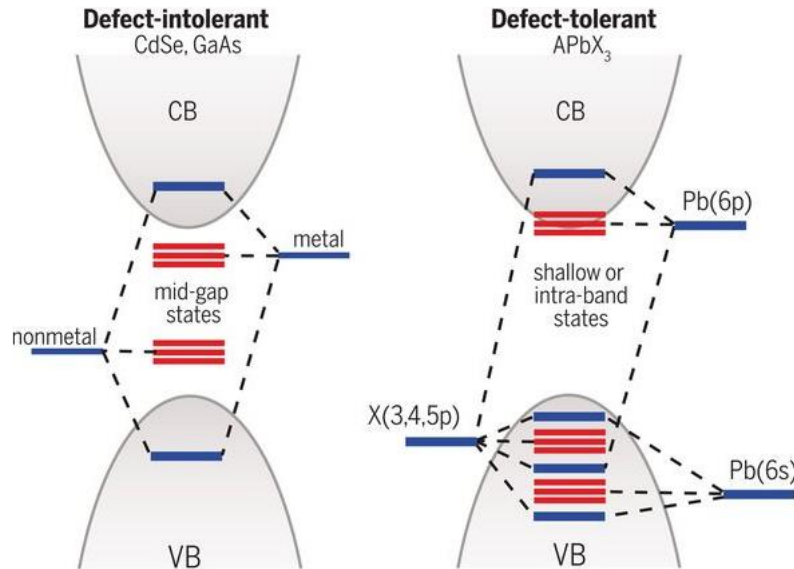


Figure 1.3: Schematic showing defect tolerant band structure of lead halide perovskites in comparison to the traditional semiconductors. The figure is reprinted from references 31 and 32 with permission. Copyright © 2017, American Association for the Advancement of Science, and Copyright © 2017, American Chemical Society, respectively.

1.4 Perovskite Structure

Perovskite, in its origin, is a mineral of calcium titanium oxide (CaTiO_3).³³ However, instead of just remaining a mineral name, perovskite has emerged as a trademark crystal structure. Materials having structure same as that of CaTiO_3 are commonly known as perovskites. The perovskite structure consists of a three-dimensional (3D) network of metal halide or metal oxide octahedra that are directly connected to each other via corner-sharing (Figure 1.4).³⁴ The 3D octahedral network gives rise to cuboctahedral voids, commonly known as the A site. The general formula of perovskites is ABX_3 , where A and B are the cations, and X is an anion. The stability of the perovskite structure is governed by the Goldschmidt tolerance factor, $t = \frac{r_A + r_B}{\sqrt{2}(r_B + r_X)}$; here, r_A and r_B are the ionic radii of the A and B cations, respectively, and r_X is the ionic radius of the X anion.³⁵⁻³⁶ For a stable perovskite structure, the value of “ t ” should be around 0.71-1.³⁵⁻³⁶ In halide perovskites, based on the size, cations like cesium (Cs^+), methylammonium (CH_3NH_3^+ ; MA^+) and formamidinium ($\text{NH}_2\text{CHNH}_2^+$; FA^+) fit in the A-site, leading to the formation of a stable perovskite structure.^{26, 37}

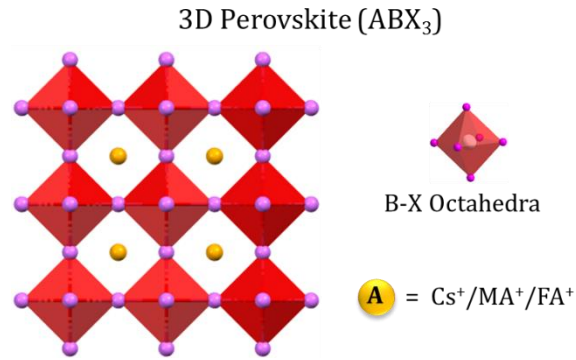


Figure 1.4: Schematic of the 3D perovskite structure showing a corner shared octahedral network.

One of the interesting features of the perovskite structure is its structural flexibility. By using large-sized A-site cations, the 3D perovskites can be reduced down to their lower-dimensional structures, known as lower-dimensional (2D, 1D and 0D) perovskites or perovskitoids.³⁸⁻³⁹ The inorganic octahedral framework in these lower-dimensional perovskites do not show 3D connectivity. It is to be mentioned here that the reduction in dimensionality is in terms of electronic connectivity only.³⁸⁻³⁹ Morphologically, these lower-dimensional perovskites are still three-dimensional. Unlike 3D perovskites, the chemical compositions of low-dimensional perovskites are not limited by the Goldschmidt tolerance factor. Consequently, it is possible to think of a large variety of organic and inorganic sub-lattices.³⁶ The compositional flexibility of these lower-dimensional perovskites gives us an opportunity to introduce various new functionalities. Compared to the 3D perovskites, the lower-dimensional perovskites show some additional interesting properties, like quantum and dielectric confinement in the bulk samples, high exciton binding energies, exciton self-trapping, large polaron formation, and sharp absorption and emission features.³⁸⁻³⁹ However, due to the reduced electronic dimensionality, the lower dimensional perovskites are expected to show poor charge carrier transport, which will be detrimental for optoelectronic applications.

1.5 2D Layered Hybrid Perovskites

The 2D layered hybrid perovskites can be obtained by slicing the inorganic layers apart in the 3D perovskites.^{38, 40-41} This can be done by the A-site cation engineering. If the A-site cation does not fit in the cuboctahedral void of the 3D perovskite structure, it splits the inorganic layers apart (Figure 1.5). The splitting of inorganic layers can occur along different crystallographic directions.³⁸ If the 3D perovskite is sliced along the (100) planes, we get (100) oriented layered perovskites. Here the 2D layers represent the (100) planes of the crystal, and the interlayer spacing is simply the distance between the (100) planes. Majority of the layered

perovskites fall in this category. Based on the number of octahedral inorganics layers that are directly connected to each other, the layered perovskites are termed as $n = 1, 2, 3$ (and so on) systems. Layered perovskites sliced along the (110) and (111) planes also exist, but these layered hybrid systems are very rare.

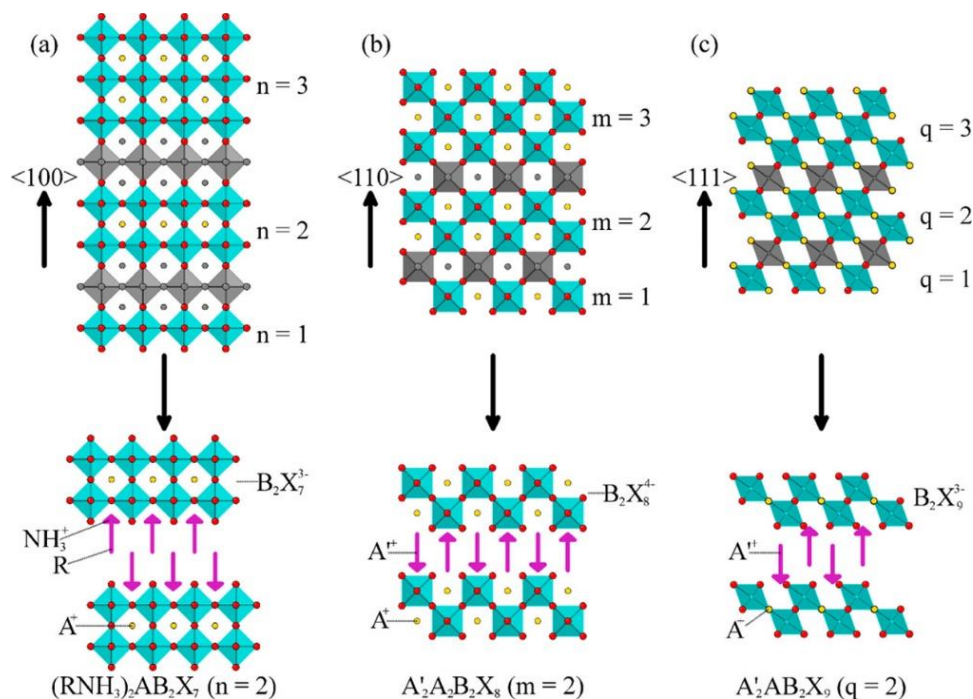


Figure 1.5: Schematic showing the slicing of a 3D perovskite into 2D layered perovskites along the different crystallographic planes. (a) (100), (b) (110), and (c) (111) oriented layered perovskites. “ n ” is the number of octahedral layers directly connected to each other in (100) layered perovskites. The analogous of “ n ” in (110) and (111) layered perovskites are “ m ” and “ q ”, respectively. The figure is reprinted from reference 38 with permission. Copyright © 2016, American Chemical Society.

In 2D layered hybrid perovskites, usually two layers of organic cations are present between the adjacent inorganic layers, each having their positively charged ammonium ions pointing towards the adjacent inorganic layers (Figure 1.6a).⁴² The organic cations are held with the inorganic layers by strong electrostatic and hydrogen-bonding interactions on both sides, forming an atomically thin single hybrid perovskite layer.^{41, 43} In a crystal, multiple hybrid perovskite layers are present and are held together by weak Van der Waals forces, which can easily be separated apart by mechanical exfoliation.⁴⁴ The adjacent inorganic layers in these perovskites are not lying exactly on top of each other; rather are shifted to some extent.⁴² However, every third layer lies exactly on top of the first layer, thus forming an ABAB type of layered structure. Due to their similarity with the Ruddlesden-Popper phase, these perovskites are usually termed as Ruddlesden-Popper layered hybrid perovskites.

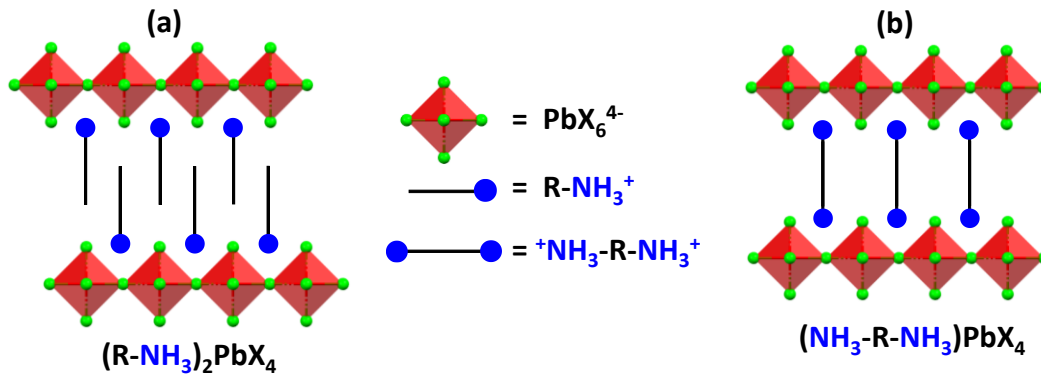


Figure 1.6: (a) Ruddlesden-Popper and (b) Dion-Jacobson type layered hybrid perovskites.

There is another class of layered hybrid perovskites that have a single layer of organic cations between the inorganic layers (Figure 1.6b).⁴⁵ In these layered systems, the organic cations have two positively charged ammonium ions on their opposite terminals, which bind with the two adjacent inorganic layers simultaneously, giving rise to a rigid layered structure. Since the inorganic layers are directly connected via single A-site bi-cations, every second inorganic layer lies exactly on top of the first layer, thus forming an AAAA type layered structure.⁴⁵ These are termed as Dion-Jacobson layered hybrid perovskites due to their similarity with the Dion-Jacobson phase. Since no Van-der Waals forces are involved, these perovskites are rigid and are not easily exfoliated.

1.6 Quantum Confinement and Quantum Well Structure

When a semiconductor absorbs light, electrons are promoted from the valance band to the conduction band and creating holes in the valance band.⁴⁶⁻⁴⁸ Because of their opposite charge, the electron and hole are attracted towards each other, leading to the formation of a quasi-particle known as exciton, an electrostatically bound electron-hole pair separated by some distance in space. The equilibrium distance between the electron and the hole in an exciton is known as Bohr exciton radius (r_B), as shown in Figure 1.7. The Bohr exciton radius in a semiconductor is analogous to the Bohr radius in the hydrogen atom. Unlike the Bohr radius, the Bohr exciton radius is not a fixed quantity, and varies from material to material. The Bohr exciton radius of a semiconductor depends on its dielectric constant and the effective masses of its electrons and the holes and is given by the equation: $r_B = \epsilon_r \frac{m_0}{\mu} a_0$; here “ ϵ_r ” is the dielectric constant of the material, “ m_0 ” is the rest mass of an electron, “ a_0 ” is the Bohr radius of hydrogen atom (0.053 nm), and “ μ ” is the reduced mass of the exciton, which is given by the equation: $\mu = \frac{m_e^* + m_h^*}{m_e^* m_h^*}$ (m_e^* and m_h^* are the effective masses of an electron and a hole, respectively).⁴⁷⁻⁴⁸

If the size of the semiconductor is reduced below its Bohr exciton radius, the electron and hole are forced to come close together, reducing the distance between the electron and hole below its neutral equilibrium distance. Now, as per the particle in a box model, the energy states are separated apart and are discretized. This phenomenon is known as the quantum confinement effect.⁴⁶⁻⁴⁷ In the particle in a box model, the absolute energy “ E ” and the energy difference between the n^{th} and $(n+1)^{\text{th}}$ states is inversely proportional to the square of the length (L^2) of the box. In a spherical crystal, the diameter of the crystal represents the length of the box.

$$E \propto \frac{1}{L^2}$$

$$\Delta E_{n,n+1} = E_{n+1} - E_n \propto \frac{1}{L^2}$$

If we consider the n^{th} and $(n+1)^{\text{th}}$ states as the valance and the conduction bands, respectively, then $\Delta E_{n,n+1}$ represents the band gap (E_g) of the semiconductor. And with the decrease in the size of the semiconductor below its Bohr exciton radius, the band gap increases.⁴⁷

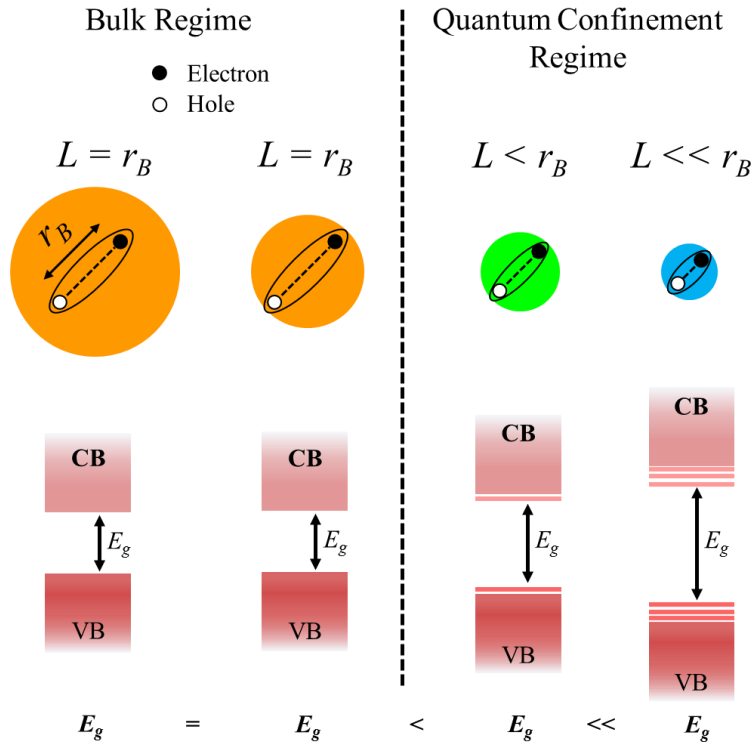


Figure 1.7: Schematic demonstrating the quantum confinement in a semiconductor. As the size of the crystal is reduced below its Bohr exciton radius (r_B), the band gap increases, and also the energy levels are discretized.

In 2D layered hybrid perovskites, the inorganic layers are semiconducting in nature, and are separated from each other by insulating organic layers.^{39, 49-52} The thickness of the semiconducting inorganic layers is usually smaller than their Bohr exciton radius, whereas their

later dimensions are very large.^{49, 53-54} The layered architecture of these semiconducting inorganic and insulating organic layers gives rise to the quantum well structure, as shown in Figure 1.8.^{39, 49-52} The semiconducting inorganic layers act as the potential wells and the insulating organic layers act as the potential barriers. The charge carriers created, like electrons, holes or excitons, gets confined to these semiconducting inorganic layers, giving rise to the quantum confinement effect.^{49, 53} Interestingly, the quantum confinement in these layered perovskites is independent of the size of the crystal. This gives rise to the nanoscale phenomenon even in bulk (size greater than the Bohr exciton radius) crystals.⁵⁴ This is quite the opposite to the 3D perovskites, where the quantum confinement can be achieved only by reducing the size of the crystal below its Bohr exciton radius.^{27, 39}

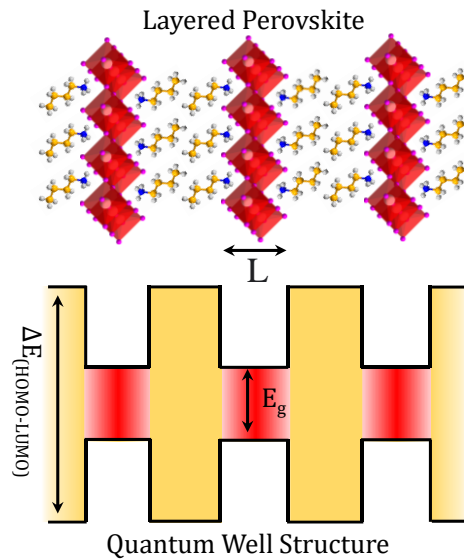


Figure 1.8: Crystal structure (top panel) and the schematic representation of the quantum well structure (bottom panel) of 2D layered perovskites. E_g is the band gap, and ΔE is the energy gap between the LUMO and HOMO levels of the organic cations.

Interestingly, the extent of the quantum confinement in layered hybrid perovskites can be varied by changing the thickness of the semiconducting inorganic well layers.^{39, 42} This can be done by changing the number of octahedral layers directly connected to each other. Figure 1.9 shows that the band gap of the layered perovskites decreases as the number of the inorganic octahedral layers directly connected to each other increase, thus following the quantum confinement effect.⁴² In the layered hybrid perovskites, there is a large dielectric contrast between the repeating inorganic and organic layers.^{39, 55-57} The inorganic layers have a high dielectric constant, whereas the organic cations usually have a very low dielectric constant. Though the excitons are created in the inorganic layer only, the organic layers also affect the electron-hole interactions by providing a low screening medium to the lines of force between

the electron and hole in an exciton.⁵²⁻⁵⁴ This increases the exciton binding energy and the excitonic confinement. This additional confinement, which arises due to the dielectric mismatch between the organic and inorganic layers, is termed as dielectric confinement.^{39, 56}

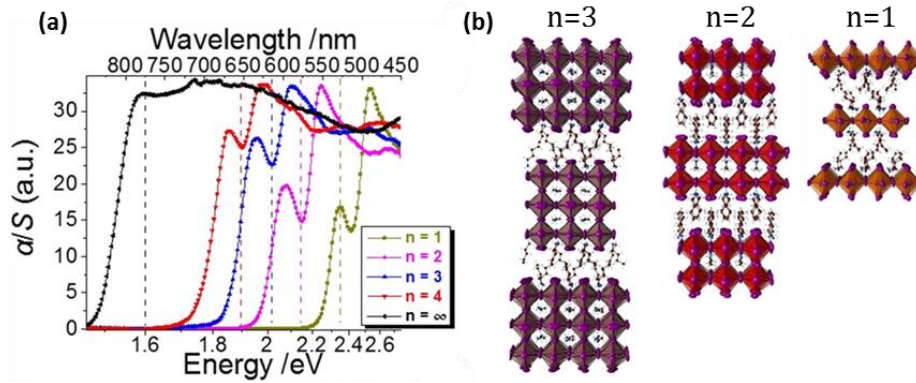


Figure 1.9: (a) Absorption spectra of $(\text{BA})_2(\text{MA})_{n-1}\text{Pb}_n\text{I}_{3n+1}$ layered perovskites ($n = 1-4$ systems). The absorption spectrum shown in black corresponds to the 3D perovskite (MAPbI_3). (b) Crystal structures of $(\text{BA})_2(\text{MA})_{n-1}\text{Pb}_n\text{I}_{3n+1}$ layered perovskites ($n = 1-3$ systems). The figure is reprinted from reference 42 with permission. Copyright © 2016, American Chemical Society.

1.7 1D and 0D Perovskites

In the previous sections, we saw that, by using large-sized A-site cations, the 3D perovskites can be reduced down to lower-dimensional 2D layered perovskites.³⁸ However, this is not always the case. Some of the A-site cations never lead to the formation of 2D layered structures rather form even lower-dimensional 1D or 0D structures, known as 1D and 0D perovskites, respectively.⁵⁸⁻⁶⁰ This mostly depends on the shape, size and symmetry of the A-site cations.^{38, 58} Linear chain A-site cations mostly form 2D layered perovskites, whereas large bulky and branched A-site cations usually lead to the formation of 1D or 0D perovskites.^{43, 61-62} These 1D and 0D perovskites have a higher degree of quantum and dielectric confinement and show a band gap higher than the 2D layered counterparts.³⁹

1.8 Interactions in Lower Dimensional Hybrid Perovskites

The 2D layered perovskite structure consists of semiconducting inorganic layers, insulating organic layers and the interfaces between the organic and inorganic layers.^{49, 53} This kind of layered architecture gives rise to various types of interactions. These include the interactions between the adjacent inorganic layers, the interactions between the organic and the inorganic layers, and the interactions among the organic A-site cations.⁶³⁻⁶⁵ The same is true for 1D and 0D perovskites. These interactions have the potential to affect the physical as well as the chemical properties of these lower-dimensional hybrid perovskites.

1.8.1 Interactions between the inorganic layers in layered hybrid perovskites

In layered hybrid perovskites, because of the quantum well structure, it is considered that the inorganic layers are electronically isolated from each other, i.e., these layers do not interact with each other.^{49, 53} However, the distance between the inorganic layers is of the order of a nanometer, and at such a small distance, a number of phenomena are possible which keep these inorganic layers connected.⁶⁴ These phenomena include Förster resonance energy transfer (FRET)⁶⁶ and interlayer exciton formation.⁶⁷⁻⁶⁹ At the layer edges, the 2D perovskite layers are quite flexible and can come close to each other quite easily, making the interaction between them more feasible. The possibility of the electronic connectivity between the adjacent inorganic layers is supported by a recent conductive atomic force microscopy (c-AFM) study in $(\text{BA})_2\text{PbI}_4$ (BA = Butylammonium) single crystals, which has shown a significant across-the-layer electrical conductivity at the layer edges of the crystal (Figure 1.10).⁷⁰ The magnitude of the current is directly proportional to the thickness of these edges. This study suggests that the 2D inorganic layers at the layer edges are indeed electronically connected to each other.

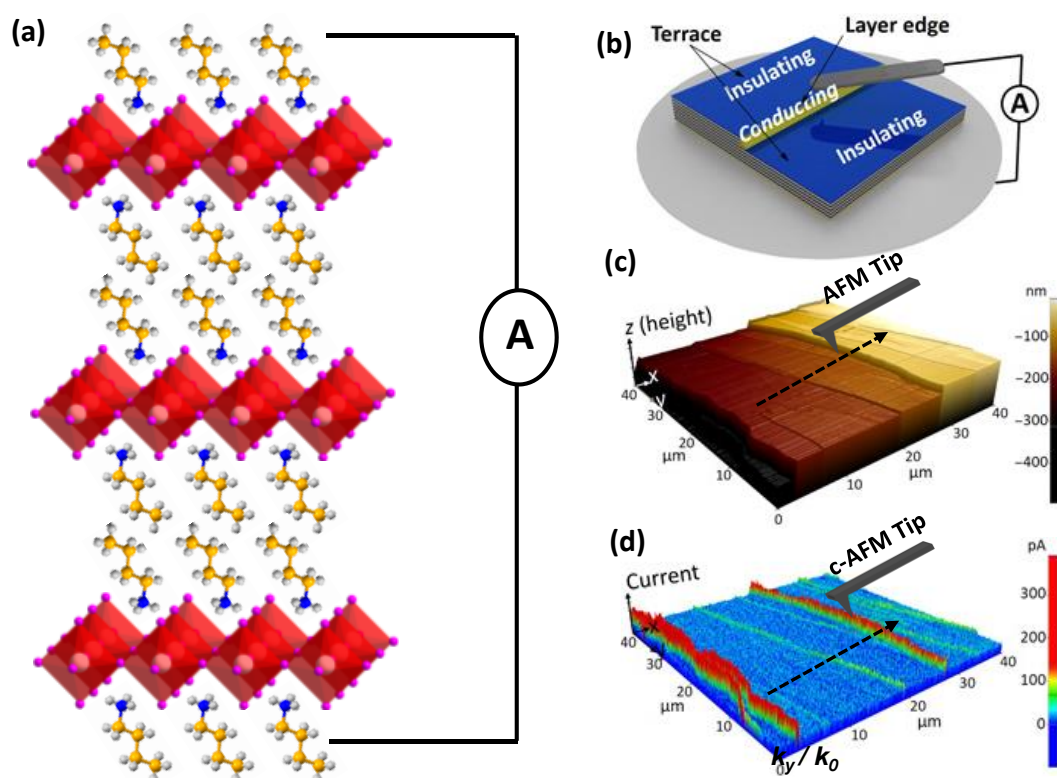


Figure 1.10: (a) Schematic demonstrating the across-the-layer electrical conductivity in layered hybrid perovskites. (b) Schematic showing the experimental c-AFM measurement setup. (c) AFM image showing the terraces and the layer edges on the surface of a $(\text{BA})_2\text{PbI}_4$ crystal. (d) c-AFM image of the same crystal showing a significant current (red) at the layer edges of the crystal. Figures b, c and d are reprinted from reference 70 with permission. Copyright © 2019, The Authors, some rights reserved; exclusive licensee AAAS.

1.8.2 Interactions between the inorganic framework and organic cations

The valence band maximum and the conduction band minimum in halide perovskites are constituted of metal and halide orbitals (inorganic framework) only.⁷¹⁻⁷³ Hence the optical and optoelectronic properties of these perovskites mostly depend on the metal halide framework only. However, the A-site cations indirectly affect the band structure and hence the properties of these layered perovskites.⁷⁴⁻⁷⁵ In the 2D layered perovskites, the organic cations are bound to the inorganic layers by electrostatic and hydrogen-bonding interactions.^{41, 43, 63} The interactions of these organic cations with the inorganic layers modify the structure of the inorganic layers, which ultimately affects their optical properties. Interestingly, these organic-inorganic interactions in these layered perovskites give us an opportunity to introduce multiple functionalities by combining various organic and inorganic properties.⁶³

1.8.3 Interactions between the organic cations

In the crystal structure of lower-dimensional perovskites, the A-site cations are closely packed in an ordered arrangement.^{43, 61-62} The A-site cations, in this closed packed structure, show some non-covalent (like Van-der Waal's) interactions among themselves.^{43, 76-77} These interactions affect the crystal structure and hence the optical properties of these perovskites. It is these non-covalent interactions between the A-site organic cations that determine the structure and the lattice type in which the perovskite crystallizes. For example, (BA)₂PbI₄ crystallizes in an orthorhombic crystal structure, whereas the (HA)₂PbI₄ (HA = hexylammonium) crystallizes in the monoclinic crystal structure, even though both have the same ammonium group that interacts with the inorganic lattice.⁴³ The interactions between the organic cations also dictate the temperature-dependent phase transitions in these lower dimensional-perovskites.⁴³ The simple linear chain A-site cations, like BA⁺ or HA⁺, usually show Van-der Waal's type of interactions only.⁴³ However, by using some specific A-site cations, other types of interactions, like intermolecular hydrogen bonding or pi-pi interactions, can also be introduced.⁶⁵

1.9 Water Instability a Major Challenge

Lead halide perovskites have now been established as a wonderful class of semiconducting materials. Irrespective of their astonishing properties, the lead halide perovskites are still far from commercialization. The main reasons are the instability of these perovskites in the ambient conditions (air and moisture)⁷⁸⁻⁸⁰ and the presence of the toxic element lead.⁸¹⁻⁸³ When the lead halide perovskites come in contact with water, they dissociate.⁷⁸⁻⁸⁰ Even the

slightest moisture can degrade these perovskites. The water instability of lead halide perovskites arises from the highly ionic nature of their A-site cations.⁸⁴⁻⁸⁶ Lead halide perovskites are composed of the lead halide framework, which is negatively charged, and the positively charged A-site cations (like Cs^+ , MA^+ , FA^+ , etc.), which counterbalance the negative charge of the lead halide framework. The lead halide framework in itself is water-insoluble. However, the A-site cations, because of their ionic nature, are highly soluble in water. Upon coming in contact with water, the A-site cations, because of their high water solubility, dissolve in water leading to the dissociation of the perovskite. Figure 1.11 demonstrates the dissociation of methylammonium lead iodide (MAPbI_3) in the presence of water or moisture to lead iodide (PbI_2) and water-soluble methylammonium iodide (MAI).⁷⁸

Two ways have been followed to address the problem of water instability of lead halide perovskites. One is the encapsulation of the perovskite material or the devices made from it.^{12, 87-89} The encapsulation improves the water stability of the lead halide perovskites to some extent. However, when the encapsulation layer breaks due to wear and tear, the perovskite material again comes in contact with the environment, where it can react with the water or moisture, leading to its degradation. The second way of addressing the issue of water instability of lead halide perovskites includes the use of long-chain hydrophobic organic A-site cations like butylammonium (BA ; $\text{CH}_3(\text{CH}_2)_3\text{NH}_3^+$), phenethylammonium (PEA ; $\text{C}_6\text{H}_5(\text{CH}_2)_2\text{NH}_3^+$) ions, etc.^{42, 90-91} Because of their large size, these cations do not fit at the A-site and result in the formations of lower-dimensional perovskites. Due to the hydrophobic nature of the long-chain A-site cations, these lower-dimensional perovskites show much-improved water stability compared to the 3D perovskites.⁹⁰ However, these long-chain organic A-site cations still have a positively charged ammonium group ($-\text{NH}_3^+$) group, which can interact with water again, leading to the dissociation of these perovskites. So the encapsulation and the use of simple long-chain hydrophobic A-site cations are not permanent solutions.

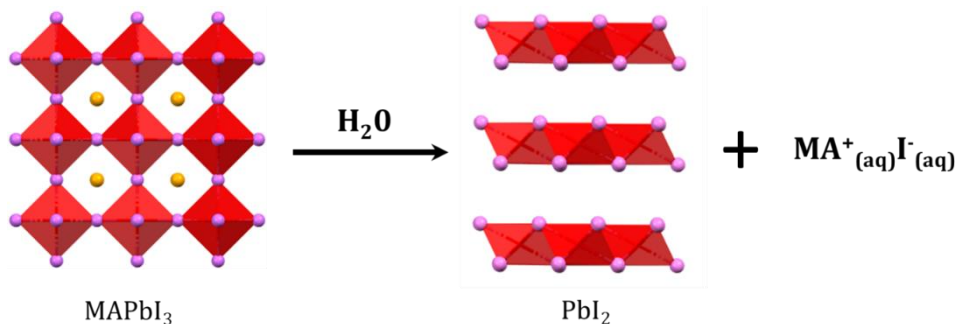


Figure 1.11: Schematic showing the dissociation of a 3D perovskite, MAPbI_3 , in the presence of water/moisture to PbI_2 and water-soluble MAI.

Water instability of lead halide perovskites is accompanied by another issue, i.e., the lead toxicity.⁸¹⁻⁸³ Lead halide perovskites, upon dissociation in water, release the toxic lead into the environment. This toxic lead contaminates the groundwater and emerges as a major health threat. Addressing the water instability issue of lead halide perovskites will automatically address their lead toxicity issue to some extent. The water-stable lead halide perovskites will not release any lead into the environment, and hence the lead toxicity will no longer be a major issue. The other way of addressing this toxicity issue is to look for non-toxic alternatives to lead. A lot of work is going on in this direction;⁹²⁻⁹⁷ however, no major breakthrough has been achieved yet. Apart from the water instability and the lead toxicity, lead halide perovskites face some other challenges as well, like thermal instability, phase instability in some compositions, photo-degradation, and halide exchange and segregation.^{29, 98-100}

1.10 Scope of this Thesis

As discussed above, the lower-dimensional perovskites show various types of interactions. These interactions impact the physical as well as the chemical properties of these perovskites. In this thesis, we explored these interactions in lower-dimensional lead halide perovskite single crystals to understand their optical properties, introduce new functionalities and address their water and moisture instability issue.

2D layered hybrid perovskites show some surprising properties, like across-the-layer electrical conductivity at the layer edges of the crystals. Similarly, compared to the 3D perovskites, the 2D layered hybrid perovskites show unusual optical properties. For example, the absorption and emission spectra of $(\text{BA})_2\text{PbI}_4$, a widely explored layered hybrid perovskite, show two features in the excitonic region, unlike the 3D perovskites which show a single absorption and emission feature in the excitonic region (Figure 1.12).^{51, 101} Also, the reported band gap of $(\text{BA})_2\text{PbI}_4$ varies from 2.24 eV to 2.43 eV.^{42, 90} This difference in the reported band gap of $(\text{BA})_2\text{PbI}_4$ is too large for such a material having a direct band gap with sharp absorption features. The same is true for other layered hybrid perovskite single crystals as well. Band gap is one of the most important properties of semiconducting materials, but for the layered hybrid perovskites, the band gap is not understood completely. As mentioned above, layered hybrid perovskites show some interesting properties; however, without a proper understanding of their band gaps and emission behavior, these properties can not be explored to their maximum potential. So the understanding of the band gap and the emission properties of these layered hybrid perovskites is of utmost importance.

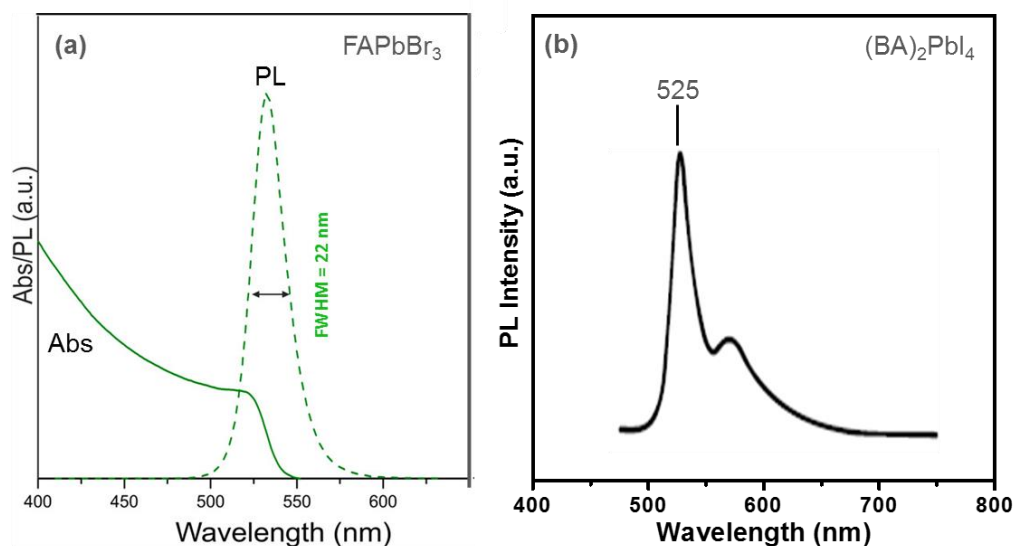


Figure 1.12: (a) Absorption and PL spectra of 3D formamidinium lead bromide (FAPbBr₃) nanocrystals. A single emission peak is observed in the PL spectrum of FAPbBr₃ nanocrystals. (b) PL spectrum of 2D BA₂PbI₄ single crystal, showing two emission peaks. Figure a is reprinted from reference 101 with permission. Copyright © 2016, American Chemical Society. Figure b is reprinted from reference 51 with permission. Copyright © 1996, American Chemical Society.

In chapter two of this thesis, we synthesized a series of layered hybrid perovskite single crystals with the motivation of understanding their band gap and emission properties. Surprisingly, all these layered perovskites showed two emission features in the visible region. By using optical absorption, temperature-dependent (10 K to 300 K) steady-state and time-resolved photoluminescence spectroscopy, we showed that both the emission features observed in layered hybrid perovskite single crystals are excitonic in nature.

The appearance of two excitonic emissions from the same single crystal is quite surprising. It seems as if there are two band gaps in these layered hybrid perovskite single crystals, which is quite absurd. In chapter three, we tried to find the origin of the two excitonic emissions observed in the layered hybrid perovskites. From the spatially resolved fluorescence microscopy imaging, we found that the higher energy emission is present throughout the crystal, while the lower-energy emission is mostly dominated at the layer-edges of the crystal. Further, by using the molecular intercalation and variable interlayer separation, we demonstrated that the higher energy emission originates from the individual 2D inorganic quantum well layers, whereas the lower energy emission originates from the possible interactions between the adjacent inorganic layers, mainly at the layer edges of the crystal. So the inorganic layers in the layered hybrid perovskites are not completely isolated from each other.

In layered hybrid perovskites, an interface is generated between the inorganic and the organic layers. This organic-inorganic interface can be utilized to introduce some new properties in these layered hybrid perovskites.^{63, 102} Some specific properties of organic molecules like chirality can be combined with the good semiconducting properties of the inorganic lattices to achieve functionalities like circular dichroism (CD), circularly polarized emission, circularly polarized second harmonic generation (SHG), circularly polarized photodetectors, chiral ferroelectricity, spin selectivity, etc.¹⁰² In chapter four of this thesis, we introduced chirality in the layered hybrid R- and S- α -methylbenzylammonium lead iodide [(R/S- α -MBA)₂PbI₄] and explored its effect on their optical properties. The chirality generates an asymmetry in their crystal structure, which gives rise to the second harmonic generation. Furthermore, the introduced chirality in (R/S- α -MBA)₂PbI₄ splits their absorption and emission lines, which is clearly visible at the cryogenic temperatures.

Lead halide perovskites dissociate in the presence of water or moisture, and this limits their extended characterizations and their device applicability. The water instability of lead halide perovskites has been attributed to the highly ionic nature of their A-site cations.⁷⁸⁻⁸⁰ Encapsulation and the use of hydrophobic A-site cations have been tried, but both these methods provided a short-term solution only.^{12, 87-90} For a permanent solution, we need A-site cations that are completely water-insoluble once incorporated in the perovskite lattice. In chapter five of this thesis, we tried to provide a permanent solution to the water instability issue in the lower dimensional hybrid perovskites. We utilized the intermolecular cation- π interactions between the A-site cations to generate a long-range cation- π stacking. We chose the 4,4'-trimethylenedipyridinium (4,4'-TMDP) and 4,4'-ethylenedipyridinium (4,4'-EDP) as the starting A-site cations because these cations are capable of showing cation- π stacking (see Figure 1.13).

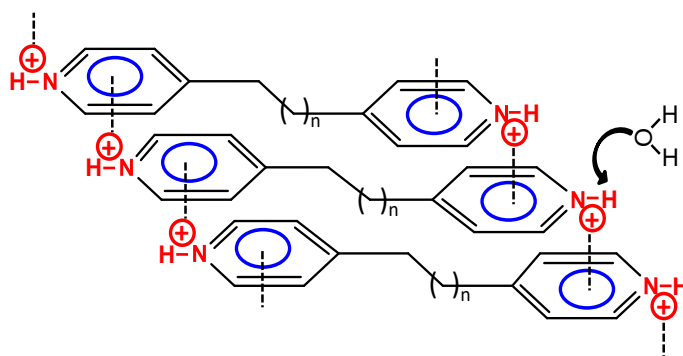


Figure 1.13: A long-range cation- π stacking in 4,4'-Dipyridinium ions. The cation- π interactions between these cations are stronger than their interactions with water. The Figure is reprinted from reference 65 with permission. Copyright © 2021, John Wiley and Sons.

Using these cations, we synthesized (4,4'-TMDP)Pb₂Br₆ and (4,4'-EDP)Pb₂Br₆ perovskites. Interestingly, the 4,4'-TMDP and 4,4'-EDP cations in (4,4'-TMDP)Pb₂Br₆ and (4,4'-EDP)Pb₂Br₆, respectively, showed a long-range cation- π stacking, extending throughout their crystals. Also, the cation- π interactions between these cations turned out to be stronger than cation water interactions, and the resulting (4,4'-TMDP)Pb₂Br₆ and (4,4'-EDP)Pb₂Br₆ perovskite were completely water stable. Furthermore, these water-stable perovskites showed a stable white light emission.

1.11 References

1. Sze, S. M. *Semiconductor Devices Physics and Technology*. JOHN WILEY & SONS, INC. **1985**.
2. Neamen, D. A. *Semiconductor Physics and Devices: Basic Principles McGraw-Hill* **2003**.
3. NREL's "Best Research-Cell Efficiencies" Chart, <https://www.nrel.gov/pv/cell-efficiency.html>.
4. Rühle, S. Tabulated values of the Shockley–Queisser Limit for Single Junction Solar Cells. *Sol. Energy* **2016**, *130*, 139-147.
5. Lee, M. M.; Teuscher, J.; Miyasaka, T.; Murakami, T. N.; Snaith, H. J. Efficient Hybrid Solar Cells Based on Meso-Superstructured Organometal Halide Perovskites. *Science* **2012**, *338*, 643-647.
6. Etgar, L.; Gao, P.; Xue, Z.; Peng, Q.; Chandiran, A. K.; Liu, B.; Nazeeruddin, M. K.; Grätzel, M. Mesoscopic CH₃NH₃PbI₃/TiO₂ Heterojunction Solar Cells. *J. Am. Chem. Soc.* **2012**, *134*, 17396-17399.
7. Swarnkar, A.; Chulliyil, R.; Ravi, V. K.; Irfanullah, M.; Chowdhury, A.; Nag, A. Colloidal CsPbBr₃ Perovskite Nanocrystals: Luminescence beyond Traditional Quantum Dots. *Angew. Chem. Int. Ed.* **2015**, *54*, 15424-15428.
8. Akkerman, Q. A.; Rainò, G.; Kovalenko, M. V.; Manna, L. Genesis, Challenges and Opportunities for Colloidal Lead Halide Perovskite Nanocrystals. *Nat. Mater.* **2018**, *17*, 394-405.
9. Moot, T.; Werner, J.; Eperon, G. E.; Zhu, K.; Berry, J. J.; McGehee, M. D.; Luther, J. M. Choose Your Own Adventure: Fabrication of Monolithic All-Perovskite Tandem Photovoltaics. *Adv. Mater.* **2020**, *32*, 2003312.
10. Haque, A.; Chonamada, T. D.; Dey, A. B.; Santra, P. K. Insights into the Interparticle Mixing of CsPbBr₃ and CsPbI₃ Nanocubes: Halide Ion Migration and Kinetics. *Nanoscale* **2020**, *12*, 20840-20848.

Chapter 1
Introduction

11. Rastogi, P.; Chu, A.; Gréboval, C.; Qu, J.; Noubé, U. N.; Chee, S.-S.; Goyal, M.; Khalili, A.; Xu, X. Z.; Cruguel, H.; Ithurria, S.; Gallas, B.; Dayen, J.-F.; Dudy, L.; Silly, M. G.; Patriarche, G.; Degiron, A.; Vincent, G.; Lhuillier, E. Pushing Absorption of Perovskite Nanocrystals into the Infrared. *Nano Lett.* **2020**, *20*, 3999-4006.
12. Ravi, V. K.; Saikia, S.; Yadav, S.; Nawale, V. V.; Nag, A. CsPbBr₃/ZnS Core/Shell Type Nanocrystals for Enhancing Luminescence Lifetime and Water Stability. *ACS Energy Lett.* **2020**, *5*, 1794-1796.
13. Xing, G.; Mathews, N.; Sun, S.; Lim, S. S.; Lam, Y. M.; Grätzel, M.; Mhaisalkar, S.; Sum, T. C. Long-Range Balanced Electron- and Hole-Transport Lengths in Organic-Inorganic CH₃NH₃PbI₃. *Science* **2013**, *342*, 344-347.
14. Stranks, S. D.; Eperon, G. E.; Grancini, G.; Menelaou, C.; Alcocer, M. J. P.; Leijtens, T.; Herz, L. M.; Petrozza, A.; Snaith, H. J. Electron-Hole Diffusion Lengths Exceeding 1 Micrometer in an Organometal Trihalide Perovskite Absorber. *Science* **2013**, *342*, 341-344.
15. Shi, D.; Adinolfi, V.; Comin, R.; Yuan, M.; Alarousu, E.; Buin, A.; Chen, Y.; Hoogland, S.; Rothenberger, A.; Katsiev, K.; Losovyj, Y.; Zhang, X.; Dowben, P. A.; Mohammed, O. F.; Sargent, E. H.; Bakr, O. M. Low Trap-State Density and Long Carrier Diffusion in Organolead Trihalide Perovskite Single Crystals. *Science* **2015**, *347*, 519-522.
16. Egger, D. A.; Rappe, A. M.; Kronik, L. Hybrid Organic–Inorganic Perovskites on the Move. *Acc. Chem. Res.* **2016**, *49*, 573-581.
17. Rosales, B. A.; Hanrahan, M. P.; Boote, B. W.; Rossini, A. J.; Smith, E. A.; Vela, J. Lead Halide Perovskites: Challenges and Opportunities in Advanced Synthesis and Spectroscopy. *ACS Energy Lett.* **2017**, *2*, 906-914.
18. Green, M. A.; Ho-Baillie, A.; Snaith, H. J. The Emergence of Perovskite Solar Cells. *Nat. Photonics* **2014**, *8*, 506-514.
19. Gao, P.; Grätzel, M.; Nazeeruddin, M. K. Organohalide Lead Perovskites for Photovoltaic Applications. *Energy Environ. Sci.* **2014**, *7*, 2448-2463.
20. Grätzel, M. The Light and Shade of Perovskite Solar Cells. *Nat. Mater.* **2014**, *13*, 838-842.
21. Wells, H. L. Über die Cäsium- und Kalium-Bleihalogenide. *Anorg. Chemi.* **1893**, *3*, 195-210.
22. MØLLER, C. K. Crystal Structure and Photoconductivity of Cæsium Plumbohalides. *Nature* **1958**, *182*, 1436-1436.
23. Kojima, A.; Teshima, K.; Shirai, Y.; Miyasaka, T. Organometal Halide Perovskites as Visible-Light Sensitizers for Photovoltaic Cells. *J. Am. Chem. Soc.* **2009**, *131*, 6050-6051.

24. Haase, F.; Hollemann, C.; Schäfer, S.; Merkle, A.; Rienäcker, M.; Krügener, J.; Brendel, R.; Peibst, R. Laser Contact Openings for Local Poly-Si-metal Contacts Enabling 26.1%-Efficient POLO-IBC Solar Cells. *Sol. Energy Mater. Sol. Cells* **2018**, *186*, 184-193.
25. Min, H.; Lee, D. Y.; Kim, J.; Kim, G.; Lee, K. S.; Kim, J.; Paik, M. J.; Kim, Y. K.; Kim, K. S.; Kim, M. G.; Shin, T. J.; Il Seok, S. Perovskite Solar Cells with Atomically Coherent Interlayers on SnO₂ Electrodes. *Nature* **2021**, *598*, 444-450.
26. Jena, A. K.; Kulkarni, A.; Miyasaka, T. Halide Perovskite Photovoltaics: Background, Status, and Future Prospects. *Chem. Rev.* **2019**, *119*, 3036-3103.
27. Protesescu, L.; Yakunin, S.; Bodnarchuk, M. I.; Krieg, F.; Caputo, R.; Hendon, C. H.; Yang, R. X.; Walsh, A.; Kovalenko, M. V. Nanocrystals of Cesium Lead Halide Perovskites (CsPbX₃, X = Cl, Br, and I): Novel Optoelectronic Materials Showing Bright Emission with Wide Color Gamut. *Nano Lett.* **2015**, *15*, 3692-3696.
28. Liu, X.-K.; Xu, W.; Bai, S.; Jin, Y.; Wang, J.; Friend, R. H.; Gao, F. Metal Halide Perovskites for Light-Emitting Diodes. *Nat. Mater.* **2021**, *20*, 10-21.
29. Ravi, V. K.; Scheidt, R. A.; DuBose, J.; Kamat, P. V. Hierarchical Arrays of Cesium Lead Halide Perovskite Nanocrystals through Electrophoretic Deposition. *J. Am. Chem. Soc.* **2018**, *140*, 8887-8894.
30. Chiba, T.; Hayashi, Y.; Ebe, H.; Hoshi, K.; Sato, J.; Sato, S.; Pu, Y.-J.; Ohisa, S.; Kido, J. Anion-Exchange Red Perovskite Quantum Dots with Ammonium Iodine Salts for Highly Efficient Light-Emitting Devices. *Nat. Photonics* **2018**, *12*, 681-687.
31. Kovalenko, M. V.; Protesescu, L.; Bodnarchuk, M. I. Properties and Potential Optoelectronic Applications of Lead Halide Perovskite Nanocrystals. *Science* **2017**, *358*, 745-750.
32. Brandt, R. E.; Poindexter, J. R.; Gorai, P.; Kurchin, R. C.; Hoye, R. L. Z.; Nienhaus, L.; Wilson, M. W. B.; Polizzotti, J. A.; Sereika, R.; Žaltauskas, R.; Lee, L. C.; MacManus-Driscoll, J. L.; Bawendi, M.; Stevanović, V.; Buonassisi, T. Searching for “Defect-Tolerant” Photovoltaic Materials: Combined Theoretical and Experimental Screening. *Chem. Mater.* **2017**, *29*, 4667-4674.
33. McHenry, M. D. G. a. M. Structure of Materials: An Introduction to Crystallography, Diffraction and Symmetry. *Cambridge University Press*, **2007**.
34. Li, C.; Lu, X.; Ding, W.; Feng, L.; Gao, Y.; Guo, Z. Formability of ABX₃ (X = F, Cl, Br, I) Halide Perovskites. *Acta Crystallogr. B* **2008**, *64*, 702-707.
35. Goldschmidt, V. M. Die Gesetze der Krystallochemie. *Naturwissenschaften* **1926**, *14*, 477-485.

Chapter 1
Introduction

36. Liu, X.; Hong, R.; Tian, C. Tolerance Factor and the Stability Discussion of ABO₃-Type Ilmenite. *J. Mater. Sci.: Mater. Electron.* **2008**, *20*, 323.
37. Li, Z.; Yang, M.; Park, J.-S.; Wei, S.-H.; Berry, J. J.; Zhu, K. Stabilizing Perovskite Structures by Tuning Tolerance Factor: Formation of Formamidinium and Cesium Lead Iodide Solid-State Alloys. *Chem. Mater.* **2016**, *28*, 284-292.
38. Saparov, B.; Mitzi, D. B. Organic–Inorganic Perovskites: Structural Versatility for Functional Materials Design. *Chem. Rev.* **2016**, *116*, 4558-4596.
39. Katan, C.; Mercier, N.; Even, J. Quantum and Dielectric Confinement Effects in Lower-Dimensional Hybrid Perovskite Semiconductors. *Chem. Rev.* **2019**, *119*, 3140-3192.
40. Mitzi, D. B.; Chondroudis, K.; Kagan, C. R. Design, Structure, and Optical Properties of Organic–Inorganic Perovskites Containing an Oligothiophene Chromophore. *Inorg. Chem.* **1999**, *38*, 6246-6256.
41. Mitzi, D. B. Templating and Structural Engineering in Organic–Inorganic Perovskites. *J. Chem. Soc., Dalton Trans.* **2001**, 1-12.
42. Stoumpos, C. C.; Cao, D. H.; Clark, D. J.; Young, J.; Rondinelli, J. M.; Jang, J. I.; Hupp, J. T.; Kanatzidis, M. G. Ruddlesden–Popper Hybrid Lead Iodide Perovskite 2D Homologous Semiconductors. *Chem. Mater.* **2016**, *28*, 2852-2867.
43. Billing, D. G.; Lemmerer, A. Synthesis, Characterization and Phase Transitions in the Inorganic–Organic Layered Perovskite-Type Hybrids [(C_nH_{2n+1}NH₃)₂PbI₄], n = 4, 5 and 6. *Acta Crystallogr. B* **2007**, *63*, 735-747.
44. Yaffe, O.; Chernikov, A.; Norman, Z. M.; Zhong, Y.; Velauthapillai, A.; van der Zande, A.; Owen, J. S.; Heinz, T. F. Excitons in Ultrathin Organic–Inorganic Perovskite Crystals. *Phys. Rev. B* **2015**, *92*, 045414.
45. Mao, L.; Ke, W.; Pedesseau, L.; Wu, Y.; Katan, C.; Even, J.; Wasielewski, M. R.; Stoumpos, C. C.; Kanatzidis, M. G. Hybrid Dion–Jacobson 2D Lead Iodide Perovskites. *J. Am. Chem. Soc.* **2018**, *140*, 3775-3783.
46. Castellan, G. W. Physical Chemistry. *Addison-Wesley* **1973**.
47. Gaponenko, S. V. *Optical Properties of Semiconductor Nanocrystals*. Cambridge University Press: Cambridge, 1998.
48. Krauss, T. D.; Peterson, J. J. Electronic Structure and Optical Transitions in Colloidal Semiconductor Nanocrystals. Colloidal Quantum Dot Optoelectronics and Photovoltaics, Sargent, E. H.; Konstantatos, G., Eds. *Cambridge University Press: Cambridge*, **2013**, 59-86.
49. Ishihara, T.; Takahashi, J.; Goto, T. Optical Properties due to Electronic Transitions in Two-Dimensional Semiconductors (C_nH_{2n+1}NH₃)₂PbI₄. *Phys. Rev. B* **1990**, *42*, 11099-11107.

50. Papavassiliou, G. C.; Koutselas, I. B.; Terzis, A.; Whangbo, M. H. Structural and Electronic Properties of the Natural Quantum-Well System $(C_6H_5CH_2CH_2NH_3)_2SnI_4$. *Solid State Commun.* **1994**, *91*, 695-698.
51. Mitzi, D. B. Synthesis, Crystal Structure, and Optical and Thermal Properties of $(C_4H_9NH_3)_2MI_4$ (M = Ge, Sn, Pb). *Chem. Mater.* **1996**, *8*, 791-800.
52. Mitzi, D. B.; Chondroudis, K.; Kagan, C. R. Organic-Inorganic Electronics. *IBM J. Res Dev.* **2001**, *45*, 29-45.
53. Ishihara, T.; Takahashi, J.; Goto, T. Exciton State in Two-Dimensional Perovskite Semiconductor $(C_{10}H_{21}NH_3)_2PbI_4$. *Solid State Commun.* **1989**, *69*, 933-936.
54. Nag, A. "Plenty of Room" at the Interface of Hybrid Metal Halide Perovskite Single Crystals. *Nano Lett.* **2021**, *21*, 8529-8531.
55. Traore, B.; Pedesseau, L.; Assam, L.; Che, X.; Blancon, J.-C.; Tsai, H.; Nie, W.; Stoumpos, C. C.; Kanatzidis, M. G.; Tretiak, S.; Mohite, A. D.; Even, J.; Kepenekian, M.; Katan, C. Composite Nature of Layered Hybrid Perovskites: Assessment on Quantum and Dielectric Confinements and Band Alignment. *ACS Nano* **2018**, *12*, 3321-3332.
56. Chakraborty, R.; Nag, A. Dielectric Confinement for Designing Compositions and Optoelectronic Properties of 2D Layered Hybrid Perovskite. *Phys. Chem. Chem. Phys.* **2021**, *23*, 82-93.
57. Chakraborty, R.; Nag, A. Correlation of Dielectric Confinement and Excitonic Binding Energy in 2D Layered Hybrid Perovskites Using Temperature Dependent Photoluminescence. *J. Phys. Chem. C* **2020**, *124*, 16177-16185.
58. Gao, P.; Bin Mohd Yusoff, A. R.; Nazeeruddin, M. K. Dimensionality Engineering of Hybrid Halide Perovskite Light Absorbers. *Nat. Commun.* **2018**, *9*, 5028.
59. Ma, C.; Shen, D.; Huang, B.; Li, X.; Chen, W.-C.; Lo, M.-F.; Wang, P.; Hon-Wah Lam, M.; Lu, Y.; Ma, B.; Lee, C.-S. High Performance Low-Dimensional Perovskite Solar Cells Based on a One Dimensional Lead Iodide Perovskite. *J. Mater. Chem. A* **2019**, *7*, 8811-8817.
60. Sun, C.; Jiang, K.; Han, M.-F.; Liu, M.-J.; Lian, X.-K.; Jiang, Y.-X.; Shi, H.-S.; Yue, C.-Y.; Lei, X.-W. A Zero-Dimensional Hybrid Lead Perovskite with Highly Efficient Blue-Violet Light Emission. *J. Mater. Chem. C* **2020**, *8*, 11890-11895.
61. Billing, D. G.; Lemmerer, A. Synthesis, Characterization and Phase Transitions of the Inorganic–Organic Layered Perovskite-Type Hybrids $[(C_nH_{2n+1}NH_3)_2PbI_4]$, (n = 12, 14, 16 and 18). *New J. Chem.* **2008**, *32*, 1736-1746.

62. Lemmerer, A.; Billing, D. G. Synthesis, Characterization and Phase Transitions of the Inorganic–Organic Layered Perovskite-Type Hybrids $[(C_nH_{2n+1}NH_3)_2PbI_4]$, $n = 7, 8, 9$ and 10 . *Dalton Trans.* **2012**, *41*, 1146-1157.
63. Jana, M. K.; Song, R.; Liu, H.; Khanal, D. R.; Janke, S. M.; Zhao, R.; Liu, C.; Valy Vardeny, Z.; Blum, V.; Mitzi, D. B. Organic-to-Inorganic Structural Chirality Transfer in a 2D Hybrid Perovskite and Impact on Rashba-Dresselhaus Spin-Orbit Coupling. *Nat. Commun.* **2020**, *11*, 4699.
64. Sheikh, T.; Nawale, V.; Pathoor, N.; Phadnis, C.; Chowdhury, A.; Nag, A. Molecular Intercalation and Electronic Two Dimensionality in Layered Hybrid Perovskites. *Angew. Chem. Int. Ed.* **2020**, *59*, 11653-11659.
65. Sheikh, T.; Maqbool, S.; Mandal, P.; Nag, A. Introducing Intermolecular Cation- π Interactions for Water-Stable Low Dimensional Hybrid Lead Halide Perovskites. *Angew. Chem. Int. Ed.* **2021**, *60*, 18265-18271.
66. Panuganti, S.; Besteiro, L. V.; Vasileiadou, E. S.; Hoffman, J. M.; Govorov, A. O.; Gray, S. K.; Kanatzidis, M. G.; Schaller, R. D. Distance Dependence of Förster Resonance Energy Transfer Rates in 2D Perovskite Quantum Wells via Control of Organic Spacer Length. *J. Am. Chem. Soc.* **2021**, *143*, 4244-4252.
67. Fieramosca, A.; De Marco, L.; Passoni, M.; Polimeno, L.; Rizzo, A.; Rosa, B. L. T.; Cruciani, G.; Dominici, L.; De Giorgi, M.; Gigli, G.; Andreani, L. C.; Gerace, D.; Ballarini, D.; Sanvitto, D. Tunable Out-of-Plane Excitons in 2D Single-Crystal Perovskites. *ACS Photonics* **2018**, *5*, 4179-4185.
68. Long, M.; Zhang, T.; Chen, D.; Qin, M.; Chen, Z.; Gong, L.; Lu, X.; Xie, F.; Xie, W.; Chen, J.; Xu, J. Interlayer Interaction Enhancement in Ruddlesden–Popper Perovskite Solar Cells Toward High Efficiency and Phase Stability. *ACS Energy Lett.* **2019**, *4*, 1025-1033.
69. Chen, Y.; Liu, Z.; Li, J.; Cheng, X.; Ma, J.; Wang, H.; Li, D. Robust Interlayer Coupling in Two-Dimensional Perovskite/Monolayer Transition Metal Dichalcogenide Heterostructures. *ACS Nano* **2020**, *14*, 10258-10264.
70. Wang, K.; Wu, C.; Jiang, Y.; Yang, D.; Wang, K.; Priya, S. Distinct Conducting Layer Edge States in Two-Dimensional (2D) Halide Perovskite. *Sci. Adv.* **2019**, *5*, eaau3241.
71. Umeybayashi, T.; Asai, K.; Kondo, T.; Nakao, A. Electronic Structures of Lead Iodide Based Low-Dimensional Crystals. *Phys. Rev. B* **2003**, *67*, 155405.
72. Filippetti, A.; Mattoni, A. Hybrid Perovskites for Photovoltaics: Insights from First Principles. *Phys. Rev. B* **2014**, *89*, 125203.

73. Xiao, Z.; Meng, W.; Wang, J.; Mitzi, D. B.; Yan, Y. Searching for Promising New Perovskite-Based Photovoltaic Absorbers: The Importance of Electronic Dimensionality. *Mater. Horiz.* **2017**, *4*, 206-216.
74. Stoumpos, C. C.; Kanatzidis, M. G. The Renaissance of Halide Perovskites and Their Evolution as Emerging Semiconductors. *Acc. Chem. Res.* **2015**, *48*, 2791-2802.
75. Motta, C.; El-Mellouhi, F.; Kais, S.; Tabet, N.; Alharbi, F.; Sanvito, S. Revealing the Role of Organic Cations in Hybrid Halide Perovskite $\text{CH}_3\text{NH}_3\text{PbI}_3$. *Nat. Commun.* **2015**, *6*, 7026.
76. Milić, J. V. Multifunctional Layered Hybrid Perovskites. *J. Mater. Chem. C* **2021**, *9*, 11428-11443.
77. Wang, H.; Ma, J.; Li, D. Two-Dimensional Hybrid Perovskite-Based Van der Waals Heterostructures. *J. Phys. Chem. Lett.* **2021**, *12*, 8178-8187.
78. Wei, W.; Hu, Y. H. Catalytic Role of H_2O in Degradation of Inorganic–Organic Perovskite ($\text{CH}_3\text{NH}_3\text{PbI}_3$) in Air. *Int. J. Energy Res.* **2017**, *41*, 1063-1069.
79. Akbali, B.; Topcu, G.; Guner, T.; Ozcan, M.; Demir, M. M.; Sahin, H. CsPbBr_3 Perovskites: Theoretical and Experimental Investigation on Water-Assisted Transition from Nanowire Formation to Degradation. *Phys. Rev. Materials* **2018**, *2*, 034601.
80. Tsvetkov, D. S.; Mazurin, M. O.; Sereda, V. V.; Ivanov, I. L.; Malyshkin, D. A.; Zuev, A. Y. Formation Thermodynamics, Stability, and Decomposition Pathways of CsPbX_3 ($\text{X} = \text{Cl}, \text{Br}, \text{I}$) Photovoltaic Materials. *J. Phys. Chem. C* **2020**, *124*, 4252-4260.
81. Hailegnaw, B.; Kirmayer, S.; Edri, E.; Hodes, G.; Cahen, D. Rain on Methylammonium Lead Iodide Based Perovskites: Possible Environmental Effects of Perovskite Solar Cells. *J. Phys. Chem. Lett.* **2015**, *6*, 1543-1547.
82. Ravi, V. K.; Mondal, B.; Nawale, V. V.; Nag, A. Don't Let the Lead Out: New Material Chemistry Approaches for Sustainable Lead Halide Perovskite Solar Cells. *ACS Omega* **2020**, *5*, 29631-29641.
83. Li, J.; Cao, H.-L.; Jiao, W.-B.; Wang, Q.; Wei, M.; Cantone, I.; Lü, J.; Abate, A. Biological Impact of Lead from Halide Perovskites Reveals the Risk of Introducing a Safe Threshold. *Nat. Commun.* **2020**, *11*, 310.
84. Rong, Y.; Liu, L.; Mei, A.; Li, X.; Han, H. Beyond Efficiency: the Challenge of Stability in Mesoscopic Perovskite Solar Cells. *Adv. Energy Mater.* **2015**, *5*, 1501066.
85. Berhe, T. A.; Su, W.-N.; Chen, C.-H.; Pan, C.-J.; Cheng, J.-H.; Chen, H.-M.; Tsai, M.-C.; Chen, L.-Y.; Dubale, A. A.; Hwang, B.-J. Organometal Halide Perovskite Solar Cells: Degradation and Stability. *Energy Environ. Sci.* **2016**, *9*, 323-356.

Chapter 1
Introduction

86. Manser, J. S.; Saidaminov, M. I.; Christians, J. A.; Bakr, O. M.; Kamat, P. V. Making and Breaking of Lead Halide Perovskites. *Acc. Chem. Res.* **2016**, *49*, 330-338.
87. Pan, J.; Sarmah, S. P.; Murali, B.; Dursun, I.; Peng, W.; Parida, M. R.; Liu, J.; Sinatra, L.; Alyami, N.; Zhao, C.; Alarousu, E.; Ng, T. K.; Ooi, B. S.; Bakr, O. M.; Mohammed, O. F. Air-Stable Surface-Passivated Perovskite Quantum Dots for Ultra-Robust, Single- and Two-Photon-Induced Amplified Spontaneous Emission. *J. Phys. Chem. Lett.* **2015**, *6*, 5027-5033.
88. Huang, H.; Chen, B.; Wang, Z.; Hung, T. F.; Susha, A. S.; Zhong, H.; Rogach, A. L. Water Resistant CsPbX₃ Nanocrystals Coated with Polyhedral Oligomeric Silsesquioxane and their Use as Solid State Luminophores in All-Perovskite White Light-Emitting Devices. *Chem. Sci.* **2016**, *7*, 5699-5703.
89. Wang, S.; Bi, C.; Yuan, J.; Zhang, L.; Tian, J. Original Core–Shell Structure of Cubic CsPbBr₃@Amorphous CsPbBr_x Perovskite Quantum Dots with a High Blue Photoluminescence Quantum Yield of Over 80%. *ACS Energy Lett.* **2018**, *3*, 245-251.
90. Cao, D. H.; Stoumpos, C. C.; Farha, O. K.; Hupp, J. T.; Kanatzidis, M. G. 2D Homologous Perovskites as Light-Absorbing Materials for Solar Cell Applications. *J. Am. Chem. Soc.* **2015**, *137*, 7843-7850.
91. Peng, W.; Yin, J.; Ho, K.-T.; Ouellette, O.; De Bastiani, M.; Murali, B.; El Tall, O.; Shen, C.; Miao, X.; Pan, J.; Alarousu, E.; He, J.-H.; Ooi, B. S.; Mohammed, O. F.; Sargent, E.; Bakr, O. M. Ultralow Self-Doping in Two-Dimensional Hybrid Perovskite Single Crystals. *Nano Lett.* **2017**, *17*, 4759-4767.
92. Hao, F.; Stoumpos, C. C.; Cao, D. H.; Chang, R. P. H.; Kanatzidis, M. G. Lead-Free Solid-State Organic–Inorganic Halide Perovskite Solar Cells. *Nat. Photonics* **2014**, *8*, 489-494.
93. Hao, F.; Stoumpos, C. C.; Guo, P.; Zhou, N.; Marks, T. J.; Chang, R. P. H.; Kanatzidis, M. G. Solvent-Mediated Crystallization of CH₃NH₃SnI₃ Films for Heterojunction Depleted Perovskite Solar Cells. *J. Am. Chem. Soc.* **2015**, *137*, 11445-11452.
94. Jellicoe, T. C.; Richter, J. M.; Glass, H. F. J.; Tabachnyk, M.; Brady, R.; Dutton, S. E.; Rao, A.; Friend, R. H.; Credgington, D.; Greenham, N. C.; Böhm, M. L. Synthesis and Optical Properties of Lead-Free Cesium Tin Halide Perovskite Nanocrystals. *J. Am. Chem. Soc.* **2016**, *138*, 2941-2944.
95. Lanzetta, L.; Marin-Beloqui, J. M.; Sanchez-Molina, I.; Ding, D.; Haque, S. A. Two-Dimensional Organic Tin Halide Perovskites with Tunable Visible Emission and Their Use in Light-Emitting Devices. *ACS Energy Lett.* **2017**, *2*, 1662-1668.

96. Pal, J.; Bhunia, A.; Chakraborty, S.; Manna, S.; Das, S.; Dewan, A.; Datta, S.; Nag, A. Synthesis and Optical Properties of Colloidal $M_3Bi_2I_9$ ($M = Cs, Rb$) Perovskite Nanocrystals. *J. Phys. Chem. C* **2018**, *122*, 10643-10649.
97. Luo, J.; Wang, X.; Li, S.; Liu, J.; Guo, Y.; Niu, G.; Yao, L.; Fu, Y.; Gao, L.; Dong, Q.; Zhao, C.; Leng, M.; Ma, F.; Liang, W.; Wang, L.; Jin, S.; Han, J.; Zhang, L.; Etheridge, J.; Wang, J.; Yan, Y.; Sargent, E. H.; Tang, J. Efficient and Stable Emission of Warm-White Light from Lead-Free Halide Double Perovskites. *Nature* **2018**, *563*, 541-545.
98. Swarnkar, A.; Marshall, A. R.; Sanhira, E. M.; Chernomordik, B. D.; Moore, D. T.; Christians, J. A.; Chakrabarti, T.; Luther, J. M. Quantum Dot-Induced Phase Stabilization of α -CspI₃ Perovskite for High-Efficiency Photovoltaics. *Science* **2016**, *354*, 92-95.
99. Palazon, F.; Dogan, S.; Marras, S.; Locardi, F.; Nelli, I.; Rastogi, P.; Ferretti, M.; Prato, M.; Krahn, R.; Manna, L. From CsPbBr₃ Nano-Inks to Sintered CsPbBr₃-CsPb₂Br₅ Films via Thermal Annealing: Implications on Optoelectronic Properties. *J. Phys. Chem. C* **2017**, *121*, 11956-11961.
100. Huang, S.; Li, Z.; Wang, B.; Zhu, N.; Zhang, C.; Kong, L.; Zhang, Q.; Shan, A.; Li, L. Morphology Evolution and Degradation of CsPbBr₃ Nanocrystals under Blue Light-Emitting Diode Illumination. *ACS Appl. Mater. Interfaces* **2017**, *9*, 7249-7258.
101. Protesescu, L.; Yakunin, S.; Bodnarchuk, M. I.; Bertolotti, F.; Masciocchi, N.; Guagliardi, A.; Kovalenko, M. V. Monodisperse Formamidinium Lead Bromide Nanocrystals with Bright and Stable Green Photoluminescence. *J. Am. Chem. Soc.* **2016**, *138*, 14202-14205.
102. Dang, Y.; Liu, X.; Cao, B.; Tao, X. Chiral Halide Perovskite Crystals for Optoelectronic Applications. *Matter* **2021**, *4*, 794-820.

Chapter 2

Dual Excitonic Emissions in 2D Layered Hybrid Lead Halide Perovskites

The work presented in this chapter is published in the following articles:

Sheikh, T.; Shinde, A.; Mahamuni, S.; Nag, A. Possible Dual Bandgap in $(\text{C}_4\text{H}_9\text{NH}_3)_2\text{PbI}_4$ 2D Layered Perovskite: Single Crystal and Exfoliated Few-Layer. *ACS Energy Lett.* **2018**, *3*, 2940-2946.

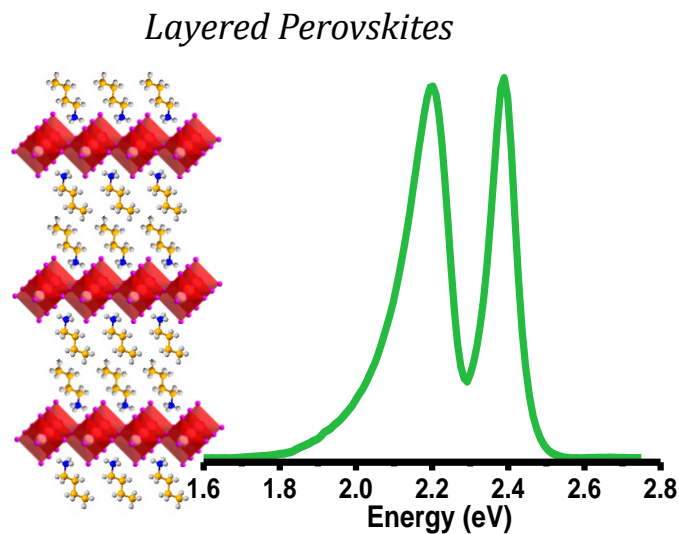
Copyright permission has been taken for the whole article from the American Chemical Society.

Sheikh, T.; Shinde, A.; Mahamuni, S.; Nag, A. Dual Excitonic Emissions and Structural Phase Transition of Octylammonium Lead Iodide 2D Layered Perovskite Single Crystal. *Mater. Res. Express* **2019**, *6*, 124002.

Copyright permission has been taken for the whole article from the IOP Publishing Ltd.

Abstract

Two-dimensional (2D) layered hybrid lead halide perovskites exhibit interesting electronic and optical properties because of their repeating quantum well structure. These materials are now being explored for various optoelectronic applications, including solar cells and light-emitting diodes. But still, there are surprises regarding the basic band gap or excitonic absorption and emission properties of these layered hybrid perovskites. In this chapter, we discuss that the 2D layered hybrid perovskite single crystals like butylammonium lead iodide [(BA)₂PbI₄] show dual excitonic emissions. A minor structural inhomogeneity between bulk crystal and the layer edges of the crystal might be responsible for the two different excitonic emissions. To explore the correlation between crystal structure and excitonic emissions, we have studied single crystal X-ray diffraction and photoluminescence in (BA)₂PbI₄ single crystals at variable temperatures. The results show that a small change in tilting of Pb-I₆ octahedra can distinctly change the band gap and the excitonic emission energy in these 2D layered hybrid perovskites.

Graphical Abstract

2.1 Introduction

3D lead-halide perovskites have now been established as an excellent material for solar cells, light-emitting diodes and other optoelectronic applications.¹⁻⁸ 2D layered hybrid lead-halide perovskites are now being explored for optoelectronic applications.⁹⁻¹⁰ 2D layered hybrid perovskites with general formula $(A)_2(A')_{n-1}Pb_nI_{3n+1}$ (where A is long-chain organic cation like $C_4H_9NH_3^+$ (BA), and A' is a smaller cation like $CH_3NH_3^+$ (MA)) exhibit photovoltaic solar cell efficiency of 12.5%.¹⁰⁻¹² In this structure, the corner-shared $(PbI_6)^{4-}$ octahedra form a layered semiconducting phase, which are separated by insulating long-chain organic cations (A), forming a repetition of the quantum well structure. Controlling “n” controls the thickness of the inorganic layer (well), and variation in the organic spacer controls the thickness of the barrier in the quantum well structure. Different compositions (by varying n, organic spacer, metal ion and halide ion) of layered hybrid perovskites have been prepared, and their optical and optoelectronic properties have been reported.¹³⁻¹⁸ These layered perovskites provide a natural multi-quantum well structure and improved moisture stability.

$(BA)_2PbI_4$ with $n = 1$ is one of the simple and stable 2D layered hybrid perovskite showing rich excitonic photophysics in the visible region.¹⁹ Therefore, $(BA)_2PbI_4$ is a good model system for understanding the optoelectronic properties of 2D layered hybrid perovskites. In this paper, we explored the optical properties of $(BA)_2PbI_4$ single crystals by using optical absorption, temperature-dependent photoluminescence (10-300 K) spectroscopies. Results suggest that the $(BA)_2PbI_4$ single crystals show a dual excitonic emission. We also elucidate the structure-bandgap relationships of the $(BA)_2PbI_4$ single crystals. Temperature-dependent photoluminescence (PL) and crystal structure studies suggest that the structural distortions increase the band gap of $(BA)_2PbI_4$ at lower temperatures. To generalize this dual excitonic emission, we studied a series of layered hybrid perovskite single crystals, all of which show the dual excitonic emission.

2.2 Experimental Section

2.2.1 Chemicals

Lead oxide (Sigma Aldrich, 99.9%), butylamine (Sigma Aldrich, 99.5%), hexylamine (Sigma Aldrich, 98%), octylamine (Sigma Aldrich, 99.5%), phenethylamine (Sigma Aldrich, 99.9%), hydriodic acid (Sigma Aldrich, 57% w/w in H_2O , 99.9%), hydrobromic acid (Sigma Aldrich, 48% w/w in H_2O , 99.9%), hypophosphorous acid (Avra, 50% w/w H_2O), diethyl ether (Rankem, 99.5%).

2.2.2 Synthesis of C₄H₉NH₃I, C₆H₁₃NH₃I and C₈H₁₅NH₃I

924 μ L (10 mmol) n-C₄H₉NH₂, 667 μ L (5 mmol) n-C₆H₁₃NH₂ and 166 μ L (1 mmol) n-C₈H₁₅NH₂ were separately neutralized with 5 mL (38 mmol) 57% w/w HI in an ice bath resulting in a clear pale yellow solution of C₄H₉NH₃I, C₆H₁₃NH₃I and C₈H₁₅NH₃I respectively.

2.2.3 Synthesis of 2D (C₄H₉NH₃)₂PbI₄ or (BA)₂PbI₄ single crystals

(C₄H₉NH₃)₂PbI₄, also termed as (BA)₂PbI₄ was prepared following a reported method.²⁰ 2232 mg (10 mmol) PbO was dissolved in a mixture of 10 ml (76 mmol) of 57% w/w aqueous HI and 1.7 ml (15.5 mmol) 50% aqueous H₃PO₂ by heating to boiling under constant magnetic stirring, which resulted in a bright yellow solution. To this yellow solution, the freshly prepared C₄H₉NH₃I solution was added, and the resultant solution was heated to boiling. The stirring was stopped immediately after boiling, and the solution was allowed to cool to room temperature naturally. During the cooling process, orange-colored plate-like crystals crystallized. The crystals were filtered and washed with diethyl ether and dried under vacuum.

2.2.4 Synthesis of 2D (C₆H₁₃NH₃)₂PbI₄ or (HA)₂PbI₄ single crystals

(C₆H₁₃NH₃)₂PbI₄, also termed as (HA)₂PbI₄ was prepared following the same method. 1116 mg (5 mmol) PbO was dissolved in a mixture of 10 ml (76 mmol) of 57% w/w aqueous HI and 1.7 ml (15.5 mmol) 50% aqueous H₃PO₂ by heating to boiling under constant magnetic stirring, which resulted in a bright yellow solution. To this solution, the freshly prepared C₆H₁₃NH₃I solution was added, and the resultant solution was heated to boiling. The rest of the steps were the same as that of the (BA)₂PbI₄.

2.2.5 Synthesis of 2D (C₈H₁₅NH₃)₂PbI₄ or (OA)₂PbI₄ single crystals

(C₈H₁₅NH₃)₂PbI₄, also termed as (OA)₂PbI₄ was prepared following the same method. 232 mg (1 mmol) PbO was dissolved in a mixture of 10 mL 57% w/w aqueous HI and 1.7 mL 50% aqueous H₃PO₂ by heating to boiling under constant stirring. A clear yellow solution was obtained. To this yellow solution, the freshly prepared C₈H₁₅NH₃I was added, and the resultant solution was heated to boiling. The rest of the steps were the same as that of the (BA)₂PbI₄.

2.2.6 Synthesis of C₄H₉NH₃Br and C₈H₉NH₃Br

924 μ L of n-C₄H₉NH₂ and 127 μ L of C₈H₉NH₂ were separately neutralized with 5 mL (44 mmol) and 2 mL (17.6 mmol) 48% w/w HBr, respectively, in an ice bath resulting in a transparent solution of C₄H₉NH₃Br and C₈H₉NH₃Br.

2.2.7 Synthesis of 2D (C₄H₉NH₃)₂PbBr₄ or (BA)₂PbBr₄ single crystals

(C₄H₉NH₃)₂PbBr₄, also termed as (BA)₂PbBr₄, was prepared by slightly modifying the method used for the synthesis of (BA)₂PbI₄. 2232 mg (10 mmol) PbO was dissolved in a mixture of 10 ml (88 mmol) of 48% w/w aqueous HBr and 1.7 ml (15.5 mmol) 50% aqueous H₃PO₂ by heating to boiling under constant magnetic stirring, which resulted in a transparent solution. To this solution, the freshly prepared C₄H₉NH₃Br solution was added, and the resultant solution was heated to boiling. The stirring was stopped immediately after boiling, and the solution was allowed to cool to room temperature. During the cooling process, transparent plate-like crystals crystallized. The crystals were filtered and washed with diethyl ether and dried under vacuum.

2.2.8 Synthesis of 2D (C₈H₉NH₃)₂PbBr₄ or (PEA)₂PbBr₄ single crystals

(C₈H₉NH₃)₂PbBr₄, also termed as (PEA)₂PbBr₄, was prepared by the same method used for the synthesis of (BA)₂PbBr₄. 223 mg (1 mmol) PbO was dissolved in a mixture of 10 ml (88 mmol) of 48% w/w aqueous HBr and 1.7 ml (15.5 mmol) 50% aqueous H₃PO₂ by heating to boiling under constant magnetic stirring, which resulted in a transparent solution. To this solution, the freshly prepared C₈H₉NH₃Br solution was added, and the resultant solution was heated to boiling. The rest of the steps were the same as that of the (BA)₂PbBr₄.

2.2.9 Characterization

Single crystal data were collected using a Bruker Smart Apex Duo diffractometer at 100 K, 250 K and 296 K using MoK α radiation ($\lambda = 0.71073 \text{ \AA}$). The frames were integrated with the Bruker SAINT software package using a narrow-frame algorithm. The structures were solved by direct method and refined by full-matrix least-squares on F² using the SHELXTL software package. The PbI₄ framework was refined anisotropically without any constraint on Pb and I atoms. All organic atoms were refined isotropically, and C–C and C–N bond lengths were restrained to ideal values.

Scanning electron microscopy (SEM) images were collected using the Zeiss Ultra Plus FESEM instrument. Differential scanning calorimetry (DSC) measurements were carried on the Mettler Toledo DSC823 system in the temperature range of -140 to 190 °C in N₂ atmosphere with heating and cooling rates 3 °C/min. About 10 mg of the polycrystalline sample was used for the measurements. Optical diffuse-reflectance spectra were collected at room temperature using a Shimadzu UV-3600 plus UV-Vis-NIR spectrophotometer. All the reflectance spectra were converted to absorbance using Kubelka-Munk transformation. Room temperature (RT) steady-state photoluminescence (PL) was recorded on FLS 980 (Edinburgh Instruments).

Fluorescence decays were collected by time-correlated single-photon counting (TCSPC) set-up from Horiba Jobin Yvon with 405 nm diode laser (IBH, UK, NanoLED-405L) as an excitation source. The fluorescence signals were collected at a magic angle using an MCP-PMT (Hamamatsu, Japan) detector. The analysis of lifetime (TCSPC) data was done by IBH DAS6 analysis software. The PL decay plots were fitted to bi-exponential fits, and the average lifetime was calculated by the following equation:

$$\tau_{av} = \frac{(A_1 \times \tau_1^2) + (A_2 \times \tau_2^2)}{(A_1 \times \tau_1) + (A_2 \times \tau_2)}$$

Where τ_{av} is the average lifetime, τ_1 , τ_2 are the two decay components; A_1 , A_2 are their respective contributions. Low-temperature (up to 10 K) PL measurements were performed on the homebuilt PL set up consisting of an excitation monochromator (Jobin Yvon Triax 180), an emission monochromator (Jobin Yvon iHR 320) and a photomultiplier tube (PMT) as the detector with a xenon lamp (450 W) as the excitation source. The low-temperature PL measurements were carried out in Prof. Shailaja Mahamuni's lab at Savitribai Phule Pune University (SPPU) with the help of Dr. Aparna Shinde (SPPU). Dr. Aparna and I carried out the low-temperature measurements jointly.

2.3 Results and Discussion

2.3.1 Synthesis and characterization of (BA)₂PbI₄ single crystals

(BA)₂PbI₄ single crystals were prepared following a previously reported method¹¹ (see the experimental section for details). Figure 2.1a shows the photograph of (BA)₂PbI₄ crystals prepared using a solution-phase synthesis. The powder X-ray diffraction pattern (PXRD) of (BA)₂PbI₄ in Figure 2.1b shows the peaks at regular intervals, which is the characteristic of layered single crystals.²⁰ The regular peak pattern corresponds to the *00l* planes of the 2D layered perovskite structure.²⁰ The first peak gives the interlayer spacing, which is the vertical distance between the adjacent inorganic layers. The interlayer spacing calculated from the PXRD pattern comes out to be 13.56 Å, which matches very well with the reported interlayer spacing of the (BA)₂PbI₄. The layered structure of (BA)₂PbI₄ is further confirmed by the scanning electron microscopy (SEM) image, shown in Figure 2.1c. Single crystals with length ~6 mm, width ~5 mm and thickness ~0.5 mm were used for measuring optical data. Smaller sized crystals (~0.5 × 0.4 × 0.2 mm³) were used for the crystal structure determination. The single-crystal x-ray diffraction (SCXRD) of (BA)₂PbI₄ is recorded at 100 K, 250 K and 296 K (RT) and is discussed in detail in section 2.3.3.

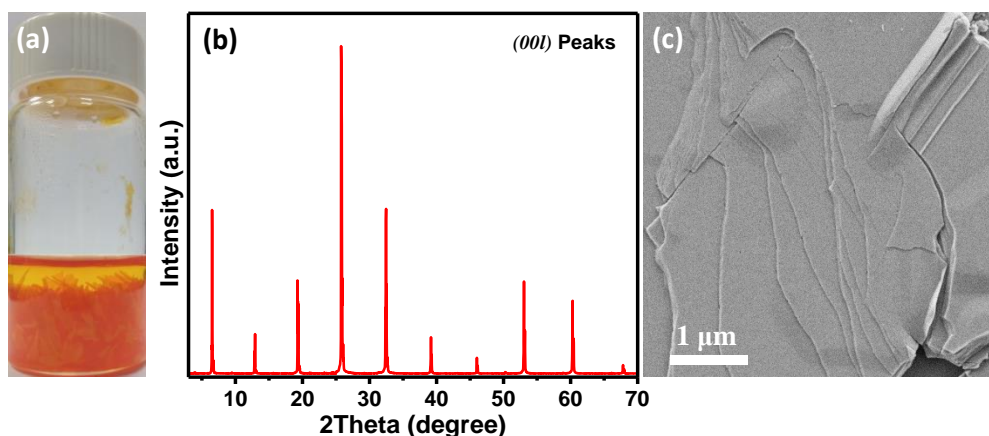


Figure 2.1: (a) Photograph of $(\text{BA})_2\text{PbI}_4$ single crystals prepared using a solution-phase synthesis. (b) PXRD pattern of $(\text{BA})_2\text{PbI}_4$ single crystal showing the peaks corresponding to the $00l$ planes. (c) SEM image of a $(\text{BA})_2\text{PbI}_4$ crystal showing a layered architecture.

2.3.2 Optical properties of $(\text{BA})_2\text{PbI}_4$ single crystals

The schematics in Figure 2.2a show that the PL data were collected by changing the angle between the excitation source and the single crystal. For brevity, we will call the PL spectra measured with 45° and 90° angles between the excitation source and sample PL- 45° and PL- 90° , respectively. A larger area on the surface of the single crystal is illuminated for PL- 45° compared to PL- 90° . Interestingly, the color of PL is different for PL- 45° (bright green) compared to PL- 90° (yellow-green mixture). Spectra (Figure 2.2b) of both PL- 45° and PL- 90° show two sharp peaks at 2.20 eV (564 nm) and 2.38 eV (521 nm). Similar unusual PL features of $(\text{BA})_2\text{PbI}_4$ were observed by Mitzi, but the origin of the two PL peaks was not understood.¹³ It is unusual that the PL peak at 2.38 eV is higher in energy compared to the lowest-energy absorption shown in the UV-visible absorbance spectrum (Figure 2.2c). The corresponding reflectance spectrum is shown in Figure 2.2d. Furthermore, we tried to measure the absorption in the transmission mode. Even thinner single crystals do not transmit enough light with energy higher than the bandgap. But the absorption edge can still be observed from the spectrum shown in Figure 2.2e. Clearly, both the transmittance and reflectance data suggest strong light absorption by $(\text{BA})_2\text{PbI}_4$ single crystals at energies below the PL peak at 2.38 eV. Therefore, 2.38 eV emission is not the lowest energy excitonic emission; instead, 2.20 eV emission appears to be the lowest energy excitonic emission.

Interestingly, Figure 2.2b shows that the intensity ratio between the two PL peaks differs significantly and reversibly with excitation angle. PL- 45° shows higher relative intensity for the peak at 2.38 eV, compared to PL- 90° , which shows higher intensity for the peak at 2.20 eV. When we detect the emission from the back-side of the crystal after exciting the front-side (see

the schematic in Figure 2.3a), the relative intensity of 2.38 eV peak further decreases (Figure 2.3b) for the given excitation angle. This decrease in the relative intensity of high energy peak is expected because of both radiative self-absorption and non-radiative Foster Resonance Energy Transfer (FRET),²¹ from higher energy (2.38 eV) donors to lower energy (2.20 eV) acceptors. The extent of both self-absorption and FRET increases as the light emitted from the front side (excitation point) of the crystal travels through the crystal before it comes out from the backside. Likewise, in Figure 2.2b, showing front-side emissions, PL-90° emission travels more inside the crystal, experiencing more self-absorption and FRET, compared to PL-45°. Therefore, these mechanisms reduce the intensity of the 2.38 eV emission peak for PL-90° compared to PL-45°. The strong self-absorption of the higher energy 2.38 eV peak by the acceptor lower energy 2.20 eV peak again suggests the presence of strong absorbing states below the higher energy 2.38 eV peak, confirming that the 2.38 eV peak is not the lowest energy excitonic emission, rather the peak at 2.2 eV is the lowest energy excitonic emission.

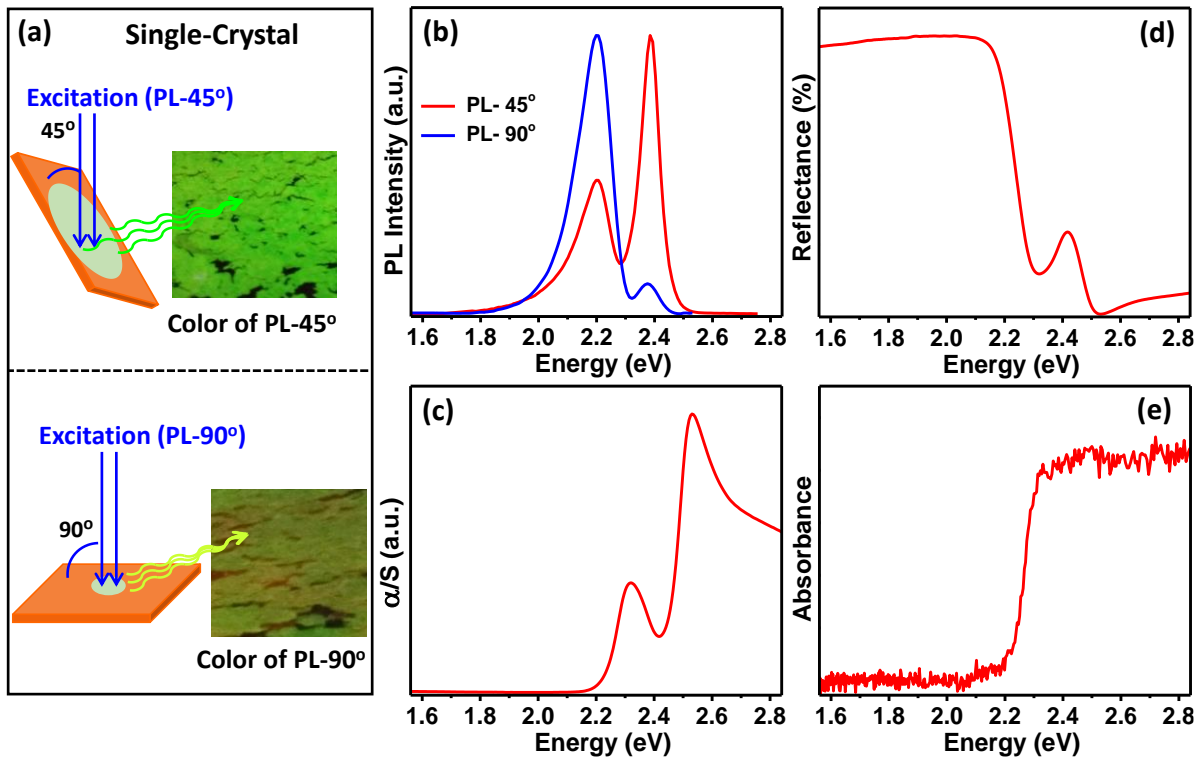


Figure 2.2: (a) Schematics showing PL emission collected using 45° and 90° angle of excitation beam on the single crystal. Photographs of (BA)₂PbI₄ single crystals under UV lamp with corresponding excitation angles. (b) PL spectra of (BA)₂PbI₄ single crystal with two different excitation angles. (c) Optical absorption spectrum of (BA)₂PbI₄ single crystal obtained from diffuse reflectance measurements by using the Kubelka-Munk equation. (d) Diffuse-reflectance spectrum of (BA)₂PbI₄ single crystal. (e) UV-Vis absorbance spectrum of (BA)₂PbI₄ single crystal obtained in transmission mode from a thinner crystal.

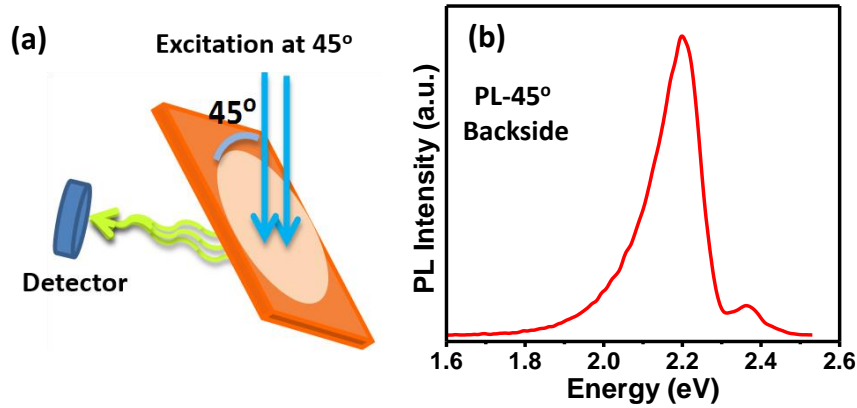


Figure 2.3: (a) Schematic showing measuring PL emission from the backside of the crystal, while excitation is on the front-side of the crystal. The excitation beam is at 45° with the single crystal. (b) PL spectra of $(\text{BA})_2\text{PbI}_4$ single crystal, collected from the backside of the crystal.

Figure 2.4 shows the PL decay dynamics of the two emission peaks observed in $(\text{BA})_2\text{PbI}_4$ single crystal. Interestingly, both the emission peaks show a similar bi-exponential decay profile. The two components of the bi-exponential decay of 2.20 eV emission are $\tau_1 = 402$ ps (18%) and $\tau_2 = 130$ ps (82%) with an average lifetime of 240 ps. For the 2.38 eV emission the two components of the bi-exponential decay are $\tau_1 = 424$ ps (24%) and $\tau_2 = 136$ ps (76%), with average lifetime of 279 ps. The short lifetimes of both the emissions suggest the strong transition probabilities for both the emission peaks.

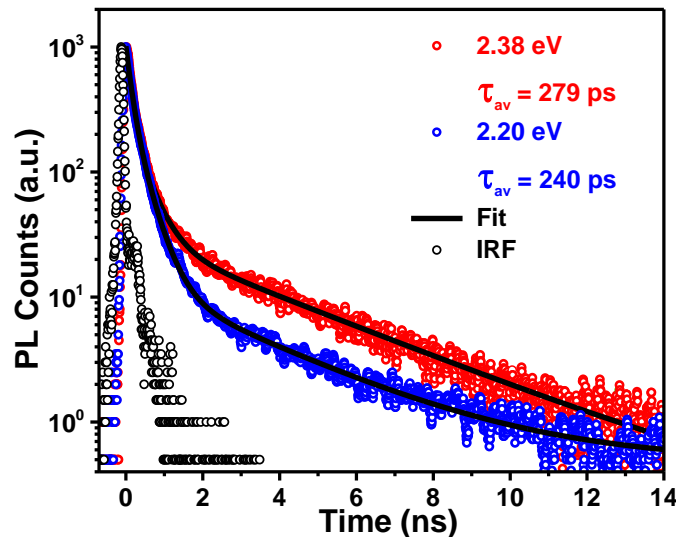


Figure 2.4: Time-resolved PL spectra of $(\text{BA})_2\text{PbI}_4$ single crystal for 2.38 eV (520 nm) and 2.20 eV (564 nm) emission peaks, both showing a bi-exponential decay.

One may assume that in single crystal PL (Figure 2.2b), the 2.38 eV peak originates from excitonic transition, and the 2.20 eV originates from defects in the crystal. But this possibility of 2.20 eV emission as a defect-related one can be ruled out based on the following

observations. Figures 2.2c-e show a strong absorbance corresponding to the 2.20 eV peak. This is further confirmed by exciting the $(\text{BA})_2\text{PbI}_4$ single crystal even below the higher energy (2.38 eV) emission. A strong emission at 2.20 eV is observed upon excitation with 2.3 eV (540 nm) and 2.28 eV (545 nm) light, as shown in Figure 2.5. This confirms that the lower energy (2.20 eV) emission has its own strong absorbing energy states. Moreover, the full width at half maxima (FWHM) for both the PL peaks at 2.38 and 2.20 eV of the single crystal are 86 meV (19 nm) and 137 meV (35 nm). The FWHM of the lower energy peak at 2.20 eV is quite narrow. Also, the lifetime of both the peaks is very short and similar. The narrow FWHM and short lifetime of the two emission peaks combined with their strong absorbance suggest that none of the emissions have a defect or trap related origin; rather, both the emissions arise due to excitonic transitions with strong transition probabilities.²²

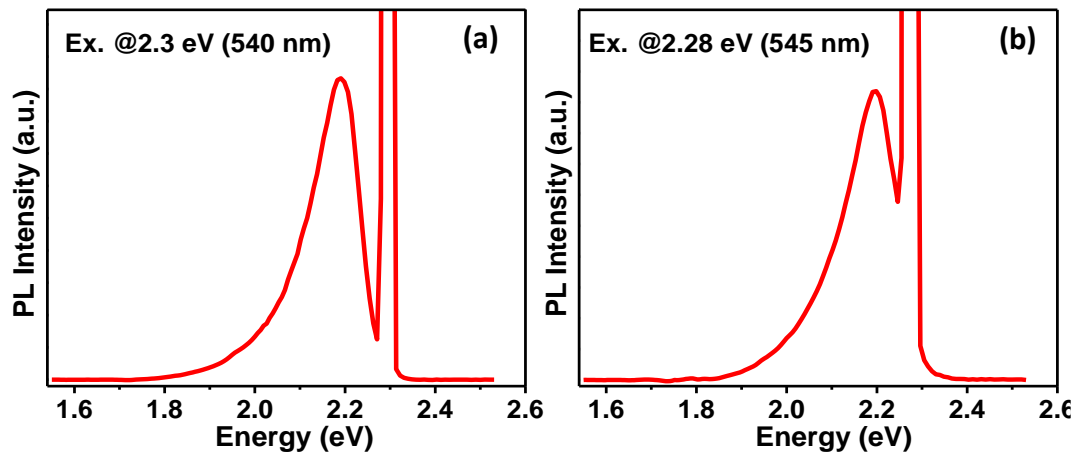


Figure 2.5: PL spectra of $(\text{BA})_2\text{PbI}_4$ single crystal recorded using (a) 2.3 eV (540 nm) and (b) 2.28 eV (545 nm) excitation wavelength. Both the excitations are lower in energy compared to the higher energy (2.38 eV) emission.

2.3.3 Temperature-dependent PL of $(\text{BA})_2\text{PbI}_4$ single crystals

$(\text{BA})_2\text{PbI}_4$ single crystal exhibits two PL-peaks at 2.20 and 2.38 eV at room temperature (RT) (Figure 2.2b). A transition in PL peak energies is observed below 250 K while cooling down the sample from RT, as shown in Figure 2.6a. While heating up the sample from 10 K, the PL energy returns back (reversible transition) to original positions above 275 K (see Figure 2.6b). The peak energies of the two emission peaks are plotted against measurement temperature in Figure 2.6c. A clear hysteresis in the transition temperature is observed between the heating and cooling cycle. To check whether this reversible transition in PL energy is associated with structural phase transition, we measured differential scanning calorimetry (DSC). Figure 2.6d shows that the DSC data also exhibits similar transition temperatures, along with a hysteresis

between the heating and cooling cycles. This agreement in transition temperatures obtained from DSC and PL data suggests that the change in the structure of the single crystal is responsible for the change in PL at lower temperatures. Note that the sample exhibits a broad emission with the peak at ~ 2.1 eV at lower temperatures. Such broad and Stoke's shifted emission from absorption edge has been previously reported as self-trapped emission,²³ and are not important for our present discussion.

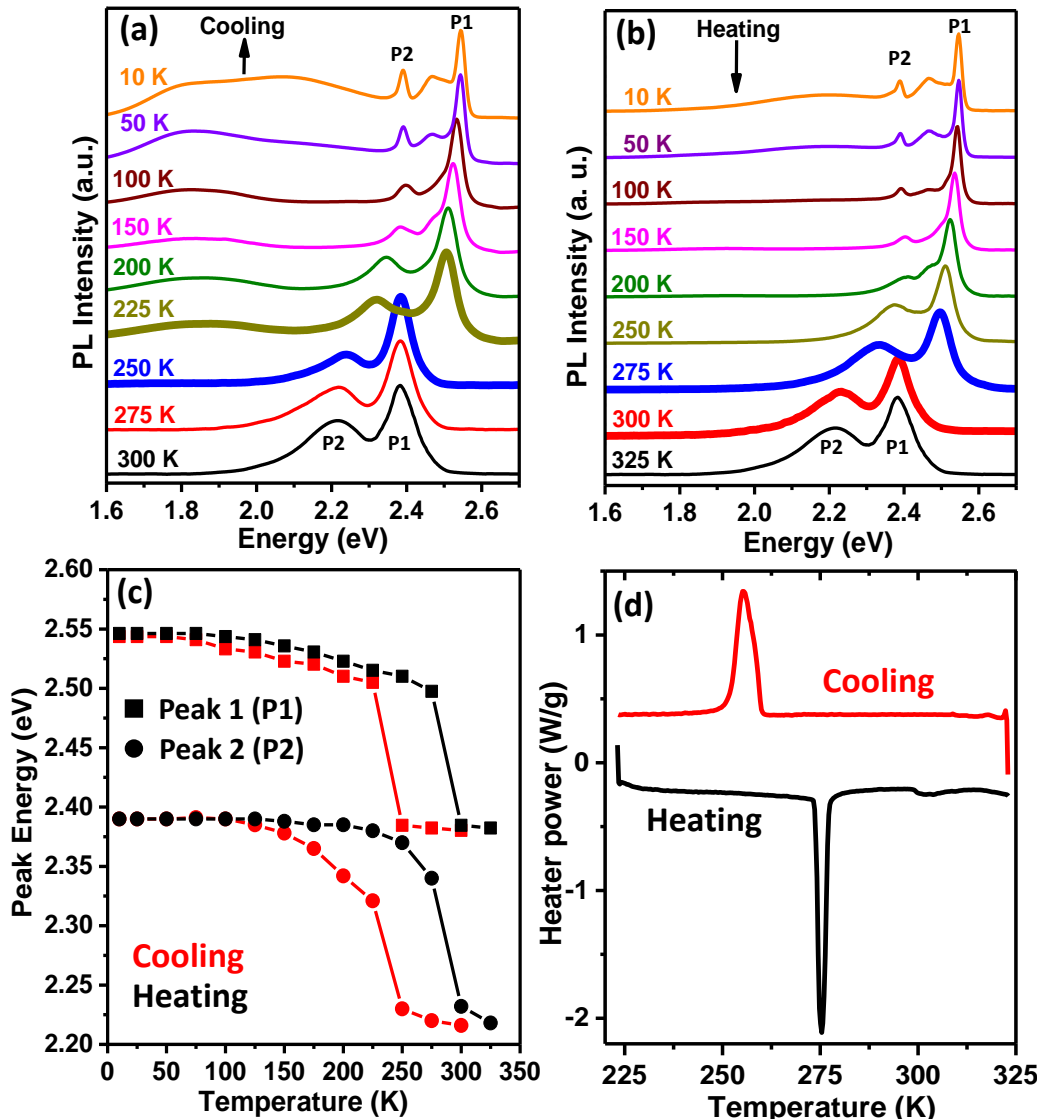


Figure 2.6: PL spectra of (BA)₂PbI₄ single crystal (with $\sim 45^\circ$ excitation angle) at different temperatures upon (a) cooling down from RT, (b) heating to RT. At room temperature, Peak 1 (P1) corresponds to 2.38 eV (520 nm) emission, and Peak 2 (P2) corresponds to the 2.20 eV (564 nm) emission. (c) PL peak energy vs. temperature plot of the two peaks for both heating and cooling cycle. (d) DSC data of (BA)₂PbI₄ single crystals showing a structural phase transition. The low-temperature PL measurements were carried out in Prof. Shailaja Mahamuni's lab at SPPU with the help of Dr. Aparna Shinde (SPPU).

2.3.4 Temperature-dependent single crystal XRD of $(\text{BA})_2\text{PbI}_4$

To understand the low-temperature PL data, we discuss the nature of structural changes by using single crystal XRD at different temperatures (100 K, 250 K and 296 K (considered here as RT)). Figure 2.7 and Table 2.1 show the details of experimentally obtained structures. The structure is orthorhombic with space group $Pbca$ at all three temperatures, similar to prior reports^{11, 13, 24}. Structural parameters at 100 K and 250 K (obtained by heating from 100 K) are similar but differ significantly from the 296 K (RT) structure.

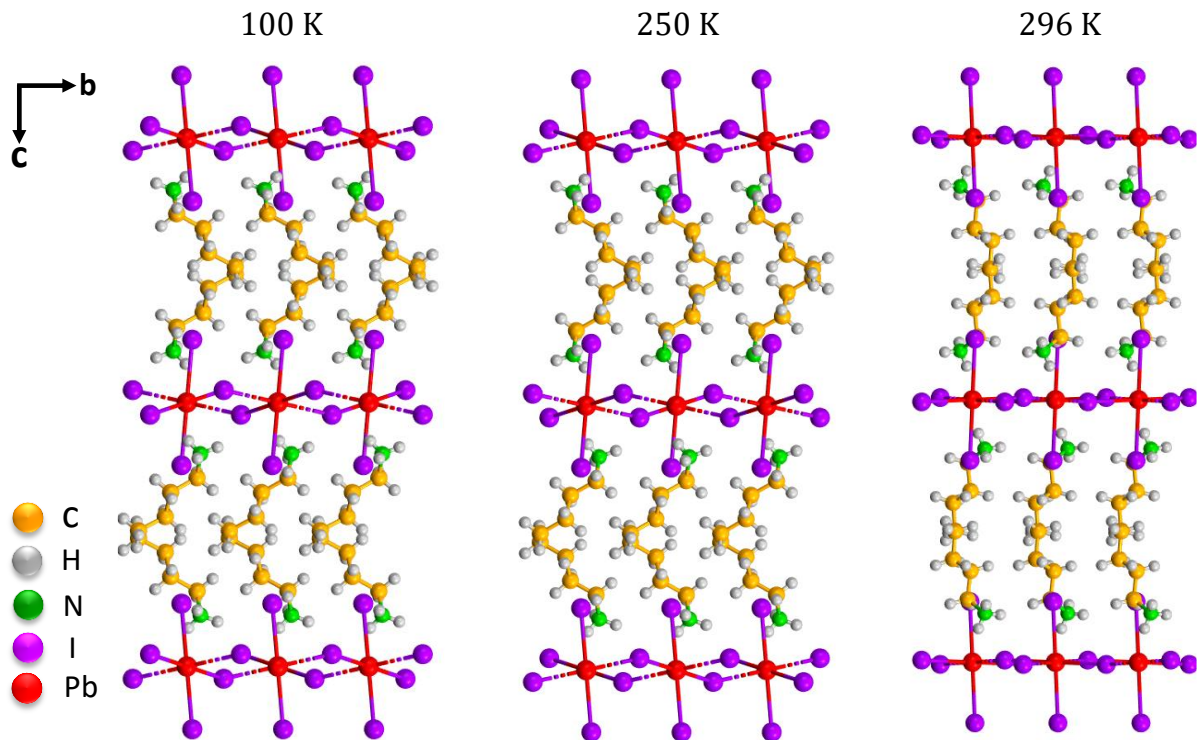


Figure 2.7: Crystal structures of $(\text{BA})_2\text{PbI}_4$ at 100 K, 250 K and 296 K (RT), viewed along the ‘ bc ’ crystallographic plane.

Representative parts of the crystal structure obtained at 100 K and RT are shown in Figure 2.8. The Pb-I_6 octahedra are more tilted at lower temperature reducing the unit cell volume from $2136.9(7) \text{ \AA}^3$ at RT to $1980.0(4) \text{ \AA}^3$ at 100 K. This octahedral tilt can be visualized further in Figure 2.8b. The ‘ ab ’ crystal plane (shown by a green dashed line) in Figure 2.8a contains the Pb atoms. In the absence of octahedral tilting, both Pb and equatorial I atoms would have lied in the ‘ ab ’ plane. But because of larger octahedral tilting, the Pb-I-Pb bend out of the ‘ ab ’ plane more at 100 K compared to that at RT. This out-of-plane Pb-I-Pb bending (δ), and also in-plane bending (by projecting the equatorial I atom on ‘ ab ’ plane) can be calculated following ref²⁵ and are shown in Figure 2.8b and c and Table 2.2.

Table 2.1: Crystal data and structure refinement for (BA)₂PbI₄

	RT (296 K)	250 K	100 K
Chemical formula	C ₈ H ₂₄ I ₄ N ₂ Pb	C ₈ H ₂₄ I ₄ N ₂ Pb	C ₈ H ₂₄ I ₄ N ₂ Pb
Formula weight	863.08 g/mol	863.08 g/mol	863.08 g/mol
Temperature	296(2) K	250(2) K	100(2) K
Wavelength	0.71073 Å	0.71073 Å	0.71073 Å
Crystal system	Orthorhombic	Orthorhombic	Orthorhombic
Space group	<i>Pbca</i>	<i>Pbca</i>	<i>Pbca</i>
Unit cell dimensions	a = 27.682(6) Å b = 8.8767(17) Å c = 8.6962(17) Å α = β = γ = 90°	a = 8.494(5) Å b = 9.021(6) Å c = 26.514(16) Å α = β = γ = 90°	a = 8.416(10) Å b = 8.8971(11) Å c = 26.23(4) Å α = β = γ = 90°
Volume	2136.9(7) Å ³	2032.0(2) Å ³	1980.0(4) Å ³
Z	4	4	4
Density	2.683 g/cm ³	2.822 g/cm ³	2.895 g/cm ³
Abs. coefficient	13.658 mm ⁻¹	14.366 mm ⁻¹	14.739 mm ⁻¹
Theta range	2.73 to 28.35°	2.85 to 28.30°	2.88 to 28.32°
Index ranges	-36 ≤ h ≤ 36, -11 ≤ k ≤ 11, -10 ≤ l ≤ 11	-11 ≤ h ≤ 11, -11 ≤ k ≤ 12, -35 ≤ l ≤ 35	-11 ≤ h ≤ 11, -10 ≤ k ≤ 11, -34 ≤ l ≤ 34
Reflections collected	33039	42524	36089
Independent reflections	2662	2523	2458
Coverage of independent reflections	99.70%	99.80%	99.60%
Absorption correction	Multi-Scan	Multi-scan	Multi-scan
Structure solution	Direct methods	Direct method	Direct method
Structure solution program	SHELXT 2014/5 (Sheldrick, 2014)	SHELXT 2014/5 (Sheldrick, 2014)	SHELXT 2014/5 (Sheldrick, 2014)
Refinement method	Full-matrix least-squares on F ²	Full-matrix least-squares on F ²	Full-matrix least-squares on F ²
Refinement program	SHELXL-2016/6 (Sheldrick, 2016)	SHELXL-2016/6 (Sheldrick, 2016)	SHELXL-2016/6 (Sheldrick, 2016)
Function minimized	Σ w(F _o ² - F _c ²) ²	Σ w(F _o ² - F _c ²) ²	Σ w(F _o ² - F _c ²) ²
Data / parameters	2662 / 72	2523 / 72	2458 / 72
Goodness-of-fit on F ²	1.066	1.139	1.365
Final R indices; I > 2σ(I)	R1 = 0.0576, wR2 = 0.1539	R1 = 0.0611, wR2 = 0.1551	R1 = 0.0478, wR2 = 0.1711
all data	R1 = 0.1494, wR2 = 0.1939	R1 = 0.1045, wR2 = 0.1768	R1 = 0.0631, wR2 = 0.1783
Weighting scheme	w=1/[σ ² (F _o ²)+(0.1000P) ²] P=(F _o ² +2F _c ²)/3	w=1/[σ ² (F _o ²)+(0.1000P) ²] P=(F _o ² +2F _c ²)/3	w=1/[σ ² (F _o ²)+(0.1000P) ²] P=(F _o ² +2F _c ²)/3
Largest diff. peak, hole	0.814, -1.195 eÅ ⁻³	1.914, -2.184 eÅ ⁻³	2.327, -2.916 eÅ ⁻³
R.M.S. deviation	0.232 eÅ ⁻³	0.355 eÅ ⁻³	0.343 eÅ ⁻³

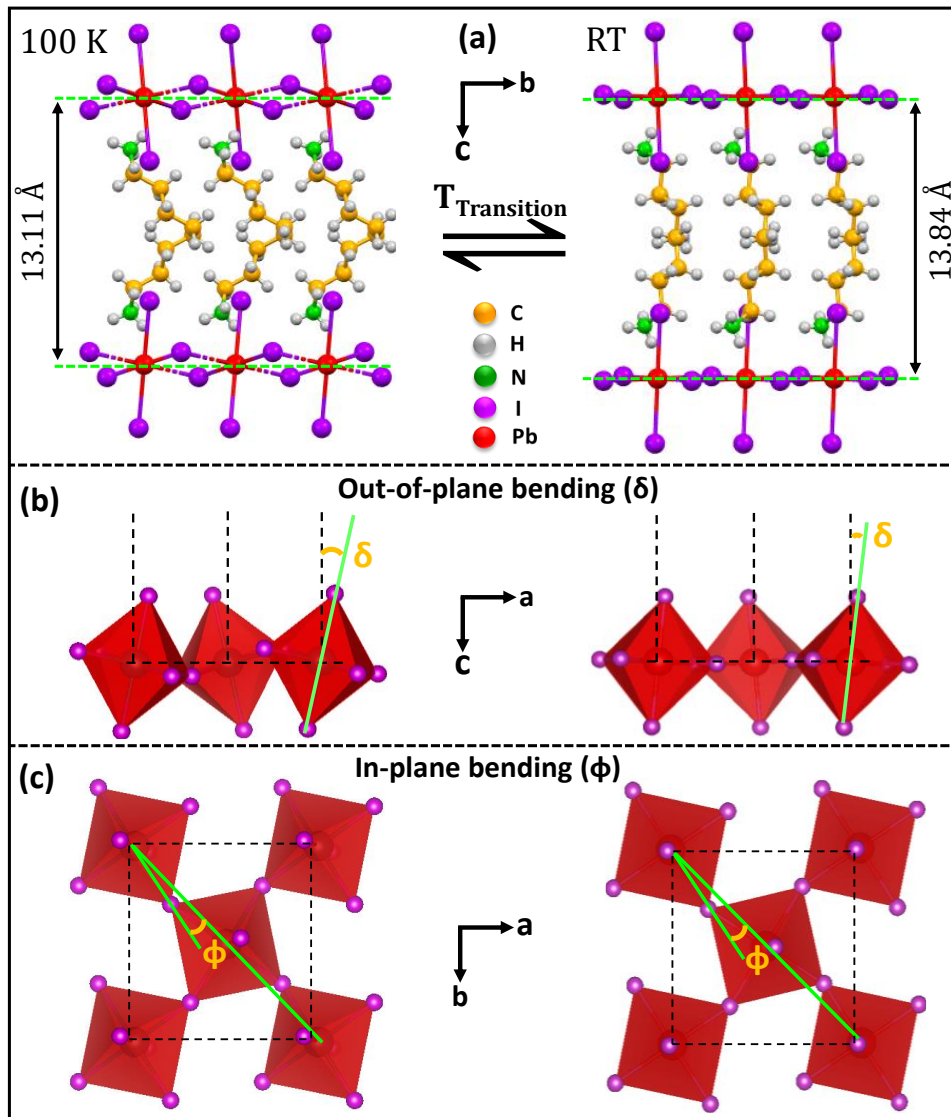


Figure 2.8: (a) Representative parts of the crystal structures of (BA)₂PbI₄ obtained from single crystal XRD data. The green dashed horizontal lines represent the side view of the “*ab*” crystal plane containing the Pb atoms. (b) Out-of-plane Pb-I-Pb bending (represented by δ) in (BA)₂PbI₄ at 100 K (left) and room temperature (right), respectively. The out-of-plane Pb-I-Pb bending changes significantly at the phase transition. (c) In-plane Pb-I-Pb bending (represented by ϕ) in (BA)₂PbI₄ at 100 K (left) and room temperature (right). The numbers are given in Table 2.2.

Now we correlate these structural changes to the increase in bandgap at low-T. The increase in octahedral tilting at low-T (100 K) decreases both (i) the distance between inorganic layers from 13.84 Å at RT to 13.11 Å at 100 K (Figure 2.8a), and (ii) the Pb-I-Pb bond angle (having a contribution from both in- and out-of-plane bending) from 155° at RT to 148° at 100 K as shown in Figure 2.9a. A decrease in interlayer spacing increases the band dispersion decreasing the bandgap.²⁶ For 2D (BA)₂PbI₄, the valance band maximum (VBM) is known to be formed by the anti-bonding interaction of Pb 6s-I 5p. As the Pb-I-Pb angle increases, the Pb 6s-I 5p

orbital overlap (or anti-bonding coupling) decreases, lowering the VBM accompanied by a less dispersive band.²⁷ Also, dispersion of Pb 6p_x and 6p_x-derived band decreases, effectively raising the conduction band minimum (CBM).²⁷ Prior computational study has shown that small change in Pb-I-Pb angle (or Sn-I-Sn angle) similar to the change observed in our RT and 100 K structures, can exhibit a few hundred meV changes in bandgap.^{25, 27} In addition to Pb-I-Pb bond angles and interlayer spacing, Figure 2.9b shows that the bond length of equatorial Pb-I increases at 100 K, which again can lower the VBM increasing the bandgap. We note here that in our present structure-bandgap discussion, the possible contribution from the difference in effective dielectric constant between the inorganic and organic layers has not been included.

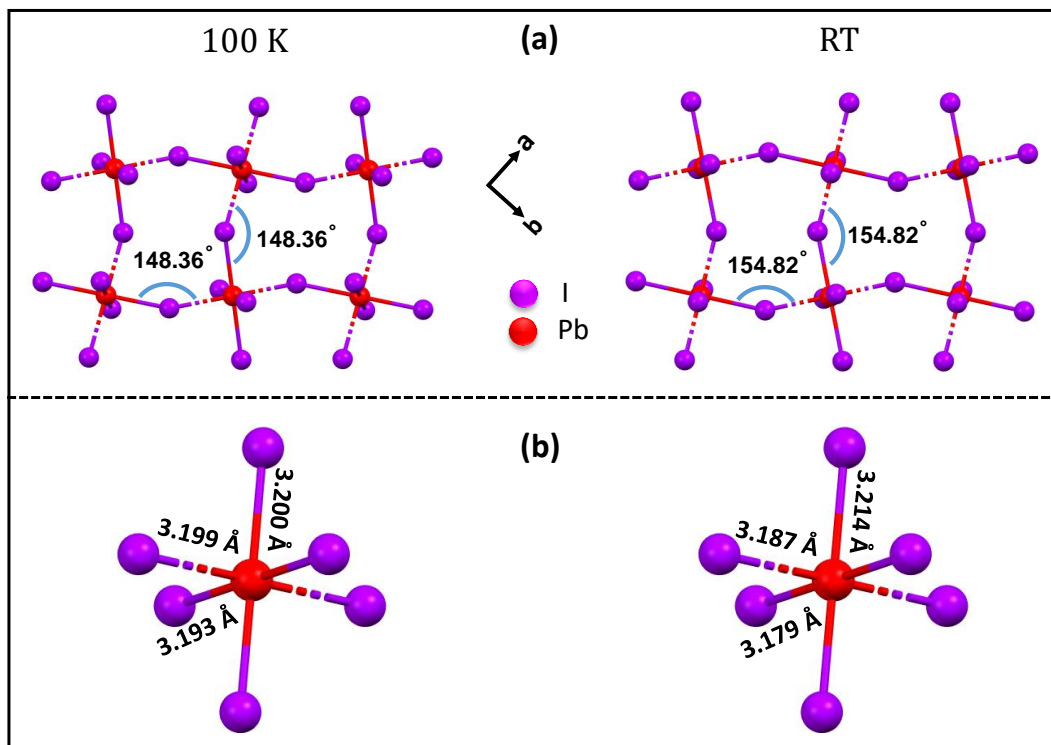


Figure 2.9: (a) Pb-I-Pb bond angle and (b) Pb-I₆ octahedra showing Pb-I bond lengths in (BA)₂PbI₄ at 100 K and RT.

Table 2.2: Structural parameters of (BA)₂PbI₄ at three different temperatures. Calculations are done following methodology shown in ref.²⁵

Temperature (K)	Pb-I-Pb bond angle (°)	In-/out-of-plane bending (°)	Eq./axial Pb-I bond lengths (Å)	Cation penetration (Å) ^a
100	148.36	22.79/12.81	3.199, 3.193/3.200	0.57
250	149.58	21.78/12.73	3.213, 3.207/3.188	0.54
RT	154.82	24.85/5.65	3.187, 3.179/3.214	0.61

^aCation penetration is defined by the distance between the planes of the N atoms of the cation and the planes of the axial I atoms of the perovskite sheet.

The similar temperature dependence of the two PL emissions across the phase transition temperature suggests that the two emissions in a $(\text{BA})_2\text{PbI}_4$ single crystal are excitonic in nature. This is in agreement with the optical absorption, diffused reflectance, steady-state, and time-resolved photoluminescence discussed in the previous sections.

2.3.5 Extending the dual excitonic emission to other layered perovskites single crystals

So far, we saw that $(\text{BA})_2\text{PbBr}_4$ single crystals show dual excitonic emission. We also established a structure bandgap relationship using temperature-dependent single crystal XRD and photoluminescence. If our findings are correct, then we would expect the dual excitonic emission in other similar layered hybrid perovskite systems as well. So, we extended our study to a series of layered hybrid perovskite systems. First, we replaced the Organic A-site cation, i.e., butylammonium (BA) ion, with hexylammonium (HA; $\text{C}_6\text{H}_{13}\text{NH}_3^+$) and octylammonium (OA; $\text{C}_8\text{H}_{15}\text{NH}_3^+$) ions, resulting in $(\text{HA})_2\text{PbI}_4$ and $(\text{OA})_2\text{PbI}_4$. The single crystals of both $(\text{HA})_2\text{PbI}_4$ and $(\text{OA})_2\text{PbI}_4$ show dual excitonic emission, as shown in Figure 2.10a. We also replaced iodide ions with bromide ions forming $(\text{BA})_2\text{PbBr}_4$. This bromide layered perovskite also showed dual excitonic emission (Figure 2.10b). Lastly, we replaced aliphatic A-site organic cation with aromatic phenethylammonium ion (PEA, $\text{C}_8\text{H}_9\text{NH}_3^+$). The single crystals of $(\text{PEA})_2\text{PbBr}_4$ again showed the dual excitonic emission, shown in Figure (Figure 2.10c). So similar to $(\text{BA})_2\text{PbI}_4$, all these layered perovskites single crystals show the dual excitonic emission irrespective of the A-site organic cations or the halide ions.

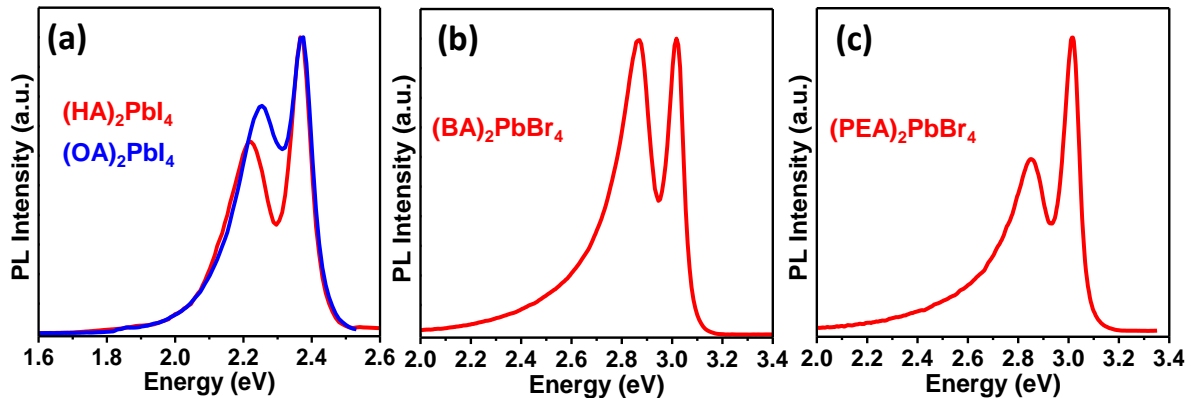


Figure 2.10: PL spectra of (a) $(\text{HA})_2\text{PbI}_4$ (red), $(\text{OA})_2\text{PbI}_4$ (blue), (b) $(\text{BA})_2\text{PbBr}_4$ and (c) $(\text{PEA})_2\text{PbBr}_4$ single crystals, showing the dual excitonic emission.

Two excitonic emissions, with different origins, in the same single crystal, are possible when there is some structural inhomogeneity in the single crystal. In literature, it has been observed that layer edges of 2D layered hybrid perovskite single crystals behave differently compared

to the terraces/bulk of the crystal.²⁸ There may be some minor structural differences between the layer edges and the bulk of the crystal. And it may be these structural differences that give rise to the two distinct excitonic emissions in these 2D layered hybrid perovskites. However, further theoretical and experimental studies are required for a better understanding.

2.4 Conclusion

Single crystalline (BA)₂PbI₄ is synthesized by employing a solution-processed method. These single crystals show dual PL emissions and corresponding two absorption features at room temperature. The time-resolved PL shows very short and similar lifetimes for both the emissions, suggesting a strong transition probability for both the emissions. To understand the structure-property relationships, we have measured single crystal XRD and PL data at different temperatures. A structural phase transition is observed below 250 K while cooling down the sample from room temperature to 10 K. Both the PL peaks equally blue shift because of the structural phase transitions. Both the emissions show a similar structural and temperature dependence. The structure dependence of the two emissions is reversible in nature, though with hysteresis in transition temperature between the heating and cooling cycle. The temperature-dependent phase transition is mainly because of a small difference in tilting of Pb-I₆ octahedra, which in turn changes the band gap, and therefore, excitonic emission energies. All these results suggest that there are two distinct excitonic absorptions and emissions in 2D layered (BA)₂PbI₄ single crystals. To generalize the dual excitonic emission, we synthesized a series of 2D layered hybrid perovskite single crystals, all of which show the dual excitonic emission.

2.5 References

1. Lee, M. M.; Teuscher, J.; Miyasaka, T.; Murakami, T. N.; Snaith, H. J. Efficient Hybrid Solar Cells Based on Meso-Superstructured Organometal Halide Perovskites. *Science* **2012**, *338*, 643-647.
2. Etgar, L.; Gao, P.; Xue, Z. S.; Peng, Q.; Chandiran, A. K.; Liu, B.; Nazeeruddin, M. K.; Gratzel, M. Mesoscopic CH₃NH₃PbI₃/TiO₂ Heterojunction Solar Cells. *J. Am. Chem. Soc.* **2012**, *134*, 17396-17399.
3. Song, J. Z.; Li, J. H.; Li, X. M.; Xu, L. M.; Dong, Y. H.; Zeng, H. B. Quantum Dot Light-Emitting Diodes Based on Inorganic Perovskite Cesium Lead Halides (CsPbX₃). *Adv. Mater.* **2015**, *27*, 7162-7167.

4. Swarnkar, A.; Marshall, A. R.; Sanehira, E. M.; Chernomordik, B. D.; Moore, D. T.; Christians, J. A.; Chakrabarti, T.; Luther, J. M. Quantum Dot-Induced Phase Stabilization of α -CspbI₃ Perovskite for High-Efficiency Photovoltaics. *Science* **2016**, *354*, 92-95.
5. Tong, Y.; Bladt, E.; Ayguler, M. F.; Manzi, A.; Milowska, K. Z.; Hintermayr, V. A.; Docampo, P.; Bals, S.; Urban, A. S.; Polavarapu, L.; Feldmann, J. Highly Luminescent Cesium Lead Halide Perovskite Nanocrystals with Tunable Composition and Thickness by Ultrasonication. *Angew. Chem. Int. Ed.* **2016**, *55*, 13887-13892.
6. Das Adhikari, S.; Dutta, S. K.; Dutta, A.; Guria, A. K.; Pradhan, N. Chemically Tailoring the Dopant Emission in Manganese-Doped CsPbCl₃ Perovskite Nanocrystals. *Angew. Chem. Int. Ed.* **2017**, *56*, 8746-8750.
7. Scheidt, R. A.; Samu, G. F.; Janaky, C.; Kamat, P. V. Modulation of Charge Recombination in CsPbBr₃ Perovskite Films with Electrochemical Bias. *J. Am. Chem. Soc.* **2018**, *140*, 86-89.
8. Akkerman, Q. A.; Rainò, G.; Kovalenko, M. V.; Manna, L. Genesis, Challenges and Opportunities for Colloidal Lead Halide Perovskite Nanocrystals. *Nat. Mater.* **2018**, *17*, 394-405.
9. Smith, I. C.; Hoke, E. T.; Solis-Ibarra, D.; McGehee, M. D.; Karunadasa, H. I. A Layered Hybrid Perovskite Solar-Cell Absorber with Enhanced Moisture Stability. *Angew. Chem. Int. Ed.* **2014**, *53*, 11232-11235.
10. Blancon, J. C.; Tsai, H.; Nie, W.; Stoumpos, C. C.; Pedesseau, L.; Katan, C.; Kepenekian, M.; Soe, C. M. M.; Appavoo, K.; Sfeir, M. Y.; Tretiak, S.; Ajayan, P. M.; Kanatzidis, M. G.; Even, J.; Crochet, J. J.; Mohite, A. D. Extremely Efficient Internal Exciton Dissociation through Edge States in Layered 2D Perovskites. *Science* **2017**, *355*, 1288-1291.
11. Stoumpos, C. C.; Cao, D. H.; Clark, D. J.; Young, J.; Rondinelli, J. M.; Jang, J. I.; Hupp, J. T.; Kanatzidis, M. G. Ruddlesden-Popper Hybrid Lead Iodide Perovskite 2D Homologous Semiconductors. *Chem. Mater.* **2016**, *28*, 2852-2867.
12. Zhou, N.; Shen, Y.; Li, L.; Tan, S.; Liu, N.; Zheng, G.; Chen, Q.; Zhou, H. Exploration of Crystallization Kinetics in Quasi Two-Dimensional Perovskite and High Performance Solar Cells. *J. Am. Chem. Soc.* **2018**, *140*, 459-465.
13. Mitzi, D. B. Synthesis, Crystal Structure, and Optical and Thermal Properties of (C₄H₉NH₃)₂MI₄ (M=Ge, Sn, Pb). *Chem. Mater.* **1996**, *8*, 791-800.
14. Pedesseau, L.; Saponi, D.; Traore, B.; Robles, R.; Fang, H. H.; Loi, M. A.; Tsai, H. H.; Nie, W. Y.; Blancon, J. C.; Neukirch, A.; Tretiak, S.; Mohite, A. D.; Katan, C.; Even, J.;

Kepenekian, M. Advances and Promises of Layered Halide Hybrid Perovskite Semiconductors. *ACS Nano* **2016**, *10*, 9776-9786.

15. Peng, W.; Yin, J.; Ho, K. T.; Ouellette, O.; De Bastiani, M.; Murali, B.; El Tall, O.; Shen, C.; Miao, X. H.; Pan, J.; Alarousu, E.; He, J. H.; Ooi, B. S.; Mohammed, O. F.; Sargent, E.; Bakr, O. M. Ultralow Self-Doping in Two-dimensional Hybrid Perovskite Single Crystals. *Nano Lett.* **2017**, *17*, 4759-4767.

16. Soe, C. M. M.; Stoumpos, C. C.; Kepenekian, M.; Traore, B.; Tsai, H.; Nie, W. Y.; Wang, B. H.; Katan, C.; Seshadri, R.; Mohite, A. D.; Eyen, J.; Marks, T. J.; Kanatzidis, M. G. New Type of 2D Perovskites with Alternating Cations in the Interlayer Space, $(\text{C}(\text{NH}_2)_3)(\text{CH}_3\text{NH}_3)_n\text{Pb}_n\text{I}_{3n+1}$: Structure, Properties, and Photovoltaic Performance. *J. Am. Chem. Soc.* **2017**, *139*, 16297-16309.

17. Zhuang, Z. W.; Peng, C. D.; Zhang, G. Y.; Yang, H. M.; Yin, J. L.; Fei, H. H. Intrinsic Broadband White-Light Emission from Ultrastable, Cationic Lead Halide Layered Materials. *Angew. Chem. Int. Ed.* **2017**, *56*, 14411-14416.

18. Chen, Y. N.; Sun, Y.; Peng, J. J.; Tang, J. H.; Zheng, K. B.; Liang, Z. Q. 2D Ruddlesden-Popper Perovskites for Optoelectronics. *Adv. Mater.* **2018**, *30*, 1703487.

19. Yaffe, O.; Chernikov, A.; Norman, Z. M.; Zhong, Y.; Velauthapillai, A.; van der Zande, A.; Owen, J. S.; Heinz, T. F. Excitons in Ultrathin Organic-Inorganic Perovskite Crystals. *Phys. Rev. B* **2015**, *92*, 045414.

20. Stoumpos, C. C.; Cao, D. H.; Clark, D. J.; Young, J.; Rondinelli, J. M.; Jang, J. I.; Hupp, J. T.; Kanatzidis, M. G. Ruddlesden-Popper Hybrid Lead Iodide Perovskite 2D Homologous Semiconductors. *Chem. Mater.* **2016**, *28*, 2852-2867.

21. Swarnkar, A.; Chulliyil, R.; Ravi, V. K.; Irfanullah, M.; Chowdhury, A.; Nag, A. Colloidal CsPbBr_3 Perovskite Nanocrystals: Luminescence beyond Traditional Quantum Dots. *Angew. Chem. Int. Ed.* **2015**, *54*, 15424-15428.

22. Jagadeeswararao, M.; Swarnkar, A.; Markad, G. B.; Nag, A. Defect-Mediated Electron-Hole Separation in Colloidal $\text{Ag}_2\text{S-AgInS}_2$ Hetero Dimer Nanocrystals Tailoring Luminescence and Solar Cell Properties. *J. Phys. Chem. C* **2016**, *120*, 19461-19469.

23. Smith, M. D.; Karunadasa, H. I. White-Light Emission from Layered Halide Perovskites. *Acc. Chem. Res.* **2018**, *51*, 619-627.

24. Billing, D. G.; Lemmerer, A. Synthesis, Characterization and Phase Transitions in the Inorganic-Organic Layered Perovskite-Type Hybrids $(\text{C}_n\text{H}_{2n+1}\text{NH}_3)_2\text{PbI}_4$, $n = 4, 5$ and 6 . *Acta Crystallogr. Sect. B-Struct. Sci.* **2007**, *63*, 735-747.

25. Knutson, J. L.; Martin, J. D.; Mitzi, D. B. Tuning The Band Gap in Hybrid Tin Iodide Perovskite Semiconductors using Structural Templating. *Inorg. Chem.* **2005**, *44*, 4699-4705.
26. Umeyama, D.; Lin, Y.; Karunadasa, H. I. Red-to-Black Piezochromism in a Compressible Pb-I-SCN Layered Perovskite. *Chem. Mater.* **2016**, *28*, 3241-3244.
27. Xiao, Z. W.; Meng, W. W.; Wang, J. B.; Mitzi, D. B.; Yan, Y. F. Searching for Promising New Perovskite-Based Photovoltaic Absorbers: The Importance of Electronic Dimensionality. *Mater. Horiz.* **2017**, *4*, 206-216.
28. Wang, K.; Wu, C.; Jiang, Y.; Yang, D.; Wang, K.; Priya, S. Distinct Conducting Layer Edge States in Two-Dimensional (2D) Halide Perovskite. *Sci. Adv.* **2019**, *5*, eaau3241.

Chapter 3

Interlayer Interactions in 2D Layered Hybrid Perovskites

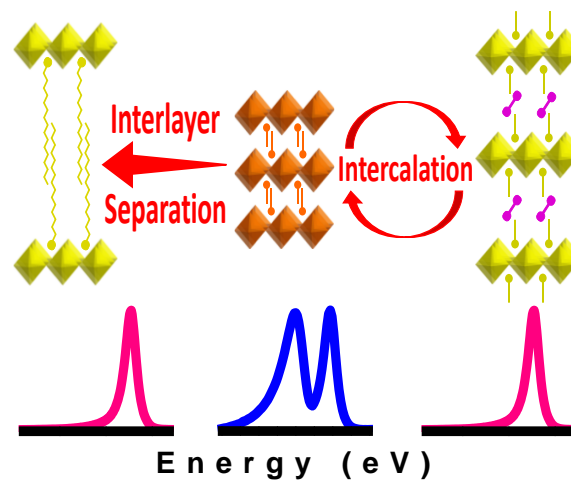
The work presented in this chapter is published in *Angewandte Chemie* with the following details:

Sheikh, T.; Nawale, V.; Pathoor, N, Phadnis, C.; Chowdhury, A.; Nag, A. Molecular Intercalation and Electronic Two Dimensionality in Layered Hybrid Perovskites. *Angew. Chem. Int. Ed.* **2020**, *59*, 11653-11659.

Copyright permission has been taken for the whole article from John Wiley and Sons.

Abstract

In layered hybrid perovskites like $(\text{BA})_2\text{PbI}_4$ ($\text{BA} = \text{C}_4\text{H}_9\text{NH}_3$), electrons and holes are considered to be confined in atomically thin two-dimensional (2D) Pb-I inorganic layers. These inorganic layers are electronically isolated from each other in the third dimension by the insulating organic layers. Our experimental findings suggest the presence of electronic interaction between the inorganic layers in some parts of the single crystals. The extent of this interaction is reversibly tuned by the intercalation of organic and inorganic molecules in the layered perovskite single crystals. Consequently, optical absorption and emission properties switch reversibly with intercalation. Furthermore, increasing the distance between inorganic layers by increasing the length of the organic spacer cations systematically decreases these electronic interactions. This finding that the parts of the layered hybrid perovskites are not strictly electronically 2D is critical for understanding the electronic, optical and optoelectronic properties of these technologically important materials.

Graphical Abstract

3.1 Introduction

Metal halide perovskites, including the layered hybrid perovskites, are now considered technologically important optical and optoelectronic materials.¹⁻¹² One of the simplest compositions of layered hybrid perovskites is $(\text{BA})_2\text{PbI}_4$ ($\text{BA} = \text{C}_4\text{H}_9\text{NH}_3^+$).¹³⁻¹⁵ It is considered that the electron and hole are confined in atomically thin two-dimensional (2D) Pb-I inorganic layers, which are electronically isolated from each other in the third dimension by the insulating organic layers.¹⁶⁻²⁰ A millimeter thick single crystal of $(\text{BA})_2\text{PbI}_4$ contains millions of atomically thin Pb-I semiconducting layers (wells) in a periodic arrangement, separated by insulating organic layers (barriers), forming a repeating quantum well structure. Typical all-inorganic quantum wells like AlAs/GaAs/AlAs are well understood,²¹⁻²² but the hybrid $(\text{BA})_2\text{PbI}_4$ quantum well is distinctly different from the all-inorganic ones. In AlAs/GaAs, the electronic properties of individual components AlAs and GaAs are well understood, which are then extended to understand the interface between the components. But both the components of $(\text{BA})_2\text{PbI}_4$, namely BA^+ and $(\text{PbI}_4)^{2-}$, do not exist independently. Furthermore, the interaction between BA^+ and $(\text{PbI}_4)^{2-}$ is ionic in nature, unlike the case of AlAs/GaAs interface. Another important difference is the huge dielectric contrast between the organic and inorganic parts, unlike the all-inorganic quantum wells. All these complexities make it difficult to understand the electronic and optical properties of the hybrid layered perovskites, demanding newer theoretical and experimental approaches to solve the problem.²³

There are some peculiarities in the experimentally observed optical and electronic data of these layered perovskites. For example, a single crystal of $(\text{BA})_2\text{PbI}_4$ and other layered hybrid perovskite systems exhibit two (band edge) excitonic absorption and emission features, as if the same crystal has two band gaps!²⁴ Further, Wang et al. found that the edges of $(\text{BA})_2\text{PbI}_4$ single crystals are significantly more electrically conducting than their terraces.²⁵ We hypothesize that some of these unusual experimental observations might arise from possible electronic interactions between the Pb-I layers. To verify such possibility, we intercalated insulating molecules in the single crystals of layered perovskites like $(\text{BA})_2\text{PbI}_4$, $(\text{DA})_2\text{PbI}_4$ ($\text{DA} = \text{decylamine}$) and $(\text{PEA})_2\text{SnI}_4$ ($\text{PEA} = \text{phenylethylammonium}$). In addition to the increase in the distance between the Pb-I layers, the molecular intercalation disturbs the interaction between hydrocarbon tails of organic cations. The photoluminescence (PL) spectra in a layered perovskite single crystal switch reversibly from dual emission to single emission upon intercalation. These results, along with the spatially resolved PL spectra, suggest that in parts of the single crystals, probably at the edges, Pb-I layers interact with each other. Further,

we tuned the strength of this electronic interaction systematically by changing the chain length of organic spacer cations.

3.2 Experimental Section

3.2.1 Chemicals

Lead(II) oxide (Sigma Aldrich, 99.9%), tin(II) oxide (Sigma Aldrich, 97%), hydriodic acid (Sigma Aldrich, 57% w/w in H₂O, 99.9%), hypophosphorous acid (Avra, 50% w/w H₂O), butylamine (Sigma Aldrich, 99.5%), hexylamine (Sigma Aldrich, 98%), octylamine (Sigma Aldrich, 98%), decylamine (Sigma Aldrich, 99%), dodecylamine (Sigma Aldrich, 99%), tetradecylamine (Sigma Aldrich, 95%), hexadecylamine (Sigma Aldrich, 98%), phenethylamine (Sigma Aldrich, 99.9%) hexafluorobenzene (Sigma Aldrich, 99%), diethyl ether (Rankem, 99.5%), iodine (Rankem, 99.5%), hexane (Rankem, 99.5%).

3.2.2 Synthesis of butylammonium iodide (C₄H₉NH₃I)

924 μ L (10 mmol) butylamine was neutralized with 5 mL (38 mmol) hydriodic acid in an ice bath resulting in a clear pale yellow solution of C₄H₉NH₃I.

3.2.3 Synthesis of butylammonium lead iodide [(BA)₂PbI₄] single crystals

(BA)₂PbI₄ single crystals were synthesized by an acid precipitation method following a prior report.²⁶ 2232 mg (10 mmol) lead(II) oxide was dissolved in a mixture of 10 mL hydriodic acid and 1.7 mL hypophosphorous acid by heating to boiling under constant magnetic stirring. A bright yellow solution was obtained, to which a freshly prepared C₄H₉NH₃I solution was added, which resulted in an orange precipitate. The solution was again heated until the precipitate got dissolved completely. The heating was stopped, and the solution was allowed to cool to room temperature. While cooling, orange-colored sheet-like crystals started to crystalize. The crystallization completed in ~2 hours. The crystals were filtered and washed with diethyl ether.

3.2.4 Synthesis of hexylammonium lead iodide [(HA)₂PbI₄] single crystals

(HA)₂PbI₄ single crystals were synthesized by slightly modifying the synthesis method used for (BA)₂PbI₄ single crystals. 1116 mg (5 mmol) of lead(II) oxide was dissolved in 20 mL hydriodic acid by heating to boiling under constant stirring, which resulted in a bright yellow solution. To this boiling solution, 667 μ L (5 mmol) of hexylamine was added, which resulted in an orange precipitate. The solution was heated until the precipitate dissolved completely. The rest of the steps are the same as those followed in the synthesis of (BA)₂PbI₄ single crystals.

3.2.5 Synthesis of octylammonium lead iodide [(OA)₂PbI₄], decylammonium lead iodide [(DA)₂PbI₄], dodecylammonium lead iodide [(DDA)₂PbI₄], tetradecylammonium lead iodide [(TDA)₂PbI₄], and hexadecylammonium lead iodide [(HDA)₂PbI₄] single crystals

All these layered hybrid lead iodide perovskite single crystals were synthesized by following the same method as that of (HA)₂PbI₄. Only the amount of lead(II) oxide and the corresponding amine were changed. Briefly, 2.5 mmol each of lead(II) oxide and octylamine for (OA)₂PbI₄, 0.5 mmol of lead(II) oxide and decylamine for (DA)₂PbI₄, 0.2 mmol of lead(II) oxide and dodecylamine for (DDA)₂PbI₄, 0.1 mmol of lead(II) oxide and tetradecylamine for (TDA)₂PbI₄ and 0.1 of lead(II) oxide and hexadecylamine (HDA)₂PbI₄ were used for their syntheses.

3.2.6 Synthesis of phenethylammonium tin iodide [(PEA)₂SnI₄] single crystals

(PEA)₂SnI₄ single crystals were synthesized by modifying the synthesis method used for (HA)₂PbI₄ single crystals. In the glove box, 0.6 mmol tin(II) oxide was taken in a vial and sealed with a rubber septum. 5 mL hydriodic acid and 3 mL hypophosphorous acid were injected into this sealed vial by a syringe. The solution was heated to 90°C under constant stirring. Tin(II) oxide dissolved, and a dark yellow solution was obtained, to which 1.2 mmol phenethylamine was injected. The heating was stopped, and the solution was allowed to cool to room temperature, during which dark brown sheet-like crystals of (PEA)₂SnI₄ precipitated out. The crystals were filtered, dried and stored in an N₂ filled glove box for further use.

3.2.7 Iodine intercalation in (BA)₂PbI₄ single crystals

(BA)₂PbI₄ single crystals were placed in an open Eppendorf tube. This Eppendorf tube was placed in a glass vial containing molecular iodine crystals. The purpose of the Eppendorf tube is to prevent direct contact between the (BA)₂PbI₄ crystals and iodine crystals. The vial was closed and kept as such for 2-3 hours. Iodine sublimates at room temperature, and the vapors generated intercalate in the perovskite single crystals.

3.2.8 Hexane intercalation in (DA)₂PbI₄ single crystals

To intercalate hexane, (DA)₂PbI₄ single crystals were dropped in hexane in a closed vial. The vial was kept as such for 1-2 hours. A color change from dark yellow to light yellow is observed in the (DA)₂PbI₄ single crystals, which indicates hexane is intercalated in the perovskite crystals.²⁷

3.2.9 Hexafluorobenzene (HFB) insertion in (PEA)₂SnI₄ single crystals forming (PEA)₂SnI₄:HFB single crystals

HFB was inserted between the (PEA)₂SnI₄ perovskite layers by following a reported method.²⁸ 50 mg (PEA)₂SnI₄ was dissolved in a mixture of 2 mL methanol and 2 mL HFB. The obtained dark yellow solution was kept open in a glove box. As the solvent evaporates (PEA)₂SnI₄:HFB, crystals precipitate out. The crystals were filtered, dried and stored in a glove box for further use.

3.2.10 Characterization

Single crystal X-ray diffraction (XRD) data were recorded on Bruker Smart Apex Duo diffractometer at room temperature (298 K) using Mo K α radiation ($\lambda = 0.71073 \text{ \AA}$). Integration of the frames was done in the Bruker SAINT software package by a narrow-frame algorithm. The structures were solved by a direct method and refined by full-matrix least-squares on F² using the SHELXTL software package. The PbX₄ framework was refined anisotropically without any constraint, whereas the organic atoms were refined isotropically with constraints on the C-C and C-N bond lengths. Powder XRD measurements were recorded on Bruker D8 Advance X-ray diffractometer using Cu K α radiation (1.54 \AA). Scanning electron microscopy (SEM) images were collected on the Zeiss Ultra Plus FESEM instrument. UV-Visible absorbance data were recorded on Cary Series UV-Vis Spectrophotometer (Agilent Technologies). Optical diffuse-reflectance spectra were collected at room temperature using a Shimadzu UV-3600 plus UV-VIS-NIR spectrophotometer. The reflectance spectra were converted to absorbance by using Kubelka-Munk transformation.²⁹ Steady-state photoluminescence (PL) data were recorded on FLS 980 (Edinburgh Instruments).

3.2.11 Fluorescence microscopy imaging and spatially resolved spectroscopy

PL imaging and spatially resolved emission spectroscopy of (BA)₂PbI₄ single crystals were performed on a home-built wide-field epi-fluorescence microscopy setup under ambient conditions (298K). The spatially resolved fluorescence microscopy imaging was carried out in Prof. Arindam Chowdhury's lab at the Indian Institute of Technology Bombay (IITB), with the help of Nithin Pathoor (IITB). The details of the experimental setup can be found elsewhere.³⁰⁻³¹ For these measurements, a 405 nm laser (LaserGlow, LRD-0405-PFR) was used to excite samples placed on an inverted microscope (Nikon Eclipse 2000U), with a 1.49NA 60x oil immersion objective to illuminate a large circular area (with diameter $\sim 100 \mu\text{m}$) of the sample. An excitation power density of $0.8\text{W}/\text{cm}^2$ was used for all the measurements. The luminescence

was collected through the same objective lens, passed through a set of emission filters to remove residual excitation light, and imaged at 100 ms exposure time using a scientific CMOS camera (Hamamatsu Orca Flash 4.0 v3). All movies were collected as a sequence of images in a 16-bit format at 10 Hz and analyzed using ImageJ 1.50 (NIH). Spectrally-resolved PL microscopy was performed using a combination of a narrow slit and a transmission grating (Optometrics, 70 grooves/mm) placed in the emission path before the detector.³⁰⁻³¹ Similar excitation conditions were used here with an exposure time of 200 ms. The spectral images were processed using ImageJ and analyzed/processed using OriginLab.

3.3 Results and Discussion

3.3.1 Spatially resolved PL in (BA)₂PbI₄ single crystal

We synthesize (BA)₂PbI₄ single crystals following a reported method (see experimental section).²⁶ Detailed characterization of (BA)₂PbI₄ single crystals can be found in chapter two of this thesis. Intriguingly, the PL spectrum of the as-synthesized single crystal shows two excitonic transitions (Figure 3.1), similar to our earlier report.²⁴ All the PL data presented in this manuscript are recorded from the front side of the crystal (inset of Figure 3.1), i.e., the excitation source and the detector are on the same side of the crystal, making a 90° angle with each other.

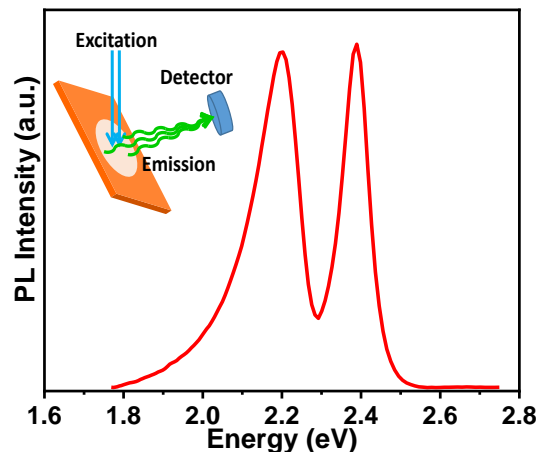


Figure 3.1: PL spectrum of a (BA)₂PbI₄ single crystal. The inset shows the geometry in which the PL was recorded. The angle between the excitation light and the crystal was adjusted in such a way that the relative intensity of the two peaks is almost equal.

To verify whether the two emissions arise from diverse spatial locations within a crystal, we performed energetically resolved PL imaging of (BA)₂PbI₄ single crystals using a home-built laser epi-fluorescence microscopy setup (details in section 3.2.11). It is worth mentioning that

the PL imaging measurements were carried out in Prof. Arindam Chowdhury's lab at IITB, with the help of Nithin Pathoor (IITB). $(\text{BA})_2\text{PbI}_4$ crystals can be easily visualized owing to the intense greenish-yellow hue originating from both the excitonic emissions. The PL image (Figure 3.2a) over both the emissions show that while the entire crystal is emissive, there is considerable spatial variation in the intensity. To selectively detect the spatial distribution of the lower-energy emission, we collected the fluorescence image of the same crystal via a 540 nm (~ 2.30 eV) long-pass filter (Figure 3.2c). Figure 3.2b shows the PL image for the emission in the range of 460 to 540 nm (higher energy emission only). These energy-mapped intensity images hinted at the dominance of the lower energy (yellow) emission near the crystal edges.

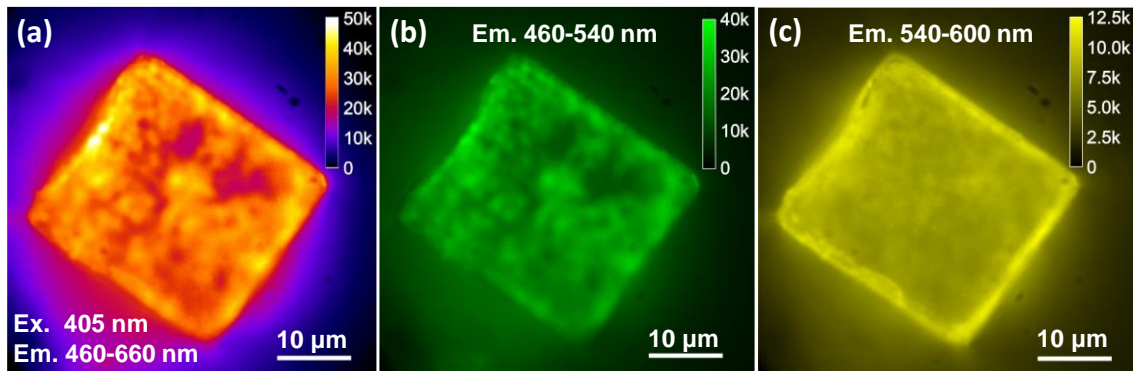


Figure 3.2: Fluorescence intensity (false color) images of a $(\text{BA})_2\text{PbI}_4$ single crystal in the wavelength range (a) 460 to 660 nm, (b) 460 nm to 540 nm and (c) 540 to 660 nm. (b) is calculated by subtracting (c) from the total PL intensity image (a).

PL spectral profiles recorded from several locations of the crystal (Figure 3.3b) reveal a remarkable spatial variation in the relative intensities of the two transitions. We find that the relative intensity of the low energy (2.25 eV) emission is much higher near the edges compared to the interior regions. On the contrary, the high energy (2.38 eV) emission is typically much more pronounced far away from the crystal boundaries. Such spatial heterogeneity in PL characteristics is clearly visible in the spectrally-resolved PL image (Figure 3.3c) obtained for a narrow strip at the bottom of the crystal. The spectral image additionally reveals a rather gradual variation in the relative intensity of the two excitonic transitions upon progression from the interior regions to the boundary zones. It is a relevant note that step-like edges are present throughout the surface of the single crystal, as evident from the field emission scanning electron microscopy (FESEM) image (Figure 3.3d) and shown schematically in Figure 3.3e. It is likely that all these step-like edges contribute significantly to the lower energy transition, and consequently, the yellow emission is spread over the entire crystal, even at locations far from the crystal boundaries. It is to be noted here that the edge-state emission from our $(\text{BA})_2\text{PbI}_4$ is

different than the previously reported^{25, 32} edge-state emissions from layered perovskites like $(\text{C}_4\text{H}_9\text{NH}_3)_2(\text{CH}_3\text{NH}_3)_2\text{Pb}_3\text{I}_{10}$ and $(\text{C}_4\text{H}_9\text{NH}_3)_2(\text{CH}_3\text{NH}_3)_3\text{Pb}_4\text{I}_{13}$ with $(n \geq 2)$. For samples with $n \geq 2$, the small A-site cations CH_3NH_3^+ lead to the formation of 3D perovskite compositions at the edges. Therefore, for $n \geq 2$, the formation of 3D perovskite edge-states gives lower energy emission with peak energy similar to that of a pure 3D perovskite.³²⁻³³ In our $(\text{BA})_2\text{PbI}_4$ ($n = 1$), neither smaller A-site cations are present nor the emission energy of edge states match with 3D perovskites.

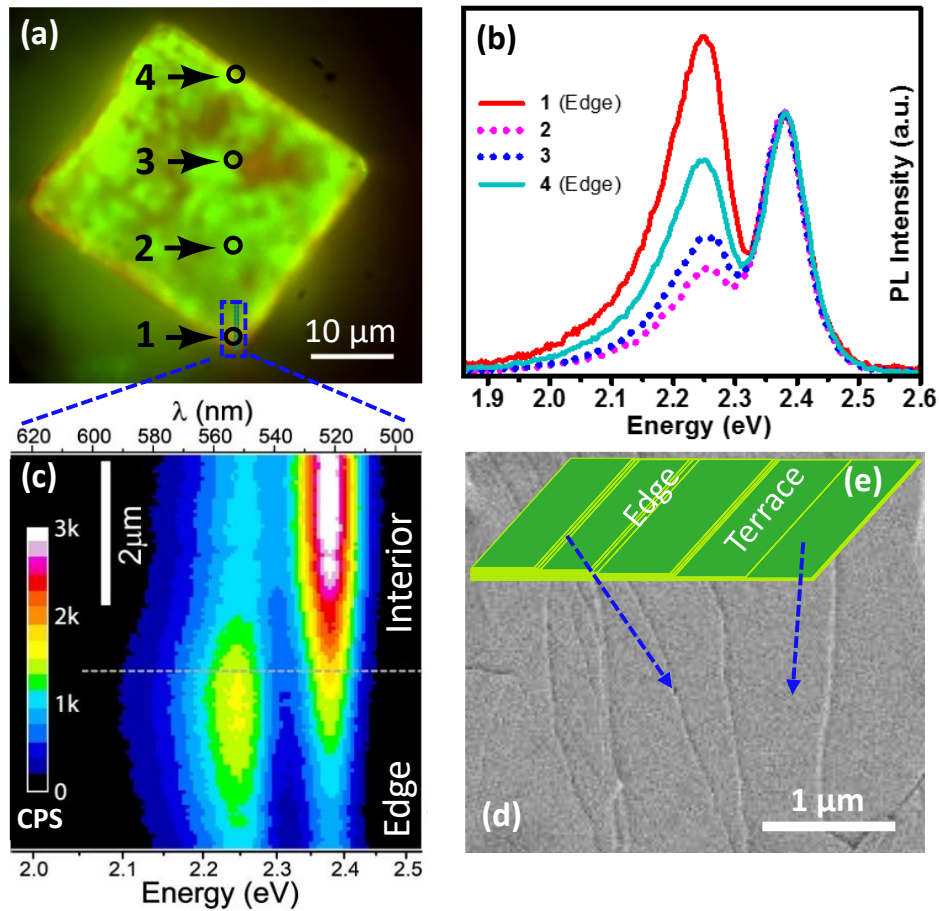


Figure 3.3: (a) Pseudo-colored PL intensity image generated by the superposition of PL images (Figure 3.2 b and c) collected at two energies. (b) Spatially resolved PL emission spectra from the edges (1,4) and the interior regions (2,3) (locations marked in (a)). (c) Spectrally-resolved PL image of a rectangular strip at the bottom of the crystal (marked using a dotted rectangular in (a)). Intensity calibration is in counts per second (cps). (d) A representative FESEM image of the top surface of $(\text{BA})_2\text{PbI}_4$ single crystal. (e) Schematic showing the edges present on the surface of a layered crystal.

3.3.2 Iodine intercalation in $(\text{BA})_2\text{PbI}_4$ single crystal

To explore the origin of two excitonic emissions, we exposed the $(\text{BA})_2\text{PbI}_4$ single crystals to the iodine (I_2) vapors, leading to insertion (intercalation) of molecular I_2 into the layered

perovskites. I₂ is selected here based on the prior report of successful intercalation of I₂ into similar layered perovskite systems.³⁴ The intercalated I₂ slowly comes out (de-intercalate) from the perovskite crystals upon removing the I₂ atmosphere. This reversibility of the I₂ intercalation process is schematically depicted in Figure 3.4a. The intercalation of I₂ is expected to increase the distance between Pb-I layers. Indeed, the powder x-ray diffraction (PXRD) patterns of (BA)₂PbI₄ single crystal (Figure 3.4b) show a shift in the peaks towards the lower angles (2θ values) upon I₂ insertion, which indicates an increase in the interlayer distance.^{24, 26} Subsequent de-intercalation process reverts the PXRD peaks to the original 2θ values.

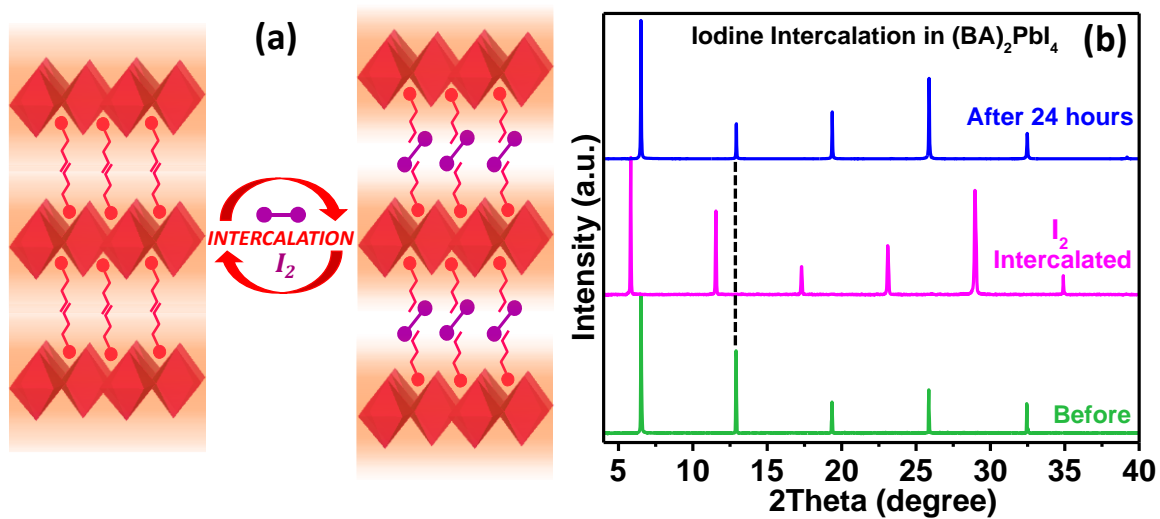


Figure 3.4: (a) Schematic showing reversible intercalation of molecular iodine into a (BA)₂PbI₄ single crystal. (b) PXRD patterns of (BA)₂PbI₄ single crystal with and without I₂ intercalation.

The PL spectrum of (BA)₂PbI₄ single crystal (Figure 3.5a) shows dual emission peaks as discussed above.^{24, 35} Interestingly, after I₂ intercalation, the lower energy (2.21 eV) emission completely disappears without affecting the higher energy (2.38 eV) emission. Subsequently, during the de-intercalation process, the low energy emission reappears within an hour, as shown in Figure 3.5b. Upon the progressive release of I₂ from the (BA)₂PbI₄ lattice, we observed a systematic increase in the intensity of low-energy emission with (de-intercalation) time. The intercalation of I₂ increases the distance between the inorganic layers (Figure 3.4a), and further, it is expected to disrupt the interactions between the hydrocarbon tails of BA⁺ ions, thereby reducing the structural rigidity across the Pb-I layers. Therefore, the reversible disappearance and reappearance of the low-energy emission at 2.21 eV with intercalation and de-intercalation of I₂, respectively, suggests that the low-energy emission originates from some electronic interaction between the Pb-I layers.

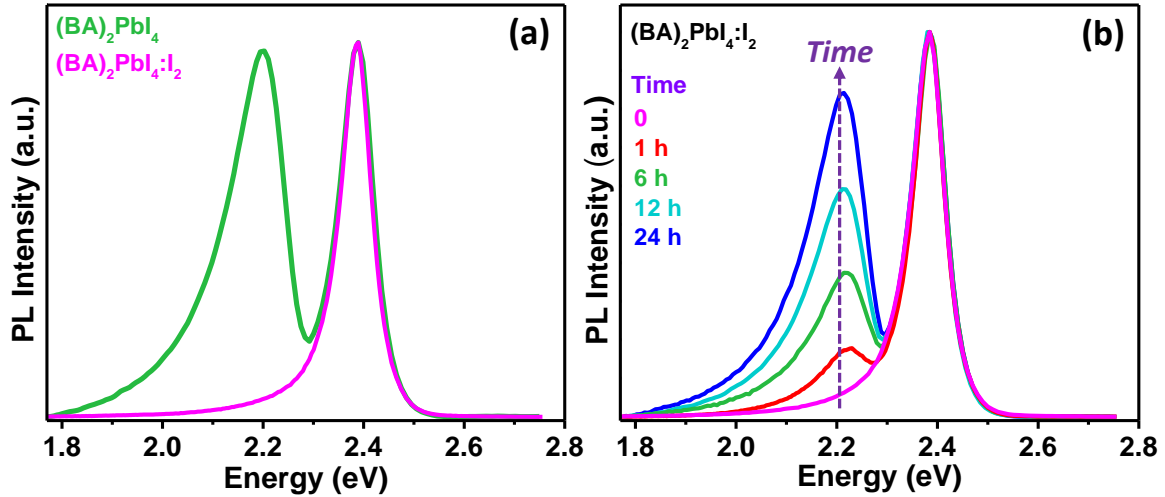


Figure 3.5: (a) PL spectra of $(\text{BA})_2\text{PbI}_4$ single crystal with and without I_2 intercalation. (b) Evolution of PL peak during the de-intercalation process of $(\text{BA})_2\text{PbI}_4:\text{I}_2$.

These results suggest that there are parts in a single crystal of $(\text{BA})_2\text{PbI}_4$ showing the high-energy PL emission, where Pb-I layers do not interact with each other, as this emission is independent of the molecular intercalation. In some other parts, Pb-I layers interact with each other originating the low-energy PL emission. Spatially resolved PL spectra (Figure 3.3) suggest that the edges of the crystals have more contribution from the low-energy PL emission. Therefore, the edges of the crystals can be considered as those locations where the Pb-I layers interact predominantly, introducing the pseudo-3D nature in the system. These results agree with the recent report that showed edges could conduct electricity, unlike other parts of $(\text{BA})_2\text{PbI}_4$ single crystal.²⁵ It is to be noted here that electron injection/extraction, required for any electronic and optoelectronic applications, occurs through these edge states because the terraces of layered perovskites are insulating. Therefore, not only the optical properties but also the charge transfer or transport properties need to consider this pseudo-3D electronic nature of the edge states

3.3.3 Hexane intercalation in $(\text{DA})_2\text{PbI}_4$ single crystal

Unfortunately, there is an overlap in the optical absorption of intercalated I_2 with $(\text{BA})_2\text{PbI}_4$ (Figure 3.6), which complicates the comparison of the absorption spectra before and after the intercalation process. To compare both absorption and emission spectra before and after the intercalation process, we searched for a system where there is no overlap in the absorption of the intercalating molecules with that of the host perovskite. From the literature, we found that molecular hexane can be intercalated into layered perovskites. However, as hexane is larger than I_2 , the chain length of organic cations in the hybrid perovskite also has to be longer to

accommodate hexane.²⁷ Consequently, $(\text{DA})_2\text{PbI}_4$ (DA = decylamine) single crystals are synthesized and intercalated with hexane. Details of synthesis, characterization and intercalation methodologies are provided in the experimental section. Schematics in Figure 3.7a depict the reversible hexane intercalation in a $(\text{DA})_2\text{PbI}_4$ single crystal. PXRD patterns (Figures 3.7b and c) show an increase in interlayer distance after hexane intercalation, and the interlayer distance comes back to the original value after the de-intercalation of hexane.

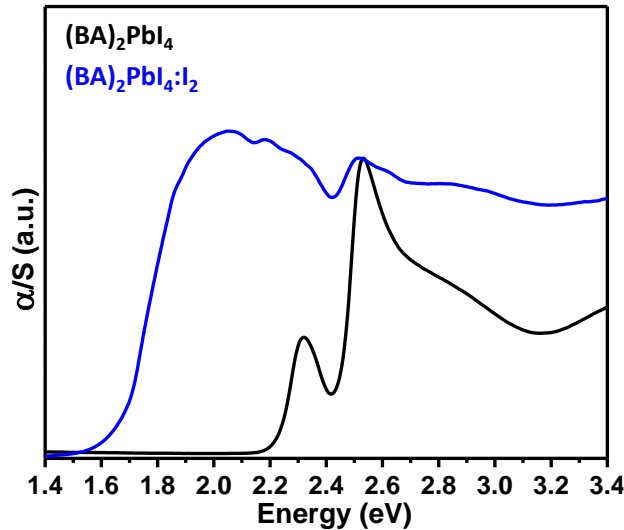


Figure 3.6: (a) UV-visible absorbance spectra of $(\text{BA})_2\text{PbI}_4$ single crystal (black) and iodine intercalated $(\text{BA})_2\text{PbI}_4$ single crystal (blue) obtained from diffuse reflectance measurements converted using the Kubelka–Munk function ($\alpha/S = (1 - R)^2/2R$); α is the absorption coefficient, and S is the scattering coefficient R is the reflectance.²⁹

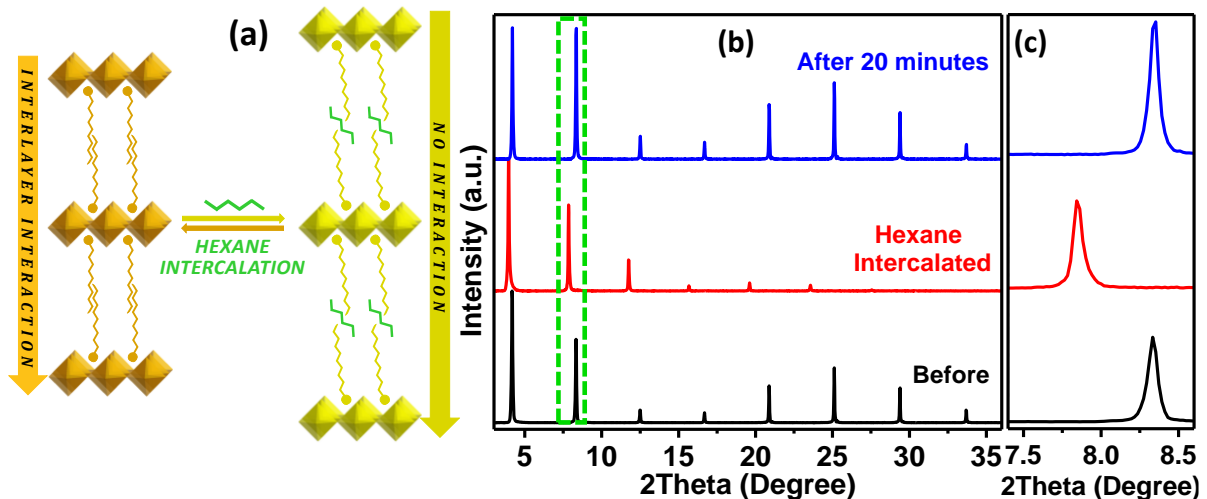


Figure 3.7: (a) Schematic showing reversible intercalation of molecular hexane in $(\text{DA})_2\text{PbI}_4$ single crystal. (b) PXRD patterns of $(\text{DA})_2\text{PbI}_4$ single crystal (black), hexane intercalated $(\text{DA})_2\text{PbI}_4$ single crystal (red) and de-intercalated $(\text{DA})_2\text{PbI}_4$ single crystal after 20 minutes from intercalation (blue). (c) A magnified view of the PXRD peak highlighted in the green box of Figure b.

PL spectra in Figure 3.8a switch from dual emission for pristine $(\text{DA})_2\text{PbI}_4$ to a single emission for hexane intercalated $(\text{DA})_2\text{PbI}_4$. The disappearance of the low-energy emission is also accompanied by a blue shift in the absorption spectrum of $(\text{DA})_2\text{PbI}_4$ after hexane intercalation, as shown in Figure 3.8b. The switching of PL from dual to single emission is again reversible with intercalation/de-intercalation of hexane, as shown in Figure 3.8a. Overall, the reversible intercalation of I_2 and hexane into $(\text{BA})_2\text{PbI}_4$ and $(\text{DA})_2\text{PbI}_4$ single crystals, respectively, resulted in similar reversible changes in optical absorption and emission. In both cases, intercalations reduce (or eliminate) interactions between the Pb-I layers, eliminating the lower energy emission.

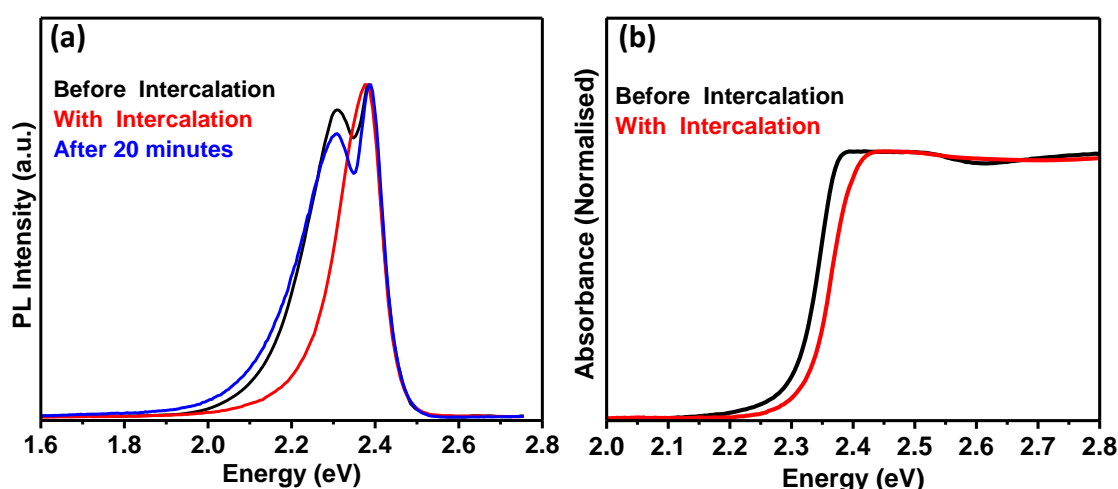


Figure 3.8: (a) PL spectra of $(\text{DA})_2\text{PbI}_4$ single crystal before (black), with (red) and after (blue) hexane intercalation. (b) UV-visible absorption spectra of $(\text{DA})_2\text{PbI}_4$ single crystals before (black) and with (red) hexane intercalation.

3.3.4 HFB intercalation in $(\text{PEA})_2\text{SnI}_4$ single crystal

We preferred reversible intercalation in the previous cases for reliable correlation of intercalation with electronic dimensionality and optical properties. However, this reversible process has one demerit. Structural analysis of the intercalated crystals using single crystal XRD is challenging because of the de-intercalation process during the measurement. So, it remains unclear whether the intercalated molecules are ordered or disordered and how many molecules are present within the intercalating layers. To address this issue, we made irreversible intercalation of hexafluorobenzene (HFB) in phenylethylammonium tin iodide [$(\text{PEA})_2\text{SnI}_4$], following the work of Mitzi et al.²⁸ The highly electron-deficient HFB strongly binds with the electron-rich phenyl rings of $(\text{PEA})_2\text{SnI}_4$, providing stability to the intercalated system that can be termed as $(\text{PEA})_2\text{SnI}_4:\text{HFB}$. Methodologies for synthesizing and

intercalating $(\text{PEA})_2\text{SnI}_4$ single crystals are given in the experimental section. PXRD patterns provided in Figure 3.9a confirm the intercalation of HFB between the $(\text{PEA})_2\text{SnI}_4$ layers. Figure 3.9b compares the crystal structure of $(\text{PEA})_2\text{SnI}_4$ before and after intercalation, obtained by recording single crystal XRD. Both $(\text{PEA})_2\text{SnI}_4$ and $(\text{PEA})_2\text{SnI}_4:\text{HFB}$ crystallize in a triclinic lattice with $P(-1)$ space group. The lattice parameters of $(\text{PEA})_2\text{SnI}_4$ and $(\text{PEA})_2\text{SnI}_4:\text{HFB}$ are $a = 8.6321(16) \text{ \AA}$, $b = 8.6344(16) \text{ \AA}$, $c = 16.358(3) \text{ \AA}$, $\alpha = 94.696(5)^\circ$, $\beta = 100.426(5)^\circ$, $\gamma = 90.450(5)^\circ$ and $a = 8.5663(12) \text{ \AA}$, $b = 8.5699(12) \text{ \AA}$, $c = 20.485(3) \text{ \AA}$, $\alpha = 98.638(4)^\circ$, $\beta = 93.594(4)^\circ$, $\gamma = 90.064(4)^\circ$ respectively (see Table 3.1 for details). The HFB molecules are sandwiched between the phenyl rings of two phenylethylammonium ions of the adjacent layers in a regular pattern.

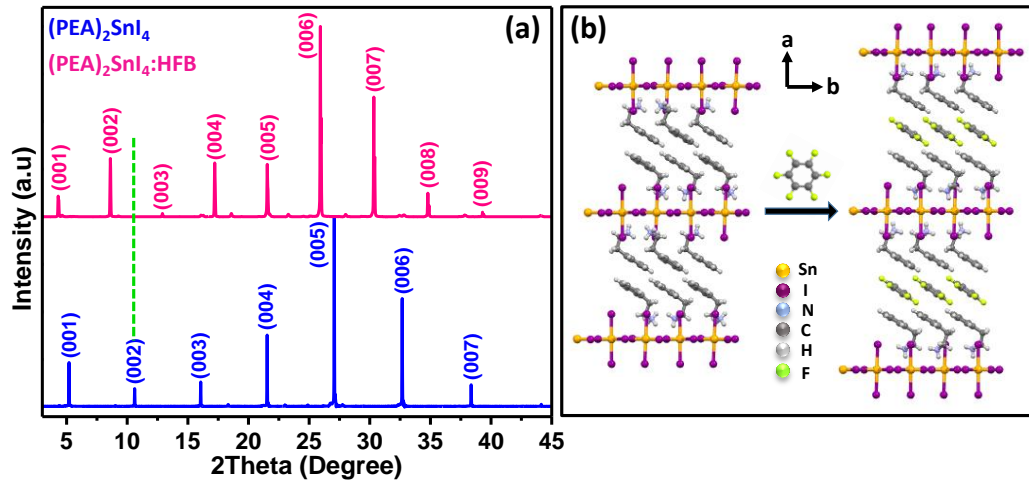


Figure 3.9: (a) PXRD pattern of $(\text{PEA})_2\text{SnI}_4$ single crystals before and after HFB insertion. The PXRD peaks shift towards the lower angles upon HFB insertion, indicating an increase in the interlayer distance. (b) Crystal structure of $(\text{PEA})_2\text{SnI}_4$ before and after HFB insertion.

Similar to the lead halide systems, $(\text{PEA})_2\text{SnI}_4$ single crystal also shows a dual emission with peak energies at 1.98 eV and 1.82 eV, as shown in Figure 3.10a. The energy difference between the two peaks is nearly similar to that observed in lead halide systems. These results rule out any significant role of spin-orbit splitting for the occurrence of dual emission since the spin-orbit coupling is significantly diminished in Sn-halides compared to Pb-halides. Interestingly, $(\text{PEA})_2\text{SnI}_4:\text{HFB}$ shows a single PL emission (Figure 3.10a). Therefore, the switching of dual PL emissions to a single PL emission after intercalation is a generic observation for all the three systems, namely, I_2 in $(\text{BA})_2\text{PbI}_4$, hexane in $(\text{DA})_2\text{PbI}_4$ and HFB in $(\text{PEA})_2\text{SnI}_4$. These results confirm that in all the three pristine layered perovskite single crystals, the lower-energy emission peaks come from the parts of crystals where Pb-I or Sn-I layers interact with each other.

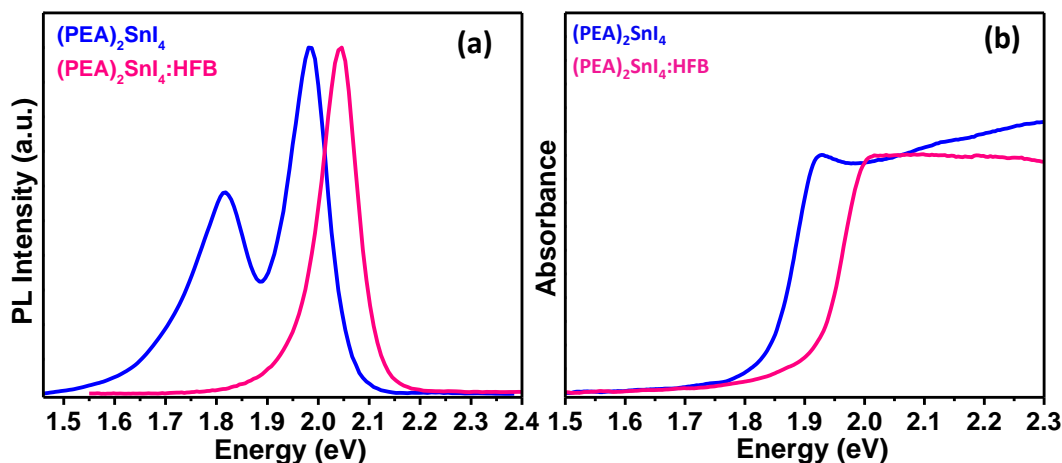


Figure 3.10: (a) PL and (b) UV-visible absorption spectra of a (PEA)₂SnI₄ single crystal before (blue) and after (magenta) HFB intercalation.

It is noteworthy here that the single emission peak in (PEA)₂SnI₄:HFB is slightly blue-shifted compared to the higher energy emission of (PEA)₂SnI₄. The absorption spectra (Figure 3.10b) also show a blue shift upon HFB insertion. The blue-shift in PL and absorbance is because of some minor structural differences between (PEA)₂SnI₄ and (PEA)₂SnI₄:HFB (see Figure 3.11) similar to the prior report.²⁸ The average Sn-I-Sn bond angle decreases from $\sim 155.9^\circ$ to $\sim 152.2^\circ$, and the average Sn-I bond length increase from $\sim 3.139 \text{ \AA}$ to $\sim 3.152 \text{ \AA}$ upon HFB intercalation in (PEA)₂SnI₄. Both the decreased bond angles and increased bond lengths support the observed blue-shift in the PL emission upon HFB intercalation.²⁴

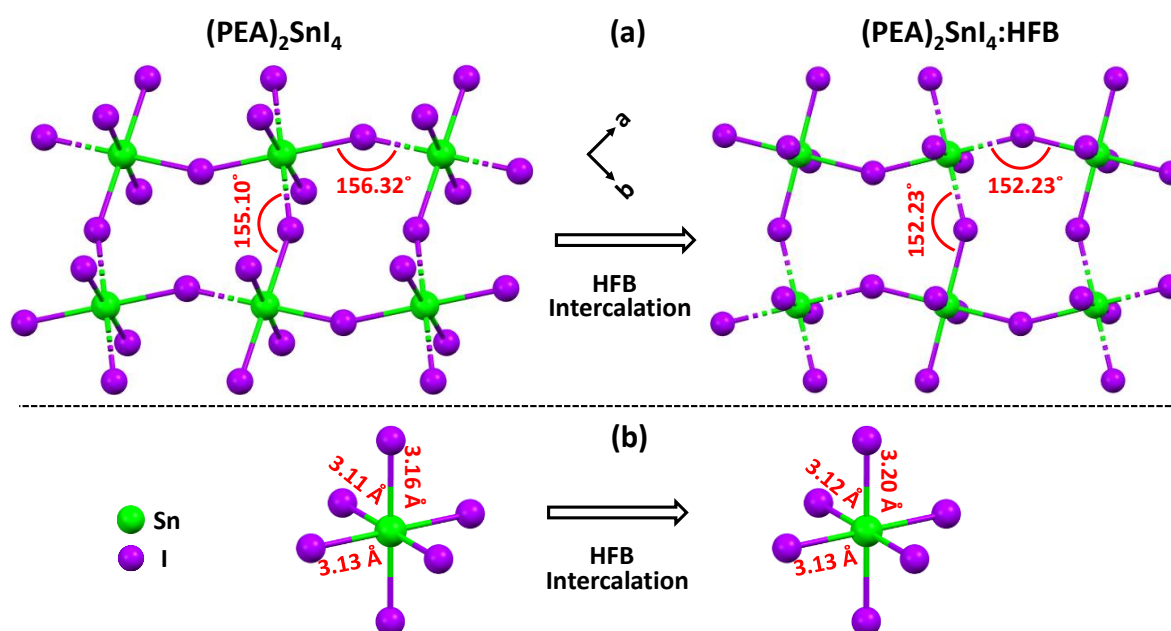


Figure 3.11: Comparison of the (a) Sn-I-Sn bond angles and (b) Sn-I bond lengths in (PEA)₂SnI₄ and (PEA)₂SnI₄:HFB. Spacer ions and molecules (PEA⁺ and HFB) have been removed for clarity.

Table 3.1: Crystal data and structure refinement for (PEA)₂SnI₄ and (PEA)₂SnI₄:HFB

	(PEA) ₂ SnI ₄	(PEA) ₂ SnI ₄ :HFB
Chemical formula	C ₁₆ H ₂₄ I ₄ N ₂ Sn	C ₂₂ H ₂₄ F ₆ I ₄ N ₂ Sn
Formula weight	870.66 g/mol	1056.72 g/mol
Temperature	298(2) K	298(2) K
Wavelength	0.71073 Å	0.71073 Å
Crystal system	triclinic	triclinic
Space group	<i>P</i> -1	<i>P</i> -1
Unit cell dimensions	a = 8.6321(16) Å α = 94.696(5)° b = 8.6344(16) Å β = 100.426(5)° c = 16.358(3) Å γ = 90.450(5)°	a = 8.5663(12) Å α = 98.638(4)° b = 8.5699(12) Å β = 93.594(4)° c = 20.485(3) Å γ = 90.064(4)°
Volume	1194.7(4) Å ³	1483.8(4) Å ³
Z	2	2
Density (calculated)	2.420 g/cm ³	2.365 g/cm ³
Absorption coefficient	6.239 mm ⁻¹	5.074 mm ⁻¹
F(000)	792	972
Theta range for data collection	2.37 to 28.33°	2.38 to 28.51°
Index ranges	-11 ≤ h ≤ 11, -11 ≤ k ≤ 11, -21 ≤ l ≤ 17	-11 ≤ h ≤ 8, -11 ≤ k ≤ 11, -27 ≤ l ≤ 27
Reflections collected	17971	23472
Independent reflections	5888 [R(int) = 0.0475]	7458 [R(int) = 0.0521]
Coverage	98.50%	98.70%
Absorption correction	Multi-Scan	Multi-Scan
Structure sol. technique	direct methods	direct methods
Structure sol. program	XS, VERSION 2013/1	SHELXT 2014/5 (Sheldrick, 2014)
Refinement method	Full-matrix least-squares on F ²	Full-matrix least-squares on F ²
Refinement program	SHELXL-2016/6 (Sheldrick, 2016)	SHELXL-2016/6 (Sheldrick, 2016)
Function minimized	Σ w(F _o ² - F _c ²) ²	Σ w(F _o ² - F _c ²) ²
Data / restraints / parameters	5888 / 0 / 153	7458 / 13 / 240
Goodness-of-fit on F ²	1.723	1.993
Δ/σ _{max}	2.922	2.239
Final R indices, I > 2σ(I)	R1 = 0.0679, wR2 = 0.2271	R1 = 0.1004, wR2 = 0.2823
all data	R1 = 0.0783, wR2 = 0.2325	R1 = 0.1276, wR2 = 0.2978
Weighting scheme	w=1/[σ ² (F _o ²)+(0.1000P) ²]; where P=(Fo ² +2Fc ²)/3	w=1/[σ ² (F _o ²)+(0.1000P) ²]; where P=(Fo ² +2Fc ²)/3
Largest diff. peak and hole	6.215 and -3.377 eÅ ⁻³	17.436 and -4.194 eÅ ⁻³
R.M.S. deviation from mean	0.427 eÅ ⁻³	0.743 eÅ ⁻³

3.3.5 Tuning the interlayer separation

To validate our hypothesis of the presence of the interactions between the Pb-I layers, we also adopted a different approach where we tuned the strength of interactions between Pb-I layers by changing the distance between the Pb-I layers. This can be achieved by changing the chain length of organic cations $R-NH_3^+$. As the length of organic cations is systematically increased from C_4 ($C_4H_9NH_3^+$ or BA) to C_{16} ($C_{16}H_{33}NH_3^+$ or HDA), including only an even number of carbon atoms, the interlayer distance and barrier width increased systematically, as shown by the schematics in Figure 3.12a. The systematic shift of PXRD peaks toward the lower 2θ values, shown in Figure 3.12b, confirms the increased distance between Pb-I layers with increasing the C-chain lengths.

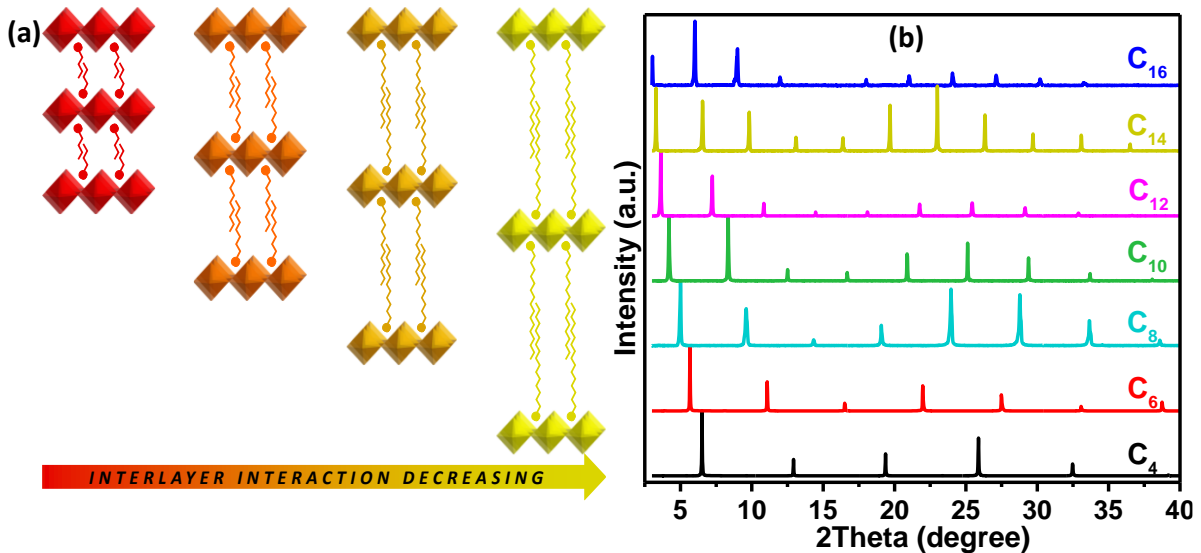


Figure 3.12: (a) Schematic showing an increase in interlayer distance by increasing the chain length of $R-NH_3^+$ spacer cation. The colors in the schematic are indicative of the actual colors of the crystals at room temperature. (b) PXRD patterns of layered lead iodide perovskites with spacer cation varying from butylammonium (C_4) to hexadecylammonium (C_{16}).

Both high thickness and high absorption cross-section do not allow light with energy above the band gap to pass through the single crystals. Consequently, when we measure the UV-visible absorption spectra of these crystals in transmission mode (Figure 13a), only the lowest energy absorption edge is observed, beyond which the absorbance saturates for all the samples. Layered perovskites exist in different phases at different temperatures. It is to be noted here that the samples C_4 to C_{10} transform to the low-temperature phase below room temperature, whereas for C_{12} to C_{16} samples, the phase transition happens above the room temperature (310-340 K).³⁶⁻³⁸ So, at room temperature, C_{12} to C_{16} samples have a different phase compared to C_4

to C₁₀ samples. To compare the optical data in the same phase, we recorded the optical data for samples C₄ to C₁₀ at room temperature, whereas for samples C₁₂ to C₁₆, optical data are recorded at 333-343 K.

Interestingly, Figure 3.13a clearly shows a systematic blue shift in the lowest energy absorption edge with increasing C-chain length. Figure 3.13b shows two well-separated emissions for samples with C-chain lengths C₄ to C₁₂. The lower energy emission peak, similar to their absorption edges, systematically blue-shifts with increasing C-chain length. In contrast, the higher energy emission at 2.38 eV remains unchanged for all the samples. For a large enough interlayer distance in the C₁₄ system [(C₁₄H₂₉NH₃)₂PbI₄], the lower energy emission overlaps with the higher energy emission giving rise to a single but asymmetric and broader emission. With a further increase in the interlayer spacing in the C₁₆ system [(C₁₆H₃₃NH₃)₂PbI₄], a single emission peak with narrower spectral width is observed. (The PL spectra of C₁₂ to C₁₆ samples recorded at high temperatures are plotted with their room temperature spectra, in Figure 3.14, for comparison).

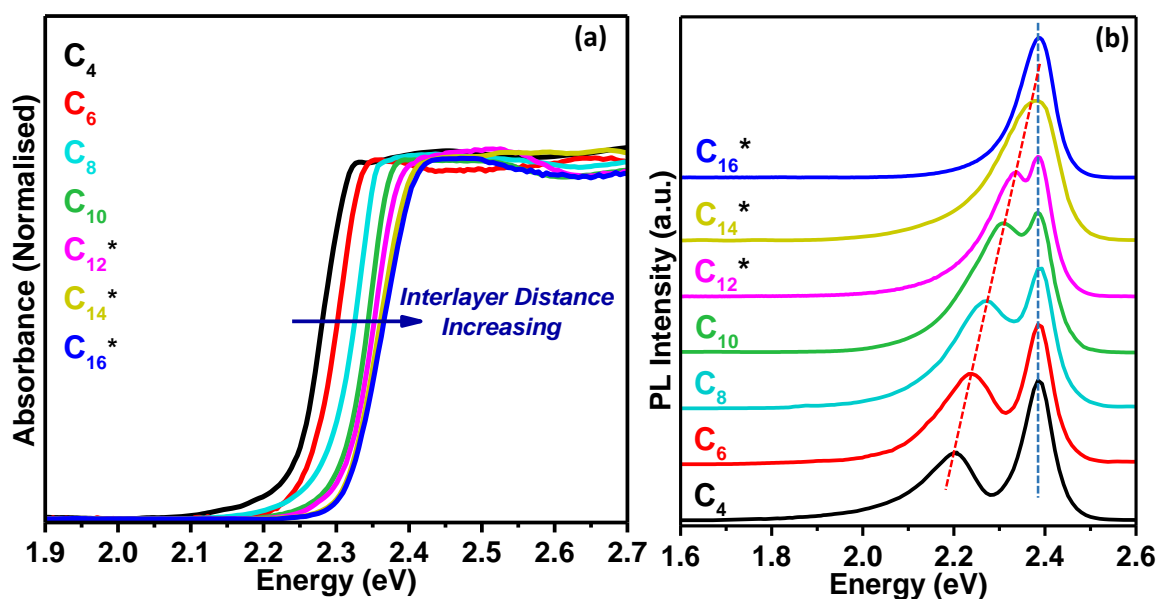


Figure 3.13: (a) UV-visible absorption spectra in transmission mode and (b) PL spectra of layered lead iodide perovskites with spacer cation varying from butylammonium (C₄) to hexadecylammonium (C₁₆). The symbol “*” indicates that the data is recorded after heating the sample to 333-343 K.

These results corroborate that the higher energy emission at 2.38 eV does not depend on barrier width (i.e., the C-chain length), similar to the intercalation results in Figures 3.5 and 3.8. Therefore, this higher energy peak is attributed to individual 2D layers and is independent of interlayer interaction, whereas the lower energy emission peak depends on barrier width.

Lower the barrier width, with a shorter carbon chain, the stronger is the interlayer electronic interaction, and therefore, more is the red-shift compared to the higher energy emission peak. For samples like C_{12} , we still observe the signature of small interlayer interactions. The crystal structure suggests a distance of ~ 1.7 nm between Pb-I layers.³⁷ This is a large distance for possible electronic interactions. However, one would expect a structural reorganization at the edges, probably reducing the Pb-I interlayer distance facilitating the interlayer electronic interactions.^{25, 32} This could be a plausible reason behind the higher relative intensity of low-energy PL near the edges, as shown in Figure 3.3. Further theoretical and experimental studies are required to understand the structural and compositional characteristics of edges of these layered perovskites.²⁷

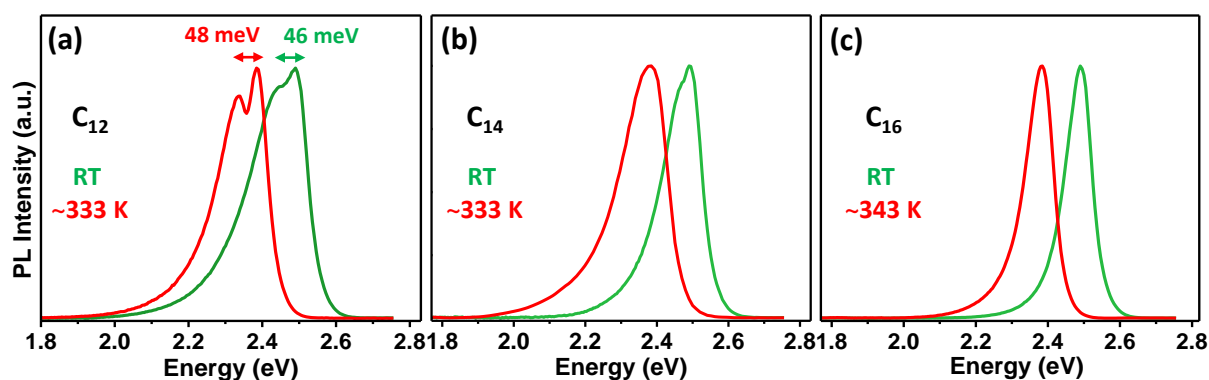


Figure 3.14: (a) PL spectra of a C_{12} [$(C_{12}H_{25}NH_3)_2PbI_4$] sample, recorded at room temperature (green) and ~ 333 K (red). (b) PL spectra of a C_{14} [$(C_{14}H_{29}NH_3)_2PbI_4$] sample, recorded at room temperature (green) and ~ 333 K (red). (c) PL spectra of a C_{16} [$(C_{16}H_{33}NH_3)_2PbI_4$] sample, recorded at room temperature (green) and ~ 343 K (red). The PL spectra are redshifted at higher temperatures (compared to room temperature) due to a structural phase transition.

3.4 Conclusion

Two excitonic emissions from single crystals of layered hybrid lead and tin halide perovskites are puzzling. Spatially resolved fluorescence microscopy imaging of $(BA)_2PbI_4$ single crystal shows that the ratio of the two emission peaks changes at different parts of the crystal, with the higher relative intensity of lower energy emission near the edges of the crystal. Interestingly, the intercalation of iodine in $(BA)_2PbI_4$ and hexane in $(DA)_2PbI_4$ reversibly switches the PL from two emission peaks to a single emission peak by disappearing the lower energy PL peak. Similarly, insertion of HFB in $(PEA)_2SnI_4$ single crystal also eliminates the lower energy PL peak. Therefore, we assign the lower energy emission peak to the Pb-I interlayer interaction. Furthermore, we decrease the strength of the interlayer interaction almost continuously by increasing the chain length (C_4 to C_{16}) of $R-NH_3^+$ spacer cations. Subsequently, the lower

energy PL peak systematically blue-shifts with an increasing chain length from C₄ to C₁₂ and eventually merges with a high energy peak for C₁₄ and C₁₆. All these results show that in parts (particularly edges) of the layered hybrid perovskites crystals, the Pb-I inorganic layers electronically interact with each other. This finding not only explains the unusual optical properties of these systems but will also be important to understand and design charge transfer and charge transport pathways in optoelectronic devices of layered perovskite.

3.5 References

1. Lee, M. M.; Teuscher, J.; Miyasaka, T.; Murakami, T. N.; Snaith, H. J. Efficient Hybrid Solar Cells Based on Meso-Superstructured Organometal Halide Perovskites. *Science* **2012**, *338*, 643-647.
2. Protesescu, L.; Yakunin, S.; Bodnarchuk, M. I.; Krieg, F.; Caputo, R.; Hendon, C. H.; Yang, R. X.; Walsh, A.; Kovalenko, M. V. Nanocrystals of Cesium Lead Halide Perovskites (CsPbX₃, X = Cl, Br, and I): Novel Optoelectronic Materials Showing Bright Emission with Wide Color Gamut. *Nano Lett.* **2015**, *15*, 3692-3696.
3. Swarnkar, A.; Chulliyil, R.; Ravi, V. K.; Irfanullah, M.; Chowdhury, A.; Nag, A. Colloidal CsPbBr₃ Perovskite Nanocrystals: Luminescence beyond Traditional Quantum Dots. *Angew. Chem. Int. Ed.* **2015**, *54*, 15424-15428.
4. Das Adhikari, S.; Dutta, S. K.; Dutta, A.; Guria, A. K.; Pradhan, N. Chemically Tailoring the Dopant Emission in Manganese-Doped CsPbCl₃ Perovskite Nanocrystals. *Angew. Chem. Int. Ed.* **2017**, *56*, 8746-8750.
5. Pal, J.; Manna, S.; Mondal, A.; Das, S.; Adarsh, K. V.; Nag, A. Colloidal Synthesis and Photophysics of M₃Sb₂I₉ (M=Cs and Rb) Nanocrystals: Lead-Free Perovskites. *Angew. Chem. Int. Ed.* **2017**, *56*, 14187-14191.
6. Akkerman, Q. A.; Rainò, G.; Kovalenko, M. V.; Manna, L. Genesis, Challenges and Opportunities for Colloidal Lead Halide Perovskite Nanocrystals. *Nat. Mater.* **2018**, *17*, 394-405.
7. Zhou, N.; Shen, Y.; Li, L.; Tan, S.; Liu, N.; Zheng, G.; Chen, Q.; Zhou, H. Exploration of Crystallization Kinetics in Quasi Two-Dimensional Perovskite and High Performance Solar Cells. *J. Am. Chem. Soc.* **2018**, *140*, 459-465.
8. Mao, L.; Ke, W.; Pedesseau, L.; Wu, Y.; Katan, C.; Even, J.; Wasielewski, M. R.; Stoumpos, C. C.; Kanatzidis, M. G. Hybrid Dion–Jacobson 2D Lead Iodide Perovskites. *J. Am. Chem. Soc.* **2018**, *140*, 3775-3783.

9. Pal, P.; Saha, S.; Banik, A.; Sarkar, A.; Biswas, K. All-Solid-State Mechanochemical Synthesis and Post-Synthetic Transformation of Inorganic Perovskite-type Halides. *Chem. Eur. J.* **2018**, *24*, 1811-1815.
10. Katan, C.; Mercier, N.; Even, J. Quantum and Dielectric Confinement Effects in Lower-Dimensional Hybrid Perovskite Semiconductors. *Chem. Rev.* **2019**, *119*, 3140-3192.
11. Li, M.; Zhou, J.; Zhou, G.; Molokeev, M. S.; Zhao, J.; Morad, V.; Kovalenko, M. V.; Xia, Z. Hybrid Metal Halides with Multiple Photoluminescence Centers. *Angew. Chem. Int. Ed.* **2019**, *58*, 18670-18675.
12. Zhou, L.; Liao, J.-F.; Huang, Z.-G.; Wei, J.-H.; Wang, X.-D.; Li, W.-G.; Chen, H.-Y.; Kuang, D.-B.; Su, C.-Y. A Highly Red-Emissive Lead-Free Indium-Based Perovskite Single Crystal for Sensitive Water Detection. *Angew. Chem. Int. Ed.* **2019**, *58*, 5277-5281.
13. Cao, D. H.; Stoumpos, C. C.; Farha, O. K.; Hupp, J. T.; Kanatzidis, M. G. 2D Homologous Perovskites as Light-Absorbing Materials for Solar Cell Applications. *J. Am. Chem. Soc.* **2015**, *137*, 7843-7850.
14. Peng, W.; Yin, J.; Ho, K.-T.; Ouellette, O.; De Bastiani, M.; Murali, B.; El Tall, O.; Shen, C.; Miao, X.; Pan, J.; Alarousu, E.; He, J.-H.; Ooi, B. S.; Mohammed, O. F.; Sargent, E.; Bakr, O. M. Ultralow Self-Doping in Two-dimensional Hybrid Perovskite Single Crystals. *Nano Lett.* **2017**, *17* (8), 4759-4767.
15. Leng, K.; Abdelwahab, I.; Verzhbitskiy, I.; Telychko, M.; Chu, L.; Fu, W.; Chi, X.; Guo, N.; Chen, Z.; Chen, Z.; Zhang, C.; Xu, Q.-H.; Lu, J.; Chhowalla, M.; Eda, G.; Loh, K. P. Molecularly Thin Two-Dimensional Hybrid Perovskites with Tunable Optoelectronic Properties due to Reversible Surface Relaxation. *Nat. Mater.* **2018**, *17*, 908-914.
16. Mitzi, D. B.; Feild, C. A.; Harrison, W. T. A.; Guloy, A. M. Conducting Tin Halides with a Layered Organic-Based Perovskite Structure. *Nature* **1994**, *369*, 467-469.
17. Mitzi, D. B.; Wang, S.; Feild, C. A.; Chess, C. A.; Guloy, A. M. Conducting Layered Organic-Inorganic Halides Containing <110> Oriented Perovskite Sheets. *Science* **1995**, *267*, 1473-1476.
18. Even, J.; Pedesseau, L.; Katan, C. Understanding Quantum Confinement of Charge Carriers in Layered 2D Hybrid Perovskites. *ChemPhysChem* **2014**, *15*, 3733-3741.
19. Zhang, R.; Mao, X.; Yang, Y.; Yang, S.; Zhao, W.; Wumaier, T.; Wei, D.; Deng, W.; Han, K. Air-Stable, Lead-Free Zero-Dimensional Mixed Bismuth-Antimony Perovskite Single Crystals with Ultra-broadband Emission. *Angew. Chem. Int. Ed.* **2019**, *58*, 2725-2729.

20. Zhou, L.; Liao, J.-F.; Huang, Z.-G.; Wei, J.-H.; Wang, X.-D.; Chen, H.-Y.; Kuang, D.-B. Intrinsic Self-Trapped Emission in 0D Lead-Free $(\text{C}_4\text{H}_{14}\text{N}_2)_2\text{In}_2\text{Br}_{10}$ Single Crystal. *Angew. Chem. Int. Ed.* **2019**, *58*, 15435-15440.
21. Gammon, D.; Shanabrook, B. V.; Katzer, D. S. Interfaces in GaAs/AlAs Quantum Well structures. *Appl. Phys. Lett.* **1990**, *57*, 2710-2712.
22. Livache, C.; Martinez, B.; Goubet, N.; Gréboval, C.; Qu, J.; Chu, A.; Royer, S.; Ithurria, S.; Silly, M. G.; Dubertret, B.; Lhuillier, E. A Colloidal Quantum Dot Infrared Photodetector and its Use for Intraband Detection. *Nat. Commun.* **2019**, *10*, 2125.
23. Traore, B.; Pedesseau, L.; Assam, L.; Che, X.; Blancon, J.-C.; Tsai, H.; Nie, W.; Stoumpos, C. C.; Kanatzidis, M. G.; Tretiak, S.; Mohite, A. D.; Even, J.; Kepenekian, M.; Katan, C. Composite Nature of Layered Hybrid Perovskites: Assessment on Quantum and Dielectric Confinements and Band Alignment. *ACS Nano* **2018**, *12*, 3321-3332.
24. Sheikh, T.; Shinde, A.; Mahamuni, S.; Nag, A. Possible Dual Bandgap in $(\text{C}_4\text{H}_9\text{NH}_3)_2\text{PbI}_4$ 2D Layered Perovskite: Single-Crystal and Exfoliated Few-Layer. *ACS Energy Lett.* **2018**, *3*, 2940-2946.
25. Wang, K.; Wu, C.; Jiang, Y.; Yang, D.; Wang, K.; Priya, S. Distinct Conducting Layer Edge States in Two-Dimensional (2D) Halide Perovskite. *Sci. Adv.* **2019**, *5*, eaau3241.
26. Stoumpos, C. C.; Cao, D. H.; Clark, D. J.; Young, J.; Rondinelli, J. M.; Jang, J. I.; Hupp, J. T.; Kanatzidis, M. G. Ruddlesden–Popper Hybrid Lead Iodide Perovskite 2D Homologous Semiconductors. *Chem. Mater.* **2016**, *28*, 2852-2867.
27. I., D. Y.; Tamotsu, I.; Yusei, M. In Situ X-Ray Observation on the Intercalation of Weak Interaction Molecules into Perovskite-Type Layered Crystals $(\text{C}_9\text{H}_{19}\text{NH}_3)_2\text{PbI}_4$ and $(\text{C}_{10}\text{H}_{21}\text{NH}_3)_2\text{CdCl}_4$. *Bull. Chem. Soc. Jpn.* **1986**, *59*, 563-567.
28. Mitzi, D. B.; Medeiros, D. R.; Malenfant, P. R. L. Intercalated Organic–Inorganic Perovskites Stabilized by Fluoroaryl–Aryl Interactions. *Inorg. Chem.* **2002**, *41*, 2134-2145.
29. Eickhoff, T.; Grosse, P.; Theiss, W. Diffuse Reflectance Spectroscopy of Powders. *Vib. Spectrosc.* **1990**, *1*, 229-233.
30. De, S.; Layek, A.; Raja, A.; Kadir, A.; Gokhale, M. R.; Bhattacharya, A.; Dhar, S.; Chowdhury, A. Two Distinct Origins of Highly Localized Luminescent Centers within InGaN/GaN Quantum-Well Light-Emitting Diodes. *Adv. Funct. Mater.* **2011**, *21*, 3828-3835.
31. Halder, A.; Chulliyil, R.; Subbiah, A. S.; Khan, T.; Chattoraj, S.; Chowdhury, A.; Sarkar, S. K. Pseudohalide (SCN^-) -Doped MAPbI_3 Perovskites: A Few Surprises. *J. Phys. Chem. Lett.* **2015**, *6*, 3483-3489.

32. Blancon, J.-C.; Tsai, H.; Nie, W.; Stoumpos, C. C.; Pedesseau, L.; Katan, C.; Kepenekian, M.; Soe, C. M. M.; Appavoo, K.; Sfeir, M. Y.; Tretiak, S.; Ajayan, P. M.; Kanatzidis, M. G.; Even, J.; Crochet, J. J.; Mohite, A. D. Extremely Efficient Internal Exciton Dissociation Through Edge States in Layered 2D Perovskites. *Science* **2017**, *355*, 1288-1292.
33. Na Quan, L.; Ma, D.; Zhao, Y.; Voznyy, O.; Yuan, H.; Bladt, E.; Pan, J.; García de Arquer, F. P.; Sabatini, R.; Piontkowski, Z.; Emwas, A.-H.; Todorović, P.; Quintero-Bermudez, R.; Walters, G.; Fan, J. Z.; Liu, M.; Tan, H.; Saidaminov, M. I.; Gao, L.; Li, Y.; Anjum, D. H.; Wei, N.; Tang, J.; McCamant, D. W.; Roeffaers, M. B. J.; Bals, S.; Hofkens, J.; Bakr, O. M.; Lu, Z.-H.; Sargent, E. H. Edge Stabilization in Reduced-Dimensional Perovskites. *Nat. Commun.* **2020**, *11*, 170.
34. Smith, M. D.; Pedesseau, L.; Kepenekian, M.; Smith, I. C.; Katan, C.; Even, J.; Karunadasa, H. I. Decreasing the Electronic Confinement in Layered Perovskites Through Intercalation. *Chem. Sci.* **2017**, *8*, 1960-1968.
35. Mitzi, D. B. Synthesis, Crystal Structure, and Optical and Thermal Properties of $(C_4H_9NH_3)_2MI_4$ ($M = Ge, Sn, Pb$). *Chem. Mater.* **1996**, *8*, 791-800.
36. Billing, D. G.; Lemmerer, A. Synthesis, Characterization and Phase Transitions in the Inorganic-Organic Layered Perovskite-Type Hybrids $[(C_nH_{2n+1}NH_3)_2PbI_4]$, $n = 4, 5$ and 6 . *Acta Crystallogr. Sect. B* **2007**, *63*, 735-747.
37. Billing, D. G.; Lemmerer, A. Synthesis, Characterization and Phase Transitions of the Inorganic-Organic Layered Perovskite-Type Hybrids $[(C_nH_{2n+1}NH_3)_2PbI_4]$ ($n = 12, 14, 16$ and 18). *New J. Chem.* **2008**, *32*, 1736-1746.
38. Lemmerer, A.; Billing, D. G. Synthesis, Characterization and Phase Transitions of the Inorganic-Organic Layered Perovskite-Type Hybrids $[(C_nH_{2n+1}NH_3)_2PbI_4]$, $n = 7, 8, 9$ and 10 . *Dalton Trans.* **2012**, *41*, 1146-1157.

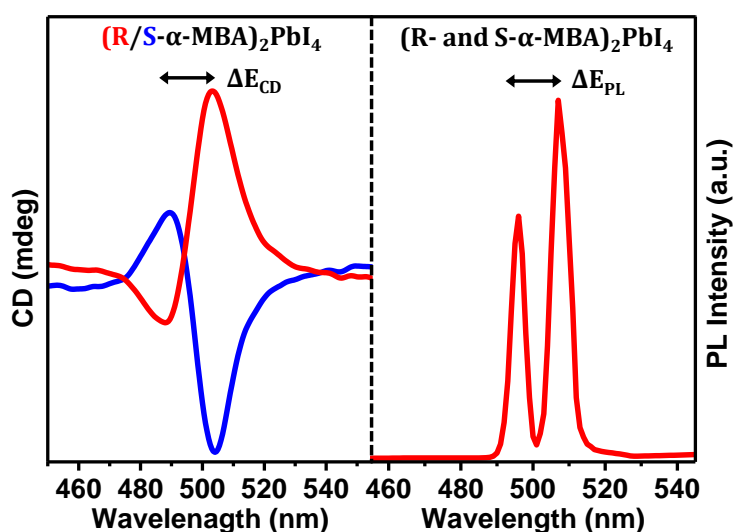
Chapter 4

Emission Splitting and Higher Exciton Binding Energies in Chiral Layered Hybrid R- and S- α -Methylbenzylammonium Lead Iodide Perovskites

Abstract

In layered hybrid lead halide perovskites, the lead and halide orbitals dominate the valance band maximum and conduction band minimum. Consequently, the optical and optoelectronic properties of these layered hybrid lead halide perovskites depend mostly on the inorganic sub-lattices only. However, the organic cations have the potential to modify or impart new properties by creating distortions or breaking the symmetry of the inorganic sub-lattices. Recently, chirality has been transferred from the chiral organic cations to the layered hybrid perovskites. These chiral layered hybrid perovskites show novel properties like circular dichroism, circularly polarized emission, etc. Here we synthesized chiral layered R- and S- α -methylbenzylammonium lead iodide [(R- and S- α -MBA) $_2$ PbI $_4$]. Single crystal x-ray diffraction and circular dichroism data confirmed the presence of chirality in the (R- and S- α -MBA) $_2$ PbI $_4$. (Rac- α -MBA) $_2$ PbI $_4$ (Rac = racemic mixture) is also synthesized for the comparison. The temperature-dependent (5 to 300K) photoluminescence (PL) showed a significant impact of chirality on the optical properties of (R- and S- α -MBA) $_2$ PbI $_4$. The PL emission splits into two peaks below 100 K in (R- and S- α -MBA) $_2$ PbI $_4$, compared to the achiral (Rac- α -MBA) $_2$ PbI $_4$, which shows a single PL peak from 5 to 300 K. Moreover, a significantly higher exciton binding energy is observed in the chiral (R- and S- α -MBA) $_2$ PbI $_4$ compared to the achiral (Rac- α -MBA) $_2$ PbI $_4$. So, the induced chirality, in addition to introducing new functionalities, has the potential to modify the existing properties as well.

Graphical Abstract



4.1 Introduction

Layered hybrid lead halide perovskites, with formula A_2PbX_4 (A = organic cation like butylammonium ion (BA), X = Cl, Br or I), are now being widely explored for optical and optoelectronic applications.¹⁻¹⁰ Unlike 3D perovskites, the 2D layered hybrid perovskites are not limited by Goldschmidt's tolerance factor.¹¹⁻¹² By using different organic cations, a large number of compositions of layered hybrid perovskites are possible. The compositional flexibility of the layered lead halide perovskites gives us an opportunity to combine various properties of organic molecules with inorganic lattices.¹³⁻¹⁵ Chirality is common in organic molecules. Chiral molecules are not superimposable on their mirror images. Unlike organic molecules, inorganic lattices typically do not show chirality. However, recently chirality has been introduced in the inorganic sub-lattices of layered hybrid perovskites by using chiral organic cations.¹³⁻¹⁵ The induced chirality in these layered hybrid perovskites gives rise to some novel properties like circular dichroism (CD), circularly polarized emission, circularly polarized second harmonic generation, chiral ferroelectricity, etc.¹³⁻¹⁹

Layered perovskites are Van der Waals solids with a repeating quantum well structure.²⁰⁻²² The wells are atomically thin inorganic semiconductors, whereas the barriers are layers of assembly of insulating organic molecules. Due to the atomically thin well layers, the layered perovskites are considered as electronically 2D.^{20-21, 23} Therefore, layered perovskites are often termed as 2D irrespective of their crystal size and shape. Consequently, 2D layered perovskites show strong quantum confinement independent of the crystal size.²⁴⁻²⁸ Due to the quantum well structure, the layered hybrid lead halide perovskites show rich excitonic photophysics. Properties like very high exciton binding energy, large polaron formation and exciton self-trapping are very common to the layered hybrid perovskites.²⁹⁻³¹

It is interesting to see the effect of chirality on the excitonic properties of layered hybrid lead halide perovskites. In this chapter, we explore the effect of induced chirality on the excitonic properties of chiral R- and S- α -methylbenzylammonium lead iodide [(R- and S- α -MBA) $_2$ PbI $_4$] by using temperature-dependent (5 to 300 K) photoluminescence (PL). At room temperature, both (R- and S- α -MBA) $_2$ PbI $_4$ show sharp excitonic emission features, similar to the (Rac- α -MBA) $_2$ PbI $_4$ (Rac = racemic). But at lower temperatures, the PL emission of (R- and S- α -MBA) $_2$ PbI $_4$ differ significantly from that of the (Rac- α -MBA) $_2$ PbI $_4$. In (R- and S- α -MBA) $_2$ PbI $_4$, the PL peak splits in two peaks below 100 K, while a single peak is observed in (Rac- α -MBA) $_2$ PbI $_4$ throughout the temperature range of 5 to 300 K. Similarly, a higher exciton binding energy is observed in (R- and S- α -MBA) $_2$ PbI $_4$ compared to the (Rac- α -MBA) $_2$ PbI $_4$.

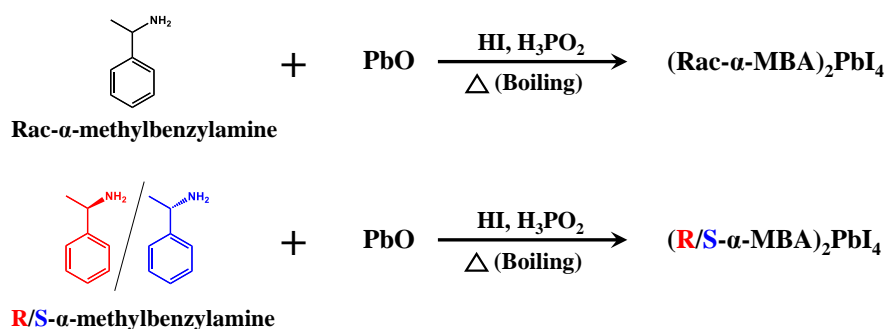
4.2 Experimental Section**4.2.1 Chemicals**

Lead(II) oxide (Sigma Aldrich, 99.9%), hydriodic acid (Sigma Aldrich, 57% w/w in H₂O, 99.9%), hypophosphorous acid (Avra, 50% w/w H₂O), R-(+)- α -methylbenzylamine (Sigma Aldrich, 99%), S-(-)- α -methylbenzylamine (Sigma Aldrich, 99%), racemic- α -methylbenzylamine (Sigma Aldrich, 98%), acetonitrile (Sigma Aldrich, 99.8%), diethyl ether (Rankem, 99.5%).

4.2.2 Synthesis of (Rac-, R- and S- α -MBA)₂PbI₄ single crystals

(Rac-, R- and S- α -MBA)₂PbI₄ single crystals were synthesized by an aqueous acid precipitation method. In three separate vials, 2.5 mmol (558 mg) lead(II) oxide were dissolved in a mixture of 10 mL aqueous hydriodic acid (57% w/w in H₂O) and 2 mL aqueous hypophosphorous acid (50% w/w H₂O) by heating to boiling under constant magnetic stirring. Once clear yellow solutions were obtained, 5 mmol of racemic- α -methylbenzylamine, R-(+)- α -methylbenzylamine and S-(-)- α -methylbenzylamine were added to these vials, respectively. The stirring was stopped once clear yellow solutions were obtained. The solutions were allowed to cool down to room temperature naturally. During the cooling process, orange-colored crystals of (Rac-, R- and S- α -MBA)₂PbI₄ started to crystalize. The crystals were filtered, washed with diethyl ether and dried under vacuum.

PbO upon dissolving in HI gives Pb²⁺ ions. The Rac-, R- and S- α -methylbenzylamine gets protonated in HI, forming Rac-, R- and S- α -methylbenzylammonium ions (Rac-, R- and S- α -MBA). Upon cooling, the solution becomes supersaturated with respect to the Pb²⁺ and Rac-, R- and S- α -MBA ions. The Pb²⁺, (Rac-, R- and S- α -MBA) and I⁻ ions react, and the (Rac-, R- and S- α -MBA)₂PbI₄ crystallizes. The H₃PO₂ acts as a reducing agent and reduces any I₂ formed back to I⁻.



4.2.3 Preparation of (Rac-, R- and S- α -MBA)₂PbI₄ thin films

(Rac-, R- and S- α -MBA)₂PbI₄ thin films were prepared on sapphire substrates. First, the sapphire substrates were washed with water, followed by isopropanol and finally by acetone. The (Rac-, R- and S- α -MBA)₂PbI₄ single crystals were separately dissolved in 0.5 mL acetonitrile. These solutions were then spin-coated on the freshly cleaned sapphire substrates at the spinning rate of 3000 rpm for 20 s. The sapphire substrates were pre-heated at 70 °C before spin coating.

4.2.4 Characterization

Single crystal X-ray diffraction (XRD) data were collected on Bruker Smart Apex Duo diffractometer at room temperature (RT) using Mo K α radiation ($\lambda = 0.71073 \text{ \AA}$). The frames were integrated with the Bruker SAINT software package by a narrow-frame algorithm. The structures were solved by a direct method and refined by full-matrix least-squares on F² using the SHELXTL software package. The PbX₄ framework was refined anisotropically without any constraint. The organic atoms were also refined anisotropically but with constraints on the C-C and C-N bond lengths.

Powder XRD measurements were carried on Bruker D8 Advance X-ray diffractometer using Cu K α radiation (1.54 \AA). UV-Visible absorbance data were measured on Cary Series UV-Vis Spectrophotometer (Agilent Technologies). The absorbance spectra were recorded in transmittance mode. Circular dichroism (CD) measurements were carried at room temperature on a Jasco J-815 spectropolarimeter. The CD spectra were measured at a scan speed of 50 nm per minute with 0.5 nm resolution and response time of 1 s. The CD spectra were also recorded in transmittance mode.

The room temperature steady-state photoluminescence (PL) measurements were carried on FLS 980 (Edinburgh Instruments). The samples were excited with a 405 nm laser. The temperature-dependent steady-state PL measurements were carried on the same instrument. For the temperature-dependent PL measurements, the sapphire substrates containing the samples were mounted on a gold-plated sample holder. The sample holder was then mounted on the cold finger attached to a closed-cycle helium cryostat (Advanced Research Systems). The cryostat was connected to a temperature controller (Lake Shore Cryotronics) to achieve the desired temperatures.

4.3 Results and Discussion

4.3.1 Synthesis and crystal structure of (Rac-, R- and S- α -MBA) $_2$ PbI $_4$ single crystals

(Rac-, R- and S- α -MBA) $_2$ PbI $_4$ single crystals were synthesized by an aqueous acid precipitation method. Refer to the experimental section for detailed synthesis. Figure 4.1 shows the crystal structures of (Rac-, R- and S- α -MBA) $_2$ PbI $_4$ obtained by solving the single crystal XRD data recorded at room temperature (296 K). All three samples show a 2D layered hybrid structure. The (R- and S- α -MBA) $_2$ PbI $_4$ crystallize in orthorhombic lattice with lattice parameters $a = 8.8203(10)$ Å, $b = 9.1821(10)$ Å, $c = 28.579(3)$ Å, $\alpha = \beta = \gamma = 90^\circ$ and $a = 8.8315(13)$ Å, $b = 9.1847(13)$ Å, $c = 28.569(4)$ Å, $\alpha = \beta = \gamma = 90^\circ$, respectively. On the contrary the (Rac- α -MBA) $_2$ PbI $_4$ crystallizes in a monoclinic lattice with lattice parameters $a = 14.660(3)$ Å, $b = 9.3799(19)$ Å, $c = 8.7777(18)$ Å, $\alpha = \gamma = 90^\circ$, $\beta = 100^\circ$. The crystal structure data of all the three samples (Rac-, R- and S- α -MBA) $_2$ PbI $_4$ follow the prior reports very well.³²⁻³³ See Table 4.1 for detailed crystal structure data and refinement parameters.

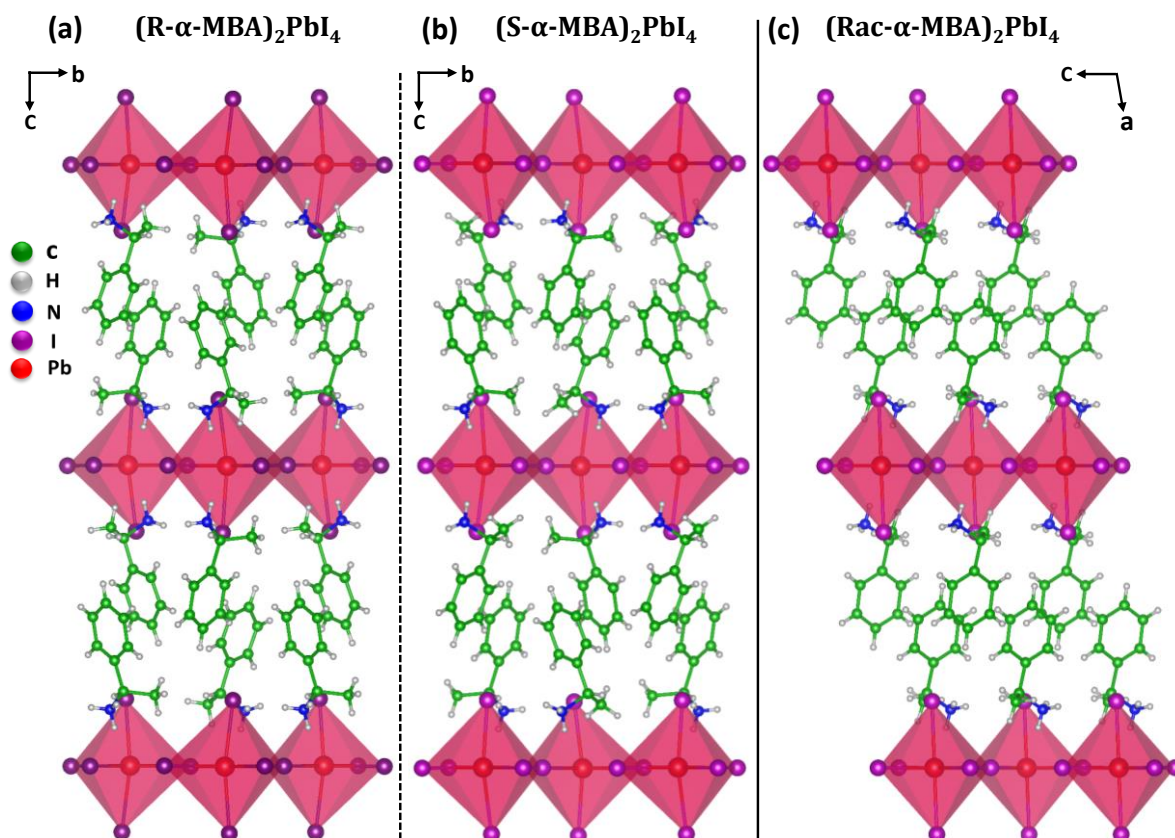


Figure 4.1: Crystal structures of (a) (R- α -MBA) $_2$ PbI $_4$, (b) (S- α -MBA) $_2$ PbI $_4$ and (c) (Rac- α -MBA) $_2$ PbI $_4$ obtained by solving the single crystal XRD data recorded at room temperature (296 K). The (R- and S- α -MBA) $_2$ PbI $_4$ have the non-centrosymmetric crystal structure, while the (Rac- α -MBA) $_2$ PbI $_4$ has the centrosymmetric crystal structure.

Emission Splitting and Higher Exciton Binding Energies in Chiral Layered Hybrid R- and S- α -Methylbenzylammonium Lead Iodide Perovskites**Table 4.1:** Crystal structure and data refinement of (Rac-, R- and S- α -MBA)₂PbI₄ at RT.

	(R- α -MBA) ₂ PbI ₄	(S- α -MBA) ₂ PbI ₄	(Rac- α -MBA) ₂ PbI ₄
Chemical formula	C ₁₆ H ₂₄ I ₄ N ₂ Pb	C ₁₆ H ₂₄ I ₄ N ₂ Pb	C ₁₆ H ₂₄ I ₄ N ₂ Pb
Formula weight	959.16 g/mol	959.16 g/mol	959.16 g/mol
Temperature	296(2) K	296(2) K	296(2) K
Wavelength	0.71073 Å	0.71073 Å	0.71073 Å
Crystal system	Orthorhombic	Orthorhombic	Monoclinic
Space group	<i>P</i> 2 ₁ 2 ₁ 2 ₁	<i>P</i> 2 ₁ 2 ₁ 2 ₁	<i>P</i> 2 ₁ / <i>c</i>
Unit cell dimensions	a = 8.8203(10) Å b = 9.1821(10) Å c = 28.579(3) Å $\alpha = \beta = \gamma = 90^\circ$	a = 8.8315(13) Å b = 9.1847(13) Å c = 28.569(4) Å $\alpha = \beta = \gamma = 90^\circ$	a = 14.660(3) Å b = 9.3799(19) Å c = 8.7777(18) Å A = $\gamma = 90^\circ$, $\beta = 100^\circ$
Volume	2314.6(5) Å ³	2317.4(6) Å ³	1189.2(4) Å ³
Z	4	4	2
Density	2.753 g/cm ³	2.749 g/cm ³	2.670 g/cm ³
Abs. coefficient	12.626 mm ⁻¹	12.611 mm ⁻¹	12.288 mm ⁻¹
Theta range	2.33 to 28.29°	3.50 to 26.37°	2.59 to 25.34°
Index ranges	-11 ≤ h ≤ 11, -10 ≤ k ≤ 12, -38 ≤ l ≤ 38	-11 ≤ h ≤ 10, -11 ≤ k ≤ 11, -35 ≤ l ≤ 35	-19 ≤ h ≤ 19, -12 ≤ k ≤ 12, -11 ≤ l ≤ 9
Reflections collected	41748	27087	19867
Independent reflections	5682 [R(int) = 0.0635]	4706 [R(int) = 0.0708]	2128 [R(int) = 0.0433]
Coverage	99.80%	99.6%	97.7%
Absorption correction	Multi-Scan	Multi-scan	Multi-scan
Structure solution	Direct methods	Direct method	Direct method
Structure solution program	SHELXT 2014/5 (Sheldrick, 2014)	SHELXT 2014/5 (Sheldrick, 2014)	SHELXT 2014/5 (Sheldrick, 2014)
Refinement method	Full-matrix least-squares on F ²	Full-matrix least-squares on F ²	Full-matrix least-squares on F ²
Refinement program	SHELXL-2018/3 (Sheldrick, 2018)	SHELXL-2018/3 (Sheldrick, 2018)	SHELXL-2018/3 (Sheldrick, 2018)
Function minimized	$\Sigma w(F_o^2 - F_c^2)^2$	$\Sigma w(F_o^2 - F_c^2)^2$	$\Sigma w(F_o^2 - F_c^2)^2$
Data / parameters	5682 / 173	4706 / 173	2128 / 96
Goodness-of-fit on F ²	0.995	0.737	1.373
Final R indices; I>2 σ (I)	R1 = 0.0838, wR2 = 0.1785	R1 = 0.0761, wR2 = 0.1696	R1 = 0.0764, wR2 = 0.1575
all data	R1 = 0.0902, wR2 = 0.1833	R1 = 0.0840, wR2 = 0.1758	R1 = 0.1089, wR2 = 0.1700
Weighting scheme	w=1/[$\sigma^2(F_o^2)+(0.02000P)^2 + 8.000P$] P=(F _o ² +2F _c ²)/3	w=1/[$\sigma^2(F_o^2)+(0.0500P)^2 + 10.5000P$] P=(F _o ² +2F _c ²)/3	w=1/[$\sigma^2(F_o^2)+(0.1000P)^2$] P=(F _o ² +2F _c ²)/3
Largest diff. peak, hole	2.005, -0.531 eÅ ⁻³	1.176, -0.606 eÅ ⁻³	0.085, -0.800 eÅ ⁻³
R.M.S. deviation	0.092 eÅ ⁻³	0.064 eÅ ⁻³	0.159 eÅ ⁻³

Emission Splitting and Higher Exciton Binding Energies in Chiral Layered Hybrid R- and S- α -Methylbenzylammonium Lead Iodide Perovskites

Interestingly both the (R- and S- α -MBA) $_2$ PbI $_4$ possess a chiral space group, $P2_12_12_1$, which suggests the chiral structures for both the samples. So the chiral organic cations (R- and S- α -MBA) induce chirality in the (R- and S- α -MBA) $_2$ PbI $_4$. Though the R and S samples have almost the same lattice parameters, they are not exactly the same. Figures 4.1a and b show that the (R- and S- α -MBA) $_2$ PbI $_4$ are the non-superimposable mirror images of each other, similar to prior reports.^{13, 19, 34} The (Rac- α -MBA) $_2$ PbI $_4$ possesses a centrosymmetric $P2_1/c$ space group, suggesting its centrosymmetric crystal structure.

The chiral organic cations, R- and S- α -MBA, break the symmetry of the inorganic (Pb-I) octahedral framework in (R- and S- α -MBA) $_2$ PbI $_4$ via an asymmetric hydrogen bonding.^{15, 33-34} In all the samples (Rac-, R- and S- α -MBA) $_2$ PbI $_4$, the PbI $_6$ octahedra are tilted, resulting in the deviation of the Pb-I-Pb bond angles from the ideal 180° of undistorted perovskite. In the (Rac- α -MBA) $_2$ PbI $_4$, the octahedral tilting is symmetric, with the Pb-I-Pb bond angles of 155° (Figure 4.2c). However, the (R- and S- α -MBA) $_2$ PbI $_4$ show an asymmetric octahedral tilting with two types of Pb-I-Pb bond angles of 151° and 156° (Figures 4.2a and b). The asymmetric octahedral tilting with two types of Pb-I-Pb bond angles indicates an asymmetric or chiral inorganic (Pb-I) lattice in (R- and S- α -MBA) $_2$ PbI $_4$, compared to the (Rac- α -MBA) $_2$ PbI $_4$, following the prior reports.^{15, 33}

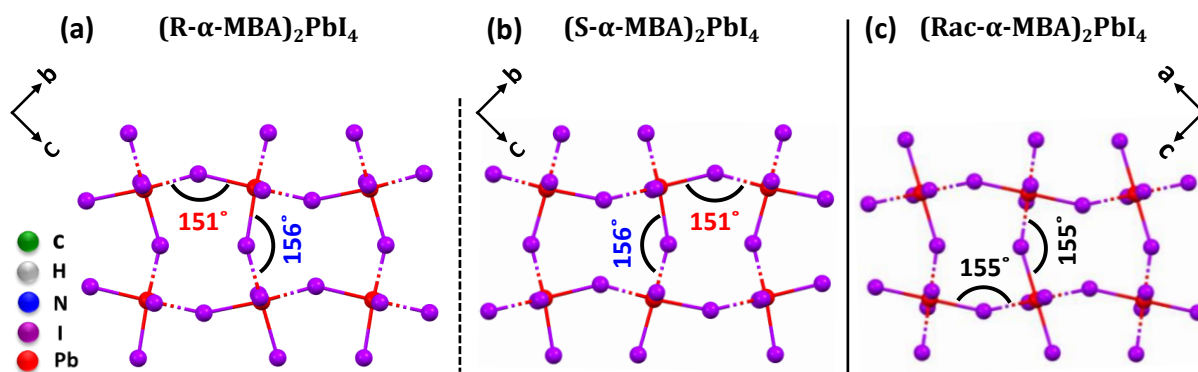


Figure 4.2: Top view of the 2D Pb-I layers in (a) (R- α -MBA) $_2$ PbI $_4$, (b) (S- α -MBA) $_2$ PbI $_4$ and (c) (Rac- α -MBA) $_2$ PbI $_4$ showing Pb-I-Pb bond angles. Two types of Pb-I-Pb bond angles are present in the chiral (R- and S- α -MBA) $_2$ PbI $_4$, whereas a single type of Pb-I-Pb bond angle is observed in (Rac- α -MBA) $_2$ PbI $_4$. Figures a-c are obtained by solving the SCXRD data recorded at RT (296 K).

The powder X-ray diffraction (PXRD) patterns of (Rac-, R- and S- α -MBA) $_2$ PbI $_4$ single crystals show a regular peak pattern, characteristic of layered single crystals (Figure 4.3).⁴ The PXRD patterns of (Rac-, R- and S- α -MBA) $_2$ PbI $_4$ are exactly the same, with peaks overlapping with

each other. The same PXRD patterns with peaks overlapping with each other suggest the similar interlayer spacing in all the three samples (Rac-, R- and S- α -MBA) $_2$ PbI $_4$ as these regular peaks in the PXRD pattern correspond to the interlayer spacing.⁴

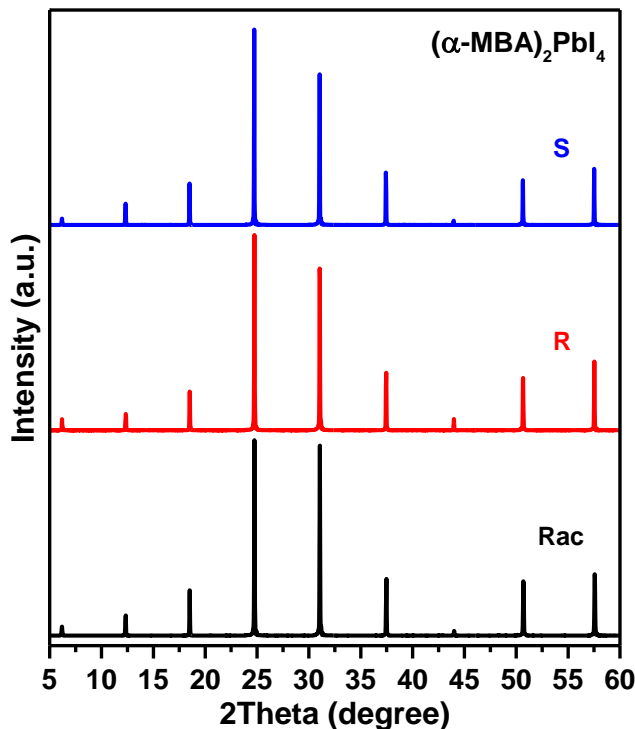


Figure 4.3: PXRD patterns of (Rac-, R- and S- α -MBA) $_2$ PbI $_4$ single crystals, showing a regular peak pattern. The regular peak pattern is the characteristic of layered single crystals.

4.3.2 Chiroptical properties of (Rac-, R- and S- α -MBA) $_2$ PbI $_4$

The crystal structure data showed a chiral structure for (R- and S- α -MBA) $_2$ PbI $_4$. To further confirm their chirality, we recorded the circular dichroism (CD) in (R- and S- α -MBA) $_2$ PbI $_4$. Chiral molecules or lattices interact with left and right circularly polarized light differently, which is characterized by their CD response. Measuring CD on single crystals is extremely difficult, as the measurements are done in transmittance mode. So instead, we recorded the CD data on thin films. For the preparation of thin films, (Rac-, R- and S- α -MBA) $_2$ PbI $_4$ single crystals were separately dissolved in acetonitrile and spin-coated on sapphire substrates. See the experimental section for details of thin-film preparation. Figure 4.4 shows the photographs of the as-prepared thin films of (Rac-, R- and S- α -MBA) $_2$ PbI $_4$. The thin films were characterized by PXRD. The PXRD patterns of as-prepared thin films match very well with that of the single crystals (Figure 4.4), with no extra peaks, confirming the formation of phase pure (Rac-, R- and S- α -MBA) $_2$ PbI $_4$ on the sapphire substrates.

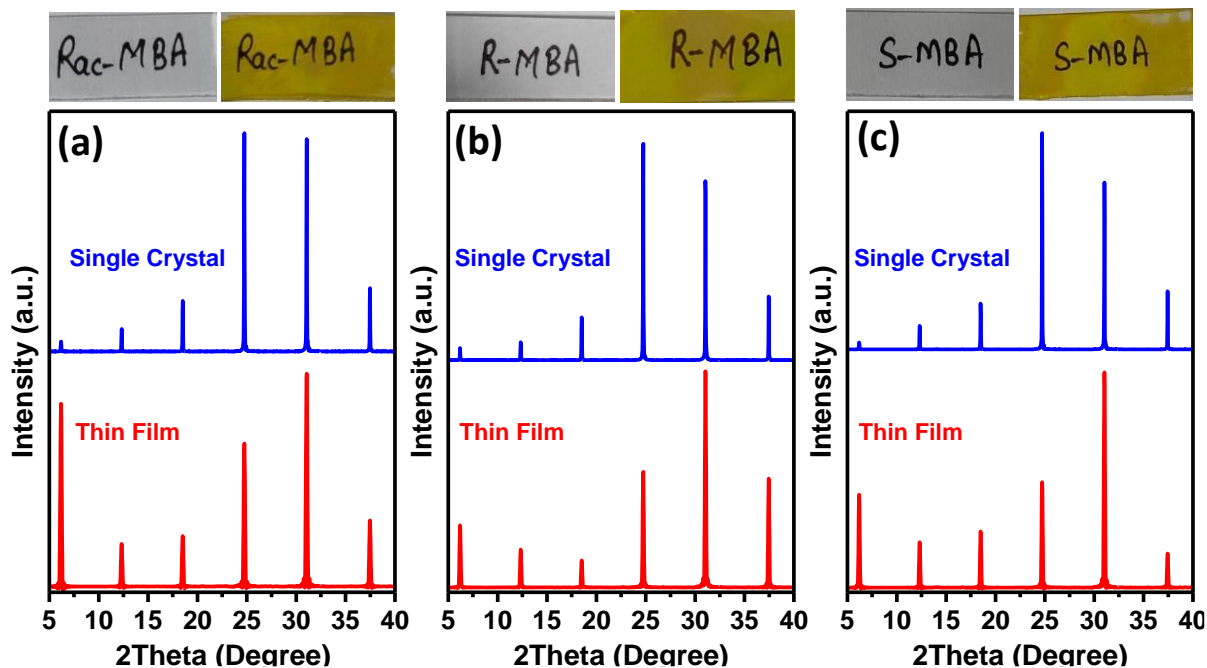


Figure 4.4: PXRD patterns of as-prepared (a) Rac-, (b) R- and (c) S- (α -MBA) $_2$ PbI $_4$ thin films overlapped with that of the (Rac-, R- and S- α -MBA) $_2$ PbI $_4$ single crystals. Top panel shows the optical photographs of the blank glass substrates and the as-prepared (Rac-, R- and S- α -MBA) $_2$ PbI $_4$ thin films (yellow color).

Figure 4.5a shows the CD spectra of (Rac-, R- and S- α -MBA) $_2$ PbI $_4$. Both (R- and S- α -MBA) $_2$ PbI $_4$ show distinct features in their CD spectra, with opposite signs, which confirm their chiral structures. Expectedly, the (Rac- α -MBA) $_2$ PbI $_4$, which has a centrosymmetric crystal structure, does not show any CD response. Interestingly, the CD spectra of (R- and S- α -MBA) $_2$ PbI $_4$ show a derivative-like response, around 498 nm (excitonic region), with both positive and negative responses. The organic cations (R- and S- α -MBA) do not absorb in this region, suggesting that the CD signals, in Figure 4.5a, originate from the inorganic sub-lattice.³⁴ A similar kind of derivative-like CD response has been previously reported as well.³⁴⁻³⁵ This kind of CD response has been attributed to the excitonic splitting in the chiral environment due to the lifting of spin degeneracy.³⁴⁻³⁷ The peak splitting energies in the CD spectra are around \sim 60 meV. The UV-visible absorption spectra (Figure 4.5b) of (Rac-, R- and S- α -MBA) $_2$ PbI $_4$ show strong excitonic features with peaks centered at 498 nm (2.49 eV). The absorption spectra of all the samples are exactly the same, suggesting no change in the band gap due to the induced chirality. Interestingly, the excitonic peak energy (2.49 eV; 498 nm) in the absorption spectrum of (R- and S- α -MBA) $_2$ PbI $_4$ match exactly with the crossover energy in their CD spectra. However, unlike CD, no splitting is observed in their excitonic absorption peaks.

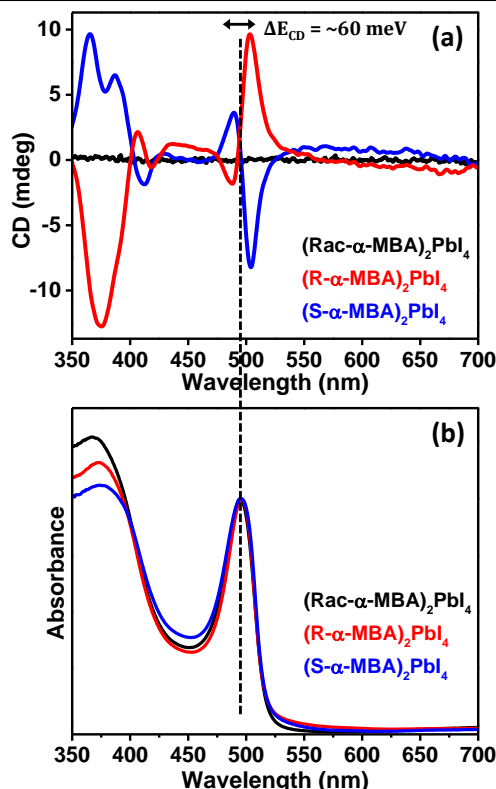


Figure 4.5: (a) CD and (b) Normalized UV-visible absorption spectra of (Rac-, R- and S- α -MBA) $_2$ PbI $_4$. Both the CD and absorption spectra were recorded in transmittance mode.

The (Rac-, R- and S- α -MBA) $_2$ PbI $_4$ show light emission at room temperature (RT), with peaks centered at 512 nm (Figure 4.6). The PL peaks in (Rac-, R- and S- α -MBA) $_2$ PbI $_4$ show a similar Stokes shift of 14 nm (68 meV) from the excitonic absorption peaks. These small Stokes shifts in the PL peaks in (Rac-, R- and S- α -MBA) $_2$ PbI $_4$ indicate that the emissions are excitonic in origin. It is noteworthy that the PL spectral profile in all three samples is asymmetric, with a tail on the longer wavelength side. Such a tail is often observed in the PL spectra of layered perovskite thin films and is attributed to the presence of some shallow trap states or possible lower energy excitonic emission.^{3, 38}

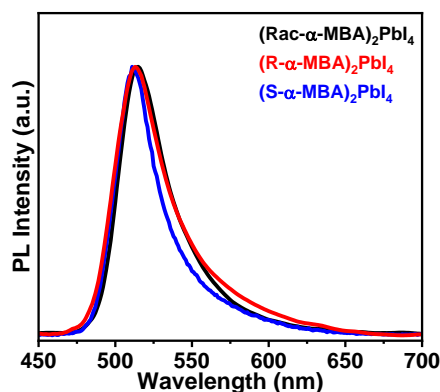


Figure 4.6: Room temperature PL spectra of (Rac-, R- and S- α -MBA) $_2$ PbI $_4$, showing excitonic emission with peaks centered at 512 nm (~ 2.42 eV).

4.3.3 Temperature-dependent PL in (Rac-, R- and S- α -MBA) $_2$ PbI $_4$

The CD spectra of (R- and S- α -MBA) $_2$ PbI $_4$ in Figure 4.5a showed distinct CD features. In contrast, (Rac- α -MBA) $_2$ PbI $_4$ shows a featureless CD spectrum. However, no difference in room temperature optical absorption and PL was observed in the chiral (R- and S- α -MBA) $_2$ PbI $_4$ and achiral (Rac- α -MBA) $_2$ PbI $_4$. The optical absorption and emission features hugely depend on the temperature, and at lower temperatures, the excitonic absorption and emission features become sharper. If the induced chirality has any effect on the excitonic properties, it should be visible at lower temperatures. So, we recorded the PL from all the three samples, i.e. (Rac-, R- and S- α -MBA) $_2$ PbI $_4$ at 5 K. Figure 4.7 shows the PL spectra of (Rac-, R- and S- α -MBA) $_2$ PbI $_4$ recorded at 5 K. Interestingly, a significant difference in the PL emission from the chiral (R and S) and achiral (Rac) samples is observed at 5 K. Two sharp peaks, centered at 507 nm (2.46 eV) and 495 nm (2.51 eV), are observed in the PL spectra of (R- and S- α -MBA) $_2$ PbI $_4$, whereas a single sharp peak centered at 510 nm (\sim 2.43 eV) is observed in the PL spectrum of (Rac- α -MBA) $_2$ PbI $_4$. Similar results have previously been observed in (Rac-, R- and S- α -MBA) $_2$ PbI $_4$ at 77 K.¹³ However, the relative intensities of the higher energy peaks in (R- and S- α -MBA) $_2$ PbI $_4$ were much lower, unlike our results, probably due to the sample inhomogeneity or the temperature difference. It is to be noted that no discussion has been made on the appearance of the new higher energy peak previously. The splitting of the PL emission in chiral (R- and S- α -MBA) $_2$ PbI $_4$ probably arises due to the lifting of the spin degeneracy in the chiral environment, as is also suggested by the room temperature CD data.³⁵ The PL peak splitting energies in (R- and S- α -MBA) $_2$ PbI $_4$ are around \sim 50 meV, which matches well with the peak splitting energy observed in CD spectra.

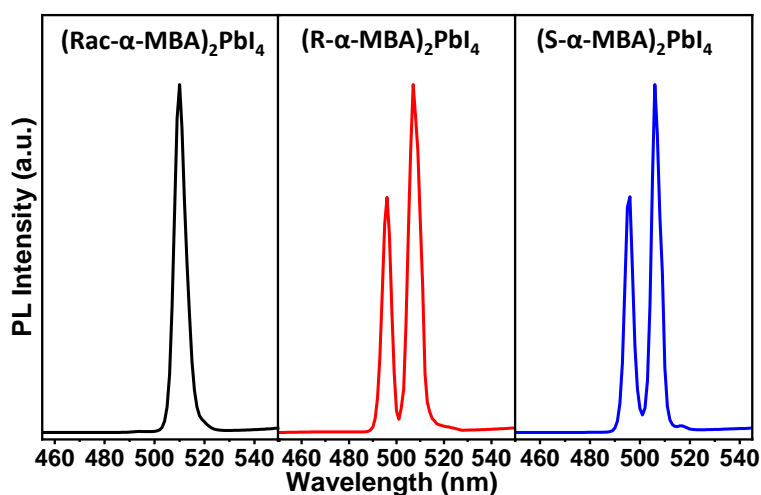


Figure 4.7: PL spectra of (Rac-, R- and S- α -MBA) $_2$ PbI $_4$, recorded at 5 K. The PL emission splits into two peaks for (R- and S- α -MBA) $_2$ PbI $_4$.

Emission Splitting and Higher Exciton Binding Energies in Chiral Layered Hybrid R- and S- α -Methylbenzylammonium Lead Iodide Perovskites

To further explore the effect of induced chirality on the emission properties, we recorded the temperature-dependent PL (300 to 5 K) in (Rac-, R- and S- α -MBA) $_2$ PbI $_4$. The PL spectra recorded at different temperatures are plotted as pseudo color maps. Figures 4.8a-c show the PL-temperature pseudo color maps of (Rac-, R- and S- α -MBA) $_2$ PbI $_4$. Due to the sharp rise in PL intensity with decreasing temperature, the color maps shown in Figures 4.8a-c do not show much visible intensity till 225 K. To make the PL emission visible throughout the temperature range (300 to 5 K), normalized PL-temperature color maps are plotted in Figures 4.8d-f. A single peak is observed till 150 K in the PL spectra of (R- and S- α -MBA) $_2$ PbI $_4$. But below 150 K, the PL emission starts to split into two peaks, and the splitting becomes more prominent at further lower temperatures. On the other hand, a single PL peak is observed in (Rac- α -MBA) $_2$ PbI $_4$ throughout the temperature range of 300 to 5 K.

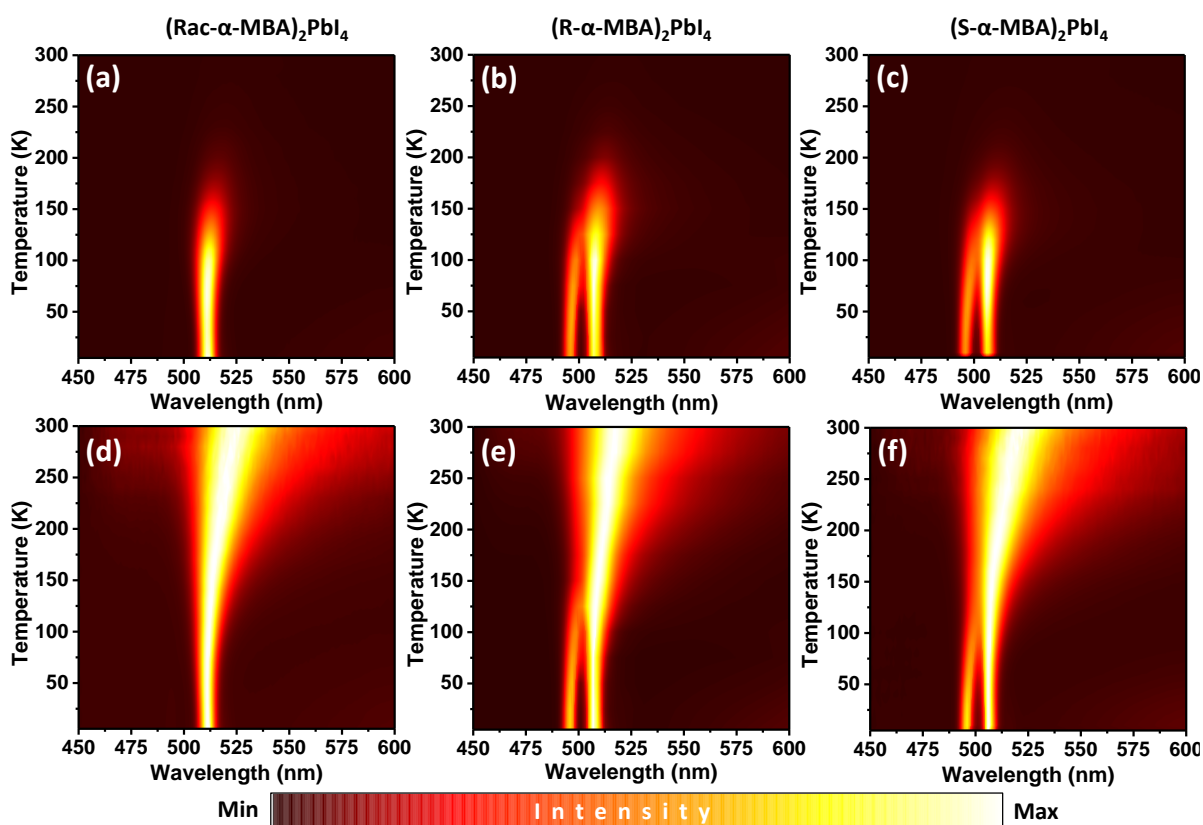


Figure 4.8: Pseudo color maps of temperature-dependent PL spectra of (a) (R- α -MBA) $_2$ PbI $_4$, (b) (S- α -MBA) $_2$ PbI $_4$ and (c) (Rac- α -MBA) $_2$ PbI $_4$ thin films. Pseudo color maps of temperature-dependent PL spectra with normalized PL intensity for (d) (R- α -MBA) $_2$ PbI $_4$, (e) (S- α -MBA) $_2$ PbI $_4$ and (f) (Rac- α -MBA) $_2$ PbI $_4$. The maximum PL intensity in d-f is normalized to one at each of the temperatures.

Figure 4.8 shows that the emission intensity in (Rac-, R- and S- α -MBA) $_2$ PbI $_4$ increases sharply with the decrease in temperature. Also, the emission shows a slight blue shift in all three

Emission Splitting and Higher Exciton Binding Energies in Chiral Layered Hybrid R- and S- α -Methylbenzylammonium Lead Iodide Perovskites

samples upon decreasing the temperature. The PL peak energy and integrated PL intensity are plotted against temperature in Figure 4.9. In all three samples, the PL peak energies do not show any sharp transition, indicating that the (Rac-, R- and S- α -MBA) $_2$ PbI $_4$ do not undergo any structural phase transition upon lowering down the temperature (Figure 4.9a). The PL peaks in (Rac-, R- and S- α -MBA) $_2$ PbI $_4$ show blue shifts of 63, 55 and 67 meV, respectively, upon decreasing the temperature from 300 to 5 K, indicating similar extents of increase in their band gaps. A similar increase in the band gap with the decrease in the temperature has been reported in other layered perovskites as well and has been attributed to the decrease in the Pb-I-Pb bond angles with the decreasing temperature.²⁵⁻²⁶ So overall, the chirality does not affect the temperature dependence of the band gap in (Rac-, R- and S- α -MBA) $_2$ PbI $_4$. Similarly, the integrated PL intensity in (Rac-, R- and S- α -MBA) $_2$ PbI $_4$ increases initially upon decreasing the temperature from 300 to 100 K due to the suppression of the thermally activated exciton dissociation and the non-radiative decay pathways (Figure 4.9b). Below 100 K, the integrated PL intensity reverses its trend, probably due to the trapping of the carriers by the non-emissive states, as reported previously.³⁹⁻⁴⁰ Above 100 K, the thermal energy is sufficient to de-trap the carriers.

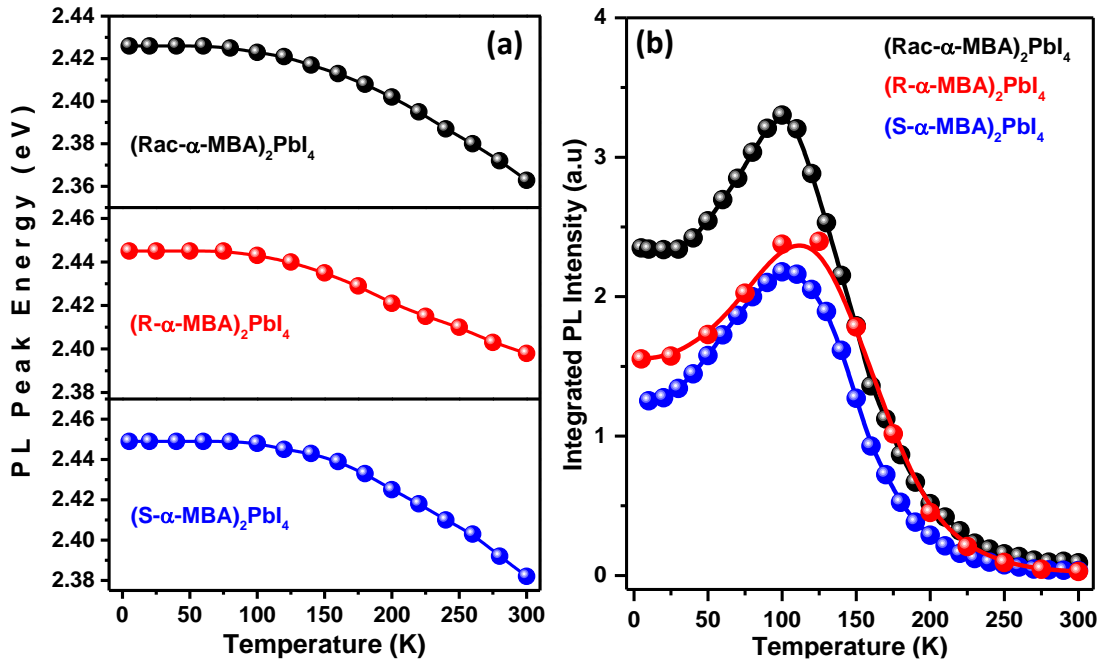


Figure 4.9: (a) Variation of the PL peak energy of the main peak (which is observed throughout the temperature range of 300 to 5 K in all three samples) with temperature in (Rac-, R- and S- α -MBA) $_2$ PbI $_4$. (b) Variation of the integrated PL intensity with temperature in (Rac-, R- and S- α -MBA) $_2$ PbI $_4$. For (R- and S- α -MBA) $_2$ PbI $_4$, integration is done over both the PL peaks. In all the panels, symbols are the experimental data, and the lines are just a guide to the eye.

Emission Splitting and Higher Exciton Binding Energies in Chiral Layered Hybrid R- and S- α -Methylbenzylammonium Lead Iodide Perovskites

Though the temperature evolution of integrated PL intensity in (Rac-, R- and S- α -MBA)₂PbI₄ is similar, there is a small difference in the intensity trend between the chiral (R- and S- α -MBA)₂PbI₄ and achiral (Rac- α -MBA)₂PbI₄. This difference in the integrated PL intensity may be due to a slight difference in the exciton binding energies (E_b) of the chiral (R and S) and achiral (Rac) samples. To see whether there is actually any difference in the exciton binding energies of the chiral (R and S) and achiral (Rac) samples, we calculated their exciton binding energies from their integrated PL intensities by using equation 1, which describes the evolution of PL intensity with temperature.

$$I(T) = \frac{I_0}{1 + Ae^{-E_b/(k_B T)}} \quad (1)$$

Here $I(T)$ is the PL intensity at temperature T , I_0 is the PL intensity at 0 K, A is the pre-exponential factor, E_b is the exciton binding energy, and k_B is the Boltzmann constant. The integrated PL intensity in all the three samples follows the above equation till 100 K only, and also below 100 K the (R- and S- α -MBA)₂PbI₄ show two PL peaks while the (Rac- α -MBA)₂PbI₄ shows only one PL peak. So, for the correct comparison, the experimental data is fitted till 100 K only. Figure 4.10 indeed shows that the exciton binding energies of the (R- and S- α -MBA)₂PbI₄ are different from that of the (Rac- α -MBA)₂PbI₄. (R- and S- α -MBA)₂PbI₄ show an exciton binding energy of about ~129 and ~125 meV, respectively, which is about 35-40 meV higher than that of the (Rac- α -MBA)₂PbI₄, which shows the exciton binding energy of 90 meV only. So the induced chirality in (R- and S- α -MBA)₂PbI₄ indeed affects their excitonic properties, which is reflected in the form of PL peak splitting and higher exciton binding energies.

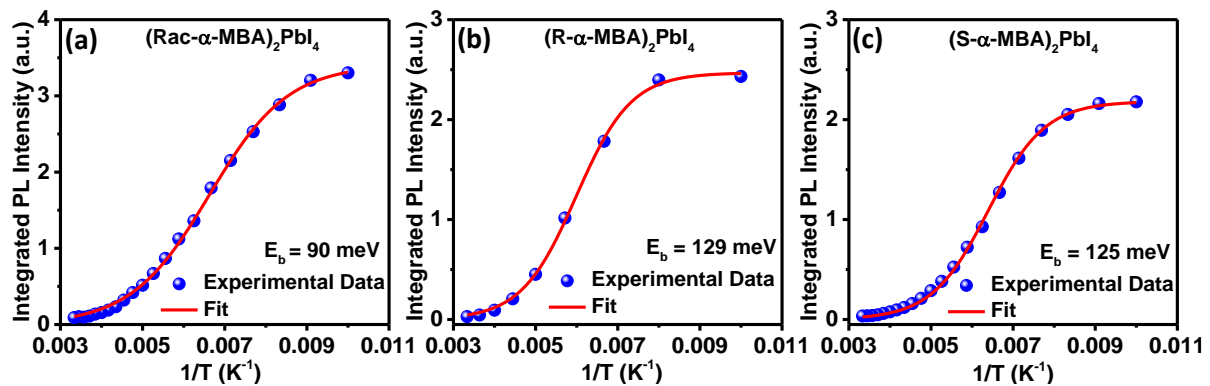


Figure 4.10: Integrated PL intensity vs. inverse of temperature ($1/T$) plots for exciton binding determination of (a) (Rac- α -MBA)₂PbI₄, (b) (R- α -MBA)₂PbI₄ and (c) (S- α -MBA)₂PbI₄.

4.4 Conclusion

We used chiral R- and S- α -MBA as the organic A-site cations to synthesize (R- and S- α -MBA)₂PbI₄ layered hybrid perovskites. Single crystal XRD data show the chiral structures for both (R- and S- α -MBA)₂PbI₄, indicating the introduction of chirality in these layered hybrid perovskites. The induced chirality is further confirmed by their CD data which show distinct signals with opposite signs for (R- and S- α -MBA)₂PbI₄. For comparison, (Rac- α -MBA)₂PbI₄ was also synthesized, which has a centrosymmetric crystal structure and consequently does not show any CD response. The CD spectra of (R- and S- α -MBA)₂PbI₄ shows a bi-polar derivative kind of response, suggesting the splitting of the excitonic states in the chiral environment. To further understand the effect of chirality on the excitonic properties, we recorded the temperature-dependent PL in (Rac-, R- and S- α -MBA)₂PbI₄. PL peak splitting is observed in chiral (R- and S- α -MBA)₂PbI₄ below 100 K, whereas a single PL peak is retained throughout the temperature range of 300 to 5 K in (Rac- α -MBA)₂PbI₄. The PL peak splitting in (R- and S- α -MBA)₂PbI₄ further supports the excitonic splitting as suggested by the CD data. Moreover, the induced chirality affects the excitonic binding energy as well. The chiral (R- and S- α -MBA)₂PbI₄ show significantly higher exciton binding energy compared to the achiral (Rac- α -MBA)₂PbI₄. The introduction of chirality in (R- and S- α -MBA)₂PbI₄ creates an asymmetry in the crystal structure of the inorganic (Pb-I) layers, which ultimately modifies the excitonic properties like PL emission and exciton binding energy.

4.5 References

1. Smith, I. C.; Hoke, E. T.; Solis-Ibarra, D.; McGehee, M. D.; Karunadasa, H. I. A Layered Hybrid Perovskite Solar-Cell Absorber with Enhanced Moisture Stability. *Angew. Chem. Int. Edit.* **2014**, *53*, 11232-11235.
2. Stoumpos, C. C.; Kanatzidis, M. G. The Renaissance of Halide Perovskites and Their Evolution as Emerging Semiconductors. *Acc. Chem. Res.* **2015**, *48*, 2791-2802.
3. Cao, D. H.; Stoumpos, C. C.; Farha, O. K.; Hupp, J. T.; Kanatzidis, M. G. 2D Homologous Perovskites as Light-Absorbing Materials for Solar Cell Applications. *J. Am. Chem. Soc.* **2015**, *137*, 7843-7850.
4. Stoumpos, C. C.; Cao, D. H.; Clark, D. J.; Young, J.; Rondinelli, J. M.; Jang, J. I.; Hupp, J. T.; Kanatzidis, M. G. Ruddlesden-Popper Hybrid Lead Iodide Perovskite 2D Homologous Semiconductors. *Chem. Mater.* **2016**, *28*, 2852-2867.
5. Blancon, J. C.; Tsai, H.; Nie, W.; Stoumpos, C. C.; Pedesseau, L.; Katan, C.; Kepenekian, M.; Soe, C. M. M.; Appavoo, K.; Sfeir, M. Y.; Tretiak, S.; Ajayan, P. M.; Kanatzidis, M. G.;

Emission Splitting and Higher Exciton Binding Energies in Chiral Layered Hybrid R- and S- α -Methylbenzylammonium Lead Iodide Perovskites

- Even, J.; Crochet, J. J.; Mohite, A. D. Extremely Efficient Internal Exciton Dissociation Through Edge States in Layered 2D Perovskites. *Science* **2017**, *355*, 1288-1291.
6. Mao, L.; Ke, W.; Pedesseau, L.; Wu, Y.; Katan, C.; Even, J.; Wasielewski, M. R.; Stoumpos, C. C.; Kanatzidis, M. G. Hybrid Dion-Jacobson 2D Lead Iodide Perovskites. *J. Am. Chem. Soc.* **2018**, *140*, 3775-3783.
7. Wang, K.; Wu, C.; Jiang, Y.; Yang, D.; Wang, K.; Priya, S. Distinct Conducting Layer Edge States in Two-Dimensional (2D) Halide Perovskite. *Sci. Adv.* **2019**, *5*, eaau3241.
8. Sheikh, T.; Nawale, V.; Pathoor, N.; Phadnis, C.; Chowdhury, A.; Nag, A. Molecular Intercalation and Electronic Two Dimensionality in Layered Hybrid Perovskites. *Angew. Chem. Int. Ed.* **2020**, *59*, 11653-11659.
9. Sheikh, T.; Maqbool, S.; Mandal, P.; Nag, A. Introducing Intermolecular Cation- π Interactions for Water-Stable Low Dimensional Hybrid Lead Halide Perovskites. *Angew. Chem. Int. Ed.* **2021**, *60*, 18265-18271.
10. Wang, H.; Ma, J.; Li, D. Two-Dimensional Hybrid Perovskite-Based Van der Waals Heterostructures. *J. Phys. Chem. Lett.* **2021**, *12*, 8178-8187.
11. Saparov, B.; Mitzi, D. B. Organic-Inorganic Perovskites: Structural Versatility for Functional Materials Design. *Chem. Rev.* **2016**, *116*, 4558-4596.
12. Katan, C.; Mercier, N.; Even, J. Quantum and Dielectric Confinement Effects in Lower-Dimensional Hybrid Perovskite Semiconductors. *Chem. Rev.* **2019**, *119*, 3140-3192.
13. Ma, J.; Fang, C.; Chen, C.; Jin, L.; Wang, J.; Wang, S.; Tang, J.; Li, D. Chiral 2D Perovskites with a High Degree of Circularly Polarized Photoluminescence. *ACS Nano* **2019**, *13*, 3659-3665.
14. Chen, C.; Gao, L.; Gao, W.; Ge, C.; Du, X.; Li, Z.; Yang, Y.; Niu, G.; Tang, J. Circularly Polarized Light Detection Using Chiral Hybrid Perovskite. *Nat. Commun.* **2019**, *10*, 1927.
15. Jana, M. K.; Song, R.; Liu, H.; Khanal, D. R.; Janke, S. M.; Zhao, R.; Liu, C.; Vally Vardeny, Z.; Blum, V.; Mitzi, D. B. Organic-to-Inorganic Structural Chirality Transfer in a 2D Hybrid Perovskite and Impact on Rashba-Dresselhaus Spin-Orbit Coupling. *Nat. Commun.* **2020**, *11*, 4699.
16. Long, G.; Jiang, C.; Sabatini, R.; Yang, Z.; Wei, M.; Quan, L. N.; Liang, Q.; Rasmita, A.; Askerka, M.; Walters, G.; Gong, X.; Xing, J.; Wen, X.; Quintero-Bermudez, R.; Yuan, H.; Xing, G.; Wang, X. R.; Song, D.; Voznyy, O.; Zhang, M.; Hoogland, S.; Gao, W.; Xiong, Q.; Sargent, E. H. Spin Control in Reduced-Dimensional Chiral Perovskites. *Nat. Photonics* **2018**, *12*, 528-533.

Emission Splitting and Higher Exciton Binding Energies in Chiral Layered Hybrid R- and S- α -Methylbenzylammonium Lead Iodide Perovskites

17. Yuan, C.; Li, X.; Semin, S.; Feng, Y.; Rasing, T.; Xu, J. Chiral Lead Halide Perovskite Nanowires for Second-Order Nonlinear Optics. *Nano Lett.* **2018**, *18*, 5411-5417.
18. Ahn, J.; Ma, S.; Kim, J.-Y.; Kyhm, J.; Yang, W.; Lim, J. A.; Kotov, N. A.; Moon, J. Chiral 2D Organic Inorganic Hybrid Perovskite with Circular Dichroism Tunable Over Wide Wavelength Range. *J. Am. Chem. Soc.* **2020**, *142*, 4206-4212.
19. Long, G.; Sabatini, R.; Saidaminov, M. I.; Lakhwani, G.; Rasmita, A.; Liu, X.; Sargent, E. H.; Gao, W. Chiral-Perovskite Optoelectronics. *Nat. Rev. Mater.* **2020**, *5*, 423-439.
20. Papavassiliou, G. C.; Koutselas, I. B.; Terzis, A.; Whangbo, M. H. Structural and Electronic Properties of the Natural Quantum-Well System $(C_6H_5CH_2CH_2NH_3)_2SnI_4$. *Solid State Commun.* **1994**, *91*, 695-698.
21. Mitzi, D. B. Synthesis, Crystal Structure, and Optical and Thermal Properties of $(C_4H_9NH_3)_2MI_4$ (M = Ge, Sn, Pb). *Chem. Mater.* **1996**, *8*, 791-800.
22. Mitzi, D. B.; Chondroudis, K.; Kagan, C. R. Organic-Inorganic Electronics. *IBM J. Res. Dev.* **2001**, *45*, 29-45.
23. Sichert, J. A.; Tong, Y.; Mutz, N.; Vollmer, M.; Fischer, S.; Milowska, K. Z.; García Cortadella, R.; Nickel, B.; Cardenas-Daw, C.; Stolarczyk, J. K.; Urban, A. S.; Feldmann, J. Quantum Size Effect in Organometal Halide Perovskite Nanoplatelets. *Nano Lett.* **2015**, *15*, 6521-6527.
24. Ishihara, T.; Takahashi, J.; Goto, T. Exciton State in Two-Dimensional Perovskite Semiconductor $(C_{10}H_{21}NH_3)_2PbI_4$. *Solid State Commun.* **1989**, *69*, 933-936.
25. Sheikh, T.; Shinde, A.; Mahamuni, S.; Nag, A. Possible Dual Bandgap in $(C_4H_9NH_3)_2PbI_4$ 2D Layered Perovskite: Single-Crystal and Exfoliated Few-Layer. *ACS Energy Letters* **2018**, *3*, 2940-2946.
26. Sheikh, T.; Shinde, A.; Mahamuni, S.; Nag, A. Dual Excitonic Emissions and Structural Phase Transition of Octylammonium Lead Iodide 2D Layered Perovskite Single Crystal. *Mater. Res. Express* **2019**, *6*, 124002.
27. Sheikh, T.; Nag, A. Mn Doping in Centimeter-Sized Layered 2D Butylammonium Lead Bromide (BA_2PbBr_4) Single Crystals and Their Optical Properties. *J. Phys. Chem. C* **2019**, *123*, 9420-9427.
28. Nawale, V. V.; Sheikh, T.; Nag, A. Dual Excitonic Emission in Hybrid 2D Layered Tin Iodide Perovskites. *J. Phys. Chem. C* **2020** *124*, 21129-21136.
29. Smith, M. D.; Karunadasa, H. I. White-Light Emission from Layered Halide Perovskites. *Acc. Chem. Res.* **2018**, *51*, 619-627.

Emission Splitting and Higher Exciton Binding Energies in Chiral Layered Hybrid R- and S- α -Methylbenzylammonium Lead Iodide Perovskites

30. Zheng, F.; Wang, L.-w. Large Polaron Formation and its Effect on Electron Transport in Hybrid Perovskites. *Energy Environ. Sci.* **2019**, *12*, 1219-1230.
31. Chakraborty, R.; Nag, A. Correlation of Dielectric Confinement and Excitonic Binding Energy in 2D Layered Hybrid Perovskites Using Temperature Dependent Photoluminescence. *J. Phys. Chem. C* **2020**, *124*, 16177-16185.
32. Billing, D. Bis(1-Phenylethylammonium) Tetraiodoplumbate(II). *Acta Cryst. E* **2002**, *58*, m669-m671.
33. Billing, D. G.; Lemmerer, A. Synthesis and Crystal Structures of Inorganic-Organic Hybrids Incorporating an Aromatic Amine with a Chiral Functional Group. *CrystEngComm* **2006**, *8*, 686-695.
34. Ahn, J.; Lee, E.; Tan, J.; Yang, W.; Kim, B.; Moon, J. A New Class of Chiral Semiconductors: Chiral-Organic-Molecule-Incorporating Organic-Inorganic Hybrid perovskites. *Mater. Horiz.* **2017**, *4*, 851-856.
35. Ben-Moshe, A.; Teitelboim, A.; Oron, D.; Markovich, G. Probing the Interaction of Quantum Dots with Chiral Capping Molecules Using Circular Dichroism Spectroscopy. *Nano Lett.* **2016**, *16*, 7467-7473.
36. Lu, H.; Wang, J.; Xiao, C.; Pan, X.; Chen, X.; Brunecky, R.; Berry, J. J.; Zhu, K.; Beard, M. C.; Vardeny, Z. V. Spin-Dependent Charge Transport Through 2D Chiral Hybrid Lead-Iodide Perovskites. *Sci. Adv.* **2019**, *5*, eaay0571.
37. Kim, Y.-H.; Zhai, Y.; Lu, H.; Pan, X.; Xiao, C.; Gauldin, E. A.; Harvey, S. P.; Berry, J. J.; Vardeny, Z. V.; Luther, J. M.; Beard, M. C. Chiral-Induced Spin Selectivity Enables a Room-Temperature Spin Light-Emitting Diode. *Science* **2021**, *371*, 1129-1133.
38. Liang, C.; Gu, H.; Xia, Y.; Wang, Z.; Liu, X.; Xia, J.; Zuo, S.; Hu, Y.; Gao, X.; Hui, W.; Chao, L.; Niu, T.; Fang, M.; Lu, H.; Dong, H.; Yu, H.; Chen, S.; Ran, X.; Song, L.; Li, B.; Zhang, J.; Peng, Y.; Shao, G.; Wang, J.; Chen, Y.; Xing, G.; Huang, W. Two-Dimensional Ruddlesden-Popper Layered Perovskite Solar Cells Based on Phase-Pure Thin Films. *Nat. Energy* **2021**, *6*, 38-45.
39. Woo, H. C.; Choi, J. W.; Shin, J.; Chin, S.-H.; Ann, M. H.; Lee, C.-L. Temperature-Dependent Photoluminescence of CH₃NH₃PbBr₃ Perovskite Quantum Dots and Bulk Counterparts. *J. Phys. Chem. Lett.* **2018**, *9*, 4066-4074.
40. Folpini, G.; Cortecchia, D.; Petrozza, A.; Srimath Kandada, A. R. The Role of a Dark Exciton Reservoir in the Luminescence Efficiency of Two-Dimensional Tin Iodide Perovskites. *J. Mater. Chem. C* **2020**, *8*, 10889-10896.

Chapter 5

Stabilizing Lower Dimensional Lead Halide Perovskites by Intermolecular Cation- π Interactions

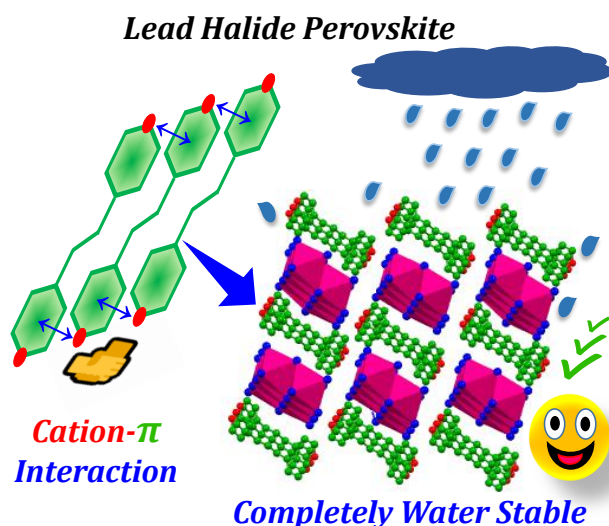
The work presented in this chapter is published in *Angewandte Chemie* with the following details:

Sheikh, T.; Maqbool, S.; Mandal, P.; Nag, A. Introducing Intermolecular Cation- π Interactions for Water-Stable Low Dimensional Hybrid Lead Halide Perovskites. *Angew. Chem. Int. Ed.* **2021**, 60, 18265-18271.

Copyright permission has been taken for the whole article from John Wiley and Sons.

Abstract

Optoelectronically active hybrid lead halide perovskites dissociate in water. To prevent this dissociation, here, we introduce long-range intermolecular cation- π interactions between A-site cations of hybrid perovskites. An aromatic diamine like 4,4'-trimethylenedipyridine, if protonated, can show a long-range cation- π stacking, and therefore, serves as our A-site cation. Consequently, 4,4'-trimethylenedipyridinium lead bromide [(4,4'-TMDP)Pb₂Br₆], a one-dimensional hybrid perovskite, remains completely stable after continuous water treatment for six months. Mechanistic insights about the cation- π interactions are obtained by single-crystal X-ray diffraction and nuclear magnetic resonance spectroscopy. The concept of long-range cation- π interaction is further extended to another A-site cation 4,4'-ethylenedipyridinium ion (4,4'-EDP), forming water-stable (4,4'-EDP)Pb₂Br₆ perovskite. These water-stable perovskites are then used to fabricate white light-emitting diode. Note that the achieved water stability is the intrinsic stability of perovskite composition, unlike the prior approach of encapsulating the unstable perovskite material (or device) by water-resistant materials. The introduced cation- π interactions can be a breakthrough strategy in designing many more compositions of water-stable low-dimensional hybrid perovskites.

Graphical Abstract

5.1 Introduction

The universal solvent water, which is polar in nature, dissolves the ionic compounds. For example, inorganic alkali metal salts and organic ammonium salts are highly soluble in water. Metal halide perovskites have generic formula like ABX_3 or A_2BX_4 ($B = \text{Pb, Sn \& X = Cl, Br or I}$), with A-site cations as organic ammonium ions (e.g., CH_3NH_3^+ , $\text{CH}_3\text{CH}_2\text{CH}_2\text{CH}_2\text{NH}_3^+$) or alkali metal ions (e.g., Cs^+ , Rb^+).¹⁻¹¹ Such water-soluble A-site cations make metal halide perovskites unstable in water and moisture.¹²⁻¹⁷ In addition, the water solubility of hybrid lead perovskites brings in the concern of contaminating groundwater with toxic lead compounds.¹⁸⁻²³ So, the true potential of the optical and optoelectronic properties of these perovskites can only be realized by making them water-stable.

In recent times, multiple strategies have been developed to either encapsulate perovskite solar cell devices or encapsulate the material itself with different water-resistant materials.²⁴⁻³⁰ But damage or leakage of the encapsulation layer brings back the concern of water instability and contamination of the groundwater. So, improving the intrinsic water-stability of hybrid lead halide perovskite still remains a fundamental materials chemistry challenge. To be more precise, the primary question is how to suppress the water solubility of A-site cation. Thinking about this question brought our attention to the cation- π interactions. It is well established that alkali metal ions and ammonium ions strongly interact with the π -electron cloud present in the aromatic systems.³¹⁻³² These interactions are mostly dominated by the electrostatic attraction between the cation and the π -electron cloud, although the possible contributions from other non-covalent interactions cannot be ignored.³³⁻³⁴ Interestingly, the cation- π interactions are stronger than the typical cation-water interactions.³³⁻³⁴ This possibility prompted us to design an A-site cation for halide perovskites that has strong intermolecular ammonium cation- π interactions. The strong cation- π interactions in these A-site cations will result in a giant polymer kind of network, thus making them insoluble in water.

Herein, we establish this idea of utilizing the cation- π interactions in hybrid halide perovskites to turn them completely stable in water for more than six months. We choose the A-site cation 4,4'-trimethylenedipyridinium ion (4,4'-TMDP) as it has both π -electron cloud and two ammonium ions (Figure 5.1). The ammonium ions in 4,4'-TMDP being positively charged can interact strongly with the π -electron cloud on the adjacent 4,4'-TMDP ions, giving rise to a long-range cation- π stacking. So, we synthesized (4,4'-TMDP) Pb_2Br_6 , a one-dimensional (1D) perovskite showing strong cation- π interactions. As a proof of generalization, we synthesized another 1D perovskite system (4,4'-EDP) Pb_2Br_6 , where 4,4'-EDP is 4,4'-ethylenedipyridinium

Stabilizing Lower Dimensional Lead Halide Perovskites by Intermolecular Cation- π Interactions

ion. Both of these 1D hybrid perovskite systems are stable in water and other polar solvents because of the strong cation- π interactions between the A-site cations resulting in a polymer kind of network. Interestingly, these hybrid perovskite systems yield stable phosphor-converted white light-emitting diodes (LEDs).

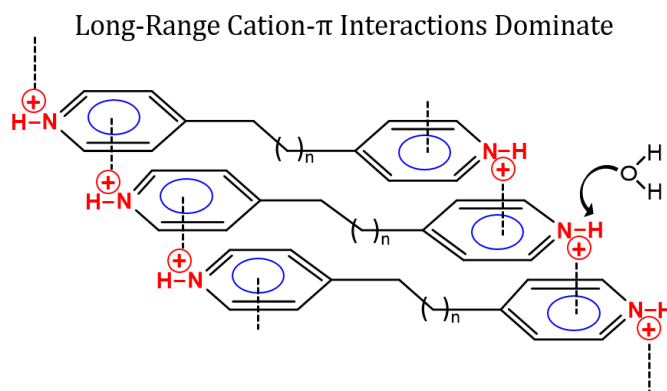


Figure 5.1: Figure 1: Schematics of 4,4'-Dipyridinium ions having both the cation and the π -electron cloud. Intermolecular cation- π interactions between the positively charged ammonium ions and the π -electron cloud, giving rise to a long-range cation- π stacking. The cation- π interactions, which are extended over the entire crystal, are likely to dominate over the interaction of individual organic cations with water molecules. Two cations of this family, namely, 4,4'-trimethylenedipyridinium ion (4,4'-TMDP) with $n = 2$, and 4,4'-ethylenedipyridinium ion (4,4'-EDP) with $n = 1$, are used here as A-site cations of hybrid halide perovskites.

5.2 Experimental Section

5.2.1 Chemicals

Lead(II) oxide (Sigma Aldrich, 99.9%), hydrobromic acid (Sigma Aldrich, 48% w/w in H_2O , 99.9%), hypophosphorous acid (Avra, 50% w/w H_2O), 4,4'-trimethylenedipyridine (Sigma Aldrich, 98%), 4,4'-ethylenedipyridine (Sigma Aldrich, 99%), acetone (Rankem, 99.5%), hexane (Rankem, 99.5%), acetonitrile (Rankem, 99.5%), dimethylformamide (Rankem, 99.5%), deuterated chloroform (Sigma Aldrich, 99%), and distilled water (Milli-Q).

5.2.2 Synthesis of (4,4'-TMDP) Pb_2Br_6 single crystals

(4,4'-TMDP) Pb_2Br_6 single crystals were synthesized by an acid precipitation method. 0.5 mmol (111.6 mg) lead(II) oxide and 0.5 mmol (99.1 mg) 4,4'-trimethylenedipyridine were dissolved in a mixture of 15 mL hydrobromic acid and 2 mL hypophosphorous acid at 120 °C under constant magnetic stirring. Once a clear transparent solution was obtained, the heating and stirring were stopped, and the solution was allowed to cool to room temperature naturally. The

Stabilizing Lower Dimensional Lead Halide Perovskites by Intermolecular Cation– π Interactions

solution was kept overnight as such without disturbing. During this process, transparent needle-shaped crystals of (4,4'-TMDP)Pb₂Br₆ precipitated out. The crystals were filtered and washed with acetone.

5.2.3 Synthesis of (4,4'-EDP)Pb₂Br₆ single crystals

(4,4'-EDP)Pb₂Br₆ single crystals were synthesized by the same method used for the synthesis of (4,4'-TMDP)Pb₂Br₆ single crystals. Instead of 4,4'-trimethylenedipyridine, 0.5 mmol (92.1 mg) of 4,4'-ethylenedipyridine was used. The rest of the steps were the same.

5.2.4 Synthesis of (4,4'-TMDP)Br₂

(4,4'-TMDP)Br₂ single crystals were synthesized by dissolving the 100 mg of 4,4'-trimethylenedipyridine in 5 mL hydrobromic acid followed by slow evaporation of excess hydrobromic acid at 60 °C. During the evaporation process, needle-shaped crystals of (4,4'-TMDP)Br₂ precipitated out. The (4,4'-TMDP)Br₂ crystals were filtered and washed with acetone.

5.2.5 Characterization

Single-crystal X-ray diffraction (XRD) measurements were carried on Bruker Smart Apex Duo diffractometer at room temperature (298 K) using Mo K α radiation ($\lambda = 0.71073 \text{ \AA}$). The frames were integrated with the Bruker SAINT software package by a narrow-frame algorithm. The structures were solved by a direct method and refined by full-matrix least-squares on F² using the SHELXTL software package. Powder XRD measurements were carried on Bruker D8 Advance X-ray diffractometer using Cu K α radiation (1.54 \AA). Optical diffused-reflectance measurements were carried on Shimadzu UV-3600 plus UV-Vis-NIR spectrophotometer. The reflectance data were converted to absorbance by using Kubelka-Munk transformation.³⁵ Steady-state photoluminescence (PL) measurements were carried on FLS 980 (Edinburgh Instruments). Time-resolved PL decays were recorded in the same instrument using a microsecond flash lamp as the excitation source. The PL decay plots were fitted to bi-exponential fits, and the average lifetime was calculated by the following equation:

$$\tau_{av} = \frac{(A_1 \times \tau_1^2) + (A_2 \times \tau_2^2)}{(A_1 \times \tau_1) + (A_2 \times \tau_2)}$$

Where τ_{av} is the average lifetime, τ_1 , τ_2 are the two decay components; A_1 , A_2 are their respective contributions. Temperature-dependent PL measurements were performed on the FLS980 (Edinburgh Instruments). The substrate containing the sample was mounted on a gold-

plated sample holder attached to a closed cycle He cryostat (Advanced Research Systems) with a temperature controller (Lake Shore Cryotronics) to achieve the desired temperatures. The absolute PL quantum yields (QY) were determined by Quanta Phi connected with Horiba Jobin Yvon Fluoromax-4 spectrofluorometer.

5.2.6 NMR spectroscopy

The solid-state ^1H and ^{13}C NMR experiments were carried at room temperature on a Bruker Advance III HD spectrometer operating at 11.7 Tesla. A 3.2 mm probe was used in all the experiments. All the spectra were recorded at 12 kHz magic angle spinning, except (4,4'-TMDP)Br₂, the spectra of which were recorded at 8 kHz magic angle spinning. ^{13}C spectra were recorded via cross-polarization (CP) from ^1H . The solution ^1H and ^{13}C NMR spectra of the neutral molecules were recorded at room temperature on a Bruker Advance III HD spectrometer operating at 9.4 Tesla. Deuterated chloroform (CDCl₃) was used as the solvent. All the NMR spectra were processed using TopSpin 3.6 software.

5.2.7 Water stability tests of (4,4'-TMDP)Pb₂Br₆ and (4,4'-EDP)Pb₂Br₆ single crystals

The as-synthesized (4,4'-TMDP)Pb₂Br₆ and (4,4'-EDP)Pb₂Br₆ single crystals were immersed in distilled water in separate vials. Photographs of the same crystals immersed in water were taken after illuminating with a 365 nm UV light. The crystals showed a bright white light emission. Then the vials were stored safely in the ambient conditions. At regular intervals, over a period of six months, the emission of the samples was recorded both under a UV lamp and in a spectrophotometer. The absorbance and PXRD data of these crystals were also checked during this period of time.

5.2.8 White LED fabrication of (4,4'-TMDP)Pb₂Br₆

(4,4'-TMDP)Pb₂Br₆ was ground with acetone till a fine dispersion was obtained. 50 μL of this fine dispersion was drop cast on a commercial UV-LED emitting 360-380 nm light. Upon drying, a fine coating of (4,4'-TMDP)Pb₂Br₆ was obtained on the surface of the LED. A variable bias ranging from 3.2 to 3.6 V was applied to the UV LED coated with our sample, achieving white light of varying intensity.

5.2.9 CIE (International Commission on Illumination), correlated color temperature (CCT) and color-rendering index (CRI) calculation

The CIE chromaticity coordinates, the CCT and CRI values were determined by using the ColorCalculator by OSRAM Sylvania, Inc.³⁶

5.3 Results and Discussion

5.3.1 Synthesis and structure showing cation- π stacking

The π - π interactions in aromatic systems are well established.³⁷⁻³⁸ However, the 4,4'-trimethylenedipyridine, an aromatic system, does not show such π - π self-stacking in its neutral form. Interestingly, the two amine groups in 4,4'-trimethylenedipyridine can be protonated. The ammonium ions in protonated 4,4'-TMDP being positively charged can interact with the π -electron cloud of the adjacent 4,4'-TMDP ions via cation- π interactions shown in Figure 5.1. The cation- π stacked 4,4'-TMDP network can further bind with the lead halide octahedral network electrostatically, leading to the formation of a hybrid organic-inorganic perovskite system. Following this approach, we synthesized (4,4'-TMDP)Pb₂Br₆ perovskite single crystals by an acid precipitation method. Briefly, lead oxide and 4,4'-trimethylenedipyridine were dissolved in aqueous hydrobromic acid upon heating to boiling, leading to a clear transparent solution. The subsequent cooling of this solution to room temperature yielded transparent needle-shaped (4,4'-TMDP)Pb₂Br₆ crystals. Room temperature single-crystal X-ray diffraction (SCXRD) data confirm that (4,4'-TMDP)Pb₂Br₆ crystalizes in a 1D structure with space group *C2/c*. The monoclinic lattice has lattice parameters $a = 23.327(5)$ Å, $b = 4.4450(9)$ Å, $c = 21.832(4)$ Å; $\alpha = \gamma = 90^\circ$ and $\beta = 102.733(9)^\circ$ (see Table 5.1 for details). The powder X-ray diffraction (PXRD) pattern of (4,4'-TMDP)Pb₂Br₆ matches well with the simulated one obtained from the SCXRD data, indicating a phase-pure sample (Figure 5.2).

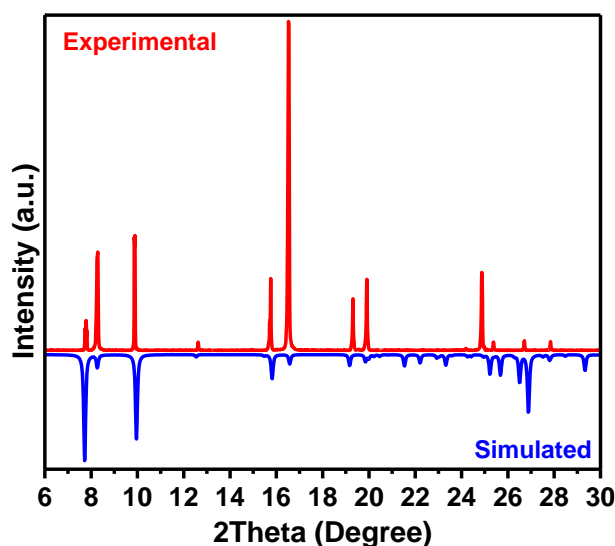


Figure 5.2: Comparison of the experimental and simulated PXRD patterns of (4,4'-TMDP)Pb₂Br₆. The simulated patterns are obtained from our single-crystal XRD data. For the sake of presentation, the intensity of the simulated pattern has been inverted, showing that both the patterns are a mirror image of each other.

Stabilizing Lower Dimensional Lead Halide Perovskites by Intermolecular Cation– π Interactions

Table 5.1: Crystal structure and data refinement of (4,4'-TMDP)Pb₂Br₆ at room temperature (RT)

(4,4'-TMDP)Pb₂Br₆	RT	
CCDC Number	2087690	
Chemical formula	C ₁₃ H ₁₆ Br ₆ N ₂ Pb ₂	
Formula weight	1094.12 g/mol	
Temperature	296(2) K	
Wavelength	0.71073 Å	
Crystal system	monoclinic	
Space group	C2/c	
Unit cell dimensions	a = 23.327(5) Å	$\alpha = 90^\circ$
	b = 4.4450(9) Å	$\beta = 102.733(9)^\circ$
	c = 21.832(4) Å	$\gamma = 90^\circ$
Volume	2208.1(7) Å ³	
Z	4	
Density (calculated)	3.291 g/cm ³	
Absorption coefficient	26.085 mm ⁻¹	
F(000)	1928	
Theta range for data collection	2.89 to 24.71°	
Index ranges	-26<=h<=26, -5<=k<=5, -25<=l<=25	
Reflections collected	15813	
Independent reflections	1876 [R(int) = 0.0923]	
Coverage of independent reflections	99.70%	
Absorption correction	Multi-Scan	
Structure solution technique	direct methods	
Structure solution program	SHELXT 2014/5 (Sheldrick, 2014)	
Refinement method	Full-matrix least-squares on F ²	
Refinement program	SHELXL-2017/1 (Sheldrick, 2017)	
Function minimized	$\Sigma w(F_o^2 - F_c^2)^2$	
Data / restraints / parameters	1876 / 0 / 107	
Goodness-of-fit on F ²	0.875	
Δ/σ_{\max}	0.001	
Final R indices	1791 data; I>2 σ (I)	R1 = 0.0422, wR2 = 0.0986
	all data	R1 = 0.0434, wR2 = 0.0992
Weighting scheme	w=1/[$\sigma^2(F_o^2)+(0.0100P)^2+4.6000P$] where P=(F _o ² +2F _c ²)/3	
Largest diff. peak and hole	0.266 and -0.249 eÅ ⁻³	
R.M.S. deviation from mean	0.051 eÅ ⁻³	

Stabilizing Lower Dimensional Lead Halide Perovskites by Intermolecular Cation- π Interactions

The crystal structure of (4,4'-TMDP)Pb₂Br₆ perovskite consists of a dimeric Pb-Br octahedral network, separated by 4,4'-TMDP cations, along the “*ac*” crystal plane, as shown in the left panel of Figure 5.3. A 1D network of the Pb-Br octahedral dimers can be observed along the “*bc*” crystal plane (right panel in Figure 5.3). Interestingly, the 4,4'-TMDP cations are arranged in such a way that the ammonium ions on one 4,4'-TMDP cation are exactly on top of the π -electron rings of the adjacent 4,4'-TMDP cation. This arrangement gives rise to a long-range cation- π stacking along the “*b*” crystallographic direction. The distance between the positively charged ammonium ion and the center of the π -electron ring is 3.8 Å. This is the optimal distance, where the cation- π interactions are expected to be the strongest.^{31-32, 34, 39}

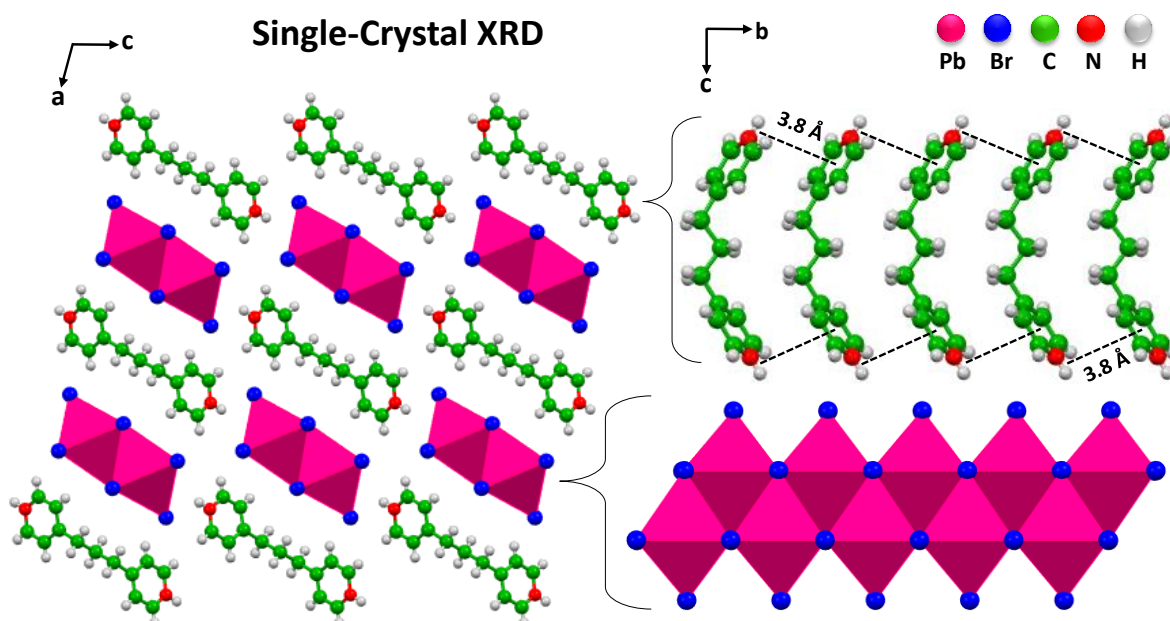


Figure 5.3: Crystal structure of (4,4'-TMDP)Pb₂Br₆ showing cation- π stacking: The left panel depicts the crystal structure viewed along the “*ac*” crystallographic plane, showing edge shared Pb-Br octahedral dimers separated by 4,4'-TMDP cations. The right panel depicts the cation- π stacking (shown by dashed black lines) between the 4,4'-TMDP cations along the “*b*” crystallographic direction and the 1D network of Pb-Br octahedral dimers.

5.3.2 Nuclear magnetic resonance (NMR) spectroscopy probing the cation- π interactions

The crystal structure of (4,4'-TMDP)Pb₂Br₆ obtained from the SCXRD shows a long-range cation- π stacking along the “*b*” crystallographic direction. Furthermore, to confirm intermolecular cation- π interactions using another independent experimental technique, we employed nuclear magnetic resonance (NMR) spectroscopy. Figure 5.4a shows the 4,4'-trimethylenedipyridine molecule indicating five different types of NMR active carbon nuclei (C1, C2, C3, C4, and C5). The solution-state ¹³C NMR spectrum (green) of the neutral 4,4'-

Stabilizing Lower Dimensional Lead Halide Perovskites by Intermolecular Cation– π Interactions

trimethylenedipyridine molecule shows five peaks corresponding to the five types of carbon atoms (Figure 5.4b). The peaks between chemical shift (δ) = 20 and 40 ppm correspond to the aliphatic carbons (C4-C5), and those between (δ) = 120 and 160 ppm correspond to the aromatic carbons (C1 to C3). The solid-state ^{13}C NMR spectrum (blue) of the neutral molecule matches well with its solution-state spectrum, with minor differences arising from the solid-state sample anisotropy, dipolar couplings and restricted molecular motions.⁴⁰ Importantly, upon protonation of the 4,4'-trimethylenedipyridine molecule and its incorporation in the 1D perovskite lattice, the peaks corresponding to the aromatic carbon atoms in its solid-state ^{13}C NMR spectrum (red) completely change (Figure 5.4b). The peaks corresponding to the C1 and C2 are shifted towards higher ppm values (downfield). In contrast, the peak corresponding to the C3 is shifted towards lower ppm values (upfield). These changes in the ^{13}C NMR spectrum indicate a drastic change in the electronic environment around these aromatic carbon atoms of 4,4'-TMDP cation upon its incorporation in the hybrid perovskite lattice.

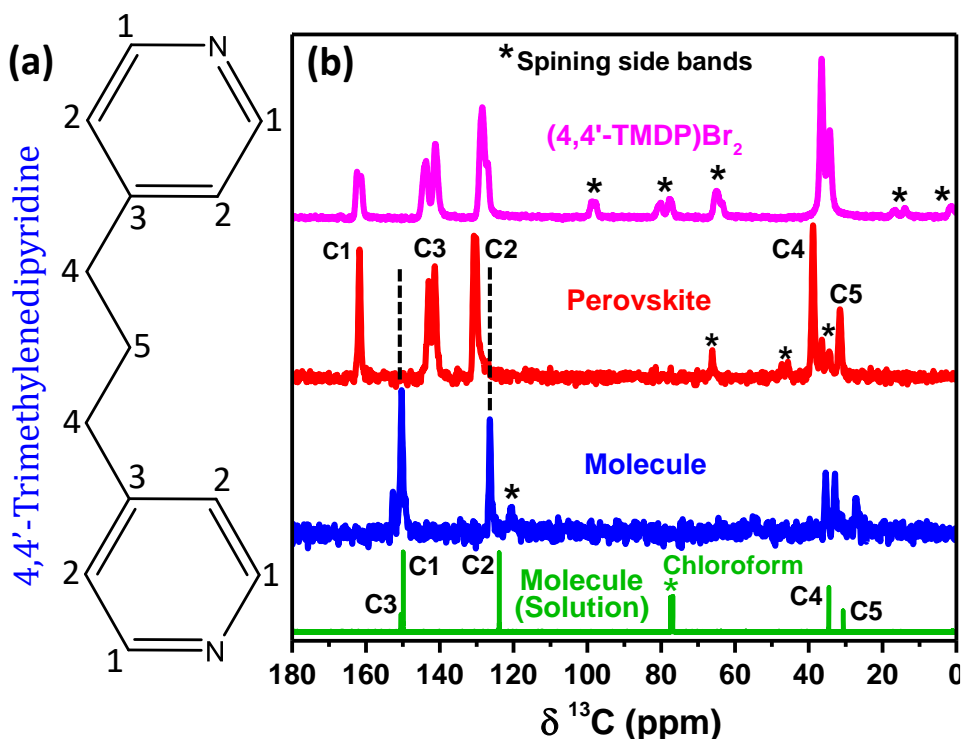


Figure 5.4: (a) 4,4'-trimethylenedipyridine molecule showing the numbering of the different types of carbon atoms from C1 to C5. (c) Solid-state ^{13}C NMR spectra of the neutral 4,4'-trimethylenedipyridine molecule (blue), the 4,4'-TMDP cation (magenta) in the form of $(4,4'\text{-TMDP})\text{Br}_2$ and the $(4,4'\text{-TMDP})\text{Pb}_2\text{Br}_6$ perovskite (red). The spectrum shown in green correspond to the solution-state ^{13}C NMR of the neutral 4,4'-trimethylenedipyridine molecule recorded in deuterated chloroform (CDCl_3). The peaks marked with “*” correspond to spinning sidebands.

Stabilizing Lower Dimensional Lead Halide Perovskites by Intermolecular Cation- π Interactions

The change in the electronic environment can be because of the cation- π interactions between the adjacent 4,4'-TMDP cations. In perovskite lattice, the C1 and C2 carbon atoms of one cation are just below the positively charged ammonium ion of the other cation (see Figure 5.1). Consequently, due to the cation- π interactions, the electron density around these carbon atoms reduces (deshielded), shifting the ^{13}C NMR peaks to higher ppm values (downfield). On the other hand, the C3 carbon atom of one cation is just below the π -electron cloud of the other cation. So, its electron density increases (shielded), shifting its ^{13}C NMR peak to lower ppm values (upfield) compared to the un-stacked neutral molecule.

The other possibilities, such as the interaction of 4,4'-TMDP ions with inorganic Pb-Br framework (see Figure 5.3), might also influence the NMR spectrum. To have more insights, we have also prepared single crystals of (4,4'-TMDP)Br₂. The (4,4'-TMDP)Br₂ crystalizes in a triclinic lattice with space group *P*-1. Refer to Table 5.2 for crystal structure data parameters. SCXRD data suggest that (4,4'-TMDP)Br₂ also has cation- π stacking (Figure 5.5), but it does not have the Pb-Br framework. Interestingly, the solid-state ^{13}C NMR spectrum (magenta) of the (4,4'-TMDP)Br₂ (without Pb-Br framework) also shows similar changes as that of the (4,4'-TMDP)Pb₂Br₆ perovskite. This similarity suggests that the cation- π interaction is the primary reason for the changes observed in the ^{13}C NMR spectrum. The aliphatic carbon atoms in (4,4'-TMDP)Pb₂Br₆ perovskite remain exclusive of cation- π interactions; hence their ^{13}C NMR peaks do not show much changes due to cation- π interactions.

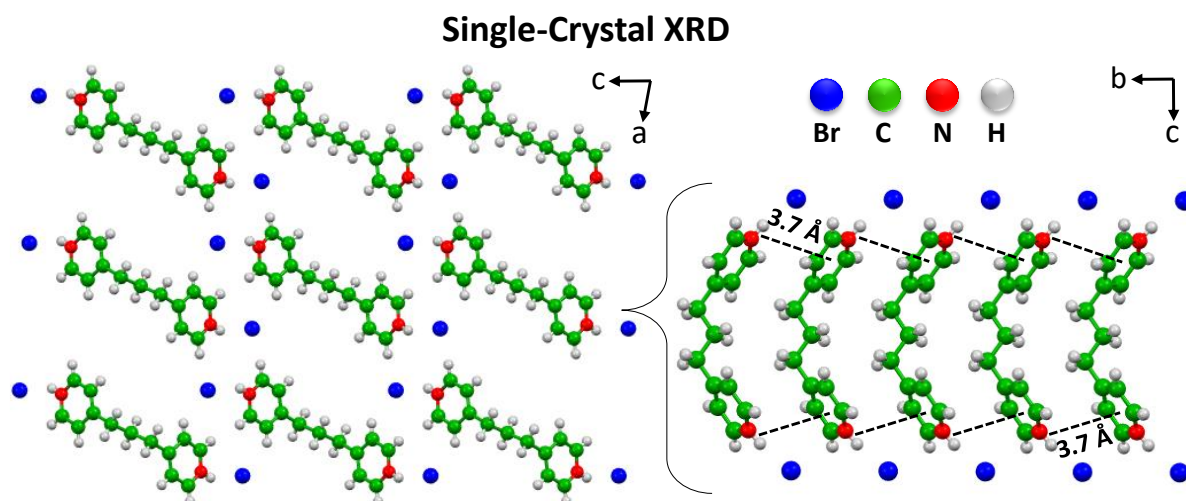


Figure 5.5: Crystal structure of (4,4'-TMDP)Br₂ obtained from single-crystal XRD data. The left panel depicts the crystal structure viewed along the “*ac*” crystallographic plane. The right panel depicts cation- π stacking (shown by dashed black lines) between the 4,4'-TMDP cations along the “*b*” crystallographic direction.

Stabilizing Lower Dimensional Lead Halide Perovskites by Intermolecular Cation– π Interactions

Table 5.2: Crystal structure and data refinement of (4,4'-TMDP)Br₂ at room temperature (RT)

(4,4'-EDP)Pb₂Br₆	RT	
CCDC Number	2087691	
Chemical formula	C ₁₂ H ₁₄ Br ₆ N ₂ Pb ₂	
Formula weight	1080.09 g/mol	
Temperature	296(2) K	
Wavelength	0.71073 Å	
Crystal system	triclinic	
Space group	P-1	
Unit cell dimensions	a = 4.292(2) Å	$\alpha = 72.218(13)^\circ$
	b = 10.767(5) Å	$\beta = 80.322(13)^\circ$
	c = 11.919(6) Å	$\gamma = 89.025(14)^\circ$
Volume	516.7(4) Å ³	
Z	1	
Density (calculated)	3.472 g/cm ³	
Absorption coefficient	27.870 mm ⁻¹	
F(000)	474	
Theta range for data collection	1.82 to 28.50°	
Index ranges	-5 <= h <= 5, -14 <= k <= 12, -16 <= l <= 15	
Reflections collected	5980	
Independent reflections	2546 [R(int) = 0.0638]	
Coverage of independent reflections	97.20%	
Absorption correction	Multi-Scan	
Structure solution technique	direct methods	
Structure solution program	SHELXT 2014/5 (Sheldrick, 2014)	
Refinement method	Full-matrix least-squares on F ²	
Refinement program	SHELXL-2018/3 (Sheldrick, 2018)	
Function minimized	$\Sigma w(F_o^2 - F_c^2)^2$	
Data / restraints / parameters	2590 / 12 / 103	
Goodness-of-fit on F ²	1.251	
Δ/σ_{\max}	0.002	
Final R indices	1880 data; I > 2 σ (I)	R ₁ = 0.0751, wR ₂ = 0.1961
	all data	R ₁ = 0.1042, wR ₂ = 0.2099
Weighting scheme	w = 1 / [$\sigma^2(F_o^2) + (0.1000P)^2$] where P = (F _o ² + 2F _c ²) / 3	
Largest diff. peak and hole	2.307 and -1.246 eÅ ⁻³	
R.M.S. deviation from mean	0.123 eÅ ⁻³	

Stabilizing Lower Dimensional Lead Halide Perovskites by Intermolecular Cation- π Interactions

Similar to the ^{13}C NMR, the ^1H NMR spectra (Figure 5.6) of 4,4'-TMDP ions also show stacking-related changes upon protonation and its incorporation in the 1D perovskite lattice. The solid-state ^1H NMR spectrum of the neutral 4,4'-trimethylenedipyridine molecule shows four peaks corresponding to the four types of hydrogen atoms present. The peaks in the solid-state spectrum of the neutral molecule are broad and are at higher chemical shifts compared to its solution-state NMR spectra. Such changes in the solid-state ^1H NMR are expected due to the dipolar couplings, sample anisotropy and the restricted molecular motions.⁴⁰ A drastic change in the ^1H NMR peaks is observed upon cation- π stacking in (4,4'-EDP) Pb_2Br_6 . A broad single peak, instead of four peaks, is observed in the ^1H NMR of (4,4'-EDP) Pb_2Br_6 . This suggests a change in the electronic environment of the hydrogen atoms. The solid-state ^1H NMR spectrum (magenta) of the (4,4'-TMDP) Br_2 (without Pb-Br framework) also shows a single peak similar to that of (4,4'-TMDP) Pb_2Br_6 perovskite. This similarity rules out the possible influence of the Pb-Br framework in the ^1H NMR data (4,4'-TMDP) Pb_2Br_6 , again suggesting that the cation- π interaction is the primary reason for single-peak in ^1H NMR spectrum.

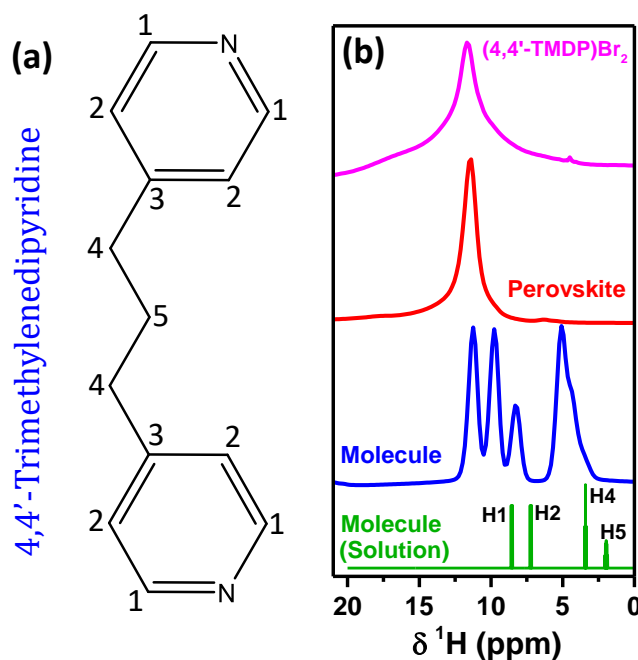


Figure 5.6: (a) 4,4'-trimethylenedipyridine molecule showing the numbering of the different types of carbon atoms from C1 to C5. Accordingly, the hydrogen atoms can also be numbered as H1, H2, H4 and H5. The C3 is a tertiary carbon; hence there is no H3 atom present. (b) Solid-state ^1H NMR spectra of the neutral 4,4'-trimethylenedipyridine molecule (blue), the 4,4'-TMDP cation (magenta) in the form of (4,4'-TMDP) Br_2 and the (4,4'-TMDP) Pb_2Br_6 perovskite (red). The spectra shown in green correspond to the solution-state NMR of the neutral 4,4'-TMDP molecule recorded in deuterated chloroform (CDCl_3).

5.3.3 Optical characterization of (4,4'-TMDP)Pb₂Br₆

After synthesizing and establishing the intermolecular cation- π interactions in 1D (4,4'-TMDP)Pb₂Br₆, we discuss its optical properties. Figure 5.7a shows that (4,4'-TMDP)Pb₂Br₆ has a sharp absorption edge (red spectrum) at 380 nm, indicating a direct bandgap. Upon exciting with 360 nm light, (4,4'-TMDP)Pb₂Br₆ shows broad photoluminescence (PL, blue spectrum) spanning over the entire visible range (400 to 800 nm), with a full width at half-maximum (FWHM) of 227 nm. The broad emission has the CIE (International Commission on Illumination) chromaticity coordinates of (0.37, 0.39) corresponding to white light emission, as shown in Figure 5.7b. The correlated color temperature (CCT) comes out to be 4362 K with a color-rendering index (CRI) value of 86, corresponding to the warm white light, which is suitable for both indoor and outdoor lighting.⁴¹ The PL quantum yield (QY) of (4,4'-TMDP)Pb₂Br₆ comes out to be 3.7%, which needs to be improved for real-life applications.

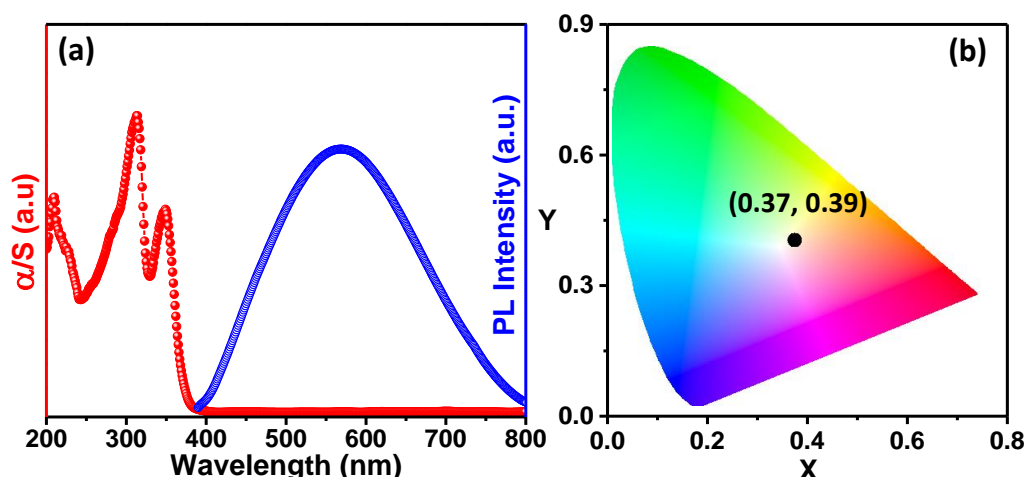


Figure 5.7: (a) UV-visible absorption (red) and PL (blue) spectra of (4,4'-TMDP)Pb₂Br₆. The absorbance data was obtained from diffuse reflectance data by using the Kubelka–Munk function [$\alpha/S = (1 - R)^2/2R$]; α is the absorption coefficient, S is the scattering coefficient, and R is the reflectance. (b) CIE diagram depicting the white color of the light emission.

The PL decay lifetime of the broad emission is long, with an average lifetime of 6.3 milliseconds, as shown in Figure 5.8a. The two components of the bi-exponential decay are $\tau_1 = 1.2$ ms (88%) and $\tau_2 = 10.5$ (12%). Broad PL with such a long lifetime and large Stokes shift compared to the absorption edge is very much prevalent in the lower dimensional perovskites and is termed as self-trapped excitonic (STE) emission.⁴²⁻⁴⁴ To further elucidate the origin of this broad emission, we recorded the temperature-dependent PL of (4,4'-TMDP)Pb₂Br₆. Figure 5.8b shows the color map of temperature-dependent PL. The PL peak position (solid white line in Figure 5.8b) largely remains unchanged at ~580 nm in the temperature range 300-200 K. Further decrease in temperature till 5 K shows a gradual blue-shift to 508 nm.

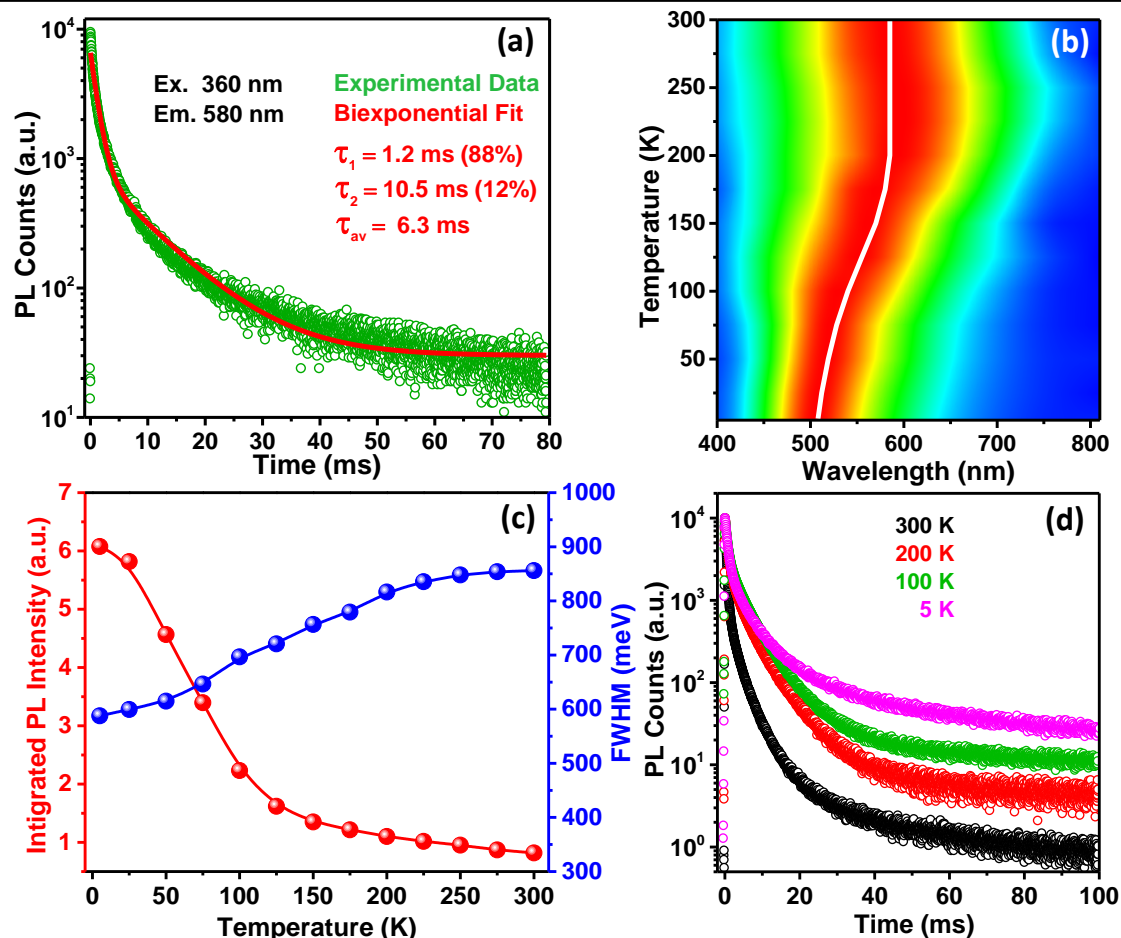


Figure 5.8: (a) PL decay dynamics of the (4,4'-TMDP)Pb₂Br₆ for emission peak at 580 nm upon excitation with 360 nm light, showing a millisecond long lifetime. (b) Pseudo-color map showing temperature-dependent PL spectra of (4,4'-TMDP)Pb₂Br₆. The solid white line traces the PL peak position at different temperatures. (c) Temperature evolution of the intensity (red) and full width at half maximum (FWHM, blue) of the PL peak of (4,4'-TMDP)Pb₂Br₆. The colored spheres are the experimental data, and the solid lines are just guide to the eye, indicating the trend. (d) PL decay dynamics of the (4,4'-TMDP)Pb₂Br₆ for emission peak at 580 nm at varying temperatures.

The PL intensity increases slightly till 125 K, below which a sharp increase in PL intensity is observed, as shown by the red spectrum in Figure 5.8c. The increase in the PL intensity with decreasing temperature is due to the suppression of the thermally activated non-radiative recombination pathways. Also, the FWHM decreases with decreasing the temperature (blue spectrum in Figure 5.8c). But still, at 5 K, the PL is broad with a large Stokes shift compared to the absorption edge, suggesting STE as the origin of this PL.⁴⁵⁻⁴⁶ The possibility of emission from a permanent defect site is less in such single crystals but cannot be ruled out completely.⁴⁷ The PL decay lifetime of the broad emission increases continuously from 300 K to 5 K, as shown in Figure 5.8d, again suggesting the suppression of the thermally activated non-radiative recombination pathways.

5.3.4 Water stability of (4,4'-TMDP)Pb₂Br₆

After the optical characterization, we now discuss the water stability of (4,4'-TMDP)Pb₂Br₆. Are the concerted intermolecular cation- π interactions between 4,4'-TMDP ions stronger than their interactions with water? If so, then (4,4'-TMDP)Pb₂Br₆ should be completely stable in water. To check that, we immersed the (4,4'-TMDP)Pb₂Br₆ crystals in distilled water and studied their water stability over a period of six months. Figure 5.9a compares the photographs of (4,4'-TMDP)Pb₂Br₆ crystals, showing white light emission, in water under a 365 nm UV lamp on days 1, 90 and 180. The white light emission looks amazingly stable even on day 180.

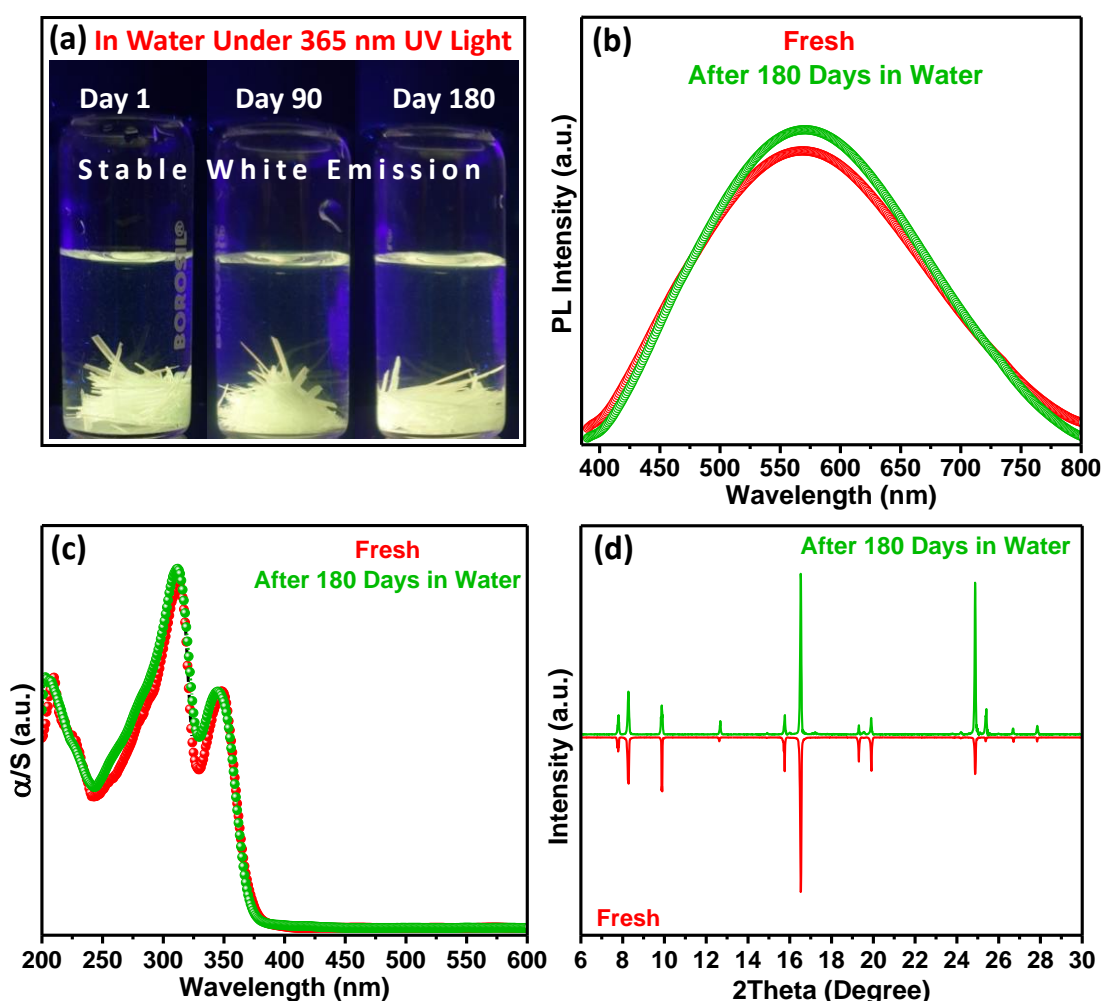


Figure 5.9: (a) Photographs of (4,4'-TMDP)Pb₂Br₆ crystals in water under 365 nm UV light on day 1, day 90 and day 180 of water treatment. Stable white light emission is observed throughout the months-long water treatment. Comparison of the (b) PL, (c) absorption spectra and (d) PXR D patterns of (4,4'-TMDP)Pb₂Br₆ before (red) and after (green) 180 days of water treatment. The PL, absorbance spectra and the PXR D patterns remain unchanged over this months-long water treatment. For the sake of presentation, the intensity of the PXR D pattern of the fresh sample has been inverted, showing that both the patterns are a mirror image of each other.

Stabilizing Lower Dimensional Lead Halide Perovskites by Intermolecular Cation- π Interactions

The PL spectra of a freshly prepared sample and that of the same sample after keeping it in water for six months (180 days) show no change (Figure 5.9b). Likewise, optical absorption (Figure 5.9c) and PXRD (Figure 5.9d) data show that there is no change in the phase of the (4,4'-TMDP)Pb₂Br₆ crystals upon water treatment over this long period of time. So the (4,4'-TMDP)Pb₂Br₆ is completely stable in water for over six months (limited by the duration of our study). To verify whether any Pb-salt got dissolved in water or not during the six months of water treatment, we separated the water from the crystals. No salt precipitation was observed after the complete evaporation of decanted water. This result suggests insignificant lead leaching into the water from (4,4'-TMDP)Pb₂Br₆.

We further confirmed the stability of the (4,4'-TMDP)Pb₂Br₆ crystals in other polar and non-polar solvents, as shown in Figure 5.10. Therefore, our material design approach, utilizing concerted cation- π interactions, allowed us to develop a hybrid lead halide perovskite system that is perfectly insoluble in water and other polar and non-polar solvents. Such water stability of hybrid perovskites is critical not only for their stable optical and optoelectronic applications but also for reducing the chances of Pb-toxicity in the groundwater.

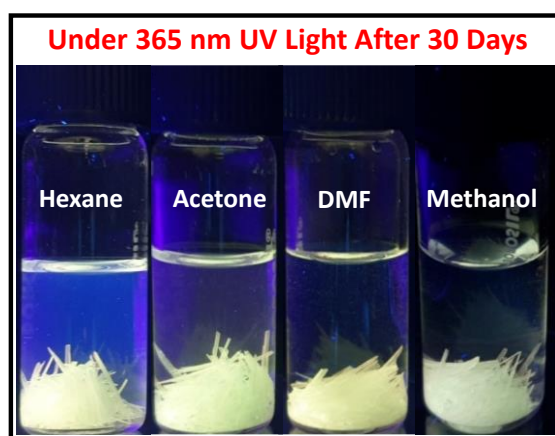


Figure 5.10: (a) Photographs of (4,4'-TMDP)Pb₂Br₆ crystals in different solvents under UV light on day 30 showing a stable white emission.

5.3.5 Application in white-LED

We apply the water-stable (4,4'-TMDP)Pb₂Br₆ perovskite for fabricating phosphor-converted white LED. A white-LED was fabricated by coating the (4,4'-TMDP)Pb₂Br₆ on a commercial UV-LED (360 to 380 nm), shown in the inset of Figure 5.11a. The LED was operated under a varying applied bias. The device starts emitting white light starting from 3.2 V applied bias. The intensity of emitting light increases rapidly with increasing applied bias to 3.6 V. The corresponding emission spectra are shown in Figure 5.11a. In addition to white light, a very

Stabilizing Lower Dimensional Lead Halide Perovskites by Intermolecular Cation- π Interactions

small emission contribution extends to the near-infrared (NIR) region. Figure 5.11b shows the emission spectra of the same white-LED at different intervals of time during its continuous operation of more than 24 hours. The integrated intensity of the emission spectra shown in Figure 5.11b is provided in Figure 5.11c. The emission intensity of the LED initially decreases slightly, probably due to a slight increase in the LED temperature. But the LED intensity then remains constant throughout the operation, indicating the thermal stability of the (4,4'-TMDP)Pb₂Br₆ under continuous operation. It is to be noted that the limited charge transport of such a hybrid 1D structure will be detrimental for the electroluminescence-based LEDs.

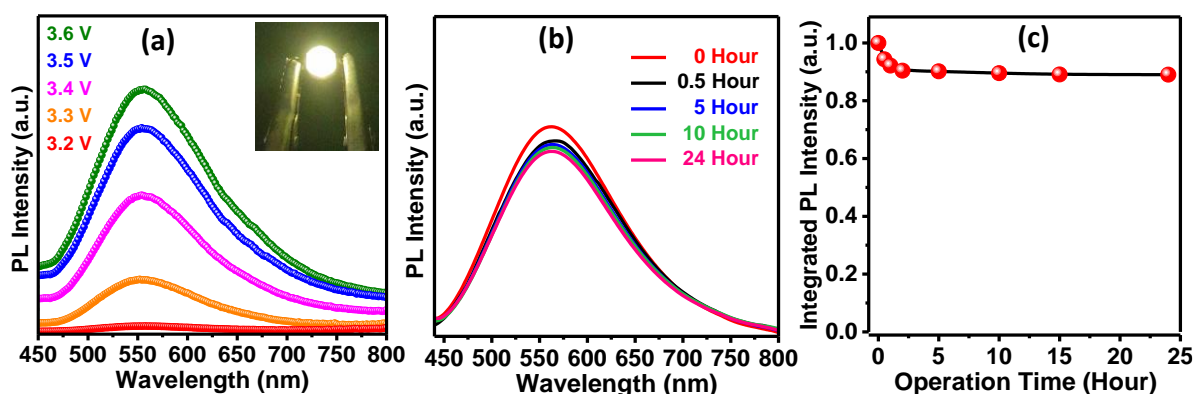


Figure 5.11: (a) Emission spectra of the white-LED, fabricated from (4,4'-TMDP)Pb₂Br₆, upon applying a variable bias ranging from 3.2 to 3.6 volts. The inset shows the photograph of the fabricated LED showing white light emission with 3.5 V applied bias. (b) Emission spectra of the same white-LED at different intervals of time during its continuous operation. The LED was kept switched on throughout the measurement. (c) The integrated emission intensity of the white-LED at different intervals of time during its operation. The red spheres are experimental data, and the solid black lines are just guide to the eye indicating the trend. The LED was operated under low voltage (3.2 V) to prevent any damage to the UV-LED itself.

5.3.6 Extending the cation- π interactions to other hybrid perovskite systems

So far, we have demonstrated the intermolecular cation- π interactions of A-site cation 4,4'-TMDP when incorporated in (4,4'-TMDP)Pb₂Br₆. Now we extend the cation- π interaction to another A-site cation, namely 4,4'-EDP, forming (4,4'-EDP)Pb₂Br₆ 1D perovskite. Figure 5.12 shows the crystal structure of (4,4'-EDP)Pb₂Br₆. The crystal structure of (4,4'-EDP)Pb₂Br₆ consists of edge shared Pb-Br octahedral dimers, separated by 4,4'-EDP cations, along the “bc” crystallographic plane. A 1D network of Pb-Br octahedral dimers is observed along “a” crystallographic direction. Refer to Table 5.3 for crystal structure data parameters. The 4,4'-EDP cations in (4,4'-EDP)Pb₂Br₆ show a long-range intermolecular cation- π stacking, similar to the previously discussed (4,4'-TMDP)Pb₂Br₆.

Stabilizing Lower Dimensional Lead Halide Perovskites by Intermolecular Cation– π Interactions

Table 5.3: Crystal structure and data refinement of (4,4'-EDP)Pb₂Br₆ at room temperature (RT)

(4,4'-EDP)Pb ₂ Br ₆	RT	
CCDC Number	2087691	
Chemical formula	C ₁₂ H ₁₄ Br ₆ N ₂ Pb ₂	
Formula weight	1080.09 g/mol	
Temperature	296(2) K	
Wavelength	0.71073 Å	
Crystal system	triclinic	
Space group	P-1	
Unit cell dimensions	a = 4.292(2) Å	$\alpha = 72.218(13)^\circ$
	b = 10.767(5) Å	$\beta = 80.322(13)^\circ$
	c = 11.919(6) Å	$\gamma = 89.025(14)^\circ$
Volume	516.7(4) Å ³	
Z	1	
Density (calculated)	3.472 g/cm ³	
Absorption coefficient	27.870 mm ⁻¹	
F(000)	474	
Theta range for data collection	1.82 to 28.50°	
Index ranges	-5<=h<=5, -14<=k<=12, -16<=l<=15	
Reflections collected	5980	
Independent reflections	2546 [R(int) = 0.0638]	
Coverage of independent reflections	97.20%	
Absorption correction	Multi-Scan	
Structure solution technique	direct methods	
Structure solution program	SHELXT 2014/5 (Sheldrick, 2014)	
Refinement method	Full-matrix least-squares on F ²	
Refinement program	SHELXL-2018/3 (Sheldrick, 2018)	
Function minimized	$\Sigma w(F_o^2 - F_c^2)^2$	
Data / restraints / parameters	2590 / 12 / 103	
Goodness-of-fit on F ²	1.251	
Δ/σ_{\max}	0.002	
Final R indices	1880 data; I>2 σ (I)	R ₁ = 0.0751, wR ₂ = 0.1961
	all data	R ₁ = 0.1042, wR ₂ = 0.2099
Weighting scheme	w=1/[$\sigma^2(F_o^2)+(0.1000P)^2$] where P=(F _o ² +2F _c ²)/3	
Largest diff. peak and hole	2.307 and -1.246 eÅ ⁻³	
R.M.S. deviation from mean	0.123 eÅ ⁻³	

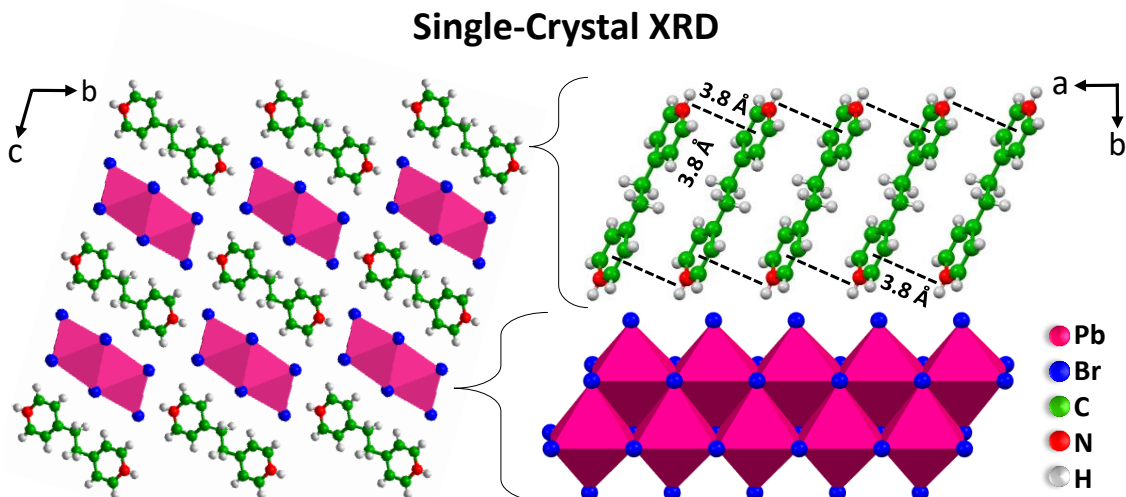


Figure 5.12: Crystal structure of (4,4'-EDP) Pb_2Br_6 obtained from single-crystal XRD data. The left panel depicts the crystal structure viewed along the “bc” crystallographic plane, showing edge shared Pb-Br octahedral dimers separated by 4,4'-EDP cations. The right panel depicts the cation- π stacking (shown by dashed black lines) between the 4,4'-EDP cations along the “a” crystallographic direction and the 1D network of Pb-Br octahedral dimers.

The (4,4'-EDP) Pb_2Br_6 show a broad PL emission at room temperature, as shown in Figure 5.13a, similar to the (4,4'-TMDP) Pb_2Br_6 . The corresponding CIE diagram, shown in the inset of Figure 5.13a, shows the chromaticity coordinates of (0.36, 0.39), with a CCT of 4643 K and a CRI value of 84, which correspond to the warm white light. The PLQY of this broad emission comes out to be 4%. Figure 5.13b shows the PL decay dynamics of the broad emission in (4,4'-EDP) Pb_2Br_6 . A bi-exponential decay with a millisecond long PL lifetime is observed.

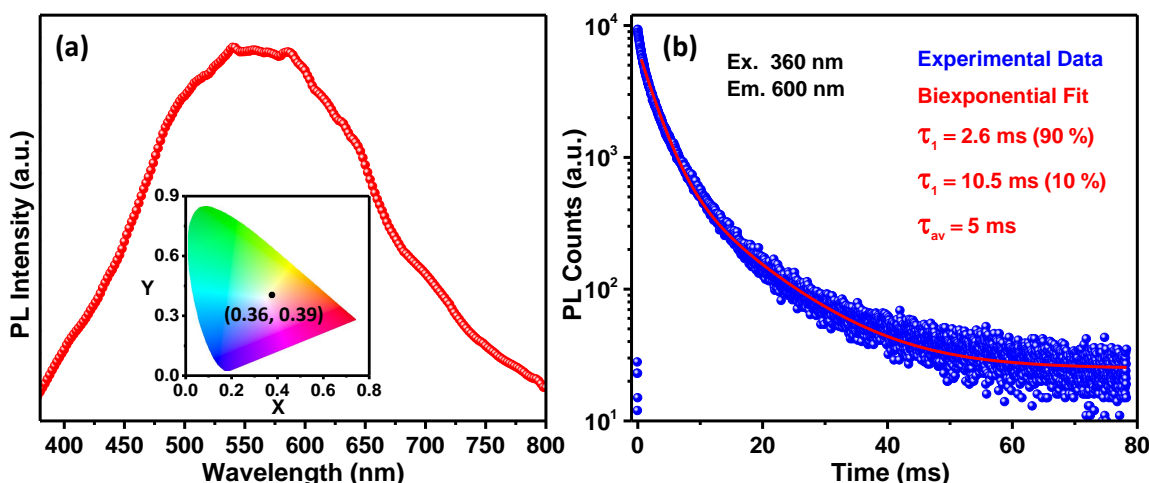


Figure 5.13: (a) PL spectrum of (4,4'-EDP) Pb_2Br_6 . Inset shows the CIE diagram depicting the white color of the light emission in (4,4'-EDP) Pb_2Br_6 . (b) PL decay dynamics of the (4,4'-EDP) Pb_2Br_6 for emission peak at 600 nm upon excitation with 360 nm light, showing a bi-exponential decay with millisecond long lifetime.

Stabilizing Lower Dimensional Lead Halide Perovskites by Intermolecular Cation- π Interactions

Importantly, (4,4'-EDP)Pb₂Br₆ crystals, when immersed in water, show a stable white emission over a period of six-month-long water treatment (inset of Figure 5.14a). The PL spectral profile also doesn't change during this month-long water treatment (Figure 5.14a), indicating the long-term water stability of (4,4'-EDP)Pb₂Br₆. The absorption spectra (Figure 5.14b) and the PXRD patterns (Figure 5.14c) of (4,4'-EDP)Pb₂Br₆ also remain unchanged during this months-long water treatment, confirming the phase stability of this 1D perovskite. Overall the optical properties and the intrinsic water stability of (4,4'-EDP)Pb₂Br₆ are similar to (4,4'-TMDP)Pb₂Br₆ as the A-site cations in the two systems differ just by a -CH₂- unit.

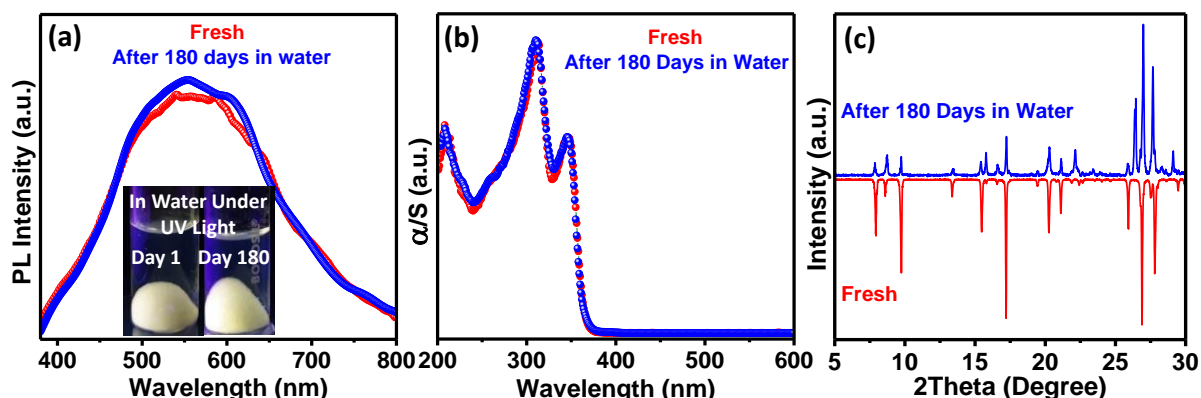


Figure 5.14: (a) PL spectra of freshly prepared (4,4'-EDP)Pb₂Br₆ and after keeping it in water for 180 days. Inset shows the photographs of (4,4'-TMDP)Pb₂Br₆ crystals in water under 365 nm UV light on day 1 and day 180 of water treatment. Comparison of the (b) absorption spectra and (c) PXRD patterns of (4,4'-EDP)Pb₂Br₆ before and after the 180 days of water treatment.

These results give us the hope that the introduced idea of cation- π interactions can possibly be extended to many other A-site cations. Unfortunately, the 3D perovskite structure of ABX₃ systems will not allow such concerted cation- π interaction. Therefore the intrinsic water stability of 3D perovskites is unlikely to be improved by the cation- π interactions. Importantly, for the low dimensional (0D, 1D, 2D) hybrid perovskites, a careful design of A-site cation might lead to the concerted long-range cation- π interactions. Such interactions might lead to intrinsic water stability to a large number of hybrid metal perovskites in the future.

5.4 Conclusion

We prepared (4,4'-TMDP)Pb₂Br₆ and (4,4'-EDP)Pb₂Br₆ 1D hybrid perovskites, which are insoluble in water, and other polar and non-polar solvents. Consequently, the structure and optical properties of these perovskites remain unchanged even after continuous water treatment for six months. Such intrinsic water stability of hybrid lead halide perovskites is unique, and it stems from our conceptually new approach of intermolecular cation- π interactions among the

Stabilizing Lower Dimensional Lead Halide Perovskites by Intermolecular Cation- π Interactions

A-site organic cations. Long-range concerted cation- π interactions between adjacent 4,4'-TMDP ions in single crystals of (4,4'-TMDP)Pb₂Br₆ have been established using SCXRD and NMR spectroscopy. Similar is the case with (4,4'-EDP)Pb₂Br₆ 1D perovskites. Both samples emit white light because of STE. LED prepared by coating (4,4'-TMDP)Pb₂Br₆ on a UV backlight emit warm white light suitable for lighting applications by applying a small bias just above 3.2 V. Overall, the introduction of cation- π interactions among the A-site cations combines the interesting optical and optoelectronic properties of hybrid halide perovskites with their extraordinary intrinsic water-stability, without requiring any encapsulation of the material or the device. We are hopeful that the idea can be extended to a large variety of 0D, 1D, and 2D hybrid perovskites in future.

5.5 References

1. Manser, J. S.; Kamat, P. V. Band Filling with Free Charge Carriers in Organometal Halide Perovskites. *Nat. Photon.* **2014**, *8*, 737-743
2. Swarnkar, A.; Chulliyil, R.; Ravi, V. K.; Irfanullah, M.; Chowdhury, A.; Nag, A. Colloidal CsPbBr₃ Perovskite Nanocrystals: Luminescence beyond Traditional Quantum Dots. *Angew. Chem. Int. Ed.* **2015**, *54*, 15424-15428.
3. Protesescu, L.; Yakunin, S.; Bodnarchuk, M. I.; Krieg, F.; Caputo, R.; Hendon, C. H.; Yang, R. X.; Walsh, A.; Kovalenko, M. V. Nanocrystals of Cesium Lead Halide Perovskites (CsPbX₃, X = Cl, Br, and I): Novel Optoelectronic Materials Showing Bright Emission with Wide Color Gamut. *Nano Lett.* **2015**, *15*, 3692-3696.
4. Zhumekenov, A. A.; Saidaminov, M. I.; Haque, M. A.; Alarousu, E.; Sarmah, S. P.; Murali, B.; Dursun, I.; Miao, X.-H.; Abdelhady, A. L.; Wu, T.; Mohammed, O. F.; Bakr, O. M. Formamidinium Lead Halide Perovskite Crystals with Unprecedented Long Carrier Dynamics and Diffusion Length. *ACS Energy Lett.* **2016**, *1*, 32-37.
5. Swarnkar, A.; Marshall, A. R.; Sanehira, E. M.; Chernomordik, B. D.; Moore, D. T.; Christians, J. A.; Chakrabarti, T.; Luther, J. M. Quantum Dot-Induced Phase Stabilization of α -CsPbI₃ Perovskite for High-Efficiency Photovoltaics. *Science* **2016**, *354*, 92-95.
6. Lian, Z.; Yan, Q.; Gao, T.; Ding, J.; Lv, Q.; Ning, C.; Li, Q.; Sun, J.-l. Perovskite CH₃NH₃PbI₃(Cl) Single Crystals: Rapid Solution Growth, Unparalleled Crystalline Quality, and Low Trap Density toward 108 cm⁻³. *J. Am. Chem. Soc.* **2016**, *138*, 9409-9412.
7. Das Adhikari, S.; Dutta, S. K.; Dutta, A.; Guria, A. K.; Pradhan, N. Chemically Tailoring the Dopant Emission in Manganese-Doped CsPbCl₃ Perovskite Nanocrystals. *Angew. Chem. Int. Ed.* **2017**, *56*, 8746-8750.

Stabilizing Lower Dimensional Lead Halide Perovskites by Intermolecular Cation- π Interactions

8. Pal, J.; Manna, S.; Mondal, A.; Das, S.; Adarsh, K. V.; Nag, A. Colloidal Synthesis and Photophysics of $M_3Sb_2I_9$ (M=Cs and Rb) Nanocrystals: Lead-Free Perovskites. *Angew. Chem. Int. Ed.* **2017**, *56*, 14187-14191.
9. Li, M.; Zhou, J.; Zhou, G.; Molokeev, M. S.; Zhao, J.; Morad, V.; Kovalenko, M. V.; Xia, Z. Hybrid Metal Halides with Multiple Photoluminescence Centers. *Angew. Chem. Int. Ed.* **2019**, *58*, 18670-18675.
10. Kundu, K.; Acharyya, P.; Maji, K.; Sasmal, R.; Agasti, S. S.; Biswas, K. Synthesis and Localized Photoluminescence Blinking of Lead-Free 2D Nanostructures of $Cs_3Bi_2I_6Cl_3$ Perovskite. *Angew. Chem. Int. Ed.* **2020**, *59*, 13093-13100.
11. Sheikh, T.; Nawale, V.; Pathoor, N.; Phadnis, C.; Chowdhury, A.; Nag, A. Molecular Intercalation and Electronic Two Dimensionality in Layered Hybrid Perovskites. *Angew. Chem. Int. Ed.* **2020**, *59*, 11653-11659.
12. Rong, Y.; Liu, L.; Mei, A.; Li, X.; Han, H. Beyond Efficiency: the Challenge of Stability in Mesoscopic Perovskite Solar Cells. *Adv. Energy Mater.* **2015**, *5*, 1501066.
13. Cao, D. H.; Stoumpos, C. C.; Farha, O. K.; Hupp, J. T.; Kanatzidis, M. G. 2D Homologous Perovskites as Light-Absorbing Materials for Solar Cell Applications. *J. Am. Chem. Soc.* **2015**, *137*, 7843-7850.
14. Berhe, T. A.; Su, W.-N.; Chen, C.-H.; Pan, C.-J.; Cheng, J.-H.; Chen, H.-M.; Tsai, M.-C.; Chen, L.-Y.; Dubale, A. A.; Hwang, B.-J. Organometal Halide Perovskite Solar Cells: Degradation and Stability. *Energy Environ. Sci.* **2016**, *9*, 323-356.
15. Manser, J. S.; Saidaminov, M. I.; Christians, J. A.; Bakr, O. M.; Kamat, P. V. Making and Breaking of Lead Halide Perovskites. *Acc. Chem. Res.* **2016**, *49*, 330-338.
16. Yang, J.; Kelly, T. L. Decomposition and Cell Failure Mechanisms in Lead Halide Perovskite Solar Cells. *Inorg. Chem.* **2017**, *56*, 92-101.
17. Ravi, V. K.; Saikia, S.; Yadav, S.; Nawale, V. V.; Nag, A. CsPbBr₃/ZnS Core/Shell Type Nanocrystals for Enhancing Luminescence Lifetime and Water Stability. *ACS Energy Lett.* **2020**, *5*, 1794-1796.
18. Babayigit, A.; Ethirajan, A.; Muller, M.; Conings, B. Toxicity of Organometal Halide Perovskite Solar Cells. *Nat. Mater.* **2016**, *15*, 247-251.
19. Babayigit, A.; Boyen, H.-G.; Conings, B. Environment Versus Sustainable Energy: The Case of Lead Halide Perovskite-based Solar Cells. *MRS Energy & Sustainability* **2018**, *5*, 15.
20. Ravi, V. K.; Mondal, B.; Nawale, V. V.; Nag, A. Don't Let the Lead Out: New Material Chemistry Approaches for Sustainable Lead Halide Perovskite Solar Cells. *ACS Omega* **2020**, *5*, 29631-29641.

-
21. Dedecker, K.; Grancini, G. Dealing with Lead in Hybrid Perovskite: A Challenge to Tackle for a Bright Future of This Technology? *Adv. Energy Mater.* **2020**, *10*, 2001471.
22. Li, J.; Cao, H.-L.; Jiao, W.-B.; Wang, Q.; Wei, M.; Cantone, I.; Lü, J.; Abate, A. Biological Impact of Lead from Halide Perovskites Reveals the Risk of Introducing a Safe Threshold. *Nat. Commun.* **2020**, *11*, 310.
23. Vidal, R.; Alberola-Borràs, J.-A.; Habisreutinger, S. N.; Gimeno-Molina, J.-L.; Moore, D. T.; Schloemer, T. H.; Mora-Seró, I.; Berry, J. J.; Luther, J. M. Assessing Health and Environmental Impacts of Solvents for Producing Perovskite Solar Cells. *Nat. Sustain.* **2021**, *4*, 277-285.
24. Pan, J.; Sarmah, S. P.; Murali, B.; Dursun, I.; Peng, W.; Parida, M. R.; Liu, J.; Sinatra, L.; Alyami, N.; Zhao, C.; Alarousu, E.; Ng, T. K.; Ooi, B. S.; Bakr, O. M.; Mohammed, O. F. Air-Stable Surface-Passivated Perovskite Quantum Dots for Ultra-Robust, Single- and Two-Photon-Induced Amplified Spontaneous Emission. *J. Phys. Chem. Lett.* **2015**, *6*, 5027-5033.
25. Palazon, F.; Akkerman, Q. A.; Prato, M.; Manna, L. X-ray Lithography on Perovskite Nanocrystals Films: From Patterning with Anion-Exchange Reactions to Enhanced Stability in Air and Water. *ACS Nano* **2016**, *10*, 1224-1230.
26. Huang, H.; Chen, B.; Wang, Z.; Hung, T. F.; Susha, A. S.; Zhong, H.; Rogach, A. L. Water Resistant CsPbX₃ Nanocrystals Coated with Polyhedral Oligomeric Silsesquioxane and their Use as Solid State Luminophores in All-Perovskite White Light-Emitting Devices. *Chem. Sci.* **2016**, *7*, 5699-5703.
27. Li, G.; Rivarola, F. W. R.; Davis, N. J. L. K.; Bai, S.; Jellicoe, T. C.; de la Peña, F.; Hou, S.; Ducati, C.; Gao, F.; Friend, R. H.; Greenham, N. C.; Tan, Z.-K. Highly Efficient Perovskite Nanocrystal Light-Emitting Diodes Enabled by a Universal Crosslinking Method. *Adv. Mater.* **2016**, *28*, 3528-3534.
28. Wang, S.; Bi, C.; Yuan, J.; Zhang, L.; Tian, J. Original Core-Shell Structure of Cubic CsPbBr₃@Amorphous CsPbBr_x Perovskite Quantum Dots with a High Blue Photoluminescence Quantum Yield of over 80%. *ACS Energy Lett.* **2018**, *3*, 245-251.
29. Ravi, V. K.; Scheidt, R. A.; Nag, A.; Kuno, M.; Kamat, P. V. To Exchange or Not to Exchange. Suppressing Anion Exchange in Cesium Lead Halide Perovskites with PbSO₄-Oleate Capping. *ACS Energy Lett.* **2018**, *3*, 1049-1055.
30. Wang, X.-D.; Huang, Y.-H.; Liao, J.-F.; Wei, Z.-F.; Li, W.-G.; Xu, Y.-F.; Chen, H.-Y.; Kuang, D.-B. Surface Passivated Halide Perovskite Single-Crystal for Efficient Photoelectrochemical Synthesis of Dimethoxydihydrofuran. *Nat. Commun.* **2021**, *12*, 1202.
31. Ma, J. C.; Dougherty, D. A. The Cation- π Interaction. *Chem. Rev.* **1997**, *97*, 1303-1324.

Stabilizing Lower Dimensional Lead Halide Perovskites by Intermolecular Cation- π Interactions

-
32. Dougherty, D. A. The Cation- π Interaction. *Acc. Chem. Res.* **2013**, *46*, 885-893.
33. Cabarcos, O. M.; Weinheimer, C. J.; Lisy, J. M. Competitive Solvation of K^+ by Benzene and Water: Cation- π Interactions and π -Hydrogen Bonds. *J. Chem. Phys.* **1998**, *108*, 5151-5154.
34. Cabarcos, O. M.; Weinheimer, C. J.; Lisy, J. M. Size Selectivity by Cation- π Interactions: Solvation of K^+ and Na^+ by Benzene and Water. *J. Chem. Phys.* **1999**, *110*, 8429-8435.
35. Eickhoff, T.; Grosse, P.; Theiss, W. Diffuse Reflectance Spectroscopy of Powders. *Vib. Spectrosc.* **1990**, *1*, 229-233.
36. <https://www.osram.us/cb/tools-and-resources/applications/led-colorcalculator/index.jsp>
37. Hunter, C. A.; Sanders, J. K. M. The Nature of π - π Interactions. *J. Am. Chem. Soc.* **1990**, *112*, 5525-5534.
38. Martinez, C. R.; Iverson, B. L. Rethinking the term “ π -Stacking”. *Chem. Sci.* **2012**, *3*, 2191-2201.
39. Mahadevi, A. S.; Sastry, G. N. Cation- π Interaction: Its Role and Relevance in Chemistry, Biology, and Material Science. *Chem. Rev.* **2013**, *113*, 2100-2138.
40. Sternberg, U.; Witter, R.; Kuprov, I.; Lamley, J. M.; Oss, A.; Lewandowski, J. R.; Samoson, A. 1H Line Width Dependence on MAS Speed in Solid State NMR-Comparison of Experiment and Simulation. *J. Magn. Reson.* **2018**, *291*, 32-39.
41. Pimputkar, S.; Speck, J. S.; DenBaars, S. P.; Nakamura, S. Prospects for LED Lighting. *Nat. Photon.* **2009**, *3*, 180-182.
42. Yuan, Z.; Zhou, C.; Tian, Y.; Shu, Y.; Messier, J.; Wang, J. C.; van de Burgt, L. J.; Kountouriotis, K.; Xin, Y.; Holt, E.; Schanze, K.; Clark, R.; Siegrist, T.; Ma, B. One-Dimensional Organic Lead Halide Perovskites with Efficient Bluish White-Light Emission. *Nat. Commun.* **2017**, *8*, 14051.
43. Zhou, G.; Su, B.; Huang, J.; Zhang, Q.; Xia, Z. Broad-Band Emission in Metal Halide Perovskites: Mechanism, Materials, and Applications. *Mater. Sci. Eng. R-Rep.* **2020**, *141*, 100548.
44. Li, Q.; Chen, Z.; Li, M.; Xu, B.; Han, J.; Luo, Z.; Tan, L.; Xia, Z.; Quan, Z. Pressure-Engineered Photoluminescence Tuning in Zero-Dimensional Lead Bromide Trimer Clusters. *Angew. Chem. Int. Ed.* **2021**, *60*, 2583-2587.
45. Smith, M. D.; Jaffe, A.; Dohner, E. R.; Lindenberg, A. M.; Karunadasa, H. I. Structural Origins of Broadband Emission from Layered Pb-Br Hybrid Perovskites. *Chem. Sci.* **2017**, *8*, 4497-4504.

Stabilizing Lower Dimensional Lead Halide Perovskites by Intermolecular Cation- π Interactions

46. Smith, M. D.; Karunadasa, H. I. White-Light Emission from Layered Halide Perovskites. *Acc. Chem. Res.* **2018**, *51*, 619-627.
47. Rao, M. J.; Shibata, T.; Chattopadhyay, S.; Nag, A. Origin of Photoluminescence and XAFS Study of $(\text{ZnS})_{1-x}(\text{AgInS}_2)_x$ Nanocrystals. *J. Phys. Chem. Lett.* **2014**, *5*, 167-173.

Appendix 1

Mn Doping in Centimeter Sized 2D Layered Butylammonium Lead Bromide, (BA)₂PbBr₄, Single Crystals

The work presented in this chapter is published in the journal of physical chemistry C with the following details:

Sheikh, T.; Nag, A. Mn Doping in Centimeter-Sized Layered 2D Butylammonium Lead Bromide (BA₂PbBr₄) Single Crystals and Their Optical Properties *J. Phys. Chem. C* **2019**, *123*, 9420-9427.

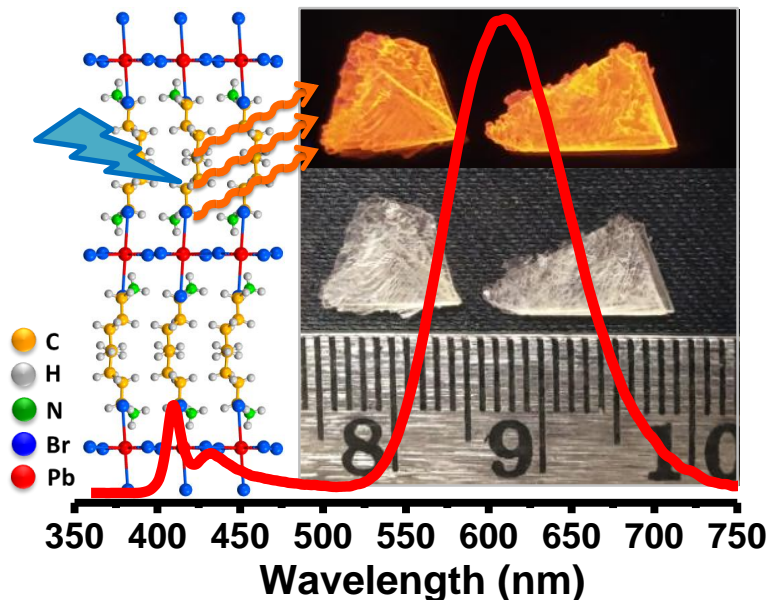
Copyright permission has been taken for the whole article from the American Chemical Society.

Mn Doping in Centimeter Sized 2D Layered Butylammonium Lead Bromide, (BA)₂PbBr₄, Single Crystals

Abstract

Layered lead halide perovskites such as butylammonium lead bromide [(BA)₂PbBr₄] possess a multiple quantum well structure, which is expected to enhance the interaction between the excitons and Mn dopants. Therefore, doping Mn in large single crystals of layered perovskites may induce interesting magneto-optic and magneto-electric properties, with minimal contributions from the detrimental grain boundary effects. Furthermore, these single crystals show stark differences in excitonic absorption and emission (dual emission) compared to the measurements done on the ensemble of corresponding micro-crystals. Therefore, exploring the exciton-Mn interactions by performing measurements on one large crystal is important. Here, we report the one-pot synthesis of centimeter-sized Mn-doped (BA)₂PbBr₄ single crystals to study the exciton-Mn interaction measured on a single crystal. Mn-doped (BA)₂PbBr₄ single crystal shows dual excitonic emission, and both the excitonic features transfer their energies non-radiatively to Mn dopants, yielding Mn d-d emission with quantum yield ~26%.

Graphical Abstract



Mn Doping in Centimeter Sized 2D Layered Butylammonium Lead Bromide, (BA)₂PbBr₄, Single Crystals

A1.1 Introduction

Intentional incorporation of impurity, termed as doping, has been a widely explored strategy for introducing new functionalities in semiconductors. For example, doping Mn in semiconductor nanocrystals introduces interesting optical and magneto-optic properties.¹⁻⁸ Subsequently, defect tolerant lead halide perovskite nanocrystals were doped with Mn to improve optical properties and thermodynamic stability of the host.⁹⁻¹⁸ CsPbX₃ (X = Cl, Br, I) perovskites nanocrystals with a 3D network of (PbX₆)⁴⁻ have been extensively studied as host materials. However, Mn-doping has remained less explored in layered lead halide perovskites with a 2D network of (PbX₄)²⁻.¹⁹⁻²⁰ In these prior reports, the optical properties were measured on films (ensemble) or dispersion (solution) of microcrystals of Mn-doped 2D layered lead halide perovskites.¹⁹⁻²⁰ In the present manuscript, we have synthesized centimeter-sized Mn-doped butylammonium lead bromide [(BA)₂PbBr₄] crystals to study the optical properties of one single crystal.

(BA)₂PbBr₄ forms a multiple quantum well structure, where the 2D semiconducting inorganic Pb-Br layers are separated by the insulating organic layers.²¹⁻²⁶ This quantum well structure results in the confinement of charge carriers in the atomically thin 2D Pb-Br individual layers, in spite of the centimeter scale large size of the crystal.²⁷ Because of this quantum confinement, the exciton (or charge carriers) in the host interacts more strongly with the dopant in Mn-doped (BA)₂PbBr₄.¹⁹ This enhanced interaction is expected to give rise to interesting magneto-optic and magneto-transport properties since Mn²⁺ ions also have magnetic moments with five unpaired electrons.²⁸⁻³⁰ Typically, the quantum confinement of charge carriers is achieved by reducing the crystallite size of semiconductor nanocrystals (quantum dots).²⁸⁻³⁰ In such small nanocrystals, the detrimental surface defects or grain boundaries often trap the charge carriers. In this regard, the big single crystals of Mn-doped (BA)₂PbBr₄ have a unique advantage, where stronger quantum confinement is achieved because of the layered structure, and there will be no grain boundary effect for the charge transport along the layers.³¹⁻³⁵

Fundamental optical properties such as absorption and emission of light by a single crystal of layered perovskite, like (BA)₂PbBr₄, differ from that of an ensemble of micro and nano crystals. For example, a single crystal of layered perovskite shows dual band gap with two excitonic emissions, which often gets blurred in an ensemble measurement.³⁶ Therefore, making a centimeter-scale large single crystal of Mn-doped (BA)₂PbBr₄ allows us to study how the different excitonic states of the host interact with Mn dopant.

Mn Doping in Centimeter Sized 2D Layered Butylammonium Lead Bromide, (BA)₂PbBr₄, Single Crystals

Here, we report Mn-doping in centimeter-sized 2D layered (BA)₂PbBr₄ single crystals by a one-pot solution process synthesis. The as-synthesized (BA)₂PbBr₄ single crystals show an intense down-converted Mn d-d emission at room temperature. Photoluminescence (PL) lifetime data suggest that both the excitonic states of the dual bandgap semiconductor host transfer their energies to Mn, giving rise to the Mn emission. The Mn emission in a (BA)₂PbBr₄ single crystal shows unusual excitation dependence. Intense Mn emission is observed when excited with light having energy nearly equal to the lowest energy excitonic gap, but the intensity drops sharply with a slight increase in excitation energy above the excitonic gap.

A1.2 Experimental Section

A1.2.1 Synthesis of C₄H₉NH₃Br

C₄H₉NH₃Br was prepared by neutralizing 924 μ L of n-C₄H₉NH₂ with 5 mL (44 mmol) 48% w/w HBr in an ice bath, resulting in a transparent solution.

A1.2.2 Synthesis of (BA)₂PbBr₄ single crystals

(BA)₂PbBr₄ single crystals were synthesized by modifying the acid precipitation method reported for the synthesis of (BA)₂PbI₄.³⁷ 1116 mg (5 mmol) of lead oxide was dissolved in 5 mL (44 mmol) of 48% w/w aqueous HBr by heating to 80 °C under constant magnetic stirring, resulting in a clear transparent solution. To this solution, a freshly prepared C₄H₉NH₃Br solution was added. The resultant solution was heated at 100 °C for about 5 to 10 minutes. The stirring was stopped, and the solution was allowed to cool to room temperature, during which crystals of (BA)₂PbBr₄ precipitated out. Finally, the crystals were filtered and washed with acetone several times.

A1.2.3 Synthesis of Mn-doped (BA)₂PbBr₄ single crystals

We developed the synthesis of Mn-doped (BA)₂PbBr₄ single crystals by modifying the above-mentioned acid precipitation method used for the synthesis of undoped samples. 1116 mg (5 mmol) of lead oxide and manganese bromide (5 mmol, 10 mmol, 20 mmol, 40 mmol or 50 mmol) were dissolved in 5 mL (44 mmol) of 48% w/w aqueous HBr by heating it to 80 °C under constant magnetic stirring, resulting in clear transparent solutions. To these solutions, the freshly prepared C₄H₉NH₃Br solution was added. The resultant solutions were heated at 100 °C for about 5 to 10 minutes. The rest of the steps were the same as that of the undoped (BA)₂PbBr₄ single crystal synthesis.

A1.2.4 Characterization

Single crystal X-ray diffraction (XRD) data were obtained using a Bruker Smart Apex Duo diffractometer at room temperature (298 K) using Mo K α radiation ($\lambda = 0.71073 \text{ \AA}$). Integration of the frames was done in the Bruker SAINT software package by a narrow-frame algorithm. The structure was solved by a direct method and refined by full-matrix least-squares on F^2 using the SHELXTL software package. The PbBr₄ framework was refined anisotropically without any constraint, whereas the organic atoms were refined isotropically with constraints on the C-C and C-N bond lengths. Powder XRD measurements were carried on Bruker D8 Advance X-ray diffractometer using Cu K α radiation (1.54 \AA). Scanning electron microscopy (SEM) measurements were performed using the Zeiss Ultra Plus FESEM instrument. X-band electron paramagnetic resonance (EPR) measurements were carried out using the JEOL JES-FA200 ESR spectrometer. Inductively coupled plasma optical emission spectroscopy (ICP-OES) measurements were carried on ARCOS M/s. Spectro, Germany. Atomic force microscopy (AFM) images were recorded by using the Keysight atomic force microscope (model: AFM 5500) by using the tapping mode technique.

The spectra presented here are collected from one single crystal. Optical diffuse-reflectance measurements were performed on Shimadzu UV-3600 plus UV-Vis-NIR spectrophotometer at room temperature. The corresponding absorbance spectra were obtained from the reflectance data using Kubelka-Munk transformation.³⁸ The absorbance spectra in transmittance mode were recorded on Cary Series UV-Vis Spectrophotometer. Steady-state and time-resolved PL measurements were carried on FLS 980 (Edinburgh Instruments). Excitonic PL decays were recorded using a 405 nm picosecond pulsed laser source, whereas Mn emission decays were recorded using a microsecond flash lamp as the excitation source. Absolute PL quantum yields (QY) were measured from the films by using Quanta Phi connected with Horiba Jobin Yvon Fluoromax-4 spectrofluorometer. Single crystals were ground into powders to make films for the measurements of PL QY.

A1.3 Results and Discussion

We have synthesized centimeter-sized layered 2D Mn-doped (BA)₂PbBr₄ single crystals by slow cooling of the aqueous hydrobromic acid solution of lead oxide, manganese bromide, and butylammonium bromide. Optical images of the as-synthesized single crystals are shown in Figure A1.1a under UV and visible light. Bright orange emission can be seen under UV light,

Mn Doping in Centimeter Sized 2D Layered Butylammonium Lead Bromide, $(BA)_2PbBr_4$, Single Crystals

corresponding to Mn d-d emission. The lateral dimension of the single crystal flakes is close to a centimeter, with thickness approaching a millimeter. SEM image in Figure A1.1b shows the layered architecture of Mn-doped $(BA)_2PbBr_4$ crystals. The presence of Mn in these single crystals was confirmed by ICP-OES. For Mn/Pb precursor ratio of 1:1, 2:1, 4:1, 8:1, and 10:1, ICP-OES shows 0.03, 0.06, 0.22, 0.38 and 1.08% Mn (compared to Pb) respectively in the product. Clearly, Mn-doping is not favored in the $(BA)_2PbBr_4$ single crystals in our reaction conditions, and only very small fractions of the Mn precursor are found in the final isolated product. Similar difficulty in doping was also reported by Dutta et al.²⁰ Hereafter, in this manuscript, we mention the dopant concentration as % of Mn compared to Pb obtained by ICP-OES measurements in the product crystals.

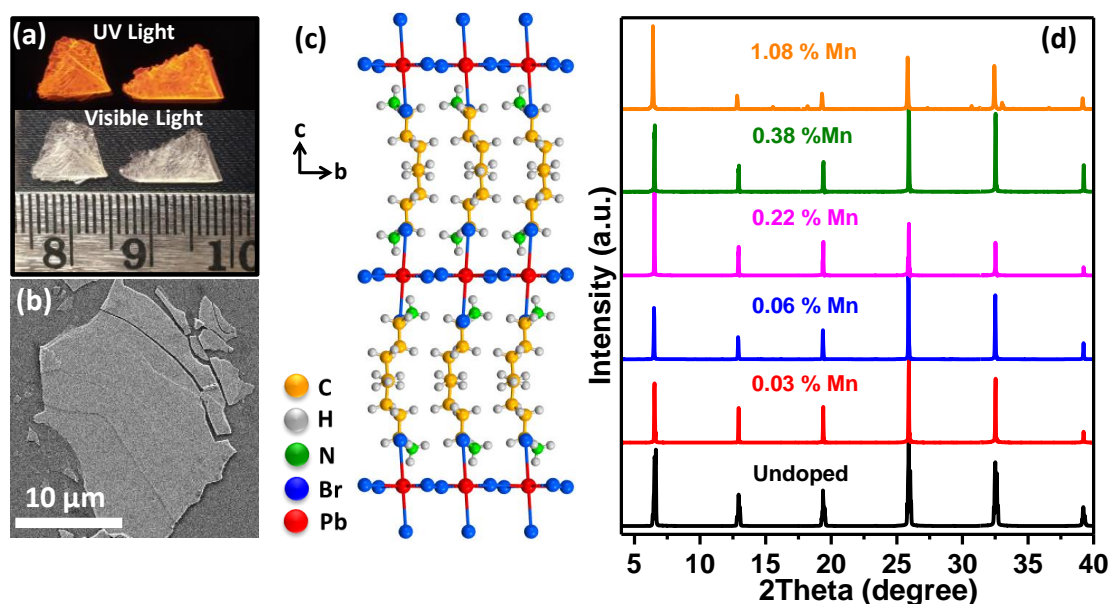


Figure A1.1: (a) Optical images of 1.08% Mn-doped $(BA)_2PbBr_4$ single crystals under UV and visible light. (b) SEM image of 1.08% Mn-doped $(BA)_2PbBr_4$ single crystal showing a layered architecture. (c) Crystal structure of 1.08% Mn-doped $(BA)_2PbBr_4$ obtained by solving single crystal XRD data, recorded at room temperature (298 K). (d) Powder XRD patterns of Mn-doped $(BA)_2PbBr_4$ single crystals having varying Mn concentrations. The peaks observed in the layered 2D materials correspond to the interlayer spacing, which does not change with a small amount of Mn incorporation.

Crystal structures of both undoped and Mn-doped $(BA)_2PbBr_4$ are determined by single crystal XRD at room temperature. Figure A1.1c shows the crystal structure of 1.08% Mn-doped $(BA)_2PbBr_4$ which crystallizes in the orthorhombic phase with space group $Pbca$ having lattice parameters $a = 8.308(7)$ Å, $b = 8.182(7)$ Å, $c = 27.62(2)$ Å, and $\alpha = \beta = \gamma = 90^\circ$. Similar results are obtained for undoped $(BA)_2PbBr_4$, which also crystallizes in orthorhombic phase

Appendix 1

Mn Doping in Centimeter Sized 2D Layered Butylammonium Lead Bromide, (BA)₂PbBr₄, Single Crystals

with space group $Pbca$ and lattice parameters $a = 8.322(8) \text{ \AA}$, $b = 8.184(9) \text{ \AA}$, $c = 27.66(3) \text{ \AA}$ and $\alpha = \beta = \gamma = 90^\circ$. The similarity in the crystal structure of undoped and Mn-doped (BA)₂PbBr₄ is shown in Table A1.1. A comparison of powder XRD patterns of Mn-doped (BA)₂PbBr₄ single crystals with that of the undoped sample is shown in Figure A1.2c. All the powder XRD patterns show a regular peak pattern, which is characteristic of layered materials.³⁶⁻³⁷ This similarity is expected as the powder XRD peaks observed in 2D layered single crystals correspond to their interlayer spacing that will not change with the small amount of Mn doping.

Now to understand the local coordination around Mn in (BA)₂PbBr₄ single crystals, we measured EPR. Figure A1.2 shows the room temperature X-band EPR spectra of Mn-doped (BA)₂PbBr₄ single crystals at varying Mn concentrations. The EPR spectra showing sharp six-fold hyperfine splitting pattern confirms the presence of isolated Mn²⁺ ions.^{10, 12, 39} The hyperfine splitting energy is around 9.6 mT (96 Gauss), which indicates the presence of Mn²⁺ ions in the octahedral coordination environment.²⁰ Therefore, the Mn²⁺ ions indeed replace the Pb²⁺ ions in the lattice of (BA)₂PbBr₄ single crystals. The 1.08% Mn-doped sample doesn't show hyperfine splitting due to the Mn-Mn interactions at higher Mn-concentration. The lattice incorporation of Mn²⁺ ions does not significantly change the XRD data discussed above, probably because of the small number of dopants.

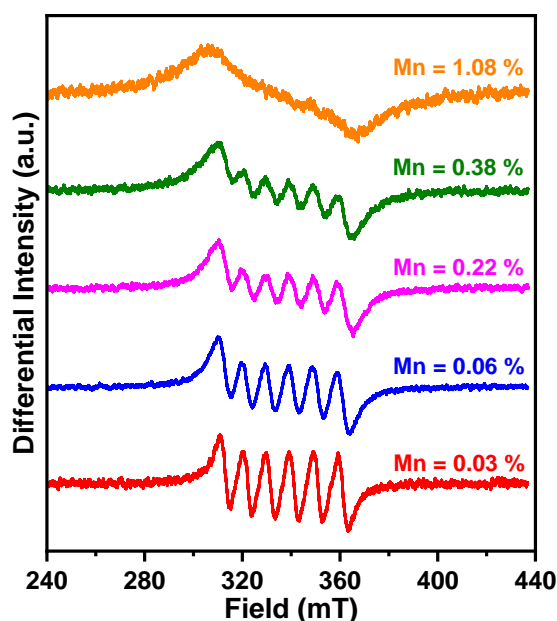


Figure A1.2: X-band EPR spectra of Mn-doped (BA)₂PbBr₄ single crystals of varying Mn concentrations.

Appendix 1

Mn Doping in Centimeter Sized 2D Layered Butylammonium Lead Bromide, (BA)₂PbBr₄, Single Crystals

Table A1.1: Crystal data and structure refinement of undoped and 1.08% Mn-doped (BA)₂PbBr₄.

	Undoped	1.08 % Mn-doped
Chemical formula	C ₈ H ₂₄ Br ₄ N ₂ Pb	C ₈ H ₂₄ Br ₄ N ₂ Pb
Formula weight	675.12 g/mol	675.12 g/mol
Temperature	298(2) K	298(2) K
Wavelength	0.71073 Å	0.71073 Å
Crystal system	Orthorhombic	Orthorhombic
Space group	<i>Pbca</i>	<i>Pbca</i>
Unit cell dimensions	a = 8.322(8) Å b = 8.184(9) Å c = 27.66(3) Å α = β = γ = 90°	a = 8.308(7) Å b = 8.182(7) Å c = 27.62(2) Å α = β = γ = 90°
Volume	1884.(4) Å ³	1877.(3) Å ³
Z	4	4
Density (calculated)	2.253 g/cm ³	2.246 g/cm ³
Absorption coefficient	17.417 mm ⁻¹	17.482 mm ⁻¹
F(000)	1136	1184
Theta range for data collection	1.47 to 28.57°	1.48 to 28.68°
Index ranges	-11 ≤ h ≤ 10, -11 ≤ k ≤ 10, -36 ≤ l ≤ 36	-11 ≤ h ≤ 12, -11 ≤ k ≤ 11, -36 ≤ l ≤ 36
Reflections collected	24655	25294
Independent reflections	2375 [R(int) = 0.1025]	2371 [R(int) = 0.2615]
Coverage of independent reflection	99.00%	98.10%
Absorption correction	Multi-Scan	Multi-Scan
Structure solution technique	Direct methods	Direct methods
Structure solution program	SHELXT 2014/5 (Sheldrick, 2014)	SHELXT 2014/5 (Sheldrick, 2014)
Refinement method	Full-matrix least-squares on F ²	Full-matrix least-squares on F ²
Refinement program	SHELXL-2016/6 (Sheldrick, 2016)	SHELXL-2016/6 (Sheldrick, 2016)
Function minimized	Σ w(F _o ² - F _c ²) ²	Σ w(F _o ² - F _c ²) ²
Data / restraints / parameters	2375 / 9 / 72	2371 / 10 / 72
Goodness-of-fit on F ²	2.029	1.865
Δ/σ _{max}	0.359	0.437
Final R indices; I>2σ(I)	R1 = 0.0975, wR2 = 0.3054	R1 = 0.1199, wR2 = 0.3173
all data	R1 = 0.1368, wR2 = 0.3191 w=1/[σ ² (F _o ²)+ (0.1000P) ²] where P=(F _o ² +2F _c ²)/3	R1 = 0.1578, wR2 = 0.3361 w=1/[σ ² (F _o ²)+ (0.1000P) ²] where P=(F _o ² +2F _c ²)/3
Weighting scheme		
Largest diff. peak and hole	2.787 and -2.830 eÅ ⁻³	2.924 and -3.347 eÅ ⁻³
R.M.S. deviation from mean	0.399 eÅ ⁻³	0.588 eÅ ⁻³

Mn Doping in Centimeter Sized 2D Layered Butylammonium Lead Bromide, (BA)₂PbBr₄, Single Crystals

After characterizing the samples, we now discuss the PL spectra obtained from single crystals of Mn-doped (BA)₂PbBr₄. PL spectra of undoped and 0.38% Mn-doped (BA)₂PbBr₄ single crystals are compared in Figure A1.3a. The undoped samples show two sharp peaks at 410 nm and 436 nm, similar to the prior report.³⁶ The 0.38% Mn-doped (BA)₂PbBr₄ single crystal shows a new strong emission centered at 606 nm, along with the suppressed excitonic emissions. This strong emission at 606 nm in Mn-doped (BA)₂PbBr₄ single crystal arises from Mn d-d de-excitation through the spin-forbidden ⁴T₁ → ⁶A₁ transition.⁴⁰ The absorbance spectra of Mn-doped (BA)₂PbBr₄ single crystal show no absorption corresponding to this 606 nm emission (Figure A1.3b). Only absorption corresponding to excitonic emission is observed. This suggests that the 606 nm emission arises through the host absorption only, which is further confirmed by the PL excitation (PLE) spectrum shown in Figure A1.3b. There is no intensity in the PLE spectrum for 606 nm emission below the host bandgap.

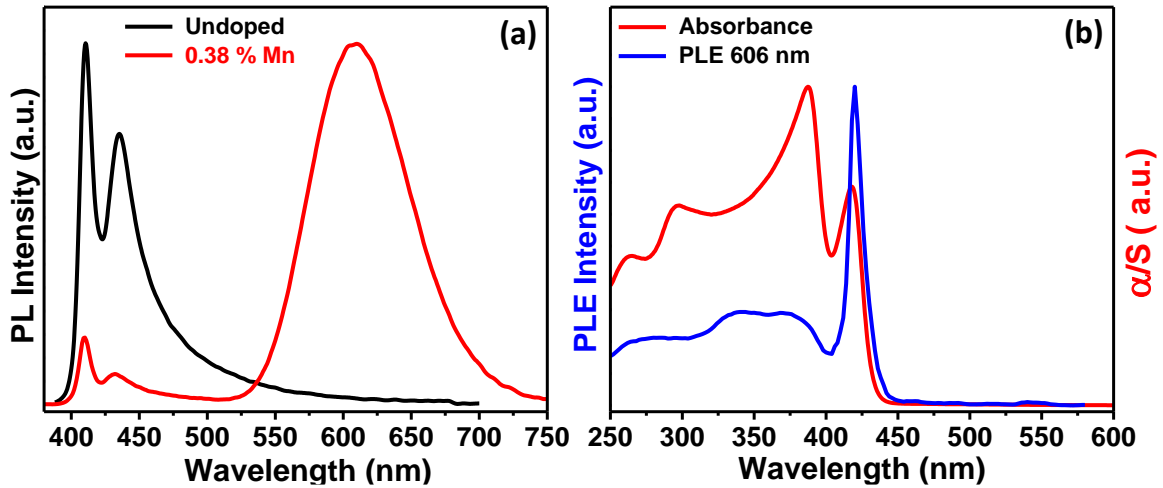


Figure A1.3: (a) Normalized PL spectra of undoped and 0.38% Mn-doped (BA)₂PbBr₄ single crystals. (b) UV-visible absorbance spectrum (red) obtained from diffuse reflectance measurements converted using the Kubelka–Munk function ($\alpha/S = (1 - R)^2/2R$) and PL excitation (606 nm emission) spectrum (blue) of 0.38% Mn-doped (BA)₂PbBr₄ single crystal.

The 606 nm Mn d-d emission in Mn-doped (BA)₂PbBr₄ single crystal shows a long lifetime of the order of hundreds of microseconds, as shown in Figure A1.4. This long lifetime arises because of the spin-forbidden nature of the Mn d-d (⁴T₁ → ⁶A₁) transition. The PL, PLE, and absorbance spectra together confirm that there is an energy transfer process from (BA)₂PbBr₄ host to Mn dopants leading to the 606 nm emission. Also, upon Mn doping, both the excitonic emissions got suppressed, indicating exciton to dopant energy transfer for both the excitonic emissions of the host.

Mn Doping in Centimeter Sized 2D Layered Butylammonium Lead Bromide, (BA)₂PbBr₄, Single Crystals

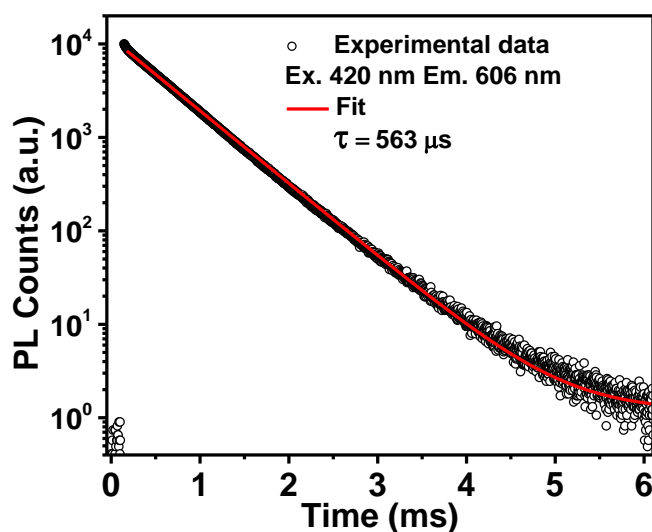


Figure A1.4: PL decay profile for Mn emission from 0.38% Mn-doped (BA)₂PbBr₄ single crystal.

The Mn emission increases sharply with the increase in dopant concentration in (BA)₂PbBr₄ single crystals, as shown in Figure A1.4a. A similar trend has been previously observed for (BA)₂PbBr₄ powders¹⁹ and also for other hosts as well,^{12, 41-42} which is because of the increase in the emitting Mn dopant centers. In contrast, the excitonic emissions show a reverse trend, i.e., the intensity of the excitonic emission decreases with an increase in the dopant concentration (Figure A1.5a). This decrease in excitonic emission is rather expected since a part of the excitons transfer their energy to Mn²⁺ non-radiatively and is in good agreement with many previous reports of Mn-doped in Pb-halide perovskite hosts.^{12, 19, 43-46} However, there is another set of reports which shows that the intensity of the excitonic emission increases with the increase in dopant concentration in perovskite NCs.^{10, 47-49} This increase in the intensity of excitonic emission with doping has been attributed to both the defect passivation on the surface of nanocrystals by the dopant precursors, and/or improving the structural parameters of the host by the incorporation of Mn in the lattice.^{17, 39, 47-48} Distinguishing out surface effect vs. lattice effect is difficult in nanocrystals owing to their large surface to volume ratio. But our large single crystals are nearly defect-free systems with minimal contribution from the surface. Hence, these single crystals are ideal systems to study the effect of Mn doping on the intensity of the excitonic emissions. Our study of Mn doping in (BA)₂PbBr₄ single crystals clearly shows that the intensity of excitonic emissions systematically decreases with an increase in Mn concentration. This trend unambiguously shows that in the absence of the role of surface defects, the exciton-Mn interaction reduces the intensity of the excitonic emission.

Mn Doping in Centimeter Sized 2D Layered Butylammonium Lead Bromide, (BA)₂PbBr₄, Single Crystals

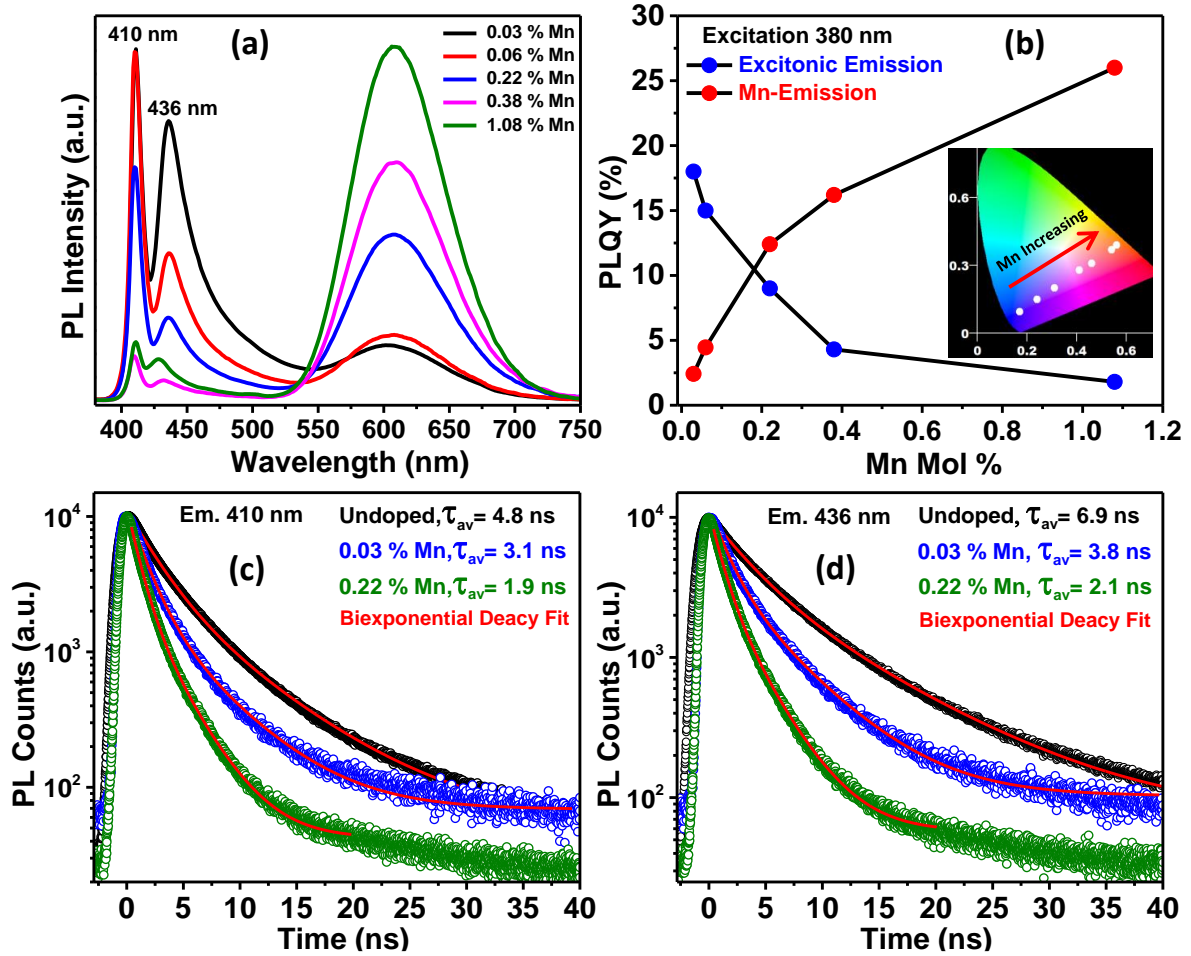


Figure A1.5: (a) PL spectra of Mn-doped (BA)₂PbBr₄ single crystals with varying Mn concentrations. (b) PL QY of excitonic (combining both excitonic peaks) and Mn emission in powdered (BA)₂PbBr₄ with increasing Mn concentrations. The inset represents the CIE diagram showing the color of the emission light with varying Mn concentrations upon 340 nm excitation. PL decay dynamics of (c) 410 nm and (d) 436 nm excitonic emissions in (BA)₂PbBr₄ single crystals with varying Mn concentrations.

Figure A1.5b shows the PL QY of Mn emission and excitonic emissions at different Mn concentrations. Due to instrumental limitations, we could not measure the PL QY of the single crystals. Instead, the measurements were done on ground powdered samples after drop-casting into films. Expectedly, the PL QY of Mn emission in these powdered Mn-doped (BA)₂PbBr₄ increases with an increase in Mn concentration and reaches a value of 26% for 1.08% Mn concentration, whereas the PL QY of the excitonic emission decreases systematically with the increasing Mn-concentrations. The colour of the emission changes systematically from blue to deep orange with the increase in Mn concentration, as shown in the inset of Figure A1.5b. This change in chromaticity of the overall light emission is because of the systematic change in the intensity ratio of excitonic emission and Mn emission. The average lifetimes of PL decay of

Mn Doping in Centimeter Sized 2D Layered Butylammonium Lead Bromide, (BA)₂PbBr₄, Single Crystals

both the excitonic emissions decrease with the increase in Mn concentration, as shown in Figures A1.5c and d. This systematic decrease in PL decay lifetime is because of the additional faster nonradiative transfer of excitonic energy of the host to the dopant states. Interestingly, both the excitonic peaks show a similar decrease in lifetimes, suggesting the interaction of Mn with both excitonic states. Note that such information of nature of both excitonic states of Mn-doped (BA)₂PbBr₄ is obtained only when the measurements are done on a centimeter scale single crystal, and the information gets blurred when the PL measurements are carried out on an ensemble of micro or nano crystals.

A1.4 Conclusion

Flakes of Mn-doped (BA)₂PbBr₄ single crystals with lateral dimensions about a centimeter and thickness close to a millimeter are synthesized. The presence of Mn in the host lattice of (BA)₂PbBr₄ is confirmed by PL, EPR, and ICP-OES measurements. The incorporation of Mn has no noticeable effect on the crystal structure of layered (BA)₂PbBr₄ perovskite. The formation of centimeter-sized crystals allowed us to study the optical properties of a single crystal, unlike prior reports where optical properties of Mn-doped perovskites are recorded on ensembles, either in the form of films or dispersion micro and nano crystals. The single crystals exhibit two excitonic peaks, and both the excitons transfer energy to Mn dopants leading to a strong (PL QY ~26%) Mn emission centered at 606 nm. The Mn emission shows a long lifetime of the order of hundreds of microseconds due to the spin-forbidden nature of the Mn d-d (⁴T₁ → ⁶A₁) transition. The chromaticity of the overall emitted light changes systematically by varying the ratio of excitonic emission (blue) and Mn emission (orange-red) for varying concentrations of Mn dopants. This reported synthesis of centimeter-sized Mn-doped (BA)₂PbBr₄ single crystals with strong exciton-Mn interactions is expected to yield interesting magneto-optic and magneto-transport properties in the future.

A1.5 References

1. Norris, D. J.; Yao, N.; Charnock, F. T.; Kennedy, T. A. High-Quality Manganese-Doped ZnSe Nanocrystals. *Nano Lett.* **2001**, *1*, 3-7.
2. Pradhan, N.; Goorskey, D.; Thessing, J.; Peng, X. An Alternative of CdSe Nanocrystal Emitters: Pure and Tunable Impurity Emissions in ZnSe Nanocrystals. *J. Am. Chem. Soc.* **2005**, *127*, 17586-17587.

Mn Doping in Centimeter Sized 2D Layered Butylammonium Lead Bromide, (BA)₂PbBr₄, Single Crystals

3. Beaulac, R.; Archer, P. I.; Ochsenein, S. T.; Gamelin, D. R. Mn²⁺-Doped CdSe Quantum Dots: New Inorganic Materials for Spin-Electronics and Spin-Photonics. *Adv. Funct. Mater.* **2008**, *18*, 3873-3891.
4. Pradhan, N.; Sarma, D. D. Advances in Light-Emitting Doped Semiconductor Nanocrystals. *J. Phys. Chem. Lett.* **2011**, *2*, 2818-2826.
5. Santra, P. K.; Kamat, P. V. Mn-Doped Quantum Dot Sensitized Solar Cells: A Strategy to Boost Efficiency over 5%. *J. Am. Chem. Soc.* **2012**, *134* (5), 2508-2511.
6. Hazarika, A.; Layek, A.; De, S.; Nag, A.; Debnath, S.; Mahadevan, P.; Chowdhury, A.; Sarma, D. D. Ultranarrow and Widely Tunable Mn²⁺-Induced Photoluminescence from Single Mn-Doped Nanocrystals of ZnS-CdS Alloys. *Phys. Rev. Lett.* **2013**, *110*, 267401.
7. Debnath, T.; Maity, P.; Maiti, S.; Ghosh, H. N. Electron Trap to Electron Storage Center in Specially Aligned Mn-Doped CdSe d-Dot: A Step Forward in the Design of Higher Efficient Quantum-Dot Solar Cell. *J. Phys. Chem. Lett.* **2014**, *5*, 2836-2842.
8. Wang, J.; Li, Y.; Shen, Q.; Izuishi, T.; Pan, Z.; Zhao, K.; Zhong, X. Mn Doped Quantum Dot Sensitized Solar Cells with Power Conversion Efficiency Exceeding 9%. *J. Mater. Chem. A* **2016**, *4*, 877-886.
9. Liu, W.; Lin, Q.; Li, H.; Wu, K.; Robel, I.; Pietryga, J. M.; Klimov, V. I. Mn²⁺-Doped Lead Halide Perovskite Nanocrystals with Dual-Color Emission Controlled by Halide Content. *J. Am. Chem. Soc.* **2016**, *138*, 14954-14961.
10. Parobek, D.; Roman, B. J.; Dong, Y.; Jin, H.; Lee, E.; Sheldon, M.; Son, D. H. Exciton-to-Dopant Energy Transfer in Mn-Doped Cesium Lead Halide Perovskite Nanocrystals. *Nano Lett.* **2016**, *16*, 7376-7380.
11. Akkerman, Q. A.; Meggiolaro, D.; Dang, Z.; De Angelis, F.; Manna, L. Fluorescent Alloy CsPb_xMn_{1-x}I₃ Perovskite Nanocrystals with High Structural and Optical Stability. *ACS Energy Lett.* **2017**, *2*, 2183-2186.
12. Mir, W. J.; Jagadeeswararao, M.; Das, S.; Nag, A. Colloidal Mn-Doped Cesium Lead Halide Perovskite Nanoplatelets. *ACS Energy Lett.* **2017**, *2*, 537-543.
13. Zou, S.; Liu, Y.; Li, J.; Liu, C.; Feng, R.; Jiang, F.; Li, Y.; Song, J.; Zeng, H.; Hong, M.; Chen, X. Stabilizing Cesium Lead Halide Perovskite Lattice through Mn(II) Substitution for Air-Stable Light-Emitting Diodes. *J. Am. Chem. Soc.* **2017**, *139*, 11443-11450.
14. Parobek, D.; Dong, Y.; Qiao, T.; Son, D. H. Direct Hot-Injection Synthesis of Mn-Doped CsPbBr₃ Nanocrystals. *Chem. Mater.* **2018**, *30*, 2939-2944.

Mn Doping in Centimeter Sized 2D Layered Butylammonium Lead Bromide, (BA)₂PbBr₄, Single Crystals

15. Swarnkar, A.; Mir, W. J.; Nag, A. Can B-Site Doping or Alloying Improve Thermal- and Phase-Stability of All-Inorganic CsPbX₃ (X = Cl, Br, I) Perovskites? *ACS Energy Lett.* **2018**, *3*, 286-289.
16. Xu, K.; Meijerink, A. Tuning Exciton–Mn²⁺ Energy Transfer in Mixed Halide Perovskite Nanocrystals. *Chem. Mater.* **2018**, *30*, 5346-5352.
17. Mir, W. J.; Swarnkar, A.; Nag, A. Postsynthesis Mn-Doping in CsPbI₃ Nanocrystals to Stabilize the Black Perovskite Phase. *Nanoscale* **2019**, *11*, 4278-4286.
18. Luo, B.; Li, F.; Xu, K.; Guo, Y.; Liu, Y.; Xia, Z.; Zhang, J. Z. B-Site Doped Lead Halide Perovskites: Synthesis, Band Engineering, Photophysics, and Light Emission Applications. *J. Mater. Chem. C* **2019**, *7*, 2781-2808.
19. Biswas, A.; Bakthavatsalam, R.; Kundu, J. Efficient Exciton to Dopant Energy Transfer in Mn²⁺-Doped (C₄H₉NH₃)₂PbBr₄ Two-Dimensional (2D) Layered Perovskites. *Chem. Mater.* **2017**, *29*, 7816-7825.
20. Dutta, S. K.; Dutta, A.; Das Adhikari, S.; Pradhan, N. Doping Mn²⁺ in Single-Crystalline Layered Perovskite Microcrystals. *ACS Energy Lett.* **2019**, *4*, 343-351.
21. Mitzi, D. B. Synthesis, Crystal Structure, and Optical and Thermal Properties of (C₄H₉NH₃)₂MI₄ (M = Ge, Sn, Pb). *Chem. Mater.* **1996**, *8*, 791-800.
22. Mitzi, D. B. Synthesis, Structure, and Properties of Organic-Inorganic Perovskites and Related Materials. *Prog. Inorg. Chem.* **2007**, *48*, 1-121.
23. Cao, D. H.; Stoumpos, C. C.; Farha, O. K.; Hupp, J. T. 2D Homologous Perovskites as Light-Absorbing Materials for Solar Cell Applications. *J. Am. Chem. Soc.* **2015**, *137*, 7843-7850.
24. Saparov, B.; Mitzi, D. B. Organic–Inorganic Perovskites: Structural Versatility for Functional Materials Design. *Chem. Rev.* **2016**, *116*, 4558-4596.
25. Polavarapu, L.; Nickel, B.; Feldmann, J.; Urban, A. S. Advances in Quantum-Confined Perovskite Nanocrystals for Optoelectronics. *Adv. Energy Mater.* **2017**, *7*, 1700267.
26. Soe, C. M. M.; Nagabhushana, G. P.; Shivaramaiah, R.; Tsai, H.; Nie, W.; Blancon, J.-C.; Melkonyan, F.; Cao, D. H.; Traoré, B.; Pedesseau, L.; Kepenekian, M.; Katan, C.; Even, J.; Marks, T. J.; Navrotsky, A.; Mohite, A. D.; Stoumpos, C. C.; Kanatzidis, M. G. Structural and Thermodynamic Limits of Layer Thickness in 2D Halide Perovskites. *Proc. Natl. Acad. Sci.* **2019**, *116*, 58-66.
27. Blancon, J. C.; Stier, A. V.; Tsai, H.; Nie, W.; Stoumpos, C. C.; Traoré, B.; Pedesseau, L.; Kepenekian, M.; Katsutani, F.; Noe, G. T.; Kono, J.; Tretiak, S.; Crooker, S. A.; Katan, C.;

Appendix 1

Mn Doping in Centimeter Sized 2D Layered Butylammonium Lead Bromide, (BA)₂PbBr₄, Single Crystals

- Kanatzidis, M. G.; Crochet, J. J.; Even, J.; Mohite, A. D. Scaling Law for Excitons in 2d Perovskite Quantum Wells. *Nat. Commun.* **2018**, *9*, 2254.
28. Liu, H.; Guyot-Sionnest, P. Magnetoresistance of Manganese-Doped Colloidal Quantum Dot Films. *J. Phys. Chem. C* **2015**, *119*, 14797-14804.
29. Rice, W. D.; Liu, W.; Baker, T. A.; Sinitsyn, N. A.; Klimov, V. I.; Crooker, S. A. Revealing Giant Internal Magnetic Fields Due to Spin Fluctuations in Magnetically Doped Colloidal Nanocrystals. *Nature Nanotechnol.* **2015**, *11*, 137.
30. Fainblat, R.; Barrows, C. J.; Hopmann, E.; Siebeneicher, S.; Vlaskin, V. A.; Gamelin, D. R.; Bacher, G. Giant Excitonic Exchange Splittings at Zero Field in Single Colloidal CdSe Quantum Dots Doped with Individual Mn²⁺ Impurities. *Nano Lett.* **2016**, *16*, 6371-6377.
31. Stoumpos, C. C.; Malliakas, C. D.; Kanatzidis, M. G. Semiconducting Tin and Lead Iodide Perovskites with Organic Cations: Phase Transitions, High Mobilities, and Near-Infrared Photoluminescent Properties. *Inorg. Chem.* **2013**, *52*, 9019-9038.
32. Dirin, D. N.; Cherniukh, I.; Yakunin, S.; Shynkarenko, Y.; Kovalenko, M. V. Solution-Grown CsPbBr₃ Perovskite Single Crystals for Photon Detection. *Chem. Mater.* **2016**, *28*, 8470-8474.
33. Lian, Z.; Yan, Q.; Gao, T.; Ding, J.; Lv, Q.; Ning, C.; Li, Q.; Sun, J.-l. Perovskite CH₃NH₃PbI₃(Cl) Single Crystals: Rapid Solution Growth, Unparalleled Crystalline Quality, and Low Trap Density toward 10⁸ cm⁻³. *J. Am. Chem. Soc.* **2016**, *138*, 9409-9412.
34. Chu, Z.; Yang, M.; Schulz, P.; Wu, D.; Ma, X.; Seifert, E.; Sun, L.; Li, X.; Zhu, K.; Lai, K. Impact of Grain Boundaries on Efficiency and Stability of Organic-Inorganic Trihalide Perovskites. *Nat. Commun.* **2017**, *8*, 2230-2230.
35. Guo, Y.; Wang, Q.; Saidi, W. A. Structural Stabilities and Electronic Properties of High-Angle Grain Boundaries in Perovskite Cesium Lead Halides. *J. Phys. Chem. C* **2017**, *121*, 1715-1722.
36. Sheikh, T.; Shinde, A.; Mahamuni, S.; Nag, A. Possible Dual Bandgap in (C₄H₉NH₃)₂PbI₄ 2D Layered Perovskite: Single-Crystal and Exfoliated Few-Layer. *ACS Energy Lett.* **2018**, *3*, 2940-2946.
37. Stoumpos, C. C.; Cao, D. H.; Clark, D. J.; Young, J.; Rondinelli, J. M.; Jang, J. I.; Hupp, J. T.; Kanatzidis, M. G. Ruddlesden–Popper Hybrid Lead Iodide Perovskite 2D Homologous Semiconductors. *Chem. Mater.* **2016**, *28*, 2852-2867.
38. Eickhoff, T.; Grosse, P.; Theiss, W. Diffuse Reflectance Spectroscopy of Powders. *Vib. Spectrosc.* **1990**, *1*, 229-233.

Mn Doping in Centimeter Sized 2D Layered Butylammonium Lead Bromide, (BA)₂PbBr₄, Single Crystals

39. De, A.; Mondal, N.; Samanta, A. Luminescence Tuning and Exciton Dynamics of Mn-Doped CsPbCl₃ Nanocrystals. *Nanoscale* **2017**, *9*, 16722-16727.
40. Pradhan, N.; Das Adhikari, S.; Nag, A.; Sarma, D. D. Luminescence, Plasmonic, and Magnetic Properties of Doped Semiconductor Nanocrystals. *Angew. Chem. Int. Ed.* **2017**, *56*, 7038-7054.
41. Nag, A.; Chakraborty, S.; Sarma, D. D. To Dope Mn²⁺ in a Semiconducting Nanocrystal. *J. Am. Chem. Soc.* **2008**, *130*, 10605-10611.
42. Lin, J.; Hu, D.-D.; Zhang, Q.; Li, D.-S.; Wu, T.; Bu, X.; Feng, P. Improving Photoluminescence Emission Efficiency of Nanocluster-Based Materials by in Situ Doping Synthetic Strategy. *J. Phys. Chem. C* **2016**, *120*, 29390-29396.
43. Chen, D.; Fang, G.; Chen, X. Silica-Coated Mn-Doped CsPb(Cl/Br)₃ Inorganic Perovskite Quantum Dots: Exciton-to-Mn Energy Transfer and Blue-Excitable Solid-State Lighting. *ACS Appl. Mater. Interfaces* **2017**, *9*, 40477-40487.
44. Das Adhikari, S.; Dutta, S. K.; Dutta, A.; Guria, A. K.; Pradhan, N. Chemically Tailoring the Dopant Emission in Manganese-Doped CsPbCl₃ Perovskite Nanocrystals. *Angew. Chem. Int. Ed.* **2017**, *56*, 8746-8750.
45. Yuan, X.; Ji, S.; De Siena, M. C.; Fei, L.; Zhao, Z.; Wang, Y.; Li, H.; Zhao, J.; Gamelin, D. R. Photoluminescence Temperature Dependence, Dynamics, and Quantum Efficiencies in Mn²⁺-Doped CsPbCl₃ Perovskite Nanocrystals with Varied Dopant Concentration. *Chem. Mater.* **2017**, *29*, 8003-8011.
46. Das Adhikari, S.; Dutta, A.; Dutta, S. K.; Pradhan, N. Layered Perovskites L₂(Pb_{1-x}Mn_x)Cl₄ to Mn-Doped CsPbCl₃ Perovskite Platelets. *ACS Energy Lett.* **2018**, *3*, 1247-1253.
47. Gao, D.; Qiao, B.; Xu, Z.; Song, D.; Song, P.; Liang, Z.; Shen, Z.; Cao, J.; Zhang, J.; Zhao, S. Postsynthetic, Reversible Cation Exchange between Pb²⁺ and Mn²⁺ in Cesium Lead Chloride Perovskite Nanocrystals. *J. Phys. Chem. C* **2017**, *121*, 20387-20395.
48. Rossi, D.; Parobek, D.; Dong, Y.; Son, D. H. Dynamics of Exciton–Mn Energy Transfer in Mn-Doped CsPbCl₃ Perovskite Nanocrystals. *J. Phys. Chem. C* **2017**, *121*, 17143-17149.
49. Mir, W. J.; Mahor, Y.; Lohar, A.; Jagadeeswararao, M.; Das, S.; Mahamuni, S.; Nag, A. Postsynthesis Doping of Mn and Yb into CsPbX₃ (X = Cl, Br, or I) Perovskite Nanocrystals for Downconversion Emission. *Chem. Mater.* **2018**, *30*, 8170-8178.

Thesis Summary and Future Outlook

Thesis Summary

Lower dimensional hybrid perovskites consist of negatively charged inorganic sub-lattices and positively charged organic cations.¹ This hybrid structure gives rise to various types of interactions. This thesis explores the interactions in lower-dimensional hybrid halide perovskites to understand their optical properties and address their water instability issue. Two dimensional (2D) layered hybrid perovskites, which have the electronic dimensionality reduced to atomic level in one direction, possess a quantum well structure.² The intrinsic quantum well structure of the 2D layered hybrid perovskites gives rise to the quantum confinement in the bulk-sized crystals.³ Due to the quantum confinement effect, the layered hybrid perovskites show sharp excitonic absorption and emission features.

A major portion of this thesis focused on understanding the anomalous band gap and the emission properties of the 2D layered hybrid perovskite single crystals. By employing various experimental techniques like optical absorption, temperature-dependent steady-state PL, and time-resolved PL, it is shown that the 2D layered hybrid perovskite single crystals exhibit two excitonic emissions. The higher energy excitonic emission arises from the isolated 2D inorganic layers. By using spatially resolved fluorescence microscopy imaging, we showed that the lower energy emission originates mostly from the layer edges of the crystal. By employing experimental methodologies like molecular intercalation and tuning interlayer separation, we showed that the 2D inorganic layers in layered hybrid perovskites interact with each other, mostly at the layer edges of the crystal. It is these interlayer interactions that give rise to the second excitonic emission in these layered hybrid perovskites.

The hybrid structure of 2D layered perovskites gives an opportunity to combine the properties characteristic of organic molecules, like chirality, with the properties of inorganic sub-lattices. Chapter four of this thesis explored the effect of induced chirality on the excitonic properties of 2D layered hybrid lead iodide perovskites. By using chiral R- and S- α -methylbenzylammonium (R- and S- α -MBA) ions, chiral layered hybrid (R- and S- α -MBA)₂PbI₄ are synthesized. By employing the low-temperature PL, it is shown that the induced chirality splits the PL peaks in these chiral (R- and S- α -MBA)₂PbI₄. Moreover, higher exciton binding energies are also observed in these chiral (R- and S- α -MBA)₂PbI₄, compared to the achiral (Rac- α -MBA)₂PbI₄.

In the last chapter of this thesis, the water instability of the lower dimensional perovskites is addressed by taking advantage of intermolecular cation- π interactions between the A-site

organic cations. By using 4,4'-trimethylenedipyridinium (4,4'-TMDP) and 4,4'-ethylenedipyridinium (4,4'-EDP) as the A-site organic cations, completely water-stable 1D (4,4'-TMDP)Pb₂Br₆ and (4,4'-EMDP)Pb₂Br₆ perovskites are synthesized. These water-stable 1D perovskites show a warm white light emission. Subsequently, a white LED is fabricated by coating the water stable (4,4'-TMDP)Pb₂Br₆ on a commercial 360 nm UV LED, which showed a stable white emission.

Relevance of the Results

The band gap is one of the most important properties of semiconducting materials. However, the reported band gaps of 2D layered hybrid perovskite single crystals vary hugely. Moreover, multiple emission peaks are observed in the layered hybrid perovskite single crystals. In the second and third chapters of this thesis, we address the unusual band gap and emission properties of layered hybrid perovskites. We have shown that the 2D inorganic layers in layered hybrid perovskites are not completely isolated from each other, as previously considered. The interactions between the adjacent inorganic layers modify the band gap as well as the PL emissions in these layered hybrid perovskites. Moreover, experimental methodologies like molecular intercalation and tuning interlayer separation have been shown to modulate or completely remove the interactions between the adjacent inorganic layers. The understanding of these interlayer interactions and their modulation is important for defining the exact band gaps and achieving color-pure emissions in these layered hybrid perovskites.

Recently chirality has been introduced in the layered hybrid perovskites. How does the induced chirality affect the excitonic properties of these layered hybrid perovskites? The fourth chapter of this thesis explores the effect of induced chirality on the emission properties of layered lead iodide perovskites. Emission splitting, probably due to the lifting of spin degeneracy, and higher exciton binding energies are observed in the chiral layered hybrid lead iodide perovskites. These results provide important insights towards the understanding of chirality induced excitonic effects, which are important for chiroptical and spin-dependent properties.

Water/moisture instability is one of the major problems of lead halide perovskites. In the last chapter of this thesis, interactions between the organic cations have been utilized to synthesize completely water-stable 1D lead bromide perovskites. The achieved water stability is intrinsic in nature and does not require any post-synthetic modification. This is a totally new approach and could be a breakthrough step towards addressing the water/moisture instability issue of the lead halide perovskites.

Future Outlook

1. Synthesizing water-stable environmentally benign tin halide perovskites

Despite having astonishing semiconducting properties, lead halide perovskites face a few challenges for commercialization. The main hurdles in the path of the commercialization of lead halide perovskites are water/moisture instability and lead toxicity.⁴⁻⁷ The traditional approaches like the encapsulation of perovskites material or their devices address these issues to some extent.⁸⁻⁹ However, encapsulation is not a permanent solution. Once the encapsulation layer breaks, the lead halide perovskite again comes in contact with the environment, bringing back the instability and the toxicity issues. In chapter 5 of this thesis, we tried to address the water instability issue of the lower dimensional lead halide perovskites by using the intermolecular cation- π interactions. We were successfully able to synthesize 1D lead bromide perovskites that show intrinsic water stability. This is a new approach to improve the intrinsic water stability of the lower dimensional lead halide perovskites.

Lead toxicity is directly related to the water instability of lead halide perovskites. Once the lead halide perovskites dissociate, the toxic lead is released into the environment. Addressing the water instability issue of lead halide perovskites will address the lead toxicity issue to some extent; however, this approach will not eliminate the lead toxicity issue completely. The best way of addressing the lead toxicity issue is to look for non-toxic alternatives of lead. Environment-friendly tin, which belongs to the same group of lead in the periodic table and has the same valence shell electronic configuration, becomes the first choice of alternatives. However, the easy oxidation of Sn^{2+} to Sn^{4+} brings in a major challenge.¹⁰⁻¹¹ Water or moisture promotes the oxidation of Sn^{2+} to Sn^{4+} in these tin halide perovskites.

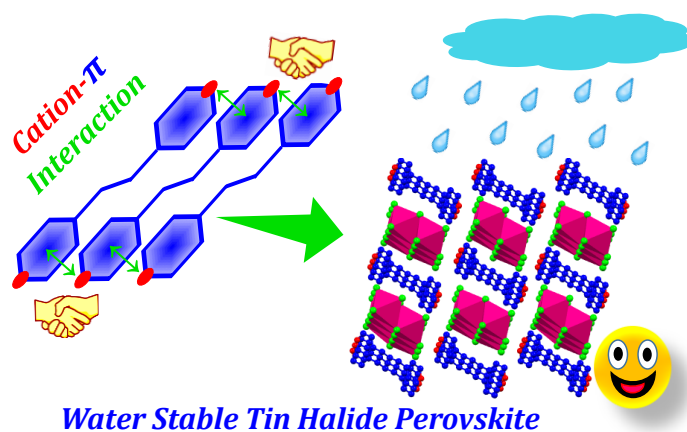


Figure F.1: Schematic demonstration of long-range cation- π interactions for stabilizing lower-dimensional tin halide perovskites.

One possible way to address the instability of tin halide perovskites is to use the intermolecular cation- π interactions that we used to stabilize the lead halide perovskites in water. The long-range intermolecular cation- π stacking will prevent the water molecules from incorporating into the perovskite lattice. This will reduce the exposure of Sn^{2+} ions to the water molecules. We believe that this approach will reduce the chances of oxidation of Sn^{2+} ions to a great extent and ultimately improve the stability of these lower-dimensional tin halide perovskites.

2. Improving the charge transport in lower-dimensional perovskites

The compositional flexibility of lower-dimensional perovskites gives us an opportunity to play with their properties. By designing organic cations with different functionalities, various new properties can be achieved, like the introduction of chirality, as shown in chapter 4 of this thesis. Moreover, the compositional flexibility of these lower-dimensional perovskites also gives an opportunity to improve their stability in the ambient conditions, for example, improving their water stability, as shown in chapter 5 of this thesis. However, due to the lower electronic dimensionality, the lower dimensional perovskites show poor charge transport. The organic cations are insulation and hence do not allow the charge carriers to pass through. The poor charge transport of these lower-dimensional perovskites becomes detrimental for their optoelectronic applications.

The compositional flexibility can be utilized to improve the charge transport in these lower-dimensional, by designing organics cations that are conducting in nature. A single type of organic cation or a combination of organic cations can be used. The inorganic sub-lattices will act as the active layers for charge carrier generation or recombination, while the conducting organic cations will provide a path for carrier transport.

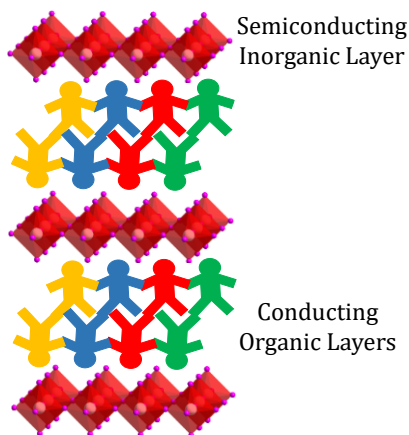


Figure F.2: Schematic demonstration of connected organic cations allowing the movement of carriers through them.

References

1. Saparov, B.; Mitzi, D. B. Organic-Inorganic Perovskites: Structural Versatility for Functional Materials Design. *Chem. Rev.* **2016**, *116*, 4558-4596.
2. Katan, C.; Mercier, N.; Even, J. Quantum and Dielectric Confinement Effects in Lower-Dimensional Hybrid Perovskite Semiconductors. *Chem. Rev.* **2019**, *119*, 3140-3192.
3. Nag, A. "Plenty of Room" at the Interface of Hybrid Metal Halide Perovskite Single Crystals. *Nano Lett.* **2021**, *21*, 8529-8531.
4. Tsvetkov, D. S.; Mazurin, M. O.; Sereda, V. V.; Ivanov, I. L.; Malyshev, D. A.; Zuev, A. Y. Formation Thermodynamics, Stability, and Decomposition Pathways of CsPbX₃ (X = Cl, Br, I) Photovoltaic Materials. *J. Phys. Chem. C* **2020**, *124*, 4252-4260.
5. Hailegnaw, B.; Kirmayer, S.; Edri, E.; Hodes, G.; Cahen, D. Rain on Methylammonium Lead Iodide Based Perovskites: Possible Environmental Effects of Perovskite Solar Cells. *J. Phys. Chem. Lett.* **2015**, *6*, 1543-1547.
6. Ravi, V. K.; Mondal, B.; Nawale, V. V.; Nag, A. Don't Let the Lead Out: New Material Chemistry Approaches for Sustainable Lead Halide Perovskite Solar Cells. *ACS Omega* **2020**, *5*, 29631-29641.
7. Li, J.; Cao, H.-L.; Jiao, W.-B.; Wang, Q.; Wei, M.; Cantone, I.; Lü, J.; Abate, A. Biological Impact of Lead from Halide Perovskites Reveals the Risk of Introducing a Safe Threshold. *Nat. Commun.* **2020**, *11*, 310.
8. Huang, H.; Chen, B.; Wang, Z.; Hung, T. F.; Susha, A. S.; Zhong, H.; Rogach, A. L. Water Resistant CsPbX₃ Nanocrystals Coated with Polyhedral Oligomeric Silsesquioxane and their Use as Solid State Luminophores in All-Perovskite White Light-Emitting Devices. *Chem. Sci.* **2016**, *7*, 5699-5703.
9. Ravi, V. K.; Saikia, S.; Yadav, S.; Nawale, V. V.; Nag, A. CsPbBr₃/ZnS Core/Shell Type Nanocrystals for Enhancing Luminescence Lifetime and Water Stability. *ACS Energy Lett.* **2020**, *5*, 1794-1796.
10. Qiu, X.; Cao, B.; Yuan, S.; Chen, X.; Qiu, Z.; Jiang, Y.; Ye, Q.; Wang, H.; Zeng, H.; Liu, J.; Kanatzidis, M. G. From Unstable CsSnI₃ to Air-Stable Cs₂SnI₆: A Lead-Free Perovskite Solar Cell Light Absorber with Bandgap of 1.48 eV and High Absorption Coefficient. *Sol. Energy Mater. Sol. Cells* **2017**, *159*, 227-234.
11. Shao, S.; Liu, J.; Portale, G.; Fang, H.-H.; Blake, G. R.; ten Brink, G. H.; Koster, L. J. A.; Loi, M. A. Highly Reproducible Sn-Based Hybrid Perovskite Solar Cells with 9% Efficiency. *Adv. Energy Mater.* **2018**, *8*, 1702019.

Included in Thesis

1. **Tariq Sheikh**, Aparna Shinde, Shailaja Mahamuni and Angshuman Nag. Possible Dual Bandgap in $(\text{C}_4\text{H}_9\text{NH}_3)_2\text{PbI}_4$ 2D Layered Perovskite: Single-Crystal and Exfoliated Few-Layer. *ACS Energy Lett.* **2018**, *3*, 2940-2946.
2. **Tariq Sheikh** and Angshuman Nag. Mn Doping in Centimeter-Sized Layered 2D Butylammonium Lead Bromide (BA_2PbBr_4) Single Crystals and Their Optical Properties. *J. Phys. Chem. C* **2019**, *123*, 9420-9427.
3. **Tariq Sheikh**, Aparna Shinde, Shailaja Mahamuni and Angshuman Nag. Dual Excitonic Emissions and Structural Phase Transition of Octylammonium Lead Iodide 2D Layered Perovskite Single Crystal. *Mater. Res. Express* **2019**, *6*, 124002.
4. **Tariq Sheikh**, Vaibhav Nawale, Nithin Pathoor, Chinmay Phadnis, Arindam Chowdhury and Angshuman Nag. Molecular Intercalation and Electronic Two Dimensionality in Layered Hybrid Perovskites. *Angew. Chem. Int. Ed.* **2020**, *59*, 11653-11659.
5. **Tariq Sheikh**, Shabnum Maqbool, Pankaj Mandal and Angshuman Nag. Introducing Intermolecular Cation- π Interactions for Water-Stable Low Dimensional Hybrid Lead Halide Perovskites. *Angew. Chem. Int. Ed.* **2021**, *60*, 18265-1827.

Not Included in Thesis

6. Abhishek Swarnkar, Wasim J. Mir, Rayan Chakraborty, Mitikoti Jagadeeswararao, **Tariq Sheikh** and Angshuman Nag. Are Chalcogenide Perovskites an Emerging Class of Semiconductors for Optoelectronic Properties and Solar Cell? *Chem. Mater.* **2019**, *31*, 565-575.
7. Wasim J. Mir, **Tariq Sheikh**, Habibul Arfin, Zhiguo Xia and Angshuman Nag. Lanthanide Doping in Metal Halide Perovskite Nanocrystals: Spectral Shifting, Quantum Cutting and Optoelectronic Applications. *NPG Asia Materials* **2020**, *12*, 1-9.
8. Habibul Arfin, Jagjit Kaur, **Tariq Sheikh**, Sudip Chakraborty and Angshuman Nag. Bi^{3+} - Er^{3+} and Bi^{3+} - Yb^{3+} Codoped $\text{Cs}_2\text{AgInCl}_6$ Double Perovskite Near-Infrared Emitters. *Angew. Chem. Int. Ed.* **2020**, *59*, 11307-11311.

List of Publications

9. Vaibhav Nawale **Tariq Sheikh** and Angshuman Nag. Dual Excitonic Emission in Hybrid 2D Layered Tin Iodide Perovskites. *J. Phys. Chem. C* **2020**, *124*, 21129-21136.
10. Rayan Chakraborty, **Tariq Sheikh**, Prasenjit Ghosh and Angshuman Nag. Neural Networks for Analysis of Optical Properties in 2D Layered Hybrid Lead Halide Perovskites. *J. Phys. Chem. C* **2021**, *125*, 5251-5259.
11. Taniya Dutta, **Tariq Sheikh** and Angshuman Nag. Temperature-Dependent Photoluminescence of Hexafluorobenzene-Intercalated Phenethylammonium Tin Iodide 2D Perovskite. *Chem. Asian J.* **2021**, *16*, 2745–2751.
12. Shabnum Maqbool, **Tariq Sheikh**, Ziyad Thekkayil, Swati Deswal, Ramamoorthy Boomishankar, Angshuman Nag and Pankaj Mandal. Third Harmonic Upconversion and Self-Trapped Excitonic Emission in 1D Pyridinium Lead Iodide. *J. Phys. Chem. C* **2021**, *125*, 22674–22683.
13. Abhijit Chatterjee, Joy Chatterjee, Subrahmanyam Sappati, **Tariq Sheikh**, Rintu M Umesh, Madan D Ambhore, Mayurika Lahiri and Partha Hazra. Emergence of Aggregation Induced Emission (AIE), Room-Temperature Phosphorescence (RTP), and Multistimuli Response from a Single Organic Luminogen by Directed Structural Modification. *J. Phys. Chem. B* **2021**, *125*, 12832–12846
14. Rayan Chakraborty, **Tariq Sheikh** and Angshuman Nag. Iodine-Iodine Interactions Suppressing Phase Transitions of 2D Layered Hybrid $(\text{I}-(\text{CH}_2)_n\text{-NH}_3)_2\text{PbI}_4$ ($n = 2-6$) Perovskites. *Chem. Mater.* **2021**, *34*, 288–296.

Copyrights and Permissions

Possible Dual Bandgap in (C₄H₉NH₃)₂PbI₄ 2D Layered Perovskite: Single-Crystal and Exfoliated Few-Layer



Author: Tariq Sheikh, Aparna Shinde, Shailaja Mahamuni, et al

Publication: ACS Energy Letters

Publisher: American Chemical Society

Date: Dec 1, 2018

Copyright © 2018, American Chemical Society

PERMISSION/LICENSE IS GRANTED FOR YOUR ORDER AT NO CHARGE

This type of permission/license, instead of the standard Terms and Conditions, is sent to you because no fee is being charged for your order. Please note the following:

- Permission is granted for your request in both print and electronic formats, and translations.
- If figures and/or tables were requested, they may be adapted or used in part.
- Please print this page for your records and send a copy of it to your publisher/graduate school.
- Appropriate credit for the requested material should be given as follows: "Reprinted (adapted) with permission from {COMPLETE REFERENCE CITATION}. Copyright {YEAR} American Chemical Society." Insert appropriate information in place of the capitalized words.
- One-time permission is granted only for the use specified in your RightsLink request. No additional uses are granted (such as derivative works or other editions). For any uses, please submit a new request.

If credit is given to another source for the material you requested from RightsLink, permission must be obtained from that source.

[BACK](#)

[CLOSE WINDOW](#)

Mn Doping in Centimeter-Sized Layered 2D Butylammonium Lead Bromide (BA₂PbBr₄) Single Crystals and Their Optical Properties



Author: Tariq Sheikh, Angshuman Nag

Publication: The Journal of Physical Chemistry C

Publisher: American Chemical Society

Date: Apr 1, 2019

Copyright © 2019, American Chemical Society

PERMISSION/LICENSE IS GRANTED FOR YOUR ORDER AT NO CHARGE

This type of permission/license, instead of the standard Terms and Conditions, is sent to you because no fee is being charged for your order. Please note the following:

- Permission is granted for your request in both print and electronic formats, and translations.
- If figures and/or tables were requested, they may be adapted or used in part.
- Please print this page for your records and send a copy of it to your publisher/graduate school.
- Appropriate credit for the requested material should be given as follows: "Reprinted (adapted) with permission from {COMPLETE REFERENCE CITATION}. Copyright {YEAR} American Chemical Society." Insert appropriate information in place of the capitalized words.
- One-time permission is granted only for the use specified in your RightsLink request. No additional uses are granted (such as derivative works or other editions). For any uses, please submit a new request.

If credit is given to another source for the material you requested from RightsLink, permission must be obtained from that source.

[BACK](#)

[CLOSE WINDOW](#)

This is a License Agreement between Tariq Ahmad Sheikh ("User") and Copyright Clearance Center, Inc. ("CCC") on behalf of the Rightsholder identified in the order details below. The license consists of the order details, the CCC Terms and Conditions below, and any Rightsholder Terms and Conditions which are included below.

All payments must be made in full to CCC in accordance with the CCC Terms and Conditions below.

Order Date	22-Nov-2021	Type of Use	Republish in a thesis/dissertation
Order License ID	1163348-1	Publisher	IOP Publishing
ISSN	2053-1591	Portion	Chapter/article

LICENSED CONTENT

Publication Title	Materials Research Express	Country	United Kingdom of Great Britain and Northern Ireland
Date	01/01/2014	Rightsholder	IOP Publishing, Ltd
Language	English	Publication Type	e-Journal

REQUEST DETAILS

Portion Type	Chapter/article	Rights Requested	Main product
Page range(s)	1-8	Distribution	Worldwide
Total number of pages	8	Translation	Original language of publication
Format (select all that apply)	Print, Electronic	Copies for the disabled?	No
Who will republish the content?	Author of requested content	Minor editing privileges?	No
Duration of Use	Life of current and all future editions	Incidental promotional use?	No
Lifetime Unit Quantity	Up to 999	Currency	USD

NEW WORK DETAILS

Title	Designing Low-Dimensional Hybrid Lead Halide Perovskites for Excitonic Photophysics, Chiroptics and Water-Stability	Institution name	Indian Institute of Science Education and Research (IISER) Pune.
Instructor name	Tariq Ahmad Sheikh	Expected presentation date	2022-02-15

ADDITIONAL DETAILS

Order reference number	1996	The requesting person / organization to appear on the license	Tariq Ahmad Sheikh
------------------------	------	---	--------------------

REUSE CONTENT DETAILS

Title, description or numeric reference of the portion(s)	Dual excitonic emissions and structural phase transition of octylammonium lead iodide 2D layered perovskite single crystal	Title of the article/chapter the portion is from	N/A
		Author of portion(s)	N/A
		Issue, if republishing an article from a serial	N/A
Editor of portion(s)	N/A	Publication date of portion	2019-11-15
Volume of serial or monograph	N/A		
Page or page range of portion	1-8		

RIGHTSHOLDER TERMS AND CONDITIONS

These special terms and conditions are in addition to the standard terms and conditions for CCC's Republication Service and, together with those standard terms and conditions, govern the use of the Works. As the User you will make all reasonable efforts to contact the author(s) of the article which the Work is to be reused from, to seek consent for your intended use. Contacting one author who is acting expressly as authorised agent for their co-author(s) is acceptable. User will reproduce the following wording prominently alongside the Work: the source of the Work, including author, article title, title of journal, volume number, issue number (if relevant), page range (or first page if this is the only information available) and date of first publication; and a link back to the article (via DOI); and if practicable, and IN ALL CASES for new works published under any of the Creative Commons licences, the words "© IOP Publishing. Reproduced with permission. All rights reserved" Without the express permission of the author(s) and the Rightsholder of the article from which the Work is to be reused, User shall not use it in any way which, in the opinion of the Rightsholder, could: (i) distort or alter the author(s)' original intention(s) and meaning; (ii) be prejudicial to the honour or reputation of the author(s); and/or (iii) imply endorsement by the author(s) and/or the Rightsholder. This licence does not apply to any article which is credited to another source and which does not have the copyright line '© IOP Publishing Ltd'. User must check the copyright line of the article from which the Work is to be reused to check that IOP Publishing Ltd has all the necessary rights to be able to grant permission. User is solely responsible for identifying and obtaining separate licences and permissions from the copyright owner for reuse of any such third party material/figures which the Rightsholder is not the copyright owner of. The Rightsholder shall not reimburse any fees which User pays for a republication license for such third party content. This licence does not apply to any material/figure which is credited to another source in the Rightsholder's publication or has been obtained from a third party. User must check the Version of Record of the article from which the Work is to be reused, to check whether any of the material in the Work is third party material. Third party citations and/or copyright notices and/or permissions statements may not be included in any other version of the article from which the Work is to be reused and so cannot be relied upon by the User. User is solely responsible for identifying and obtaining separate licences and permissions from the copyright owner for reuse of any such third party material/figures where the Rightsholder is not the copyright owner. The Rightsholder shall not reimburse any fees which User pays for a republication license for such third party content. User and CCC acknowledge that the Rightsholder may, from time to time, make changes or additions to these special terms and conditions without express notification, provided that these shall not apply to permissions already secured and paid for by User prior to such change or addition. User acknowledges that the Rightsholder (which includes companies within its group and third parties for whom it publishes its titles) may make use of personal data collected through the service in the course of their business. If User is the author of the Work, User may automatically have the right to reuse it under the rights granted back when User transferred the copyright in the article to the Rightsholder. User should check the copyright form and the relevant author rights policy to check whether permission is required. If User is the author of the Work and does require permission for proposed reuse of the Work, User should select 'Author of requested content' as the Requestor Type. The Rightsholder shall not reimburse any fees which User pays for a republication license. If User is the author of the article which User wishes to reuse in User's thesis or dissertation, the republication licence covers the right to include the Version of Record of the article, provided it is not then shared or deposited online. User must include citation details. Where User wishes to share their thesis or dissertation online, they should remove the Version of Record before uploading it. User may include a Preprint or the Accepted Manuscript (after the embargo period) in the online version of the thesis or dissertation, provided they do so in accordance with the Rightsholder's policies on sharing Preprints or Accepted Manuscripts. User may need to obtain separate permission for any third party content included within the article. User must check this with the copyright owner of such third party content. Any online or commercial use of User's thesis or dissertation containing the article, including publication via ProQuest, would need to be expressly notified in writing to the Rightsholder at the time of request and would require separate written permission from the Rightsholder. As well as CCC, the Rightsholder shall have the right to bring any legal action that it deems necessary to enforce its rights should it consider that the Work infringes those rights in any way. For content reuse requests that qualify for permission under the STM Permissions Guidelines, which may be updated from time to time, the STM Permissions Guidelines supplement the terms and conditions contained in this license.

SPECIAL RIGHTSHOLDER TERMS AND CONDITIONS

When you transferred the copyright in your article to IOP, we granted back to you certain rights, including the right to include all or part of the Final Published Version of the article within any thesis or dissertation. Please note you may need to

obtain separate permission for any third party content you included within your article. Please include citation details, "© IOP Publishing. Reproduced with permission. All rights reserved" and for online use, a link to the Version of Record. The only restriction is that if, at a later date, you wanted your thesis/dissertation to be published commercially, further permission would be required.

CCC Terms and Conditions

1. Description of Service; Defined Terms. This Republication License enables the User to obtain licenses for republication of one or more copyrighted works as described in detail on the relevant Order Confirmation (the "Work(s)"). Copyright Clearance Center, Inc. ("CCC") grants licenses through the Service on behalf of the rightsholder identified on the Order Confirmation (the "Rightsholder"). "Republication", as used herein, generally means the inclusion of a Work, in whole or in part, in a new work or works, also as described on the Order Confirmation. "User", as used herein, means the person or entity making such republication.
2. The terms set forth in the relevant Order Confirmation, and any terms set by the Rightsholder with respect to a particular Work, govern the terms of use of Works in connection with the Service. By using the Service, the person transacting for a republication license on behalf of the User represents and warrants that he/she/it (a) has been duly authorized by the User to accept, and hereby does accept, all such terms and conditions on behalf of User, and (b) shall inform User of all such terms and conditions. In the event such person is a "freelancer" or other third party independent of User and CCC, such party shall be deemed jointly a "User" for purposes of these terms and conditions. In any event, User shall be deemed to have accepted and agreed to all such terms and conditions if User republishes the Work in any fashion.
3. Scope of License; Limitations and Obligations.
 - 3.1. All Works and all rights therein, including copyright rights, remain the sole and exclusive property of the Rightsholder. The license created by the exchange of an Order Confirmation (and/or any invoice) and payment by User of the full amount set forth on that document includes only those rights expressly set forth in the Order Confirmation and in these terms and conditions, and conveys no other rights in the Work(s) to User. All rights not expressly granted are hereby reserved.
 - 3.2. General Payment Terms: You may pay by credit card or through an account with us payable at the end of the month. If you and we agree that you may establish a standing account with CCC, then the following terms apply: Remit Payment to: Copyright Clearance Center, 29118 Network Place, Chicago, IL 60673-1291. Payments Due: Invoices are payable upon their delivery to you (or upon our notice to you that they are available to you for downloading). After 30 days, outstanding amounts will be subject to a service charge of 1-1/2% per month or, if less, the maximum rate allowed by applicable law. Unless otherwise specifically set forth in the Order Confirmation or in a separate written agreement signed by CCC, invoices are due and payable on "net 30" terms. While User may exercise the rights licensed immediately upon issuance of the Order Confirmation, the license is automatically revoked and is null and void, as if it had never been issued, if complete payment for the license is not received on a timely basis either from User directly or through a payment agent, such as a credit card company.
 - 3.3. Unless otherwise provided in the Order Confirmation, any grant of rights to User (i) is "one-time" (including the editions and product family specified in the license), (ii) is non-exclusive and non-transferable and (iii) is subject to any and all limitations and restrictions (such as, but not limited to, limitations on duration of use or circulation) included in the Order Confirmation or invoice and/or in these terms and conditions. Upon completion of the licensed use, User shall either secure a new permission for further use of the Work(s) or immediately cease any new use of the Work(s) and shall render inaccessible (such as by deleting or by removing or severing links or other locators) any further copies of the Work (except for copies printed on paper in accordance with this license and still in User's stock at the end of such period).
 - 3.4. In the event that the material for which a republication license is sought includes third party materials (such as photographs, illustrations, graphs, inserts and similar materials) which are identified in such material as having been used by permission, User is responsible for identifying, and seeking separate licenses (under this Service or otherwise) for, any of such third party materials; without a separate license, such third party materials may not be used.
 - 3.5. Use of proper copyright notice for a Work is required as a condition of any license granted under the Service. Unless otherwise provided in the Order Confirmation, a proper copyright notice will read substantially as follows: "Republished with permission of [Rightsholder's name], from [Work's title, author, volume, edition number and year of copyright]; permission conveyed through Copyright Clearance Center, Inc. " Such notice

must be provided in a reasonably legible font size and must be placed either immediately adjacent to the Work as used (for example, as part of a by-line or footnote but not as a separate electronic link) or in the place where substantially all other credits or notices for the new work containing the republished Work are located. Failure to include the required notice results in loss to the Rightsholder and CCC, and the User shall be liable to pay liquidated damages for each such failure equal to twice the use fee specified in the Order Confirmation, in addition to the use fee itself and any other fees and charges specified.

3.6. User may only make alterations to the Work if and as expressly set forth in the Order Confirmation. No Work may be used in any way that is defamatory, violates the rights of third parties (including such third parties' rights of copyright, privacy, publicity, or other tangible or intangible property), or is otherwise illegal, sexually explicit or obscene. In addition, User may not conjoin a Work with any other material that may result in damage to the reputation of the Rightsholder. User agrees to inform CCC if it becomes aware of any infringement of any rights in a Work and to cooperate with any reasonable request of CCC or the Rightsholder in connection therewith.

4. Indemnity. User hereby indemnifies and agrees to defend the Rightsholder and CCC, and their respective employees and directors, against all claims, liability, damages, costs and expenses, including legal fees and expenses, arising out of any use of a Work beyond the scope of the rights granted herein, or any use of a Work which has been altered in any unauthorized way by User, including claims of defamation or infringement of rights of copyright, publicity, privacy or other tangible or intangible property.

5. Limitation of Liability. UNDER NO CIRCUMSTANCES WILL CCC OR THE RIGHTSHOLDER BE LIABLE FOR ANY DIRECT, INDIRECT, CONSEQUENTIAL OR INCIDENTAL DAMAGES (INCLUDING WITHOUT LIMITATION DAMAGES FOR LOSS OF BUSINESS PROFITS OR INFORMATION, OR FOR BUSINESS INTERRUPTION) ARISING OUT OF THE USE OR INABILITY TO USE A WORK, EVEN IF ONE OF THEM HAS BEEN ADVISED OF THE POSSIBILITY OF SUCH DAMAGES. In any event, the total liability of the Rightsholder and CCC (including their respective employees and directors) shall not exceed the total amount actually paid by User for this license. User assumes full liability for the actions and omissions of its principals, employees, agents, affiliates, successors and assigns.

6. Limited Warranties. THE WORK(S) AND RIGHT(S) ARE PROVIDED "AS IS". CCC HAS THE RIGHT TO GRANT TO USER THE RIGHTS GRANTED IN THE ORDER CONFIRMATION DOCUMENT. CCC AND THE RIGHTSHOLDER DISCLAIM ALL OTHER WARRANTIES RELATING TO THE WORK(S) AND RIGHT(S), EITHER EXPRESS OR IMPLIED, INCLUDING WITHOUT LIMITATION IMPLIED WARRANTIES OF MERCHANTABILITY OR FITNESS FOR A PARTICULAR PURPOSE. ADDITIONAL RIGHTS MAY BE REQUIRED TO USE ILLUSTRATIONS, GRAPHS, PHOTOGRAPHS, ABSTRACTS, INSERTS OR OTHER PORTIONS OF THE WORK (AS OPPOSED TO THE ENTIRE WORK) IN A MANNER CONTEMPLATED BY USER; USER UNDERSTANDS AND AGREES THAT NEITHER CCC NOR THE RIGHTSHOLDER MAY HAVE SUCH ADDITIONAL RIGHTS TO GRANT.

7. Effect of Breach. Any failure by User to pay any amount when due, or any use by User of a Work beyond the scope of the license set forth in the Order Confirmation and/or these terms and conditions, shall be a material breach of the license created by the Order Confirmation and these terms and conditions. Any breach not cured within 30 days of written notice thereof shall result in immediate termination of such license without further notice. Any unauthorized (but licensable) use of a Work that is terminated immediately upon notice thereof may be liquidated by payment of the Rightsholder's ordinary license price therefor; any unauthorized (and unlicensable) use that is not terminated immediately for any reason (including, for example, because materials containing the Work cannot reasonably be recalled) will be subject to all remedies available at law or in equity, but in no event to a payment of less than three times the Rightsholder's ordinary license price for the most closely analogous licensable use plus Rightsholder's and/or CCC's costs and expenses incurred in collecting such payment.

8. Miscellaneous.

8.1. User acknowledges that CCC may, from time to time, make changes or additions to the Service or to these terms and conditions, and CCC reserves the right to send notice to the User by electronic mail or otherwise for the purposes of notifying User of such changes or additions; provided that any such changes or additions shall not apply to permissions already secured and paid for.

8.2. Use of User-related information collected through the Service is governed by CCC's privacy policy, available online here: <https://marketplace.copyright.com/rs-ui-web/mp/privacy-policy>

8.3. The licensing transaction described in the Order Confirmation is personal to User. Therefore, User may not assign or transfer to any other person (whether a natural person or an organization of any kind) the license

created by the Order Confirmation and these terms and conditions or any rights granted hereunder; provided, however, that User may assign such license in its entirety on written notice to CCC in the event of a transfer of all or substantially all of User's rights in the new material which includes the Work(s) licensed under this Service.

- 8.4. No amendment or waiver of any terms is binding unless set forth in writing and signed by the parties. The Rightsholder and CCC hereby object to any terms contained in any writing prepared by the User or its principals, employees, agents or affiliates and purporting to govern or otherwise relate to the licensing transaction described in the Order Confirmation, which terms are in any way inconsistent with any terms set forth in the Order Confirmation and/or in these terms and conditions or CCC's standard operating procedures, whether such writing is prepared prior to, simultaneously with or subsequent to the Order Confirmation, and whether such writing appears on a copy of the Order Confirmation or in a separate instrument.
- 8.5. The licensing transaction described in the Order Confirmation document shall be governed by and construed under the law of the State of New York, USA, without regard to the principles thereof of conflicts of law. Any case, controversy, suit, action, or proceeding arising out of, in connection with, or related to such licensing transaction shall be brought, at CCC's sole discretion, in any federal or state court located in the County of New York, State of New York, USA, or in any federal or state court whose geographical jurisdiction covers the location of the Rightsholder set forth in the Order Confirmation. The parties expressly submit to the personal jurisdiction and venue of each such federal or state court. If you have any comments or questions about the Service or Copyright Clearance Center, please contact us at 978-750-8400 or send an e-mail to support@copyright.com.

JOHN WILEY AND SONS LICENSE
TERMS AND CONDITIONS

Nov 22, 2021

This Agreement between Mr. Tariq Sheikh ("You") and John Wiley and Sons ("John Wiley and Sons") consists of your license details and the terms and conditions provided by John Wiley and Sons and Copyright Clearance Center.

License Number 5194131221603

License date Nov 22, 2021

Licensed Content
Publisher John Wiley and Sons

Licensed Content
Publication Angewandte Chemie International Edition

Licensed Content
Title Molecular Intercalation and Electronic Two Dimensionality in Layered Hybrid Perovskites

Licensed Content
Author Tariq Sheikh, Vaibhav Nawale, Nithin Pathoor, et al

Licensed Content
Date May 4, 2020

Licensed Content
Volume 59

Licensed Content
Issue 28

Licensed Content
Pages 7

Type of use Dissertation/Thesis

Requestor type Author of this Wiley article

Format Print and electronic

Portion Full article

Will you be translating? No

Title Designing Low-Dimensional Hybrid Lead Halide Perovskites for Excitonic Photophysics, Chiroptics and Water-Stability

Institution name Indian Institute of Science Education and Research (IISER) Pune

Expected presentation date Feb 2022

Order reference number 2000

Requestor Mr. Tariq Sheikh
Location IISER Campus
Pashan
Pune
Pune, 411008
India
Attn: Mr. Tariq Sheikh

Publisher Tax ID EU826007151

Total 0.00 USD

Terms and Conditions

TERMS AND CONDITIONS

This copyrighted material is owned by or exclusively licensed to John Wiley & Sons, Inc. or one of its group companies (each a "Wiley Company") or handled on behalf of a society with which a Wiley Company has exclusive publishing rights in relation to a particular work (collectively "WILEY"). By clicking "accept" in connection with completing this licensing transaction, you agree that the following terms and conditions apply to this transaction (along with the billing and payment terms and conditions established by the Copyright Clearance Center Inc., ("CCC's Billing and Payment terms and conditions"), at the time that you opened your RightsLink account (these are available at any time at <http://myaccount.copyright.com>).

Terms and Conditions

- The materials you have requested permission to reproduce or reuse (the "Wiley Materials") are protected by copyright.
- You are hereby granted a personal, non-exclusive, non-sub licensable (on a stand-alone basis), non-transferable, worldwide, limited license to reproduce the Wiley Materials for the purpose specified in the licensing process. This license, **and any CONTENT (PDF or image file) purchased as part of your order**, is for a one-time

use only and limited to any maximum distribution number specified in the license. The first instance of republication or reuse granted by this license must be completed within two years of the date of the grant of this license (although copies prepared before the end date may be distributed thereafter). The Wiley Materials shall not be used in any other manner or for any other purpose, beyond what is granted in the license. Permission is granted subject to an appropriate acknowledgement given to the author, title of the material/book/journal and the publisher. You shall also duplicate the copyright notice that appears in the Wiley publication in your use of the Wiley Material. Permission is also granted on the understanding that nowhere in the text is a previously published source acknowledged for all or part of this Wiley Material. Any third party content is expressly excluded from this permission.

- With respect to the Wiley Materials, all rights are reserved. Except as expressly granted by the terms of the license, no part of the Wiley Materials may be copied, modified, adapted (except for minor reformatting required by the new Publication), translated, reproduced, transferred or distributed, in any form or by any means, and no derivative works may be made based on the Wiley Materials without the prior permission of the respective copyright owner. **For STM Signatory Publishers clearing permission under the terms of the [STM Permissions Guidelines](#) only, the terms of the license are extended to include subsequent editions and for editions in other languages, provided such editions are for the work as a whole in situ and does not involve the separate exploitation of the permitted figures or extracts,** You may not alter, remove or suppress in any manner any copyright, trademark or other notices displayed by the Wiley Materials. You may not license, rent, sell, loan, lease, pledge, offer as security, transfer or assign the Wiley Materials on a stand-alone basis, or any of the rights granted to you hereunder to any other person.
- The Wiley Materials and all of the intellectual property rights therein shall at all times remain the exclusive property of John Wiley & Sons Inc, the Wiley Companies, or their respective licensors, and your interest therein is only that of having possession of and the right to reproduce the Wiley Materials pursuant to Section 2 herein during the continuance of this Agreement. You agree that you own no right, title or interest in or to the Wiley Materials or any of the intellectual property rights therein. You shall have no rights hereunder other than the license as provided for above in Section 2. No right, license or interest to any trademark, trade name, service mark or other branding ("Marks") of WILEY or its licensors is granted hereunder, and you agree that you shall not assert any such right, license or interest with respect thereto
- NEITHER WILEY NOR ITS LICENSORS MAKES ANY WARRANTY OR REPRESENTATION OF ANY KIND TO YOU OR ANY THIRD PARTY, EXPRESS, IMPLIED OR STATUTORY, WITH RESPECT TO THE MATERIALS OR THE ACCURACY OF ANY INFORMATION CONTAINED IN THE MATERIALS, INCLUDING, WITHOUT LIMITATION, ANY IMPLIED WARRANTY OF MERCHANTABILITY, ACCURACY, SATISFACTORY QUALITY, FITNESS FOR A PARTICULAR PURPOSE, USABILITY, INTEGRATION OR NON-INFRINGEMENT AND ALL SUCH WARRANTIES ARE HEREBY EXCLUDED BY WILEY AND ITS LICENSORS AND WAIVED BY YOU.
- WILEY shall have the right to terminate this Agreement immediately upon breach of this Agreement by you.
- You shall indemnify, defend and hold harmless WILEY, its Licensors and their respective directors, officers, agents and employees, from and against any actual or threatened claims, demands, causes of action or proceedings arising from any breach of this Agreement by you.
- IN NO EVENT SHALL WILEY OR ITS LICENSORS BE LIABLE TO YOU OR ANY OTHER PARTY OR ANY OTHER PERSON OR ENTITY FOR ANY SPECIAL, CONSEQUENTIAL, INCIDENTAL, INDIRECT, EXEMPLARY OR PUNITIVE DAMAGES, HOWEVER CAUSED, ARISING OUT OF OR IN

CONNECTION WITH THE DOWNLOADING, PROVISIONING, VIEWING OR USE OF THE MATERIALS REGARDLESS OF THE FORM OF ACTION, WHETHER FOR BREACH OF CONTRACT, BREACH OF WARRANTY, TORT, NEGLIGENCE, INFRINGEMENT OR OTHERWISE (INCLUDING, WITHOUT LIMITATION, DAMAGES BASED ON LOSS OF PROFITS, DATA, FILES, USE, BUSINESS OPPORTUNITY OR CLAIMS OF THIRD PARTIES), AND WHETHER OR NOT THE PARTY HAS BEEN ADVISED OF THE POSSIBILITY OF SUCH DAMAGES. THIS LIMITATION SHALL APPLY NOTWITHSTANDING ANY FAILURE OF ESSENTIAL PURPOSE OF ANY LIMITED REMEDY PROVIDED HEREIN.

- Should any provision of this Agreement be held by a court of competent jurisdiction to be illegal, invalid, or unenforceable, that provision shall be deemed amended to achieve as nearly as possible the same economic effect as the original provision, and the legality, validity and enforceability of the remaining provisions of this Agreement shall not be affected or impaired thereby.
- The failure of either party to enforce any term or condition of this Agreement shall not constitute a waiver of either party's right to enforce each and every term and condition of this Agreement. No breach under this agreement shall be deemed waived or excused by either party unless such waiver or consent is in writing signed by the party granting such waiver or consent. The waiver by or consent of a party to a breach of any provision of this Agreement shall not operate or be construed as a waiver of or consent to any other or subsequent breach by such other party.
- This Agreement may not be assigned (including by operation of law or otherwise) by you without WILEY's prior written consent.
- Any fee required for this permission shall be non-refundable after thirty (30) days from receipt by the CCC.
- These terms and conditions together with CCC's Billing and Payment terms and conditions (which are incorporated herein) form the entire agreement between you and WILEY concerning this licensing transaction and (in the absence of fraud) supersedes all prior agreements and representations of the parties, oral or written. This Agreement may not be amended except in writing signed by both parties. This Agreement shall be binding upon and inure to the benefit of the parties' successors, legal representatives, and authorized assigns.
- In the event of any conflict between your obligations established by these terms and conditions and those established by CCC's Billing and Payment terms and conditions, these terms and conditions shall prevail.
- WILEY expressly reserves all rights not specifically granted in the combination of (i) the license details provided by you and accepted in the course of this licensing transaction, (ii) these terms and conditions and (iii) CCC's Billing and Payment terms and conditions.
- This Agreement will be void if the Type of Use, Format, Circulation, or Requestor Type was misrepresented during the licensing process.
- This Agreement shall be governed by and construed in accordance with the laws of the State of New York, USA, without regards to such state's conflict of law rules. Any legal action, suit or proceeding arising out of or relating to these Terms and Conditions or the breach thereof shall be instituted in a court of competent jurisdiction in New York County in the State of New York in the United States of America and each party hereby consents and submits to the personal jurisdiction of such court, waives any objection to venue in such court and consents to service of process by registered or certified mail, return receipt requested, at the last known address of such party.

WILEY OPEN ACCESS TERMS AND CONDITIONS

Wiley Publishes Open Access Articles in fully Open Access Journals and in Subscription journals offering Online Open. Although most of the fully Open Access journals publish open access articles under the terms of the Creative Commons Attribution (CC BY) License only, the subscription journals and a few of the Open Access Journals offer a choice of Creative Commons Licenses. The license type is clearly identified on the article.

The Creative Commons Attribution License

The [Creative Commons Attribution License \(CC-BY\)](#) allows users to copy, distribute and transmit an article, adapt the article and make commercial use of the article. The CC-BY license permits commercial and non-

Creative Commons Attribution Non-Commercial License

The [Creative Commons Attribution Non-Commercial \(CC-BY-NC\)License](#) permits use, distribution and reproduction in any medium, provided the original work is properly cited and is not used for commercial purposes.(see below)

Creative Commons Attribution-Non-Commercial-NoDerivs License

The [Creative Commons Attribution Non-Commercial-NoDerivs License](#) (CC-BY-NC-ND) permits use, distribution and reproduction in any medium, provided the original work is properly cited, is not used for commercial purposes and no modifications or adaptations are made. (see below)

Use by commercial "for-profit" organizations

Use of Wiley Open Access articles for commercial, promotional, or marketing purposes requires further explicit permission from Wiley and will be subject to a fee.

Further details can be found on Wiley Online Library
<http://olabout.wiley.com/WileyCDA/Section/id-410895.html>

Other Terms and Conditions:

v1.10 Last updated September 2015

Questions? customercare@copyright.com or +1-855-239-3415 (toll free in the US) or +1-978-646-2777.

JOHN WILEY AND SONS LICENSE
TERMS AND CONDITIONS

Nov 22, 2021

This Agreement between Mr. Tariq Sheikh ("You") and John Wiley and Sons ("John Wiley and Sons") consists of your license details and the terms and conditions provided by John Wiley and Sons and Copyright Clearance Center.

License Number 5194131013103

License date Nov 22, 2021

Licensed Content
Publisher John Wiley and Sons

Licensed Content
Publication Angewandte Chemie International Edition

Licensed Content
Title Introducing Intermolecular Cation- π Interactions for Water-Stable Low Dimensional Hybrid Lead Halide Perovskites

Licensed Content
Author Tariq Sheikh, Shabnum Maqbool, Pankaj Mandal, et al

Licensed Content
Date Jul 9, 2021

Licensed Content
Volume 60

Licensed Content
Issue 33

Licensed Content
Pages 7

Type of use Dissertation/Thesis

Requestor type Author of this Wiley article

Format Print and electronic

Portion	Full article
Will you be translating?	No
Title	Designing Low-Dimensional Hybrid Lead Halide Perovskites for Excitonic Photophysics, Chiroptics and Water-Stability
Institution name	Indian Institute of Science Education and Research (IISER) Pune
Expected presentation date	Feb 2022
Order reference number	1999
Requestor Location	Mr. Tariq Sheikh IISER Campus Pashan Pune Pune, 411008 India Attn: Mr. Tariq Sheikh
Publisher Tax ID	EU826007151
Total	0.00 USD

Terms and Conditions

TERMS AND CONDITIONS

This copyrighted material is owned by or exclusively licensed to John Wiley & Sons, Inc. or one of its group companies (each a "Wiley Company") or handled on behalf of a society with which a Wiley Company has exclusive publishing rights in relation to a particular work (collectively "WILEY"). By clicking "accept" in connection with completing this licensing transaction, you agree that the following terms and conditions apply to this transaction (along with the billing and payment terms and conditions established by the Copyright Clearance Center Inc., ("CCC's Billing and Payment terms and conditions"), at the time that you opened your RightsLink account (these are available at any time at <http://myaccount.copyright.com>).

Terms and Conditions

- The materials you have requested permission to reproduce or reuse (the "Wiley Materials") are protected by copyright.
- You are hereby granted a personal, non-exclusive, non-sub licensable (on a stand-alone basis), non-transferable, worldwide, limited license to reproduce the Wiley Materials for the purpose specified in the licensing process. This license, **and any**

CONTENT (PDF or image file) purchased as part of your order, is for a one-time use only and limited to any maximum distribution number specified in the license. The first instance of republication or reuse granted by this license must be completed within two years of the date of the grant of this license (although copies prepared before the end date may be distributed thereafter). The Wiley Materials shall not be used in any other manner or for any other purpose, beyond what is granted in the license. Permission is granted subject to an appropriate acknowledgement given to the author, title of the material/book/journal and the publisher. You shall also duplicate the copyright notice that appears in the Wiley publication in your use of the Wiley Material. Permission is also granted on the understanding that nowhere in the text is a previously published source acknowledged for all or part of this Wiley Material. Any third party content is expressly excluded from this permission.

- With respect to the Wiley Materials, all rights are reserved. Except as expressly granted by the terms of the license, no part of the Wiley Materials may be copied, modified, adapted (except for minor reformatting required by the new Publication), translated, reproduced, transferred or distributed, in any form or by any means, and no derivative works may be made based on the Wiley Materials without the prior permission of the respective copyright owner. **For STM Signatory Publishers clearing permission under the terms of the [STM Permissions Guidelines](#) only, the terms of the license are extended to include subsequent editions and for editions in other languages, provided such editions are for the work as a whole in situ and does not involve the separate exploitation of the permitted figures or extracts,** You may not alter, remove or suppress in any manner any copyright, trademark or other notices displayed by the Wiley Materials. You may not license, rent, sell, loan, lease, pledge, offer as security, transfer or assign the Wiley Materials on a stand-alone basis, or any of the rights granted to you hereunder to any other person.
- The Wiley Materials and all of the intellectual property rights therein shall at all times remain the exclusive property of John Wiley & Sons Inc, the Wiley Companies, or their respective licensors, and your interest therein is only that of having possession of and the right to reproduce the Wiley Materials pursuant to Section 2 herein during the continuance of this Agreement. You agree that you own no right, title or interest in or to the Wiley Materials or any of the intellectual property rights therein. You shall have no rights hereunder other than the license as provided for above in Section 2. No right, license or interest to any trademark, trade name, service mark or other branding ("Marks") of WILEY or its licensors is granted hereunder, and you agree that you shall not assert any such right, license or interest with respect thereto
- NEITHER WILEY NOR ITS LICENSORS MAKES ANY WARRANTY OR REPRESENTATION OF ANY KIND TO YOU OR ANY THIRD PARTY, EXPRESS, IMPLIED OR STATUTORY, WITH RESPECT TO THE MATERIALS OR THE ACCURACY OF ANY INFORMATION CONTAINED IN THE MATERIALS, INCLUDING, WITHOUT LIMITATION, ANY IMPLIED WARRANTY OF MERCHANTABILITY, ACCURACY, SATISFACTORY QUALITY, FITNESS FOR A PARTICULAR PURPOSE, USABILITY, INTEGRATION OR NON-INFRINGEMENT AND ALL SUCH WARRANTIES ARE HEREBY EXCLUDED BY WILEY AND ITS LICENSORS AND WAIVED BY YOU.
- WILEY shall have the right to terminate this Agreement immediately upon breach of this Agreement by you.
- You shall indemnify, defend and hold harmless WILEY, its Licensors and their respective directors, officers, agents and employees, from and against any actual or threatened claims, demands, causes of action or proceedings arising from any breach of this Agreement by you.
- IN NO EVENT SHALL WILEY OR ITS LICENSORS BE LIABLE TO YOU OR ANY OTHER PARTY OR ANY OTHER PERSON OR ENTITY FOR ANY SPECIAL, CONSEQUENTIAL, INCIDENTAL, INDIRECT, EXEMPLARY OR

PUNITIVE DAMAGES, HOWEVER CAUSED, ARISING OUT OF OR IN CONNECTION WITH THE DOWNLOADING, PROVISIONING, VIEWING OR USE OF THE MATERIALS REGARDLESS OF THE FORM OF ACTION, WHETHER FOR BREACH OF CONTRACT, BREACH OF WARRANTY, TORT, NEGLIGENCE, INFRINGEMENT OR OTHERWISE (INCLUDING, WITHOUT LIMITATION, DAMAGES BASED ON LOSS OF PROFITS, DATA, FILES, USE, BUSINESS OPPORTUNITY OR CLAIMS OF THIRD PARTIES), AND WHETHER OR NOT THE PARTY HAS BEEN ADVISED OF THE POSSIBILITY OF SUCH DAMAGES. THIS LIMITATION SHALL APPLY NOTWITHSTANDING ANY FAILURE OF ESSENTIAL PURPOSE OF ANY LIMITED REMEDY PROVIDED HEREIN.

- Should any provision of this Agreement be held by a court of competent jurisdiction to be illegal, invalid, or unenforceable, that provision shall be deemed amended to achieve as nearly as possible the same economic effect as the original provision, and the legality, validity and enforceability of the remaining provisions of this Agreement shall not be affected or impaired thereby.
- The failure of either party to enforce any term or condition of this Agreement shall not constitute a waiver of either party's right to enforce each and every term and condition of this Agreement. No breach under this agreement shall be deemed waived or excused by either party unless such waiver or consent is in writing signed by the party granting such waiver or consent. The waiver by or consent of a party to a breach of any provision of this Agreement shall not operate or be construed as a waiver of or consent to any other or subsequent breach by such other party.
- This Agreement may not be assigned (including by operation of law or otherwise) by you without WILEY's prior written consent.
- Any fee required for this permission shall be non-refundable after thirty (30) days from receipt by the CCC.
- These terms and conditions together with CCC's Billing and Payment terms and conditions (which are incorporated herein) form the entire agreement between you and WILEY concerning this licensing transaction and (in the absence of fraud) supersedes all prior agreements and representations of the parties, oral or written. This Agreement may not be amended except in writing signed by both parties. This Agreement shall be binding upon and inure to the benefit of the parties' successors, legal representatives, and authorized assigns.
- In the event of any conflict between your obligations established by these terms and conditions and those established by CCC's Billing and Payment terms and conditions, these terms and conditions shall prevail.
- WILEY expressly reserves all rights not specifically granted in the combination of (i) the license details provided by you and accepted in the course of this licensing transaction, (ii) these terms and conditions and (iii) CCC's Billing and Payment terms and conditions.
- This Agreement will be void if the Type of Use, Format, Circulation, or Requestor Type was misrepresented during the licensing process.
- This Agreement shall be governed by and construed in accordance with the laws of the State of New York, USA, without regards to such state's conflict of law rules. Any legal action, suit or proceeding arising out of or relating to these Terms and Conditions or the breach thereof shall be instituted in a court of competent jurisdiction in New York County in the State of New York in the United States of America and each party hereby consents and submits to the personal jurisdiction of such court, waives any objection to venue in such court and consents to service of process by registered or certified mail, return receipt requested, at the last known address of such party.

WILEY OPEN ACCESS TERMS AND CONDITIONS

Wiley Publishes Open Access Articles in fully Open Access Journals and in Subscription journals offering Online Open. Although most of the fully Open Access journals publish open access articles under the terms of the Creative Commons Attribution (CC BY) License only, the subscription journals and a few of the Open Access Journals offer a choice of Creative Commons Licenses. The license type is clearly identified on the article.

The Creative Commons Attribution License

The [Creative Commons Attribution License \(CC-BY\)](#) allows users to copy, distribute and transmit an article, adapt the article and make commercial use of the article. The CC-BY license permits commercial and non-

Creative Commons Attribution Non-Commercial License

The [Creative Commons Attribution Non-Commercial \(CC-BY-NC\)License](#) permits use, distribution and reproduction in any medium, provided the original work is properly cited and is not used for commercial purposes.(see below)

Creative Commons Attribution-Non-Commercial-NoDerivs License

The [Creative Commons Attribution Non-Commercial-NoDerivs License](#) (CC-BY-NC-ND) permits use, distribution and reproduction in any medium, provided the original work is properly cited, is not used for commercial purposes and no modifications or adaptations are made. (see below)

Use by commercial "for-profit" organizations

Use of Wiley Open Access articles for commercial, promotional, or marketing purposes requires further explicit permission from Wiley and will be subject to a fee.

Further details can be found on Wiley Online Library
<http://olabout.wiley.com/WileyCDA/Section/id-410895.html>

Other Terms and Conditions:

v1.10 Last updated September 2015

Questions? customercare@copyright.com or +1-855-239-3415 (toll free in the US) or +1-978-646-2777.

Reuse of figures in thesis; non profit

ACS Publications <support@services.acs.org>

Mon, Nov 22, 2021 at 9:51 PM

Reply-To: support@services.acs.org

To: tariq.sheikh@students.iiserpune.ac.in

Hello Dr. Sheikh,

Your permission requested is granted and there is no fee for this reuse.

In your planned reuse, you must cite the ACS article as the source, add this direct link: <https://pubs.acs.org/doi/10.1021/nl5048779> and include a notice to readers that further permission related to the material excerpted should be directed to the ACS.

Please do not hesitate to contact me if you need any further assistance.

Drew Jenkins
ACS Publications Support
Customer Services & Information
Website: <https://acs.service-now.com/acs>
Email: support@services.acs.org
Phone: 800-227-9919 | 202-872-(HELP) 4357

Case Info:

Case Number : CSCSI0037401

Created On: 11-22-2021 09:31:50 AM EST

Short Description: Reuse of figures in thesis; non profit

Description: Dear ACS Team,

I would like to reuse two figures from the paper mentioned below in the introduction part of my thesis. I pledge to give the proper citations and credits.

Details of figure and paper:

Link to the paper: <https://pubs.acs.org/doi/10.1021/nl5048779>

Title of the paper: Nanocrystals of Cesium Lead Halide Perovskites (CsPbX₃, X = Cl, Br, and I): Novel Optoelectronic Materials Showing Bright Emission with Wide Color Gamut.

Figure details: (1) TOC figure and (2) figure number 2.

Details where the content will be used:

Thesis Author: Tariq Ahmad Sheikh

Thesis Title: Designing Low-Dimensional Hybrid Lead Halide Perovskites for Excitonic Photophysics, Chiroptics and Water-Stability.

presentation data: February 2022.

Institute: Indian Institute of Science Education and Research (IISER) pune.

Please grant me permission for the same. I would be highly thankful to you for this.

Thanks and Regards

Tariq Ahmad Sheikh

Tariq Sheikh

IISER Pune

Department of Chemistry,

Dr. Homi Bhabha Road,

*Pashan, **Pune-411008*

India.

Sincerely,

Drew Jenkins

ACS Chemistry for Life
American Chemical Society

Ref:MSG0255531_caGjavHRmLXvpjRJDoJo

This is a License Agreement between Tariq Ahmad Sheikh ("User") and Copyright Clearance Center, Inc. ("CCC") on behalf of the Rightsholder identified in the order details below. The license consists of the order details, the CCC Terms and Conditions below, and any Rightsholder Terms and Conditions which are included below.

All payments must be made in full to CCC in accordance with the CCC Terms and Conditions below.

Order Date	22-Nov-2021	Type of Use	Republish in a thesis/dissertation
Order License ID	1163352-1	Publisher	AMERICAN ASSOCIATION FOR THE ADVANCEMENT OF SCIENCE
ISSN	0036-8075	Portion	Image/photo/illustration

LICENSED CONTENT

Publication Title	Science	Publication Type	Journal
Article Title	Properties and potential optoelectronic applications of lead halide perovskite nanocrystals.	Start Page	745
		End Page	750
		Issue	6364
Date	01/01/1880	Volume	358
Language	English		
Country	United States of America		
Rightsholder	American Association for the Advancement of Science		

REQUEST DETAILS

Portion Type	Image/photo/illustration	Distribution	Worldwide
Number of images / photos / illustrations	1	Translation	Original language of publication
Format (select all that apply)	Print, Electronic	Copies for the disabled?	No
		Minor editing privileges?	No
Who will republish the content?	Not-for-profit entity	Incidental promotional use?	No
Duration of Use	Life of current edition	Currency	USD
Lifetime Unit Quantity	Up to 9,999		
Rights Requested	Main product		

NEW WORK DETAILS

Title	Designing Low-Dimensional Hybrid Lead Halide Perovskites for Excitonic Photophysics, Chiroptics and Water-Stability	Institution name	Indian Institute of Science Education and Research (IISER) Pune
		Expected presentation date	2022-02-15
Instructor name	Tariq Ahmad Sheikh		

ADDITIONAL DETAILS

Order reference number	N/A
------------------------	-----

The requesting person / organization to appear on the license

Tariq Ahmad Sheikh

REUSE CONTENT DETAILS

Title, description or numeric reference of the portion(s)	figure 4a	Title of the article/chapter the portion is from	Properties and potential optoelectronic applications of lead halide perovskite nanocrystals.
Editor of portion(s)	Kovalenko, Maksym V; Protesescu, Loredana; Bodnarchuk, Maryna I	Author of portion(s)	Kovalenko, Maksym V; Protesescu, Loredana; Bodnarchuk, Maryna I
Volume of serial or monograph	358	Issue, if republishing an article from a serial	6364
Page or page range of portion	745-750	Publication date of portion	2017-11-10

RIGHTSHOLDER TERMS AND CONDITIONS

If the AAAS material covered by this permission was published in Science during the years 1974 - 1994, you must also obtain permission from the author, who may grant or withhold permission, and who may or may not charge a fee if permission is granted. See original article for author's address. This condition does not apply to news articles. Whenever possible, we ask that electronic uses of the AAAS material permitted herein include a hyperlink to the original work on AAAS's website (hyperlink may be embedded in the reference citation). AAAS material reproduced in your work identified herein must not account for more than 30% of the total contents of that work. AAAS must publish the full paper prior to use of any text. AAAS material must not imply any endorsement by the American Association for the Advancement of Science. AAAS makes no representations or warranties as to the accuracy of any information contained in the AAAS material covered by this permission, including any warranties of merchantability or fitness for a particular purpose.

CCC Terms and Conditions

1. Description of Service; Defined Terms. This Republication License enables the User to obtain licenses for republication of one or more copyrighted works as described in detail on the relevant Order Confirmation (the "Work(s)"). Copyright Clearance Center, Inc. ("CCC") grants licenses through the Service on behalf of the rightsholder identified on the Order Confirmation (the "Rightsholder"). "Republication", as used herein, generally means the inclusion of a Work, in whole or in part, in a new work or works, also as described on the Order Confirmation. "User", as used herein, means the person or entity making such republication.
2. The terms set forth in the relevant Order Confirmation, and any terms set by the Rightsholder with respect to a particular Work, govern the terms of use of Works in connection with the Service. By using the Service, the person transacting for a republication license on behalf of the User represents and warrants that he/she/it (a) has been duly authorized by the User to accept, and hereby does accept, all such terms and conditions on behalf of User, and (b) shall inform User of all such terms and conditions. In the event such person is a "freelancer" or other third party independent of User and CCC, such party shall be deemed jointly a "User" for purposes of these terms and conditions. In any event, User shall be deemed to have accepted and agreed to all such terms and conditions if User republishes the Work in any fashion.
3. Scope of License; Limitations and Obligations.
 - 3.1. All Works and all rights therein, including copyright rights, remain the sole and exclusive property of the Rightsholder. The license created by the exchange of an Order Confirmation (and/or any invoice) and payment by User of the full amount set forth on that document includes only those rights expressly set forth in the Order Confirmation and in these terms and conditions, and conveys no other rights in the Work(s) to User. All rights not expressly granted are hereby reserved.
 - 3.2. General Payment Terms: You may pay by credit card or through an account with us payable at the end of the month. If you and we agree that you may establish a standing account with CCC, then the following terms apply: Remit Payment to: Copyright Clearance Center, 29118 Network Place, Chicago, IL 60673-1291. Payments Due: Invoices are payable upon their delivery to you (or upon our notice to you that they are available to you for downloading). After 30 days, outstanding amounts will be subject to a service charge of 1-

1/2% per month or, if less, the maximum rate allowed by applicable law. Unless otherwise specifically set forth in the Order Confirmation or in a separate written agreement signed by CCC, invoices are due and payable on "net 30" terms. While User may exercise the rights licensed immediately upon issuance of the Order Confirmation, the license is automatically revoked and is null and void, as if it had never been issued, if complete payment for the license is not received on a timely basis either from User directly or through a payment agent, such as a credit card company.

- 3.3. Unless otherwise provided in the Order Confirmation, any grant of rights to User (i) is "one-time" (including the editions and product family specified in the license), (ii) is non-exclusive and non-transferable and (iii) is subject to any and all limitations and restrictions (such as, but not limited to, limitations on duration of use or circulation) included in the Order Confirmation or invoice and/or in these terms and conditions. Upon completion of the licensed use, User shall either secure a new permission for further use of the Work(s) or immediately cease any new use of the Work(s) and shall render inaccessible (such as by deleting or by removing or severing links or other locators) any further copies of the Work (except for copies printed on paper in accordance with this license and still in User's stock at the end of such period).
 - 3.4. In the event that the material for which a republication license is sought includes third party materials (such as photographs, illustrations, graphs, inserts and similar materials) which are identified in such material as having been used by permission, User is responsible for identifying, and seeking separate licenses (under this Service or otherwise) for, any of such third party materials; without a separate license, such third party materials may not be used.
 - 3.5. Use of proper copyright notice for a Work is required as a condition of any license granted under the Service. Unless otherwise provided in the Order Confirmation, a proper copyright notice will read substantially as follows: "Republished with permission of [Rightsholder's name], from [Work's title, author, volume, edition number and year of copyright]; permission conveyed through Copyright Clearance Center, Inc. " Such notice must be provided in a reasonably legible font size and must be placed either immediately adjacent to the Work as used (for example, as part of a by-line or footnote but not as a separate electronic link) or in the place where substantially all other credits or notices for the new work containing the republished Work are located. Failure to include the required notice results in loss to the Rightsholder and CCC, and the User shall be liable to pay liquidated damages for each such failure equal to twice the use fee specified in the Order Confirmation, in addition to the use fee itself and any other fees and charges specified.
 - 3.6. User may only make alterations to the Work if and as expressly set forth in the Order Confirmation. No Work may be used in any way that is defamatory, violates the rights of third parties (including such third parties' rights of copyright, privacy, publicity, or other tangible or intangible property), or is otherwise illegal, sexually explicit or obscene. In addition, User may not conjoin a Work with any other material that may result in damage to the reputation of the Rightsholder. User agrees to inform CCC if it becomes aware of any infringement of any rights in a Work and to cooperate with any reasonable request of CCC or the Rightsholder in connection therewith.
4. Indemnity. User hereby indemnifies and agrees to defend the Rightsholder and CCC, and their respective employees and directors, against all claims, liability, damages, costs and expenses, including legal fees and expenses, arising out of any use of a Work beyond the scope of the rights granted herein, or any use of a Work which has been altered in any unauthorized way by User, including claims of defamation or infringement of rights of copyright, publicity, privacy or other tangible or intangible property.
 5. Limitation of Liability. UNDER NO CIRCUMSTANCES WILL CCC OR THE RIGHTSHOLDER BE LIABLE FOR ANY DIRECT, INDIRECT, CONSEQUENTIAL OR INCIDENTAL DAMAGES (INCLUDING WITHOUT LIMITATION DAMAGES FOR LOSS OF BUSINESS PROFITS OR INFORMATION, OR FOR BUSINESS INTERRUPTION) ARISING OUT OF THE USE OR INABILITY TO USE A WORK, EVEN IF ONE OF THEM HAS BEEN ADVISED OF THE POSSIBILITY OF SUCH DAMAGES. In any event, the total liability of the Rightsholder and CCC (including their respective employees and directors) shall not exceed the total amount actually paid by User for this license. User assumes full liability for the actions and omissions of its principals, employees, agents, affiliates, successors and assigns.
 6. Limited Warranties. THE WORK(S) AND RIGHT(S) ARE PROVIDED "AS IS". CCC HAS THE RIGHT TO GRANT TO USER THE RIGHTS GRANTED IN THE ORDER CONFIRMATION DOCUMENT. CCC AND THE RIGHTSHOLDER DISCLAIM ALL OTHER WARRANTIES RELATING TO THE WORK(S) AND RIGHT(S), EITHER EXPRESS OR IMPLIED, INCLUDING WITHOUT LIMITATION IMPLIED WARRANTIES OF MERCHANTABILITY OR FITNESS FOR A PARTICULAR PURPOSE. ADDITIONAL RIGHTS MAY BE REQUIRED TO USE ILLUSTRATIONS, GRAPHS, PHOTOGRAPHS, ABSTRACTS, INSERTS OR OTHER PORTIONS OF THE WORK (AS OPPOSED TO THE ENTIRE WORK) IN A MANNER CONTEMPLATED BY USER; USER

UNDERSTANDS AND AGREES THAT NEITHER CCC NOR THE RIGHTSHOLDER MAY HAVE SUCH ADDITIONAL RIGHTS TO GRANT.

7. Effect of Breach. Any failure by User to pay any amount when due, or any use by User of a Work beyond the scope of the license set forth in the Order Confirmation and/or these terms and conditions, shall be a material breach of the license created by the Order Confirmation and these terms and conditions. Any breach not cured within 30 days of written notice thereof shall result in immediate termination of such license without further notice. Any unauthorized (but licensable) use of a Work that is terminated immediately upon notice thereof may be liquidated by payment of the Rightsholder's ordinary license price therefor; any unauthorized (and unlicensable) use that is not terminated immediately for any reason (including, for example, because materials containing the Work cannot reasonably be recalled) will be subject to all remedies available at law or in equity, but in no event to a payment of less than three times the Rightsholder's ordinary license price for the most closely analogous licensable use plus Rightsholder's and/or CCC's costs and expenses incurred in collecting such payment.

8. Miscellaneous.

8.1. User acknowledges that CCC may, from time to time, make changes or additions to the Service or to these terms and conditions, and CCC reserves the right to send notice to the User by electronic mail or otherwise for the purposes of notifying User of such changes or additions; provided that any such changes or additions shall not apply to permissions already secured and paid for.

8.2. Use of User-related information collected through the Service is governed by CCC's privacy policy, available online here:<https://marketplace.copyright.com/rs-ui-web/mp/privacy-policy>

8.3. The licensing transaction described in the Order Confirmation is personal to User. Therefore, User may not assign or transfer to any other person (whether a natural person or an organization of any kind) the license created by the Order Confirmation and these terms and conditions or any rights granted hereunder; provided, however, that User may assign such license in its entirety on written notice to CCC in the event of a transfer of all or substantially all of User's rights in the new material which includes the Work(s) licensed under this Service.

8.4. No amendment or waiver of any terms is binding unless set forth in writing and signed by the parties. The Rightsholder and CCC hereby object to any terms contained in any writing prepared by the User or its principals, employees, agents or affiliates and purporting to govern or otherwise relate to the licensing transaction described in the Order Confirmation, which terms are in any way inconsistent with any terms set forth in the Order Confirmation and/or in these terms and conditions or CCC's standard operating procedures, whether such writing is prepared prior to, simultaneously with or subsequent to the Order Confirmation, and whether such writing appears on a copy of the Order Confirmation or in a separate instrument.

8.5. The licensing transaction described in the Order Confirmation document shall be governed by and construed under the law of the State of New York, USA, without regard to the principles thereof of conflicts of law. Any case, controversy, suit, action, or proceeding arising out of, in connection with, or related to such licensing transaction shall be brought, at CCC's sole discretion, in any federal or state court located in the County of New York, State of New York, USA, or in any federal or state court whose geographical jurisdiction covers the location of the Rightsholder set forth in the Order Confirmation. The parties expressly submit to the personal jurisdiction and venue of each such federal or state court. If you have any comments or questions about the Service or Copyright Clearance Center, please contact us at 978-750-8400 or send an e-mail to support@copyright.com.

Searching for "Defect-Tolerant" Photovoltaic Materials: Combined Theoretical and Experimental Screening



Author: Riley E. Brandt, Jeremy R. Poindexter, Prashun Gorai, et al

Publication: Chemistry of Materials

Publisher: American Chemical Society

Date: Jun 1, 2017

Copyright © 2017, American Chemical Society

PERMISSION/LICENSE IS GRANTED FOR YOUR ORDER AT NO CHARGE

This type of permission/license, instead of the standard Terms and Conditions, is sent to you because no fee is being charged for your order. Please note the following:

- Permission is granted for your request in both print and electronic formats, and translations.
- If figures and/or tables were requested, they may be adapted or used in part.
- Please print this page for your records and send a copy of it to your publisher/graduate school.
- Appropriate credit for the requested material should be given as follows: "Reprinted (adapted) with permission from {COMPLETE REFERENCE CITATION}. Copyright {YEAR} American Chemical Society." Insert appropriate information in place of the capitalized words.
- One-time permission is granted only for the use specified in your RightsLink request. No additional uses are granted (such as derivative works or other editions). For any uses, please submit a new request.

If credit is given to another source for the material you requested from RightsLink, permission must be obtained from that source.

[BACK](#)

[CLOSE WINDOW](#)

Organic-Inorganic Perovskites: Structural Versatility for Functional Materials Design



Author: Bayrammurad Saparov, David B. Mitzi

Publication: Chemical Reviews

Publisher: American Chemical Society

Date: Apr 1, 2016

Copyright © 2016, American Chemical Society

PERMISSION/LICENSE IS GRANTED FOR YOUR ORDER AT NO CHARGE

This type of permission/license, instead of the standard Terms and Conditions, is sent to you because no fee is being charged for your order. Please note the following:

- Permission is granted for your request in both print and electronic formats, and translations.
- If figures and/or tables were requested, they may be adapted or used in part.
- Please print this page for your records and send a copy of it to your publisher/graduate school.
- Appropriate credit for the requested material should be given as follows: "Reprinted (adapted) with permission from {COMPLETE REFERENCE CITATION}. Copyright {YEAR} American Chemical Society." Insert appropriate information in place of the capitalized words.
- One-time permission is granted only for the use specified in your RightsLink request. No additional uses are granted (such as derivative works or other editions). For any uses, please submit a new request.

If credit is given to another source for the material you requested from RightsLink, permission must be obtained from that source.

[BACK](#)

[CLOSE WINDOW](#)



Reuse of figures in thesis; non profit

ACS Publications <support@services.acs.org>

Mon, Nov 22, 2021 at 10:17 PM

Reply-To: support@services.acs.org

To: tariq.sheikh@students.iiserpune.ac.in

Hello Dr. Sheikh,

Your permission requested is granted and there is no fee for this reuse.

In your planned reuse, you must cite the ACS article as the source, add this direct link: <https://pubs.acs.org/doi/10.1021/acs.chemmater.6b00847> and include a notice to readers that further permission related to the material excerpted should be directed to the ACS.

Please do not hesitate to contact me if you need any further assistance.

Drew Jenkins
ACS Publications Support
Customer Services & Information
Website: <https://acs.service-now.com/acs>
Email: support@services.acs.org
Phone: 800-227-9919 | 202-872-(HELP) 4357

Case Info:

Case Number : CSCSI0037415

Created On: 11-22-2021 10:31:30 AM EST

Short Description: Reuse of figures in thesis; non profit

Description: Dear ACS Team,

I would like to reuse two figures from the paper mentioned below in the introduction part of my thesis. I pledge to give the proper citations and credits.

Details of figure and paper:

Link to the paper: <https://pubs.acs.org/doi/10.1021/acs.chemmater.6b00847>

Title of the paper: Ruddlesden–Popper Hybrid Lead Iodide Perovskite 2D Homologous Semiconductors

Figure details: (1) figure number 2 (2) figure number 5.

Details where the content will be used:

Thesis Author: Tariq Ahmad Sheikh

Thesis Title: Designing Low-Dimensional Hybrid Lead Halide Perovskites for Excitonic Photophysics, Chiroptics and Water-Stability.

Presentation data: February 2022.

Institute: Indian Institute of Science Education and Research (IISER) pune.

Please grant me permission for the same. I would be highly thankful to you for this.

Thanks and Regards

Tariq Ahmad Sheikh

Tariq Sheikh
IISER Pune
Department of Chemistry,
Dr. Homi Bhabha Road,
*Pashan, **Pune-411008*
India.

Sincerely,

Drew Jenkins

ACS Chemistry for Life
American Chemical Society

Ref:MSG0255565_dRldeGLvIOjerkNTIVqk



Tariq Sheikh <tariq.sheikh@students.iiserpune.ac.in>

THESIS/DISSERTATION USE - SCI ADVANCES FIGURE - WANG ET AL 2019

1 message

permissions <permissions@aaas.org>
To: Tariq Sheikh <tariq.sheikh@students.iiserpune.ac.in>

Fri, Dec 3, 2021 at 12:53 AM

Reproducing Science Advances figures in your Thesis or Dissertation

Dear Tariq Ahmad Sheikh:

Thank you very much for your request and interest in the content requested in your email below. We are happy to have you include the figures in your thesis or dissertation.

The following should be done when reproducing the Science Advances figure/s:

1. Credit the author and credit the original Science Advances article.

Appropriate credit lines follow this format: "Reprinted/(modified from if applicable) [INSERT Science Advances REFERENCE CITATION]. © The Authors, some rights reserved; exclusive licensee AAAS. Distributed under a CC BY-NC 4.0 License (<http://creativecommons.org/licenses/by-nc/4.0/>)"

2. If any modifications are made to the material, those changes must be identified.

3. Use of the material must not imply any endorsement by the authors or by AAAS and Science Advances.

4. No legal terms or technological measures may be applied to the reproduced material that conflicts with CC BY-NC license terms.

5. Permission covers the distribution of your dissertation or thesis on demand by a third party distributor (e.g. ProQuest / UMI), provided the AAAS material covered by this permission remains in situ and is not distributed by that third party outside of the context of your Thesis/Dissertation.

Please note: Portions, images, or figures appearing in the original Science Advances article that are attributed to other publishers or individuals are not subject to the article's Creative Commons license. Permission from the credited party should be sought prior to reproduction of such material.

If anything more is needed, please let me know.

Kind regards,

Liz

Elizabeth Sandler (Ms.)

Rights & Permissions, *Science* family of journals

American Association for the Advancement of Science (AAAS)

1200 New York Avenue

Washington, DC 20005

E: esandler@aaas.org

Tel: +1-202-326-6765

From: Tariq Sheikh <tariq.sheikh@students.iiserpune.ac.in>

Sent: Monday, November 22, 2021 9:30 AM

To: permissions <permissions@aaas.org>

Subject: Permission required for reproducing one figure of science advance articles in my thesis

[EXTERNAL EMAIL]

Dear AAAS Team,

I am a PhD research scholar at IISER Pune India. I want to use one figure from the following Science Advance articles in my thesis. I request your permission for the same.

The use is completely non-commercial non-profit. Please find the details below.

Name: Tariq Ahmad Sheikh

Institute: Indian institute of science education and research, Pune, India

Mail: tariq.sheikh@students.iiserpune.ac.in

Ph. no.: +919682516508

Details of the content to be used:

Publication Title: Science Advance

Article Title: Distinct conducting layer edge states in two-dimensional (2D) halide perovskite

Authors: Kai Wang, Congcong Wu, Yuanyuan Jiang, Dong Yang, Ke Wang and Shashank Priya

Volume and Date: Vol. 5, 12 July 2019

Materials used: Figure 1

Link to the Article: <https://www.science.org/doi/10.1126/sciadv.aau3241>

Usage Details: Use in thesis

Thesis title: Designing Low-Dimensional Hybrid Lead Halide Perovskites for Excitonic Photophysics, Chiroptics and Water-Stability.

Article Title:

Thesis Author: Tariq Ahmad Sheikh

Expected Presentation: February 2022

Institute: Indian Institute of Science Education and Research (IISER) Pune.

Format: Print and electronic

Rights Seeking: Reproducing in thesis

Please grant me permission for the same. I would be highly thankful to you for this.

Thanks and Regards

Tariq Ahmad Sheikh

Tariq Sheikh

IISER Pune

Department of Chemistry,

Dr. Homi Bhabha Road,

Pashan, Pune-411008

India.

Reuse of figure in thesis; non profit

ACS Publications <support@services.acs.org>

Mon, Nov 22, 2021 at 10:52 PM

Reply-To: support@services.acs.org

To: tariq.sheikh@students.iiserpune.ac.in

Dear Dr. Sheikh,

Thank you for contacting ACS Publications Support.

Your permission requested is granted and there is no fee for this reuse. In your planned reuse, you must cite the ACS article as the source, add this direct link <<https://pubs.acs.org/doi/full/10.1021/jacs.6b08900>>, and include a notice to readers that further permissions related to the material excerpted should be directed to the ACS.

Sincerely,

Budimir Jelic
ACS Publications
Customer Services & Information
Website: <https://help.acs.org>

Case Info:

Case Number : CSCSI0037426

Created On: 11-22-2021 11:33:16 AM EST

Short Description: Reuse of figure in thesis; non profit

Description: Dear ACS Team,

I would like to reuse one figure from the paper mentioned below in the introduction part of my thesis. I pledge to give the proper citations and credits.

Details of figure and paper:

Link to the paper: <https://pubs.acs.org/doi/full/10.1021/jacs.6b08900>

Title of the paper: Monodisperse Formamidinium Lead Bromide Nanocrystals with Bright and Stable Green Photoluminescence

Figure details: Figure number 1

Details where the content will be used:

Thesis Author: Tariq Ahmad Sheikh

Thesis Title: Designing Low-Dimensional Hybrid Lead Halide Perovskites for Excitonic Photophysics, Chiroptics and Water-Stability.

Presentation data: February 2022.

Institute: Indian Institute of Science Education and Research (IISER) Pune.

Please grant me permission for the same. I would be highly thankful to you for this.

Thanks and Regards

Tariq Ahmad Sheikh

Tariq Sheikh

IISER Pune

Department of Chemistry,

Dr. Homi Bhabha Road,

*Pashan, **Pune-411008*

India.

Ref:MSG0255606_kRAfUjdlylZNidIUileE

Synthesis, Crystal Structure, and Optical and Thermal Properties of $(C_4H_9NH_3)_2MI_4$ (M = Ge, Sn, Pb)



Author: David B. Mitzi

Publication: Chemistry of Materials

Publisher: American Chemical Society

Date: Jan 1, 1996

Copyright © 1996, American Chemical Society

PERMISSION/LICENSE IS GRANTED FOR YOUR ORDER AT NO CHARGE

This type of permission/license, instead of the standard Terms and Conditions, is sent to you because no fee is being charged for your order. Please note the following:

- Permission is granted for your request in both print and electronic formats, and translations.
- If figures and/or tables were requested, they may be adapted or used in part.
- Please print this page for your records and send a copy of it to your publisher/graduate school.
- Appropriate credit for the requested material should be given as follows: "Reprinted (adapted) with permission from {COMPLETE REFERENCE CITATION}. Copyright {YEAR} American Chemical Society." Insert appropriate information in place of the capitalized words.
- One-time permission is granted only for the use specified in your RightsLink request. No additional uses are granted (such as derivative works or other editions). For any uses, please submit a new request.

If credit is given to another source for the material you requested from RightsLink, permission must be obtained from that source.

[BACK](#)

[CLOSE WINDOW](#)